Spectral signatures and properties of carbon defects in GaN and AlN

vorgelegt von
M. Sc.
Ivan Gamov
ORCID: 0000-0003-2307-6860

an der Fakultät II – Mathematik und Naturwissenschaften
der Technischen Universität Berlin
zur Erlangung des akademischen Grades

Doktor der Naturwissenschaften
– Dr. rer. nat. –
genehmigte Dissertation

Promotionsausschuss:
Vorsitzender: Prof. Dr. Michael Lehmann
Gutachter: Prof. Dr. Michael Kneissl
Gutachter: Prof. Dr. Matthias Bickermann
Gutachter: Prof. Dr. Michael Reshchikov

Tag der wissenschaftlichen Aussprache: 28. Februar 2022

Berlin 2022

“All colours will agree in the dark”

— **Francis Bacon**

Abstract

Semi-insulating GaN and UV-transparent AlN are in demand in optoelectronics based on III-nitrides. Carbon (C) as an impurity is responsible for these properties of the materials. However, neither the compensation mechanism for C-doping of GaN nor the nature of the 4.7 eV absorption band in AlN is fully understood since C impurity is amphoteric. The variety of possible defect types is enormous and includes also complexes and intrinsic defects (such as nitrogen vacancies) while the proportion between the defects can change depending on the growth parameters and impurity concentrations. Unfortunately, usually, only indirect methods can be used for the identification of the point defect structure, which sometimes leads to excessive speculation. In this work, the structure of C-contained defects is determined by the isotope-mass effect in vibration spectra, which is one of the most direct methods of analysis. Then, the new properties related to particular types of C-containing defects are investigated in GaN and AlN.

In Chapter 5 of this work, the signatures of the defects in vibrational spectra are investigated. Seven types of C-containing defects in GaN and two in AlN are described by means of Fourier-Transform Infrared absorption Spectroscopy (FTIR) and Raman scattering. An excellent match of experimental results with calculated vibration frequencies is observed for numerous vibrational modes. In most cases, the isotope-mass analysis leaves no doubt about the origin of the vibrations.

It is illustrated how the chemical carbon concentration [C] defines the proportion between the defects in GaN and affects the (self-) compensation mechanism of C-doping. Signal intensities at different [C] in two series of GaN samples are discussed in Chapter 6. The defect-related vibrations are found in all intentionally doped samples at [C] from 2×10^{17} to 3.5×10^{19} cm^{-3}. Thus, it has been demonstrated that Raman scattering under the condition of resonant excitation of defects improves the sensitivity threshold by 1 - 2 orders of doping concentrations in comparison with trivial Raman scattering technique. At high [C] > 10^{19} cm^{-3}, the broadening of the Raman lines indicated the significant drop of the lattice quality. The FTIR experiments under the UV-Vis excitation (photo-FTIR) at energy ~0.8×Eg or above evidence the interaction of the part of the defects with light. Also, the excitation of defects in their absorption range results in different emission bands found also in a good agreement with the theoretical predictions.

The photo-induced band-mediated charge transfer is proposed for an explanation of the photo-FTIR effects in GaN. In the final Chapter 7, the influence of ~0.8×Eg irradiation now on AlN crystals is investigated. In addition to similar changes of the vibrational mode intensities, the UV irradiation results in photochromism. The photochromism of absorption bands (i.e., reversible, nevertheless, long-time stable, change of the absorption intensity) is a new observation in AlN crystals (and GaN though this phenomenon is not in the focus of this study) investigated by polarized UV-Vis absorption spectroscopy. Photochromism, in fact, provides the memory effect and the transparency control at one wavelength by excitation at another one in well-compensated material. The absorption polarization provided a qualitative comparison of the present defects and demonstrated an agreement of the effects with the band-mediated charge transfer model. Although C-containing defects are not the cause of photochromism, they are realized as an important criterion for its observation in samples.

Zusammenfassung

Semi-isolierendes GaN und UV-transparentes AlN sind gefragte Materialien für die auf Gruppe-III-Nitriden basierende Optoelektronik. Kohlenstoff (C) als Verunreinigung beeinflusst diese Materialeigenschaften in entscheidender Weise. Allerdings ist weder der Kompensationsmechanismus der C-Dotierung in GaN noch die Natur des 4.7 eV-Absorptionsbandes in AlN vollständig geklärt, da C eine amphotere Verunreinigung ist. Es ist ein breites Spektrum an möglichen Defekttypen denkbar, einschließlich der Bildung von Komplexen und intrinsischen Defekten (wie Stickstoffleerstellen), wobei sich das Verhältnis zwischen verschiedenen Defekten mit den Wachstumsparametern und Verunreinigungskonzentrationen ändern kann. Leider sind in der Regel nur indirekte Methoden zur Identifizierung der Punktdefektstruktur möglich, und das führt manchmal zu übermäßigen Spekulationen. In dieser Arbeit wird die Struktur von C-haltigen Defekten durch den Isotopen-Massen-Effekt in Schwingungsspektren bestimmt, eine der direktesten Analysemethoden. Anschließend werden neue Eigenschaften von GaN und AlN untersucht, die auf die verschiedenen C-haltigen Defekte zurückzuführen sind.

In Kapitel 5 dieser Arbeit werden Signaturen der Defekte in Schwingungsspektren untersucht. Sieben unterschiedliche C-haltige Defekte in GaN und zwei in AlN werden mittels Fourier-Transform-Infrarot-Absorptionsspektroskopie (FTIR) und Raman-Streuung untersucht. Für zahlreiche Schwingungsmoden wird eine hervorragende Übereinstimmung der experimentellen Ergebnisse mit den berechneten Schwingungsfrequenzen festgestellt. In den meisten Fällen kann die Schwingungsmode über die die Isotopen-Massen-Analyse zweifelsfrei zugeordnet werden.

Es wird gezeigt, dass wie chemische Konzentration an Kohlenstoff [C] das Verhältnis zwischen verschiedenen Defekten in GaN bestimmt und den (Selbst-) Kompensationsmechanismus der C-Dotierung beeinflusst. In Kapitel 6 werden die Signalintensitäten bei verschiedenem [C]-Gehalt in zwei Serien von GaN-Proben besprochen. Defektinduzierte Schwingungsmoden werden in allen absichtlich dotierten Proben mit einem [C]-Gehalt zwischen 2×10^{17} und 3.5×10^{19} cm^{-3} gefunden. Damit wurde nachgewiesen, dass die Raman-Streuung unter der Bedingung der Resonanzanregung von Defekten eine Empfindlichkeitsschwelle in Bezug auf die Dotierungskonzentration besitzt, die im Vergleich zur einfachen Raman-Streuung um 1–2 Größenordnungen niedriger liegt. Bei hohem [C]-Gehalt von über 10^{19} cm^{-3} deutet die Verbreiterung der Raman-Banden auf eine deutliche Verschlechterung der Kristallqualität hin. Die FTIR-Experimente unter UV-Vis-Anregung (Photo-FTIR) zeigen, dass ein Teil der Defekte bei einer bandkantennahen Anregung ($0.8\times E_g = 2.72$ eV und darüber) mit dem Licht wechselwirkt. Auch die Anregung der Defekte in ihrem jeweiligen Absorptionsbereich führt zu verschiedenen Emissionsbanden, die ebenfalls in guter Übereinstimmung mit den theoretischen Vorhersagen gefunden wurden.

Der photoinduzierte, über das Valenz- oder Leitungsband ablaufende Ladungstransfer wird als Erklärung für die Photo-FTIR-Effekte in GaN vorgeschlagen. Im abschließenden Kapitel 7 wird der Einfluss einer Bestrahlung bei $0.8\times E_g = 4.88$ eV auf AlN-Kristalle untersucht. UV-Bestrahlung führt sowohl zu einer ähnlichen Änderung der Intensität der Schwingungsmoden als auch zu einem photochrome Effekt. Der photochrome Effekt der Absorptionsbanden (d.h. eine reversible, aber dennoch langzeitstabile Änderung der Absorptionsintensität) wurde in AlN-Kristallen (und GaN, obwohl dieses Phänomen nicht im Fokus dieser Arbeit steht) bisher nicht beobachtet und hier durch polarisierte UV-Vis-Absorptionsspektroskopie untersucht. Der photochrome Effekt sorgt für den Memory-Effekt und die Kontrolle der Transparenz eines gut kompensierten Materials bei einer Wellenlänge durch optische Anregung bei einer anderen Wellenlänge. Die Polarisation der Absorption ermöglicht die qualitative Bestimmung der vorliegenden Defekte und die Effekte stimmen mit dem Modell eines über das Valenz- oder Leitungsband ablaufenden Ladungstransfers gut überein. Obwohl C-haltige Defekte den photochromen Effekt nicht direkt verursachen, dienen sie als wichtiges Kriterium für das Auftreten dieser Eigenschaft.

List of abbreviations

PL – photoluminescence
LED – light emitting diode
LD – laser diode
UV – ultraviolet
Vis – visible
MOVPE – metalorganic vapor-phase epitaxy
BPVE – bulk photovoltaic effect
DFT – Density Functional Theory
FTIR – Fourier-Transform Infrared (IR)
XRD – X-Ray Diffraction
SIMS – Secondary Ion Mass Spectrometry
HVPE – Hydride (or Halide) Vapor Phase Epitaxy
PVT – Physical Vapor Transport
Am – Ammonothermal Growth
FWHM – Full Width on Half Maximum
CC – Configuration Coordinate
TDD – Threading Dislocation Density
ZPL – zero phonon line
RT – room temperature
LT – low temperature
CB – conduction band
VB – valence band
DOS – Density of States (see Figure 3.2)
CIT – Change in Transmission (see Sect. 4.1)
DOP – Degree of Polarization (see Sect. 4.1)

List of terms

C, H, Si, O, Al, N, Ga – Carbon, Hydrogen, Silicon, Oxygen, Aluminum, Nitrogen, Gallium

[C], [H], [O], [Si] – corresponding chemical concentrations (in this work measured by SIMS for most of discussed samples, Sect. 2.1)

R = ([O] + [Si])/[C] – ratio of corresponding chemical concentrations

GaN, AlN – Gallium Nitride, Aluminum Nitride

AlN-A, AlN-B, AlN-D – names of bulk AlN crystals further cut to different wafers (e.g., AlN-A0, AlN-B2, see Sect. 2).

"GaN", GaG", "GaSap" – names of GaN sample series (see Sect. 2).

GaN003, GaG007, etc. – sample names with additional numbers after the series name indicating [C] in units of 10^{17} cm^{-3}, e.g., GaN090 with [C] = 90×10^{17} cm^{-3}

mono-C, di-C, tri-C – defect structure contained one, two, three C atoms

Di-C1, Di-C2, Tri-C1 – vibrational modes of corresponding defects in AlN (Sect. 5.3)

MC, DC, TC = vibrational modes of mono-C, di-C, and tri-C defects in GaN, correspondingly. Usually, appear in text with additional subnumbers (e.g., MC1, TC5, …).

CH – a particular mono-C defect with one C and one H atom

C-H – a chemical bond between C and H atoms or its vibration

C-C, C=C, C≡C – depending on context, carbon-carbon bond of first, second, third order, or a pair of C atoms with corresponding bond between atoms.

C-C-C, C=C=C – the forms of Tri-C defects presented by the triatomic molecule-like chain with C-C or C=C bonds between C atoms

C-X-C – linear triatomic molecule-like chain of three atoms where X atom can be represented by O, N, C, or Al in AlN crystal (Section 5.3). Belongs to di-C defects if X is not a C atom, or tri-C defects if X is C.

C_N, C_{Ga}, C_{Al}, C_i – a particular mono-C defect, C substituting N, Ga, Al atom of the crystal lattice, or occupying interstitial (i) position between host atoms.

C_N-C_i – a particular di-C defect, a C-pair with the double bond substituted one N atom in GaN

V_N, V_{Al}, V_{Ga} – vacancy defect, absence of one of the host atoms, N, Al, Ga

LO, TO = longitudinal-optical, transverse-optical phonon modes (see Sect. 3.1)

A_1, B_1, E_1, E_2 - are the irreducible representations used in the symmetry group terms to characterize the symmetry of vibronic motions. E_2(high), A_1 (LO), etc. is related to particular intrinsic vibrations of AlN or GaN crystals (Sec. 3.1)

x(yy)x, z(xx)z, etc. – Raman scattering geometry in Porto notations, see Sect. 3.1

E∥c, E⊥c – orientation of the plane polarized light wave parallel, perpendicular to the crystal c-axis

Contents

1. Introduction 1
Optical application of GaN and AlN 1
AlN and GaN in electronics 2
Application in quantum informatics 3
Outline 3
2. Samples description and growth methods 4
2.1. Tables of SIMS data for GaN and AlN samples 5
2.2. Methods of crystal growth and the description of GaN sample series 6
Methods of GaN crystal growth 6
"GaN" series: bulk-like GaN self-separated from sapphire 6
C1213 and C13 samples: doped with ^{13}C isotope 7
"GaSap" series: ~50 μm GaN films unseparated from the sapphire wafers 7
"GaG" series: GaN on Am-GaN 7
2.3. Methods of growth and the description of AlN bulk crystals 7
Methods of AlN crystal growth 7
AlN-A, AlN-B, AlN-D bulk crystals 9
AlN-C13 doped by ^{13}C isotope 9
3. Physics of Semiconductors 10
3.1. Crystal symmetry and vibrational properties of GaN and AlN 10
Unit cell and symmetry of wurtzite GaN and AlN 10
The Brillouin zone and collective vibrations 11
The intrinsic Raman modes of GaN and AlN crystals 12
Activity and polarization of IR absorption vibrational modes 14
Activity and polarization of Raman scattering modes 14
Raman tensor of intrinsic vibrational modes 15
3.2. The basis of harmonic oscillator model 17
Influence of masses and vibrational amplitudes of atoms on the frequency shift 17
Maximum and minumum isotope-mass-related shift of frequency 18
3.3. Determination of the structure of the molecule-like defects 20
X-Y-Z notation of defect (molecule) structures 20
Orientation of the vibrating dipole moment in a defect (molecule) 21
Isotope effect in molecule-like defects. Isotopomers 22
Determination of the number of C atoms the isotopic splitting 23
3.4 Harmonic oscillators in quantum mechanics 24
IR absorption. Configuratino coordinate (CC) diagram 24
UV-Vis absorption of point defects on CC diagrams 25
3.5. Properties and structure of point defects calculated by DFT 26
DFT calculations of defect structure, ZPL, absorption, and emission energy 26
Mono-C defects in GaN: C_N, C_{Ga}, C_i, C-H 27
Di-C defects in GaN: C_i-C_{Ga}, C_i-C_N, C_N-C_{Ga}, ... 29
Intrinsic defects with low formation energy in GaN 30
Large variety of point defects in AlN 31
Absorption band at 4.7 eV 31
Compensation of the main dopant by intrinsic defects and complex formation 32

4. Experimental methods 33

4.1. Measurements of optical absorption or transmission 33
Corrected absorption coefficient, transittance, reflectivity, and scattering 33
Secondary parameters CIT and DOP 33
UV-Vis spectrometer Lambda 1050 34
Experimental details of photochromism measuements in AlN 34

4.2. Infrared absorption (FTIR) 35
Spectrometer Bruker Vertex 80v 35
FTIR under additional UV-Vis excitation (photo-FTIR) 35

4.3 Raman scattering and PL spectroscopy 36
Raman scattering experiments 36
Photoluminescence experiments 36

5. Determination of the defect types in GaN and AlN 37

5.1. Modes of mono-C defects in GaN 39
Appearance of MC1 – MC4 modes and their second harmonics 39
Origination of MC1-MC4 from mono-C defect 40
CH mode at 2670 cm^{-1} 41
Carbon-Hydrogen origination of CH mode 41
MC1 – MC4 modes: C_N, C_{Ga}, or C_I? 42

5.2. Di-carbon defects in GaN 45
Appearance of modes DC1, DC2 in FTIR and Raman spectra 45
Isotope effects for DC1, DC2. 45
Orientation of the defects in crystal. C_N-C_i? 47

5.3. Di-carbon and Tri-carbon defects in AlN 48
Di-C1, Di-DC2 and Tri-C1 Raman modes in AlN. 48
Isotope effects of DC1 and DC2 49
Orientation of the defects in crystal 50

5.4. Tri-carbon defects in GaN 51
Spectral positions of TC modes 51
Isotope effect of TC modes 52
Orientation of the defects in crystal. Axial and basal configurations 53
Detail structure of tri-C defects. Order of carbon-carbon bonds 55
Molecular angle of axial and basal C=C=C defects 55

5.5. Summary 57
C_N defects in GaN (and AlN) 57
C-H vibrations in GaN. 57
Di-carbon in GaN 57
Tri-carbon defects in GaN 58
Carbon vibrations in AlN 58
Conclusion 58

6. Light-induced defects-related effects in GaN:C 60

6.1. Major and minor defect vibrations in FTIR spectra 62
Tri-C modes TC1-TC2 dominate in IR absorption 62
Comparison of C=C=C and C_N defects in GaN090 62
The minor modes in FTIR spectra at low and mid [C] 63
The minor modes in FTIR spectra at high [C] 64

6.2. Light-induced changes in FTIR spectra (photo-FTIR). 64
Simultaneous change of IR modes under 3.22 eV, 2.72 eV and 1.32 eV excitation 64
Distribution of the intensity of light on the sample depth 66
Power dependences in GaN019, GaN140, and GaN350 67
Time dependences of the light-induced effects 68
Excitation of inactive defects 69
On the origin of the photo-FTIR changes 70
Charge states and meta-stable states of Tri-C defect 71

6.3. Resonance Raman spectra of major and minor defects 72
Normalization of Raman spectra 72
Anharmonic processes due to carbon doping influenced the intrinsic vibrations 72
Resonant amplification of the defect-related and phonon-band scattering 73
Coupling of the intrinsic and defect vibrations 74
Vibrational modes of C_N defect 74
The minor modes in Raman spectra 75

6.4. UV-Vis absorption and PL 76
UV-Vis absorption 76
YL1, BL_C, and BL2 emission bands at above-bandgap excitation 78
GL2, YL1, and YL_C luminescence bands at below-bandgap excitation 79
Red luminescence and YL_C bands at the highest [C] 81
Absorption and emission of tri-C defects 82

6.5. Summary 83

7. Photochromism in AlN 85
UV-Vis absorption AlN 85
Possible origins of photochromism. Similarity of AlN and GaN 86

7.1. Photochromism in AlN-A and AlN-B samples 88
UV-Vis spectra of photochromic samples 88
Optically induced absorption and optical restoration of the initial state 88
Thermal restoration of the initial state 90
Identification of defects by polarized UV-Vis absorption 91

7.2. The band-mediated charge transfer model 94
Charge exchange diagrams 94

7.3. Absorption bands in AlN 95
Table and diagram of absorption processes in AlN-B2 95
2.8 eV absorption band 95
4.0 eV induced absorption band 96
2.6 eV absorption band 96
3.4 eV absorption band 96
5.2 eV induced absorption band 97
The photochromic original absorption bands around 4.7 eV in area B2 97

7.4. Summary 98

8. Conclusion and outlook 99
A. Reference list 101
B. Peer-reviewed Articles 110
C. Conference contributions 111
D. Acknowledgments 112

1. Introduction

The metals from group III of the periodic table combined with nitrogen: InN, GaN, AlN and their ternary and quaternary compounds such as AlGaN and AlInGaN are referred to as III-nitride materials.[1–3] In this work, optical methods are used to study only two types of bulk III-nitride crystals, GaN and AlN, with different concentrations of impurity atoms. This research focuses on the defects containing carbon atoms, their influence on optical and vibrational properties and the structure of these defects in GaN and AlN crystal.

Optical application of GaN and AlN

The main interest in GaN and AlN has been in the realization of light-emitting devices. The large values of the bandgap make ideal GaN crystals transparent in the entire visible spectrum, and AlN also in the deep UV range up to 6.1 eV. Most recently, the invention of the GaN-based blue light emitting diodes (LEDs) was awarded the Nobel Prize (2014).[4] Due to the breakthrough on epitaxial growth of group-III nitrides in last decades, these devices are widely used nowadays. They have proven themselves as very efficient sources of visible light and demonstrated the potential for low-cost semiconductor UV light-emitting devices. At the moment, the blue LEDs reached the efficiency light emission of 83% of the electrical input power.[5,6] The loss of the blue LEDs is so low that they are successfully used to the excitation of the luminophore which further re-generate light at lower energy.[7] Blue laser diodes (LDs) reach ~40% efficiency, possibly due to electrical losses in p-type area of the devices.[6] An example of a GaN based laser (405 nm) application is Blu-ray technology that served as a logical development of CD (780 nm) and DVD (650 nm).

Enormous efforts have been made on developing UV LEDs.[8] The AlN UV LEDs have already demonstrated wavelengths down to 210 nm (5.9 eV),[9] while UV laser diodes reached the wavelength 222 nm (5.6 eV) deep into the UV-C.[10–13] AlN-based LEDs and LDs can solve the effectivity problem of UV sources, that are required in particular for disinfection of water and air. At the moment, the AlN-based LEDs themselves did not reach high external quantum efficiency (e.g., it is equal to 3.3% at 293 nm for AlGaN on AlN LED).[14] But they are still attractive due to the benefits of the solid-state sources versus mercury lamps such as fast switching and wide range of the wavelength or better control of outcoming power. With this respect, the knowledge of point defects and the non-radiative recombination processes becomes an important task for further development of this technology.[15]

In the context of optical application, it should be noted that carbon impurity causes intense light absorption with energies above ~ 0.7 E_g in both materials accompanied by bright photoluminescence (PL) at lower energies.[16–21] Carbon is an essential component of organic precursors in atomic layer deposition technique or the metalorganic vapor-phase epitaxy (MOVPE), one of the most common methods for producing commercial devices.[16,22–24] Investigation of the photoluminescence in carbon-doped GaN showed appearance of nonradiative recombination centers and decrease of quantum efficiency when the concentration of carbon atoms increases from 4×10^{14} to 2×10^{16} cm^{-3}.[25] Within the negative effects of carbon doping, one can mention a decrease of UV-photodetectors performance, as it was demonstrated for GaN.[26]

In addition, carbon defects are involved in such exotic optical effects as photochromism and bulk photovoltaic effect (BPVE) that one can observe at excitation above ~ 0.7 E_g but which

were not widely discussed up to now.[27,28] BPVE is associated with the violation of the principle of the balancing for photoexcited (nonequilibrium) carriers in different directions, for example, because of inelastic scattering of carriers from asymmetric centers or asymmetric potential of a defect center.[29] In GaN, BPVE results in the appearance of high voltage on the facets of the crystals under the light excitation, according to our measurements.[27] Photochromism is vivid at specific ratio of doping in GaN and AlN. For AlN, one of the related effects is the halving of absorption coefficient in the range of UV-excitation for a long period (up to a few weeks) after the excitation.[28] This results in a large difference between the absorption coefficient values at low and high power of transmitting light (e.g., light during a spectroscopic measurement versus intense light emitted by a LED structure). The ability to control transmission coefficient independently at two wavelengths may find application in quantum informatics.

AlN and GaN in electronics

Another important area of GaN and AlN application is electronics. Due to high breakdown voltage, high carrier mobility, and extremely high thermal conductivity, these two materials stand out favorably for applications in the field of high-power, fast electronics, especially if the devices operate under extreme conditions.[24,30–33] A daily reminder of the effectiveness of GaN electronics are powerful yet compact chargers for smartphones and laptops. In contrast to 15 years old bulky and heavy charges with silicon chips and massive metal cooling elements, the GaN-based electronic components are compact and they lower heat emission due to greater conversion efficiency. In addition, fundamental advantages in electron mobility make GaN high-electron-mobility transistors great for high-speed switching devices.[33] Resistance to chemical reactions and radiation allows expanding the use of these materials. For instance, these devices can exist in harsher conditions for the industry, or even aerospace, or military applications.

Carbon can be a dopant that compensates donors and creates semi-insulating material useful in many device designs.[34] Carbon effectively compensates n-type doping; on the other hand, deep-level transient spectroscopy (DLTS) measurements have also shown that C can act as a hole trap, compensating Mg doping in p-type GaN.[35,36] Very recently, p-type conductivity related to carbon defects was demonstrated in carbon-doped GaN at high temperatures with activation energy around 1.0 eV.[37–39] However, there are still unresolved problems concerning the doping mechanism of carbon and its self-compensation.[40] Also, vibrational properties of point defects are of interest for research because influence the thermal conductivity of crystals.[41–43] Carbon doping can be a superior doping technique to achieve semi-insulating GaN since it provides up to 5 orders of magnitude lower dark current compared with Fe doping at the same concentration range.[44] Though carbon lowers the thermal conductivity due to the resonance interaction between the impurity vibrations and the lattice vibrations, among other p-type dopants (Mg, Fe) in GaN, this effect is minimal.[42] Carbon in GaN has been better and more reliably studied, while the properties of AlN:C are not well investigated mostly due to high concentrations of intrinsic defects and background impurities such as oxygen and silicon. For AlN, only carbon-related surface p-type conductivity was demonstrated.[45]

Finally, both materials are piezoelectric and pyroelectric. It has been shown for AlN:C, that in the case of high resistivity carbon doping layers used for piezoelectric sensors operating at elevated temperatures, the efficiency is advantageously comparable to alternative materials.[46,47]

Application in quantum informatics

Like other previously investigated III-V compounds, nitrides are suitable not only for electronic but also for photonic integrated circuits.[48,49] Generation and manipulation of single photons is the future of light-based quantum technologies, thus single-photon emitter (SPE) is one crucial component in any quantum device. The best SPE is a single atom, as only one electron transition can be activated simultaneously on it. Point defects in GaN or AlN are perfect solutions for true pure (not attenuated) single photon emitters.[50–55] Earlier, AlGaN quantum dots, packing defects, and point defects demonstrated the generation of single photons even at elevated temperatures.[50–55] On the other hand, carbon single defects and carbon clusters in hexagonal boron nitride demonstrated the emission of single photons.[56–58] With the further development of the topic of SPEs, carbon defects in GaN and AlN could be prospective candidates due to their bright luminescence.

Outline

Basically, C-containing defects are studied by indirect methods such as photoluminescence, allowing various interpretations based on Density Functional Theory (DFT) or other computational methods. Using the example of the tri-atomic molecule-like C clusters (tri-C), I show that DFT cannot predict the appearance of this pronounced defect.[34,59,60] The defect is very pronounced in GaN, despite the high formation energy (~7 eV). The structure of observed tri-C defect is reliably identified by its isotope-mass effect in the vibration spectra. In such a situation, when the structure is clearly known, DFT perfectly describes the properties of defects with high accuracy. With this respect, vibrational frequencies, absorption and emission energies found by DFT for tri-C, and a mono-atomic substituting defect (mono-C)[34,59–62] agree very well with the experimental data.

Since C is an amphoteric impurity,[63] the variety of possible defects is enormous. No evidence is presented for the particular defects originating self-compensation upon carbon doping in GaN, while the origin of the intense carbon-related UV-absorption band at 4.7 eV in AlN has several explanations with theoretical indirect evidence. In this work, the veil of secrecy can be opened by unambiguously identifying point defects by vibrational modes with isotope ^{13}C doping. In GaN and AlN, over 20 vibration modes of C-containing defects, found in this work, can serve as a guideline for quantitative comparison of samples and clarification of the electronic and optical properties of C doping. In GaN, I verify the structure of mono-C defect, show that all C-doped GaN samples contain tri-C complexes and at which concentrations C pairs and CH defects appear. Also, attention is paid to the strong vibrational coupling of C-containing defects with the GaN lattice that can be indicated in Raman spectra. Finally, I provide evidence of the interaction of some types of point defects with the light. I assume an important role of the charge transfer between point defects in the materials, and illustrate how this phenomenon leads to many interesting features, such as photochromism in AlN, which was previously associated with photo-induced metastable defects.

2. Samples description and growth methods

In this part of the work, the main attention is paid to the object of this research – to crystals of GaN and AlN with enhanced levels of carbon impurity. It discusses methods of growth and C doping used for our samples. The traditional methods of the bulk crystal-melt growth (such as Czochralski or Bridgman methods) are not suitable for the growth of GaN and AlN. The next methods used for producing of our samples are overviewed here: Hydride (or Halide) Vapor Phase Epitaxy (HVPE), Physical Vapor Transport (PVT), and Ammonothermal growth (Am). Three groups of GaN samples ("GaN", "GaSap", and "GaG") were grown by HVPE and intentionally doped with C by adding gas precursors; Am-GaN templates were used as for one of them ("GaG" series). Three bulk AlN crystals were grown by PVT technique with the change of growth parameter that resulted in a gradient distribution of incorporated impurities (including C). The crystals were cut to wafers and then the different areas of a single inhomogeneous wafer or central homogeneous areas of different wafers of AlN crystals were investigated. In additionally ^{13}C-doped samples, an increased[1] abundance of ^{13}C isotope was provided by adding an enriched gas to the reactor chamber (for GaN) or enriched powder to the source (for AlN). Crystalline quality of samples is checked using X-Ray Diffraction (XRD) methods and the impurity chemical concentrations was measured by Secondary Ion Mass Spectrometry (SIMS) and summarized in Tables on the next page.[2]

[1] The abundance of carbon isotopes in nature is 98.9% of ^{12}C and 1.1% of ^{13}C.

[2] SIMS of "GaG" samples was provided by Institute of High Pressure Physics, Warsaw, Poland; all other SIMS measurements are performed at RTG Mikroanalyse GmbH, Schwarzschildstraße 1, 12489, Berlin, Germany.

2.1. Tables of SIMS data for GaN and AlN samples

Table I. SIMS data for main impurities: C, O, Si, H, and appearance of *vibrational signals MC, DC, TC, CH associated with carbon defects, mono-C (MC), di-C (DC), tri-C (TC), and C-H (further discussed in Chapters 5 and 6). The thickness of samples along c-axis (l) is shown.*

	[C]=[^{12}C] + [^{13}C]	[^{13}C%]	[O]	[Si]	[H]	*l*	MC	DC	TC	CH
	10^{17} cm^{-3}		10^{17} cm^{-3}			μm				
GaN000	< 0.24	1%	< 0.2	< 0.07	1	1050	-	-	-	-
GaN003	3.2	1%	~0.35	~0.13		980	+	-	+	+
GaN005	5.0	1%				585	+	-	+	+
GaN019	19	1%				807	+	+	+	+
GaN058	58	1%				790	+	+	+	+
GaN090	90	1%			6	410	+	+	+	-
GaN140	140	1%				736	+	+	+	-
GaN300	300	1%				806	+	+	+	-
GaN350	350	1%			8	754	+	+	+	-
C1213	51	**50%**	3.5				+	+	+	+
C13	25	**99%**					+	+	+	-
GaSap000	0.3	1%	~0.35	~0.13		33				
GaSap002	1.9	1%				47				
GaSap015	15	1%				32				
GaSap110	110	1%				30				
GaSap220	220	1%				31				
GaG004	3.5	1%	2	0.7	2	420	+	-	+	-
GaG005	5.0	1%	0.7	0.8	2	440	+	+	+	-
GaG007	7.0	1%	0.7	0.6	2.5	340	+	+	+	-
GaG015	15	1%	0.8	0.9	2	290	+	+	+	-
GaG035	35	1%	2	1.5	4	390	+	+	+	-

Table II. SIMS data for main impurities: C, O, Si, in AlN, corresponding R = ([O]+[Si])/[C] and values of UV absorption coefficient at 4.7 eV in cm^{-1} are provided.

	[^{12}C]	[^{13}C%]	[O]	[Si]	R	4.7eV
	10^{17} cm^{-3}		10^{17} cm^{-3}			
AlN-A0	15.5	1%	17	6.5	1.5	≥240
AlN-A1	-		-	-	-	180
AlN-A2	10.7	1%	15	8.6	2.2	70
AlN-A3	8.8	1%	15	8.8	2.7	40
AlN-A4	-		-	-	-	<30
AlN-A5	7	1%	11	11.5	3.2	<30
AlN-B1	57	1%	21	0.7	0.4	≥1100
AlN-B2	18	1%	33	3.7	2.0	110
AlN-B3	18	1%	64	3.3	3.7	<15
AlN-D	58	1%	24	0.31	0.42	1450
AlN-C13	104	**~14%**	37	2.5	0.37	-

2.2. Methods of crystal growth and the description of GaN sample series

Methods of GaN crystal growth

Both AlN and GaN crystals can be grown by HVPE methods but in this work HVPE is used only for GaN growth. In the HVPE process, epitaxy of GaN happens at the chemical deposition on a substrate of Ga and N atoms from gaseous GaCl and NH_3 at growth temperatures, typically 1000 – 1100 ˚C, and nearly atmospheric pressure.[38,64–66] Deposition on foreign substrates (heteroepitaxy) is a more familiar technology, but these suffer from lattice bowing and high threading dislocation density (TDD). The heteroepitaxy stems from significant differences between the lattice constants and thermal expansion coefficients of the substrate and the nitride film, but commercial high-quality GaN templates for homoepitaxial are still arduous. Most often (as in series "GaN" and "GaSap"),[38] sapphire substrates with various seed layers are used. The growth rate can be as high as 0.5 mm/h (in comparison to MOVPE about 1–2 μ/h, to get high-quality layers or ~50 μ/h if optimized for bulk growth)[67] and a boule thickness above 1 cm has been reported on 2 inches substrates.[67] Since the lattice quality directly depends on the substrate, a significant perfection of the lattice and further devices efficiency can be achieved if high-quality Am-GaN is used as a substrate.[39,65,68,69]

The idea of Ammonothermal growth is the following: GaN, used as feedstock, is dissolved in a supercritical ammonia-based solution.[68,69] The dissolved material is transported to the growth zone, where the solution is supersaturated and crystallization of GaN on native seeds takes place. Seeds such as Am-GaN or HVPE-GaN grown on Am-GaN result into the best lattice perfection of the outcome crystals.[70] The temperature gradient between the dissolution and crystallization zones enabled the mass transport and crystallization of GaN. Because of the negative temperature coefficient of solubility, the chemical transport of GaN is directed from the low-temperature (~700 K) solubility zone with feedstock to the high-temperature (~830 K) crystallization zone with seeds.[69,71] Basically, the allowed size of GaN crystal is about 2 inches in diameter, the crystals have the highest structural quality, crystallographically flat, etch pit density is as low as 10^2 cm^{-2}, and low TDD.[69,72] The typical ammonia pressure during a crystal growth run is slightly lower than 400 MPa and a typical crystallization process lasts around 70 days.[69]

"GaN" series: bulk-like GaN self-separated from sapphire

Within this work, bulk-like GaN grown only by HVPE is investigated. Two sample series, "GaN", "GaSap", and single samples C1213, C13 are grown on (0001)-oriented 2 inches sapphire substrates at Ferdinand Braun Institute Berlin (FBH).[38] XRD analysis of the main series "GaN" (including the reference sample GaN000) shows from the first look independent values of the full width on half maximum (FWHM). The FWHM of the diffraction line is influenced by the mosaicity of the material (polycrystalline-like structure) and the upper limit of threading dislocations density.[73] For the reference sample GaN000 the values are in the range of 85-95 arcsec while for carbon-doped samples GaN003 – GaN350 both peaks of diffraction (0002) and (30$\underline{3}$2) have FWHM in the range from 70 to 120 arcsec. These XRD data allow the estimation of TDD below 10^7 cm^{-2} for "GaN" samples.[18,38]

In sample GaN000, three main impurity have chemical concentrations [C], [O], and [Si] below the respective SIMS detection limits: [C] < 2.4×10^{16} cm^{-3}, [O] < 2×10^{16} cm^{-3}, and [Si] < 7×10^{15} cm^{-3}. Pentane precursor was used as a source of carbon atoms during the growth of "GaN" and "GaSap" series.[38] The samples doped by pentane show [O] and [Si] slightly raised

above the detection limit to 3.5×10^{16} cm^{-3} and 1.3×10^{16} cm^{-3}, respectively.[38] For all series of GaN crystals, the three numbers after the series name show the SIMS measured [C] in units of 10^{17} cm^{-3}. Hydrogen concentration [H] was found correlated with [C] but expected below 8×10^{17} cm^{-3} for all samples of "GaN" series.[38] The summarized data of SIMS measurements are presented in Table I. The thickness of samples in the range 400 – 1200 μm provides bright coloration gradually changing with the carbon doping (Figure 2.1). Furthermore, in some cases, after additional processing of sample facets, the measurements could be carried out on (or through) the facet.

C1213 and C13 samples: doped with ^{13}C isotope

Similar growth conditions but ^{13}C enriched butane precursor were used for preparation of GaN two bulk-like samples (C1213 and C13) doped by ^{13}C isotope. In the samples doped with isotopically enriched butane, [O] attains 3.5×10^{17} cm^{-3}. SIMS measurements included in Table I confirmed abundance 50% and 99% of ^{13}C isotope at the total carbon concentration.

"GaSap" series: ~50 μm GaN films unseparated from the sapphire wafers

An additional series of GaN samples ("GaSap") are films similar to "GaN" series but not separated from sapphire and with the significantly lower thicknesses (30-50 μm). This series was used only for demonstration of the intense UV-Vis absorption at absorption coefficient values well above 100 cm^{-1} induced by strong carbon doping (Chapter 6).

"GaG" series: GaN on Am-GaN

A set of HVPE GaN on Ammonothermal GaN templates ("GaG") was grown at Institute of High Pressure Physics (Unipress).[37] It is expected for heteroepitaxial GaN to have in two order lower TDD comparing to "GaN" series. Gas methane was used for carbon doping.[37] SIMS measurement for this sample group are included into the Table I**.** The thickness of the samples is 290 – 440 μm.

2.3. Methods of growth and the description of AlN bulk crystals

Methods of AlN crystal growth

There are three major approaches of the AlN bulk (bulk-like) growth: sublimation of PVT, HVPE, and MOVPE.[1] MOVPE and HVPE are used typically for the growth of thin or thick AlN films on a substrates when the result crystal perfection is determined by the quality of the substrate. PVT bulk crystals then can be used as high-quality substrates with perfect structural quality.[74–80] It was demonstrated, that the high crystalline perfection of PVT-AlN substrate, does not decrease due to epitaxial growth.[81] Reports of the homoepitaxy of films on PVT wafers look promising,[82,83] while the heteroepitaxy results in similar disadvantages as in the case of GaN epitaxy.[81,84] The concentrations of impurities much below 5×10^{17} cm^{-3} of each, carbon, silicon, and oxygen are easier achievable in HVPE due to low (relative to PVT) growth temperatures and near to equilibrium conditions.[83,84] With this respect, great UV transparency of HVPE films was reported.[83] Usually, PVT AlN has tailings of oxygen and carbon at significant concentrations,[85,86] on the other hand, recently, low impurity concentrations [C] =

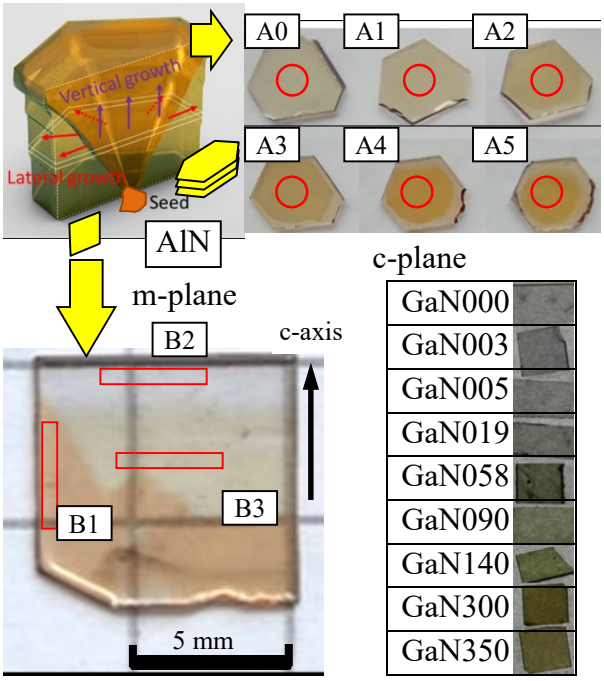

Figure 2.1. GaN (c-plane "GaN" sample series) and AlN (A and B) crystals. GaN c-cut wafers size (5…10)×(4…6)×(0.5…1) mm³. Different wafers of the two bulk AlN PVT crystals cut to m-plane and c-plane wafers with thickness 450 – 550 µm. Schematically shown single-crystal growth explains the color difference between the central parts (vertical growth along c-axis) and the laterally grown rims of c-cut AlN wafers. The areas B1-B3 of the UV-Vis absorption measurements include the respective SIMS probe areas.

2.0×10^{17}, [O] = 2.0×10^{17}, and [Si] = 1.0×10^{16} cm^{-3} were reported for colorless PVT AlN (though the crystals have a weak 4.7 eV UV-absorption band).[87]

Currently, PVT is the most promising method providing voluminous bulk crystals of high lattice quality.[77–80] The AlN PVT process comprises the sublimation of a powder or polycrystalline AlN source below the triple point in a closed or semi-open crucible in a nitrogen ambient of several tens kPa.[79] Special attention is paid to the purification of powder source materials from impurities (mainly oxygen).[79] The atomic Al and N in the gaseous phase are then transported to the cooler growth region by a thermal gradient, and there, the gas species can be deposited epitaxially. The growth is possible in heteroepitaxy, freestanding (during the freestanding growth, there is no initial template and AlN first is nucleated process and then overgrow) as well as in homoepitaxy modes.[79] Typical growth rates achieved with this method are 100 - 250 µm/h.[80] The method still faces a challenge associated with an increase in size.[80] In addition, one of the problems of the method is the lateral growth of AlN, which leads to the appearance on the crystal periphery of a frame that is significantly different from the main central region (illustrated in Figure 2.1) More about PVT techniques can be found in corresponding references.[77–80]

The lattice perfection of PVT crystals and the growth progress can be illustrated by X-ray diffraction (XRD). FWHM of the rocking curve (002)-peak for first available PVT crystals was equal to few hundred arcsec,[1] when the best results of last years denote FWHM nearly 10 arcsec.[88] For comparison, the mentioned HVPE samples grown on PVT AlN template with perfect 15 arcsec FWHM had worsened the FWHM up to still good 30 arcsec.[83] The appropri-

ate quality of PVT-AlN crystal lattice of our samples allows us to focus attention on point defects.[74] All AlN bulk crystals samples have a high quality crystal lattice providing narrow XRD lines (25 - 45 arcsec).

AlN-A, AlN-B, AlN-D bulk crystals

Three bulk AlN crystals (A, B, D) were grown by PVT method and cut in different crystalline planes (c-plane and m-plane; see Figure 2.1 and Figure 3.1). The growth parameters were varied to obtain crystal regions with different impurity concentrations and optical properties.[74] Correspondingly, the central areas of c-cut samples AlN-A0 – AlN-A5 of crystal A, three areas AlN-B1 – AlN-B3 of a single m-cut of crystal B, and central area including the area of SIMS measurement (AlN-D) of m-cut crystal D can be considered as separate samples in optical measurements. Two main factors contribute to the concentrations of impurities: first, there are two different growth facets[89] (e.g., low [C] areas B2 and B3 were grown on -c [000$\underline{1}$] and high [C] area B1 on m [10$\underline{1}$0] facets) and second, there is a transient effect during growth: the oxygen supply in the crucible and the incorporation of oxygen into the crystal decreases with growth time (from B3 to B2 leads to decrease [O]). For sample areas SIMS concentrations of the three main impurities, [Si], [O], [C] are provided in Table I.

AlN-C13 doped by ^{13}C isotope

There is an additional sample AlN-C13 enriched by ^{13}C isotope. Only this sample stems from a crystal intentionally doped with carbon during the PVT growth by adding tungsten carbide synthesized from ^{13}C-graphite to the AlN source powder.[20] This procedure suppressed premature evaporation of ^{13}C from the source as had been observed in an experiment using ^{13}C graphite powder. However, it did not provide continuous delivery of ^{13}C and led to its inhomogeneous incorporation. The SIMS data reveal that the crystal of sample AlN-C13 shows an inhomogeneous ^{13}C distribution with ^{13}C locally constituting up to 35% of the total carbon concentration (this SIMS probe is not included in Table II).

3. Physics of Semiconductors

This Chapter discusses theoretical aspects closely related to the results of this work. References are given to modern (and not so modern) books on spectroscopy for more detail overlook.[90–97] Among the topics covered, there are the structure of crystals and their wave properties, as well as the symmetry and structure of molecules and molecule-like defects. The vibration and optical properties of defects in GaN and AlN provided by DFT calculations are discussed; the classification of carbon defects in the framework of this research is provided. The approximation of a harmonic oscillator, the physics of vibrational spectroscopy methods, the isotope-mass effect, which is of critical importance for the interpretation of further results, are presented.

3.1. Crystal symmetry and vibrational properties of GaN and AlN

Unit cell and symmetry of wurtzite GaN and AlN

GaN and AlN crystallize in wurtzite structure (Figure 3.1 (a)) which belongs to the space group C^4_{6v}. The description of the perfect crystal structure includes the complete determination of the unit cell and the symmetry operations. The space group C^4_{6v} contains the symmetry elements representing the translation (vectors $\boldsymbol{a_1}$, $\boldsymbol{a_2}$, $\boldsymbol{a_3}$, and $\boldsymbol{c}$ in (b)), reflection (six mirror planes σ_v), and rotation operations ($\boldsymbol{c}$ helical axis of rotation (C_{3v}), (b)).[98] The unit cell contains four atoms (e.g., the four atoms connected by the greed lines) and can be described by the lattice parameters: angles $\beta \equiv \beta_1 \approx \beta_2$, γ, the two distances a, c, and parameter u, that characterizes distance $d = d_1 \approx d_2 \approx uc$, (as d_1 and d_2 between the nearest atoms only slightly differ).

The unique **c** vector and the three vectors **a1**, **a2**, and **a3** provide the translation symmetry of the wurtzite structure. The angle between two of **a** translation vectors is 120˚ and all of them are orthogonal to **c** translation vector (i.e., **a**-vectors lie in the basal plane or c-plane

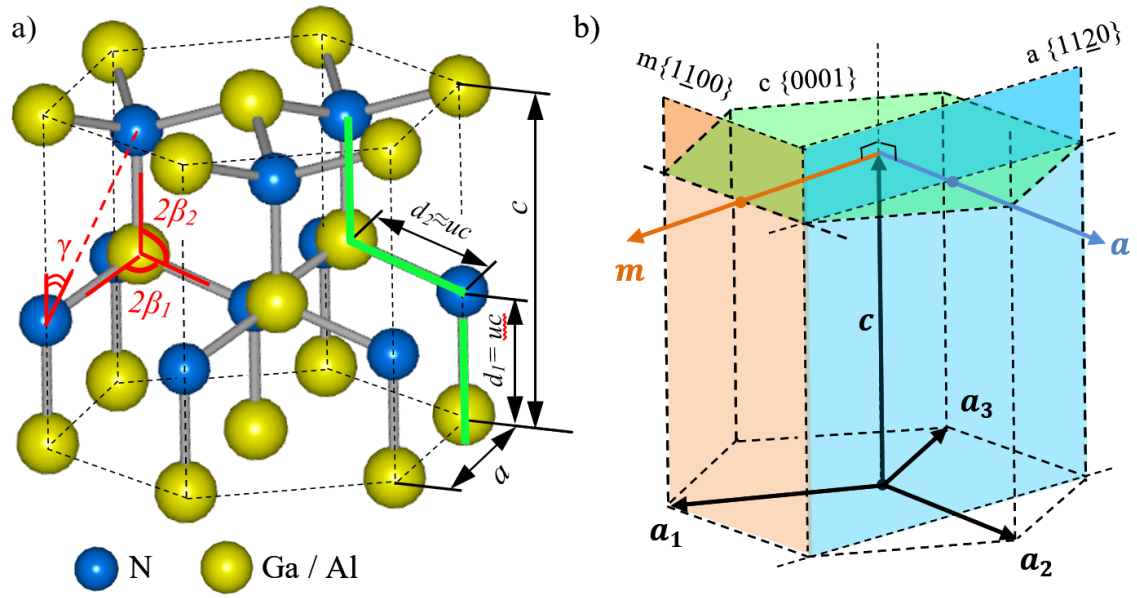

Figure 3.1. (a) Wurtzite GaN or AlN crystal lattice[102] *with the lattice parameters a, c, u, and angles β, γ (see Table III). Important lattice planes a, m, c and the crystal axes a, m, c are illustrated. The four atoms connected by the green line is an example of the chosen unit cell.*

0001} in (b)). The length of the translation vectors (lattice parameters *a* and *c*, see Table III) determine the distances between the nearest crystallographically equivalent atoms of the crystal in the corresponding directions. The values of *a* and *c* are found in both materials experimentally and theoretically.[99,100] Vectors **a1**, **a2**, **c** can be used as the basis in the three-index notation (**a1**, **a2**, **c**). Then, the nearest but not crystallographically equivalent atoms of metal located at (0, 0, 0) and (1/3, 2/3, 1/2) (i.e. (a/3, 2a/3, c/2)), and the two nitrogen atoms located on the nitrogen sublattice at (0, 0, *u*) and (2/3, 1/3, 1/2+*u*) consist the unit cell (representative unit cell can be chosen by different ways, green line in (a) connected four atoms shows one of them). Within the unit cell, the distances *uc* and *d* (*d*≈*uc*) characterize the metal-N chemical bond length in a crystal along and perpendicular to the c-axis, respectively. Vesta software is used for visualization of the crystal structure in (a) and the evaluation of the angles *β, γ* and the distance *d* (see Table III). Carbon-carbon bonds in molecules provide shorter distance between atoms than the equilibrium distance between the neighboring crystal atoms. To give a clear vision of the further discussion, an approximate bond length typical for molecules with C-C, C=C, or C≡C bonds are ~1.5, ~1.3, and ~1.2 Å.[101]

Above, the coordinates of the atoms are written in the Miller index system, however, some crystallographically equivalent directions of the hexagonal structure in this notation can be described by several different indices. The Miller-Bravais four-index notation with the basis (**a1**; **a2**, **a3**, **c**) solves this problem and better illustrate the symmetry properties, therefore it is more often used for wurtzite crystals. In (b) the main planes and directions widely used in this work are shown: the polar c-plane {0001}, non-polar a-plane {11$\underline{2}$0} and m-plane {1$\underline{1}$00}.

The c-axis is also called the optical c-axis of the crystal because the optical properties observed perpendicular and parallel to it are different. In contrast, along **a**, **m**, **-a**, and **-m** directions (and in all other directions perpendicular to the optical c-axis) they are identical. The c-axis is not just the rotation C_3 axis, but a helical axis of rotation of the 6th order labeled "6_3". This indicates that despite the angle between the crystallographically equivalent axis equal to 120˚, a turn to 60˚ reproduces the same axes after an additional mirror reflection operation.

Table III. lattice parameters and approximate values of molecular bond length for carbon-carbon bonds at different bond order

Lattice parameter	GaN	AlN
a, Å	3.19[a)]	3.10 [a)]
c, Å	5.17[a)]	4.96 [a)]
d, Å	1.95[b)]	1.88 [b)]
2β, ˚	108.9 [b)]	111.2 [b)]
γ, ˚	34.9 [b)]	35.8 [b)]
u	0.37 [b)]	0.38 [b)]

[a)]Lyons, 2014[100]
[b)]Vesta software[102]

The Brillouin zone and collective vibrations

To describe the vibrational properties of a crystal, the concept of Brillouin zone (momentum reciprocal space or $\vec{\kappa}$ - space) is introduced. The wave vector $\vec{\kappa}$ (Figure 3.2) is a measure of the spatial periodicity of a wave, spreading in one of the crystal directions, i.e., the number

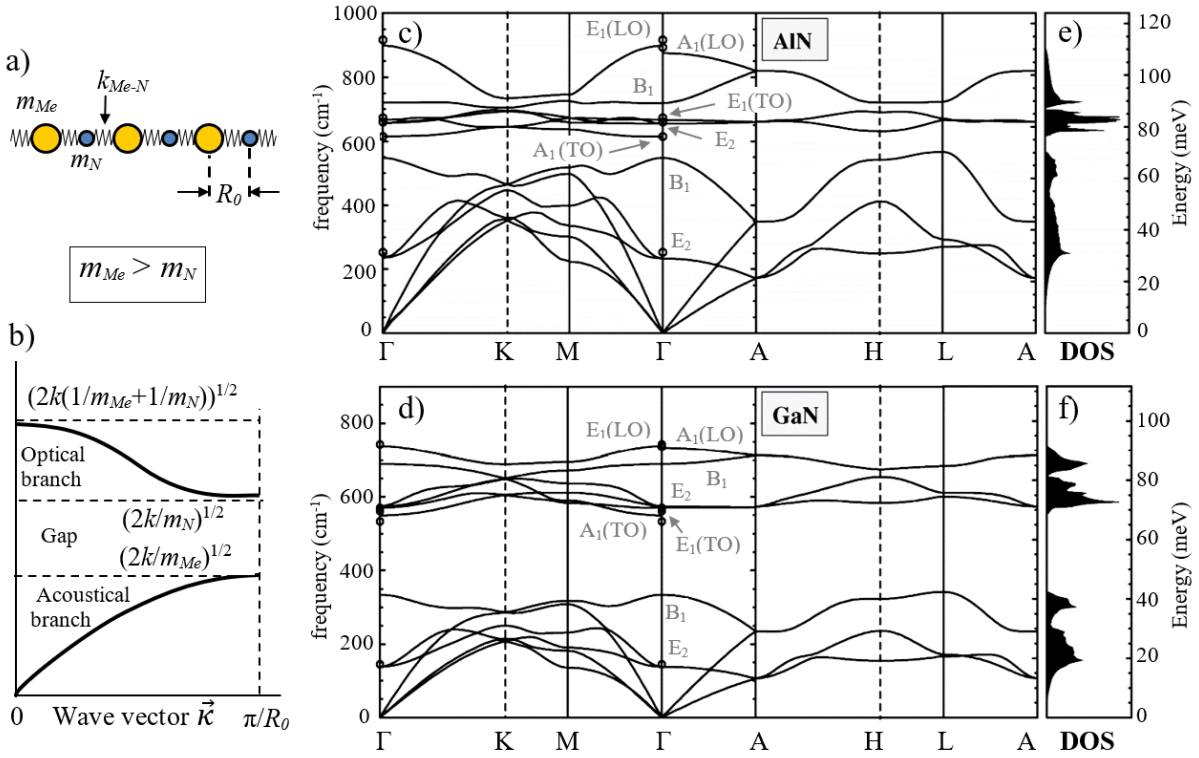

Figure 3.2. (a) The model of a diatomic alternating Me-N chain with one structural parameter R_0 and (b) corresponding dispersion law. The acoustic and optical branches are separated by the gap due to the large difference of the mass between Me (metal) and nitrogen (N) atoms. (c, d) Ab initio phonon dispersion curves and (e, f) corresponding density of states (DOS) for phonons in AlN, and GaN. The allowed ranges of phonon frequencies in are determined by the stiffnesses and masses of atoms. (c- f) are adapted from [105]. Circles: Raman-scattering data (Figure 3.6)

of oscillations per length. Thus, the frequency of the propagating wave obeys the dispersion law in the Brillouin zone and can be associated with the direction of the wave vector in the real space.[90–92] In the simplest periodic system, a regular monoatomic crystal lattice, the frequencies of allowed vibrations exist in a certain continuum range.[91,92,103] The model of alternating diatomic lattice introduces well-known splitting of the continuous frequency range into two bands, the acoustical and the optical, separated by a gap of forbidden frequencies.[104] The same can be observed for the simple one-dimensional diatomic chain model shown in Figure 3.2 (a). The corresponding dispersion law is given in Figure 3.2 (b). The Brillouin zone has the primitive view and only two typical branches (acoustical and optical) as only one "lattice" parameter (R_0) and only two atoms in the unit cell characterize the structure of the chain. Despite the simplicity, this model reproduces the basic properties of a bulk crystal.[90–92] The dispersion curves for GaN and AlN in Figure 3.2 (c, d) are reprinted from Bungaro et. al.[105] In the alternating chain the two atoms with masses $m_{Me} > m_N$ connected by spring-like chemical bonds with the elastic constant k and the equilibrium distance between the nearest atoms R_0 also limits the Brillouin zone (Figure 3.2 (b)). The parameters k, m_{Me}, and m_N are sufficient to describe the boundaries of the allowed frequency ranges of optical and acoustic vibrations.[91,92]

The intrinsic Raman modes of GaN and AlN crystals

The phonon branches of the wurtzite crystal are much more complicated than one shown for the chain. The unit cell and the Brillouin zone of the wurtzite crystal includes four atoms

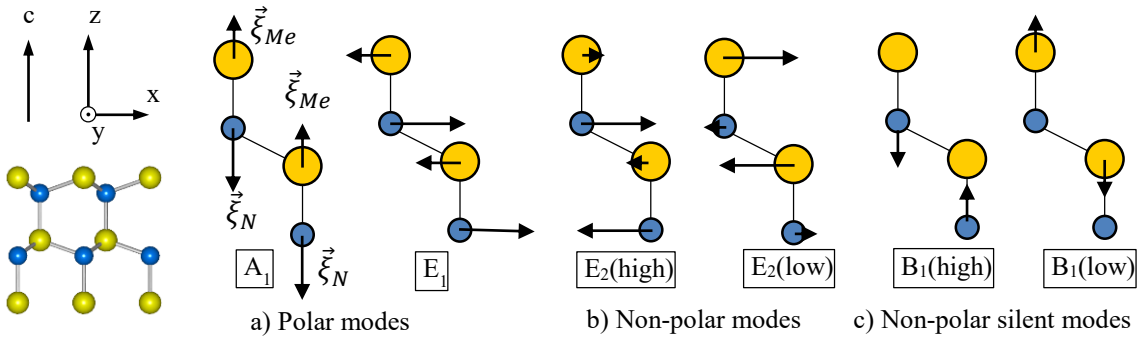

Figure 3.3. Displacements $\vec{\xi}_N$ and $\vec{\xi}_{Me}$ (Me=Ga, Al) of atoms in the unit cell of GaN and AlN are schematically shown for different intrinsic modes: (a) polar, active in absorption and Raman, (b) non-polar, active in Raman, and (c) non-polar silent modes. It should be noted that for real crystals and molecules $\xi \cong 0.01\ R_0$,[94] though $\xi \cong R_0$ in illustrations here and below. The orientation of the x, y, z axis for Porto notation is given relative to the unit cell and the c-axis.

and two lattice constants.[92,105] Thus, several dispersion curves (Figure 3.2 (c, d)) represent different normal vibrational modes (Figure 3.3) in different directions of the crystal (Brillouin zone points Γ, K, M, A, H, L are shown in Figure 3.4).

The vibrational modes in crystals can be associated with particular types of atomic movements.[106–108] The representative unit cell and atomic displacements of its individual atoms (ξ) for several intrinsic vibrational modes in GaN and AlN crystals is schematically show in Figure 3.3. This interpretation got experimental evidence in the Raman scattering research of the isotopic replacement of host GaN atoms and the measurements of these vibrational modes in the external electric field.[106,107] The A_1 and B_1 modes provide atomic displacements along the c-axis, while E_1 and E_2 give atomic displacements perpendicular to the c-axis. The labels A_1, B_1, E_1, E_2, are the irreducible representation related to the symmetry properties of crystals and the vibration provided the view of the corresponding Raman tensor discussed below.[1,92]

According to the momentum conservation law, only phonons at $\vec{\kappa} \approx 0$, can be generated in the Raman first-order process. It makes allowed only frequencies at Γ-point, while the zone continuum frequencies are forbidden. These frequencies are shown by the circles in Figure 3.2 (c, d). However, in chapter 6, the broad scattering signals in the range of phonon bands appear in spectra. The impact of whole density of states (DOS) becomes significant due to involving

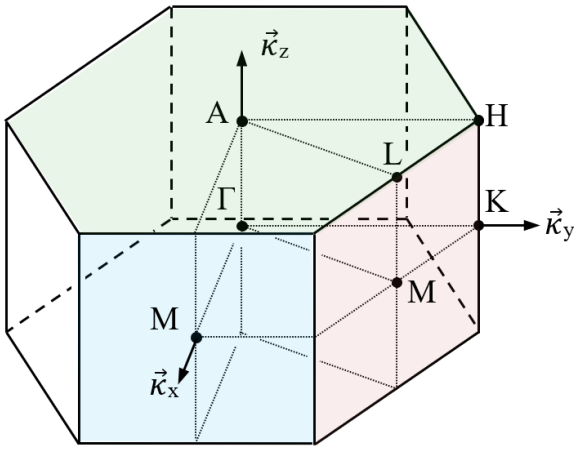

Figure 3.4. The first Brillouin zone of the wurtzite crystal structure adapted from Gil.[1] Significant reciprocal lattice points and directions are labelled.

of additional phonons (in our case, associated with point defects), then the momentum conservation law is fulfilled for the four particles (two phonons and two photons), diminishing in this way the limitations of the momentum.[93]

Activity and polarization of IR absorption vibrational modes

Only part of vibrational modes can be observed by means of Raman or IR absorption methods. To see which normal vibrational modes are visible in the IR absorption spectrum is relatively straightforward. During the IR-active vibrations, there is a change of dipole moment: $\Delta\vec{\mu} \neq 0$. The atomic positions (displacements $\vec{\xi}_i$) and the charge e_i of atom *i* then determine the oscillating dipole moment:

$$\Delta\vec{\mu} = \vec{\mu} - \vec{\mu}_0 = \sum_{i=1,2\ldots} \mathrm{e}_i\vec{\xi}_i \tag{3.1}$$

When the vibrational frequency of the dipole momentum change coincides with the IR frequency, the radiation can be effectively absorbed. Determining whether a mode is active in Raman scattering is not trivial. Polarizability α represents the "sensitivity" of the oscillator to an external electric field. More strictly, the property of the structure to change its dipole moment $\Delta\mu_p$ in the direction p under the action of the electric field E_q in the direction q is represented by the second rank tensor α_{pq}:

$$\Delta\mu_p = \sum_{p,q=x,y,z} \alpha_{pq}E_q \tag{3.2}$$

The orientation of $\Delta\vec{\mu}$ for a defect vibration in crystal can be recognized by making polarized absorption measurements since light absorption occurs only when $\Delta\vec{\mu} \parallel \vec{E}$ and zero when $\Delta\vec{\mu} \perp \vec{E}$. Due to the symmetry axis c, each point defect has crystallographically equivalent representations which should be considered together. In this way, the three equivalent defects reproduced by the symmetry operations provide $\Delta\vec{\mu}$ expressed by the three different vectors. In the dipole approximation, the absorption $A(\varphi,\gamma)$ as a function of the angles γ (the tilt angle of the dipole - between the oscillating dipole and wurtzite symmetry axis *c*) and φ (between $\vec{E}$ and *c*) is proportional to the square of the scalar product of electric field vector $\vec{E}$ and $\Delta\vec{\mu}$: $A(\varphi,\gamma) \sim \left(\vec{E} \cdot \Delta\vec{\mu}\right)^2$. Further it is simple to find the dependence of the absorption intensity on the angle φ which is equal to 0° for E∥c polarization and 90° for E⊥c polarization:[21]

$$A(\varphi,\gamma) = A_0(sin^2\gamma + (2 - 3sin^2\gamma) \cdot cos^2\varphi) \tag{3.3}$$

Where A_0 is the normalization constant. From this equation the orientation of a defect can be found just by two measurements of the linearly polarized absorption coefficient.

Activity and polarization of Raman scattering modes

Analysis of Raman scattering spectra is more complicated. Not the polarizability itself, but its change characterizes the Raman activity. According to the view of the Raman scattering cross section,[90,93,97] the vibrational mode is Raman active when the change in polarizability is nonzero due to the displacement of atoms from their equilibrium position ($\xi = 0$). Then, the value of the third rank derived polarizability tensor at is the Raman tensor:

$$r_{ij} = \left(\frac{d\alpha_{ij}(\xi(t))}{d\xi}\right)_{\xi=0} \tag{3.4}$$

Visually, the polarizability can be depicted in 3D as the ellipsoid breathing during the vibration period. The axes of the ellipsoid are determined by the values of $\alpha^{-0.5}$ in the x, y, z directions of the real space: the larger ellipsoid diameter is due to the lower the polarizability. The total polarizability of a vibrating molecule (defect/crystal) can be compiled from the polarizability of individual chemical bonds. Triatomic molecules can be a good example (see caption of Figure 3.5). One can evaluate the change of polarizability and in a vibrational mode:

- A chemical bond has the maximum polarizability when its direction coincides with *E*.
- Increase of the distance between two atoms increases the polarizability of the corresponding chemical bond, and vice versa, if the bond is compressed, the polarizability in this direction decreases.
- The polarizability of the whole molecule can be evaluated as a superposition of the polarizability of all its chemical bonds.

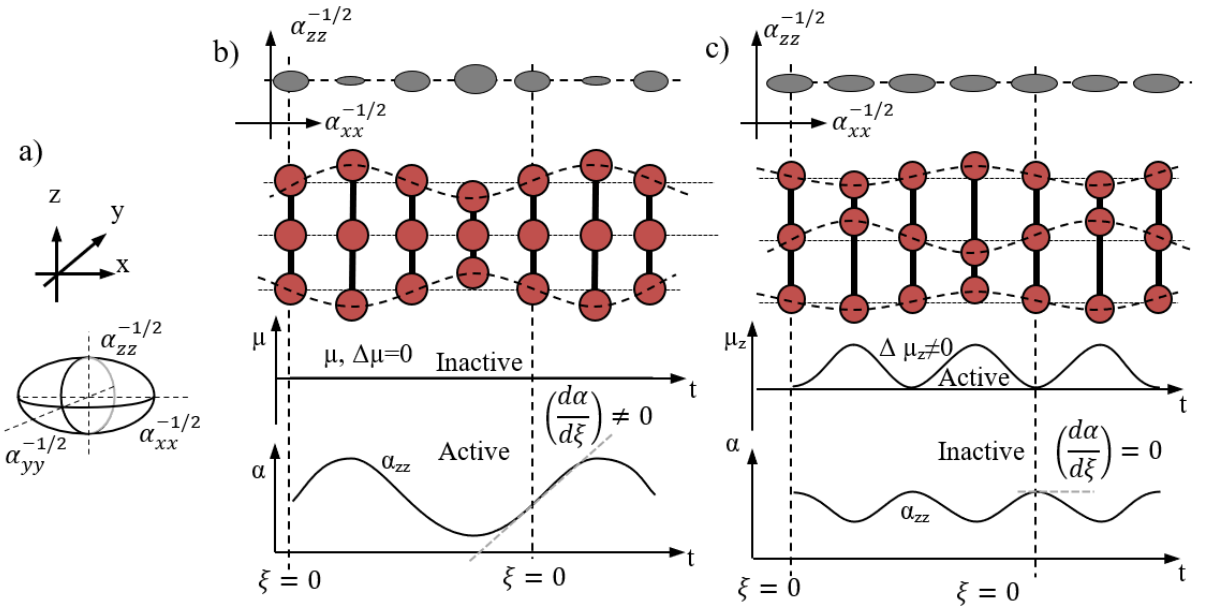

Figure 3.5. (a) The polarizability ellipsoid and the xyz space axes for a molecule. (b) The cross-section ellipse (α_{xx}, α_{zz}) of the polarizability ellipsoid for the symmetric stretching mode of a triatomic linear molecule, the values of the dipole moment and the polarizability during the vibration periods. The moments of time t with zero atomic displacement are marked by the vertical dashed lines. The symmetric vibration (b) is active only in Raman, while the antisymmetric vibration of the same molecule (c) is active only in IR.

Raman tensor of intrinsic vibrational modes

Polar modes of optical phonons A_1(LO), A_1(TO), E_1(LO), E_1(TO) are both infrared and Raman active as they provide change of the polarizability and the dipole moment change; E_2(low), E_2(high) are only Raman active; the two B_1 modes are neither Raman nor IR active (silent modes).[92] Thus, the six modes can be observed in Raman spectra. Usually, the number of the peaks in any individual spectrum is lower because of the selection rules imposed by the

scattering geometry and the Raman tensors components. For wurtzite GaN or AlN, whose symmetry characteristics are given by the point group C_{6v}, the Raman tensors have the following matrix form, where r_1- r_4 denote the Raman tensor elements:[98,109–113]

$$r[A_1] = \begin{bmatrix} r_1 & 0 & 0 \\ 0 & r_1 & 0 \\ 0 & 0 & r_2 \end{bmatrix}, r[E_1] = \begin{bmatrix} 0 & 0 & -r_3 \\ 0 & 0 & r_3 \\ -r_3 & r_3 & 0 \end{bmatrix}, r[E_2] = \begin{bmatrix} r_4 & r_4 & 0 \\ r_4 & -r_4 & 0 \\ 0 & 0 & 0 \end{bmatrix}. \quad (3.5)$$

The matrix form of the Raman tensors depends on the choice of the coordinate axes. The tensors listed above are defined with respect to the basis axes of a right-angled coordinate system x, y, and z, depicted in Figure 3.3 with z parallel to the c-axis. From the tensor view one can determine if a Raman active lattice vibration is allowed or forbidden for a particular experimental scattering geometry (Table IV).[98,109,110,113] The various scattering configurations are labeled by the Porto notation:[98] $k_i(e_ie_s)k_s$, where the symbols k_i and k_s outside the parentheses denote the propagation directions of the incident and scattered radiation with respect to the crystal axes, respectively. The direction of corresponding polarization vectors is given by the two symbols e_i and e_s inside the parentheses. In backscattering geometry, the propagation directions of the incident and scattered light are antiparallel, e.g., x(yy)x̲ denotes a measurement in which the incident radiation propagates along the x axis and the scattered radiation is detected along the -x axes while their polarization vectors are directed along the y axis. The modes allowed (+) and forbidden (-) by the polarization selection rules are listed in Table IV.[92,111,114] Figure 3.6 shows measurements of the high-quality reference GaN sample (GaN000). The found phonon vibrations are in complete agreement with the earlier researches, though LO forbidden modes are also observable in the spectra.[92,111,112,114]

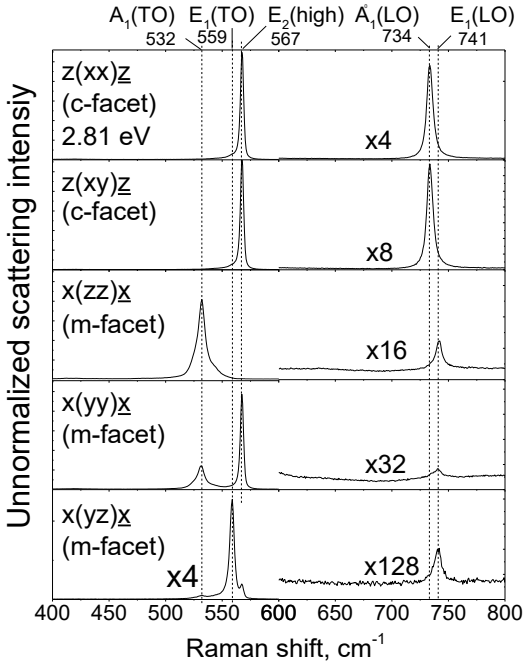

Figure 3.6. Raman scattering spectra measured for a reference GaN sample (GaN000) for five different geometries (given in Porto notation) according to axis orientation shown in Figure 3.3 (z∥c). The excitation energy is equal to 2.81 eV (442 nm). Labelled modes are found in a good agreement with earlier reported intrinsic Raman scattering data.[111,112,114]

Table IV. Polarization selection rules of Raman modes on different facets of crystals GaN and AlN for five different geometries (given in Porto notation). About a few disagreements of selections rules in case of LO can be found in [92,111,112,114]

Polarization	sample	A_1 (TO)	E_1 (TO)	E_2	A_1(LO)	E_1 (LO)
z(xx)z̲ / z(yy)z̲	c-facet	-	-	+	+	-
z(xy)z̲ / z(yx)z̲	c-facet	-	-	+	-	-
x(zz)x̲ / y(zz)y̲	m-facet	+	-	-	-	-
x(yy)x̲ / y(xx)y̲	m-facet	+	-	+	-	-
x(zy)x̲ / x(yz)x̲ y(zx)y̲ / y(xz)y̲	m-facet	-	+	-	-	-

3.2. The basis of harmonic oscillator model

Influence of masses and vibrational amplitudes of atoms on the frequency shift

The basement of the description of any vibrational process is the unchanged center of mass during the vibration:

$$\sum_i m_i \vec{\xi}_i(t) = 0 \tag{3.6}$$

Here, $\vec{\xi}_i(t)$ is the real-space displacement vector of the atom i with the mass m_i at any moment of time t. The letters $\vec{\xi}_i$ or $\xi_i = |\vec{\xi}_i|$ are also used in the meaning of the maximum deviation or vibration amplitude (time-independent). The formal description of the differential equations of motions in frames of the classic mechanics for molecules[94] or crystals[91,92,97] based on Eq. (3.6) can be found in corresponding literature. This relation in particular leads to the limited number of allowed normal vibrational modes in crystals, and in molecules: equal to (3*N*-5) or (3*N*-6) for the linear or bent N-atomic molecules, respectively.[94]

Vibrational properties of crystals, defects, or molecules can be considered within the approximation of the harmonic oscillator. Metal atoms (Al or Ga) form a stable bond with nitrogen atoms. Covalent or ionic bond promotes the attraction of atoms on long distances; on the other hand, when the distance between the two atoms *R* decreases, the Pauli Exclusion Principle originates the rapidly increasing repulsion forces. These two forces constitute the net force *F* shown in Figure 3.7 as a function of the distance R (the green curve). The attraction and repulsion forces are equivalent (F=0) at R=R_0 (equilibrium bond length). This distance in GaN or AlN is expressed by the lattice parameters *uc* that could be compared with the bond lengths of carbon-carbon bonds in molecules (see Table III). For a diatomic system, the potential energy *U* (orange curve) has a minimum at this point, and the deviation of the distance *R* from the equilibrium is the atomic displacement ξ=(R_0-R) results in potential energy increase.[1]

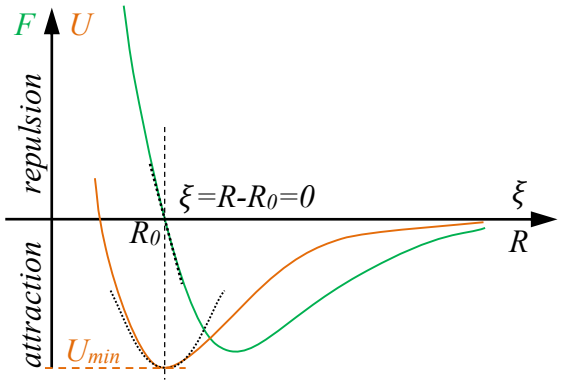

Figure 3.7. The net force F and the vibronic energy U, as a function of the distance R between atoms or the displacement ξ=R-R_0 where R_0 is the equilibrium distance. At this point the energy reaches its minimum U_{min} (while F=0). The harmonic approximation relevant at $\xi \to 0$ shown by the dotted lines $U \sim \xi^2$ and $F = k\xi$

[1] the formal approach requires talking here about the potential energy depending on 3*N* Cartesian or normal coordinates for *N* atoms of a molecule (or crystal).[94,97]

By approximating the net force by the linear function as $F \approx k\xi$ (dashed straight line), the system becomes similar to a *harmonic spring oscillator*. The damping, exchange of energy between different normal vibrational modes, and other *anharmonic* processes are discussed, e.g., in chapter 10.3 of Baldassare and Powell.[97] The harmonic potential energy depends on the displacement ξ as $U(\xi) \sim k\xi^2/2$ (dotted parabolic curve in Figure 3.7). The masses of vibrating atoms (m, m_i, …) and the force constant (stiffness of the chemical bond) determine the vibration frequency (ν). The kinetics of the harmonic oscillator provides the well-known relations for ν and the potential energy U:

$$\nu^2 = \frac{k}{M}, \tag{3.7}$$

$$U(\xi) = \frac{k\xi^2}{2} = \frac{M\nu^2\xi^2}{2}. \tag{3.8}$$

where M is a representation of atomic masses determined by Eq. (3.6), e.g., in Eq. (*5.1*) the reduced mass $M = \frac{m_1+m_2}{m_1 m_2}$ for a diatomic oscillator (similar equations appear for limits of the phonon bands in Figure 3.2). For any normal vibrational mode of a multiparticle harmonic oscillator, total energy of the oscillator U_{tot} is a constant in time and can be considered as the sum of energies of each atom; the energy U_i of atom i is proportional to the mass m_i and the square of the atomic amplitude ξ_i:

$$U_{tot}(t) = const = \sum_{i=1}^{i=n} U_i = \sum_{i=1}^{i=n} \frac{m_i \nu^2 \xi_i^2}{2} = \frac{\nu^2}{2} \sum_{i=1}^{i=n} m_i \xi_i^2 \tag{3.9}$$

Maximum and minumum isotope-mass-related shift of frequency

In this work, the isotopic replacement $^{12}C \rightarrow {}^{13}C$ is widely used inspecting the possible modes of the carbon point defects in the lattice of GaN and AlN crystals. The ideal isotope replacement $m_i \rightarrow m_i^*$ does not change any elastic constant and, hence, the atomic forces. With this respect, the potential energy curve of the system does not change too:[1]

$$U^*\left(\vec{\xi}^*(t)\right) = U\left(\vec{\xi}(t)\right), \tag{3.10}$$

Then, for the replacement of one single atom (e.g., atom $i=n$):

$$U^*(\xi) = \frac{\nu^{*2}}{2}\left(m_n^* \xi_n^{*2} + \sum_{i=1}^{i=n-1} m_i \xi_i^{*2} \right). \tag{3.11}$$

The mass m_i of defect atom i affects the frequency of the vibrational modes proportionally to its vibrating amplitude in square. With this respect, the frequency change $\nu \rightarrow \nu^*$ due to the replacing of the single atom and corresponding frequency ratio f are:

$$\frac{\nu^2}{\nu^{*2}} = \frac{m_1\xi_1^{*2} + m_2\xi_2^{*2} + \cdots + m_n^*\xi_n^{*2}}{m_1\xi_1^2 + \cdots + m_n\xi_n^2}, \qquad f = \frac{\nu}{\nu^*} \tag{3.12}$$

[1] note, a little change of k follows from different structure of isotopic atoms; the highest effect is expected for the lightest nuclei, e.g., for hydrogen-deuterium replacement. For $^{12}C \rightarrow {}^{13}C$ the difference is below a couple of percent.

The further analytics of this issue requires a qualification of the specific case and additional parameters, as it can found for many particular examples.[94] It is clear that the isotope shift of a certain vibrational frequency will be very small when the replaced atom moves with low amplitude in the particular normal vibrational mode, whereas the shift will be relatively large when the atom in question has a large amplitude in that normal mode. It makes sense to note the maximum and minimum theoretically possible shifts as they both can be observed for the $^{12}C \rightarrow ^{13}C$ replacement in GaN.

The maximum shift appears due to the replacement of all mobile carbon atoms participating in the particular vibration (m=12 a.u.) with the heavier isotope (m^*=13 a.u.) and there are no other mobile atoms impacting the energy. Then the theoretical limitation of the maximum frequency shift is given by the ratio η_{max}:

$$\frac{\nu^2}{\nu^{*2}} = \frac{m^*(\xi_1^2 + \cdots + \xi_n^2)}{m\,(\xi_1^2 + \cdots + \xi_n^2)} = \frac{m^*}{m} = \frac{13\ a.u.}{12\ a.u.} \approx 1.083, \qquad f_{max} = \frac{\nu}{\nu^*} \approx 1.041 \tag{3.13}$$

Obviously, the minimum shift equal to zero appears when the relaced carbon atom(s) do(es) not move in the particular vibrational mode. In this case, the zero vibrational amplitude of a replaced atom results in zero impact on the energy of the system. A classic example here is the replacement of a heavy chlorine atom in CH_3Cl tetragonal molecule. Even though the chlorine atom should be mobile at several normal vibrations, its huge atomic mass comparing to the three hydrogen atoms provides neglecting ξ_{Cl}^2. With this respect, only one fundamental frequency, 732 cm^{-1}, shows an appreciable isotope splitting due to $^{35}Cl \rightarrow ^{37}Cl$ replacement.[94,115] It must therefore correspond essentially to the C-Cl stretching vibration, a conclusion that is qualitatively and quantitatively in agreement with the observed shift.[94,115]

Similar virtually zero shift is possible for the defect vibrational mode in crystal when the normal vibration includes a large group of host atoms in addition to the defect atom(s). Figure 3.8 shows the relative vibrational amplitudes of atoms in the diatomic chain with a defect (atom with the mass m_d) at different localization of the vibration. Figure 3.8 (a) is the case of zero isotope shift when the lattice propagates driven oscillations lying in the range of the optical or acoustical phonon bands. In contrast, when the defect frequency is out of the phonon bands, the defect oscillation is centered on the defect atom and its neighbors Figure 3.8 (b), i.e. the stimulated frequencies are damped out in a short distance.[104] The first case is called *band vibrational modes* while the latest can be called *localized vibrational modes* (more about this can

a) delocalized defect mode b) localized defect mode

Figure 3.8. An atom with mass m_d substitutes nitrogen atom forming a defect in Me-N diatomic chain. If the defect vibrational frequency lies in the range of the chain allowed frequencies, the mode is significantly delocalized (a). If the defect frequency is far from the allowed ranges, it should be spatially localized in the area of the defect atom (b), when the localization is maximum ($\xi_2 \approx 0$). The intermediate case can be proposed for a real defect.

be found in Sect. 10.5 from Baldassare and Powell).[97] The impact the host atoms to the potential energy (Eq. (3.9)) and the frequency shift (Eq. (3.12)) of the band mode makes the influence of the defect atoms neglective. When only the nearest neighbors of the defect atom are mobile ($\xi_2 \cong 0$) it is, in fact, a simplification to a triatomic molecule model.[116] In chapter 5, I reference to the numerical evaluation of the isotopic replacement for the mono-C defect in the resonance with GaN host atoms based on DFT calculations provided by Lyons.[34,117]

3.3. Determination of the structure of the molecule-like defects

X-Y-Z notation of defect (molecule) structures

In many cases, a point defect can be considered as a molecule in the matrix of the host crystal since the defect vibrational properties are often (but not always) are determined either exclusively by the atoms of the defect and its nearest shell. The defect structure has its own symmetry which can be described using the molecular symmetry groups. This symmetry is different from the symmetry of the hosting crystal, affects the vibrational properties, and can be established in isotopic analysis. Nevertheless, any defect has several representations determined by reproducible crystal symmetry operations, and hence, measuring the anisotropy of any point defect property, the result obeys the more general crystal symmetry.

Emphasizing the difference of vibrational properties, following Heizberg,[94] and use Latin capital letters X, Y, Z to designate structural elements of a defect in some analogy with the chemical formulas. For example, NaOH molecule has three atoms and three different structural elements, therefore it belongs to the XYZ-type molecules, and H_2O has two hydrogen atoms with identical structural positions, therefore it belongs to the XY_2-type. In fact, even some more complex molecules, such as CH_3-CH_2-Cl can be considered as X-Y-Z tri-particle molecules.[118] Like this, the defects can also be grouped according to their structure. Moreover, if the same chemical element occupies different positions in the structure of a crystalline defect or a molecule (e.g., O in HNO_2 molecule), it should be designated by the different letters. As an example, Figure 3.9 shows different molecules in where the same-size balls show the particles consisted from the same chemical units. In Figure 3.9 (d), the defect consists from the three chemically equal particles (labeled X, Y, Z), however, the internal structure of such defect belongs to XYZ-type because the non-symmetric chemical bonds with the nearest-shell host atoms (Ga and N in the illustration) require to consider the sites X and Z as the different.

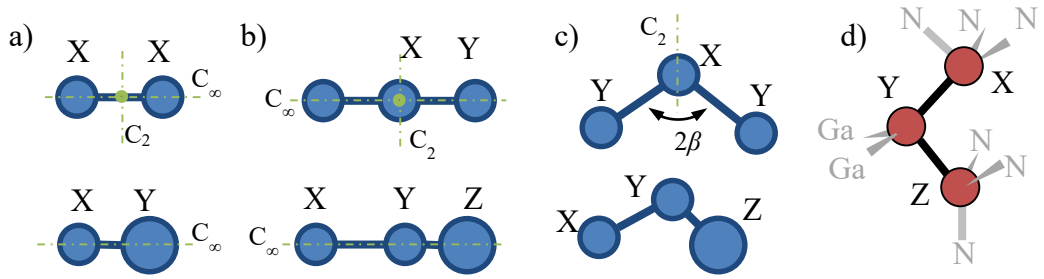

Figure 3.9. The examples of di-atomic (a), linear tri-atomic (b), bent tri-atomic (c) molecules. The balls of the same size indicate the structural units with the same chemical compound, while the Latin letters X, Y, Z indicate the structural difference units. In (d) the XYZ defect in the shell of Ga and N atoms is shown. The symmetry elements are shown by green dash-dot lines and points.[94,95]

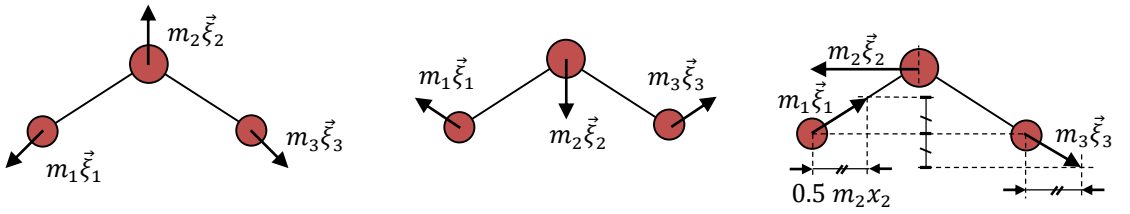

a) symmetric stretching (v_1) b) bending (v_2) c) antisymmetric stretching (v_3)

Figure 3.10. Three normal modes of a triatomic XY_2 molecule. The mass displacement $m_i\vec{\xi}_i$ vector of atom i is illustrated by the black arrows. (c) The requirement of the immobile gravity center (Eq (3.6)) is illustrated. Equal components of the mass displacements i=1 and i=3 are marked.

In essence, the vibrational properties of a defect can be considered as properties of a molecule, which, however, additionally complicated by the bonds and interactions with the host atoms of the crystals. As an exclusion here is the delocalized defect vibration mentioned above (Figure 3.8 (a)) while the localized vibration would be a clear example of Y-X-Y "molecule". Tri-atomic bent molecules XY_2, has three fundamental frequencies in vibrational mode shown in Figure 3.10: bending (ν_2), symmetric (ν_1) and antisymmetric stretching (ν_3) modes. Vectors $\vec{\xi}_i$ show the atomic displacements depending on the elastically constants and the masses of the vibrating particles in the molecule. Some relations follow directly from the condition of the fixed center of mass (Eq. (3.6)); the simple requirements for the geometry are marked on the sketch for ν_3 mode in Figure 3.10 (c).

Orientation of the vibrating dipole moment in a defect (molecule)

In contrast to molecules, the defects in the crystal lattice have a strict orientation relative to the symmetry axes. Several examples of the vibrating dipole moment orientations in triatomic bent molecules (or defects) are shown in Figure 3.11. XY_2 (a, b) and XYZ (c) oscillators are illustrated at the zero atomic displacement, while the black arrows show the maximum displacements $\vec{\xi}_i$. Suggesting the Y and Z atoms (i=1, 3) charged negatively and X atoms (i=2) charged positively, one can plot the dipole moments $\vec{\mu}_0$ and $\vec{\mu}$ for the two cases and find $\Delta\vec{\mu}$ as the difference of the two vectors. For the same XY_2 structure, the orientation of $\Delta\vec{\mu}$ depends on the type of the normal mode and can be along the symmetry axis and $\vec{\mu}_0$ (Figure 3.11(a)) or perpendicular to it (Figure 3.11 (b)). For the third illustrated case, XYZ structures $\Delta\vec{\mu}$ is tilt relative to $\vec{\mu}_0$.

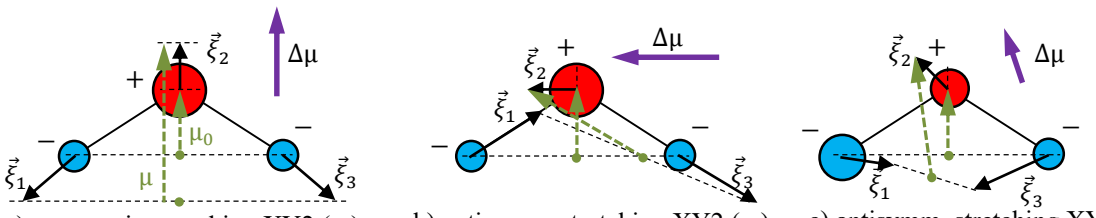

a) symmetric stretching XY2 (v_1) b) antisymm. stretching XY2 (v_3) c) antisymm. stretching XYZ (v_3)

Figure 3.11. Vibrating dipole moment ($\Delta\vec{\mu}$) for different IR active vibrational modes of XY_2 and XYZ molecules. The dipole moment at the equilibrium positions of atoms ($\vec{\mu}$) and at the maximum atomic displacement ($\vec{\mu}_0$) both determine the direction of $\Delta\vec{\mu}$ and the absorption properties. The atomic displacements $\vec{\xi}_1$, $\vec{\xi}_2$, $\vec{\xi}_3$ of XYZ molecules are reproduced in proportion as for Cl-CH_3-CH_2 (see Fig. 62 in Herzberg)[94]

Isotope effect in molecule-like defects. Isotopomers

The presence of both carbon isotopes at significant concentrations can lead to multifold splitting of the vibration frequencies of the carbon-containing defects. The occupation of a carbon atom site in the defect structure by one of the two isotopes is a statistical random event due to nearly the identical properties of the isotopes. Taking into account the relative concentrations for the two isotopes [^{12}C%] and [^{13}C%] in the meaning of the probabilities ([^{12}C%] + [^{13}C%] = 1 or 100%), the event is considered in the terms of the binomial distribution. The number of combinations of the two isotopes on n structurally different sites is equal to 2^n, furthermore, each atom of the defect has a unique vibrational amplitude. In this case, mono-C, di-C, and tri-C defects with n = 1, 2, or 3, have 2, 4, or 8 combinations of isotopes, respectively, that vibrate at unique frequencies according to Eq. (3.12). On the other hand, atoms in structurally equal sites vibrate with identical amplitude so corresponding frequencies degenerate. With degeneracy, the number of peaks for a di-C defect decreases from 4 (XY) to 3 (XX); for a tri-C defect, it decreases to 4 (XXX) or 6 (YXY) individual frequencies. The defects with identical structural formula but different isotope compound are called by *isotopomers*.

For example, the Di-carbon XY defect, $C_X - C_Y$, has four combinations; their probabilities and the type of isotopomers (^{13}C-pure, ^{12}C-pure, or mix) are given in Table V (next page). The two mix isotopomers have the same probability but different frequencies for XY structure, while for higher XX symmetry, these isotopomers become identical and the frequencies degenerate.

Figure 3.12 illustrates how the probabilities for different isotopomers (i.e., the relative intensity of absorption or scattering of different isotopomers) depend on the isotope abundance in the cases of mono-C, di-C, and tri-C defects without the frequency degeneracy. With degeneration, the intensity is multiplied to the corresponding binomial coefficients. The dependences help to distinguish the cases when some of the peaks are degenerated or unresolved and allow to determine the number of atoms by the isotope splitting almost clearly. At the specific point of equal probabilities [^{12}C] = [^{13}C], the isotopes become statistically undistinguishable, and hence, the basic probabilities of all combinations are equal. It is the case of GaN crystal C1213 with equal chemical concentrations of the two isotopes. In such sample, all isotopomers are possible and the observable divisible difference of intensity between their peaks is determined by the binomial coefficients. The expected signatures of the isotope-related splitting are shown by the stick-spectra in Figure 3.13.

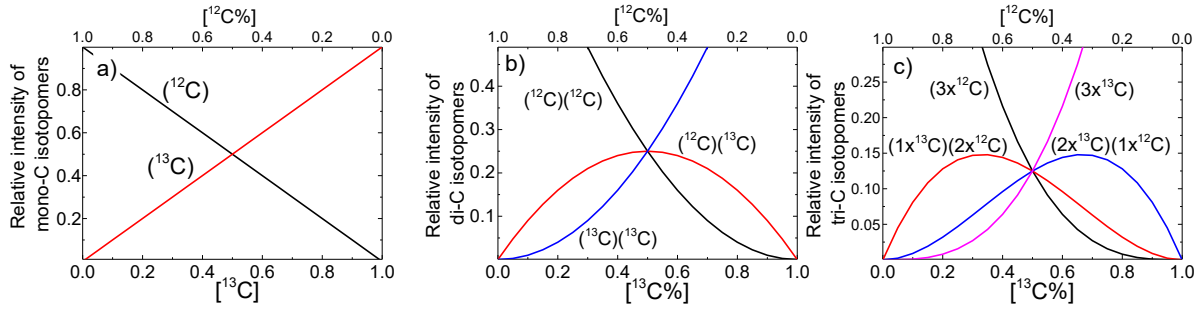

Figure 3.12. Relative probability (intensity) of isotopomers in spectra at different relative isotope concentrations [^{12}C%] + [^{13}C%] = 1 for the case of mono-C (a), di-C (b), and tri-C (c) defects. The label of each curve indicates the number of isotopes in the structure of an isotopomer.

Table V. Configurations and probabilities of isotopomers of C_X–C_Y as a function of the relative isotope concentrations $[^{12}C\%] + [^{13}C\%] = 1$. The case $[^{12}C\%] = [^{13}C\%] = 0.5$ is illustrated in Figure 3.13 (b, c).

Configuration	Isotopomer type	Probability	Shorten notation
$^{13}C_X - {}^{13}C_Y$	^{13}C-pure	$[^{12}C\%]^0 \times [^{13}C\%]^2$	$[^{13}C\%]^2$
$^{13}C_X - {}^{12}C_Y$	mix	$[^{12}C\%]^1 \times [^{13}C\%]^1$	$[^{12}C\%] \times [^{13}C\%]$
$^{12}C_X - {}^{13}C_Y$	mix	$[^{12}C\%]^1 \times [^{13}C\%]^1$	$[^{12}C\%] \times [^{13}C\%]$
$^{12}C_X - {}^{12}C_Y$	^{12}C-pure	$[^{12}C\%]^2 \times [^{13}C\%]^0$	$[^{12}C\%]^2$

Determination of the number of C atoms the isotopic splitting

The stick spectra depict the relative spectral positions and magnitudes of the peaks in the isotope splitting. The labels in the bottom part indicate the defect structure and the masses of isotopes filling the carbon sites X, Y, Z. With an increase in the mass of the elements, the vibration frequency decreases. In Figure 3.13 (a), a defect with only one carbon atom mobile at the particular vibration gives the splitting into two equal peaks. The surrounding unknown carbon-free structure influenced only the magnitude of the frequency change is labeled by R. The next two stick spectra show the defects at particular vibrational mode with two mobile carbon atoms, on equal (b) or different (c) structural positions. The next three stick spectra (d – f) are associated with the tri-C defects with different symmetry, X_3, XY_2, and XYZ, respectively. Where the defect symmetry results in the degeneration of the peaks (b, d, e), the degree of degeneration is marked as the multiplier.

The fundamental features of the symmetry in spectral positions are shown by the green arrows and the dash-dot lines. This symmetry follows from the invariance of the isotope replacements in some cases. For example, two isotopomers $^{12}Y^{12}X^{12}Y$ and $^{13}Y^{12}X^{13}Y$ in Figure 3.13 (e) obviously differ from $^{12}Y^{12}X^{13}Y$ by the replacement of the single Y atom. As in all three cases the relative amplitude of the Y atom is approximately the same, the corresponding frequency ratios are equal. Furthermore, the invariance and the same frequency ratio can be found for the pairs $^{13}X^{13}Y^{13}Z$ - $^{12}X^{13}Y^{13}Z$ and $^{12}X^{12}Y^{12}Z$ - $^{13}X^{12}Y^{12}Z$, etc. The equidistant position of the peaks and their relative intensity is an important criterion for recognizing the isotope effect. Formulas for calculations of the shift in particular cases are provided in corresponding sections of Chapter 5.

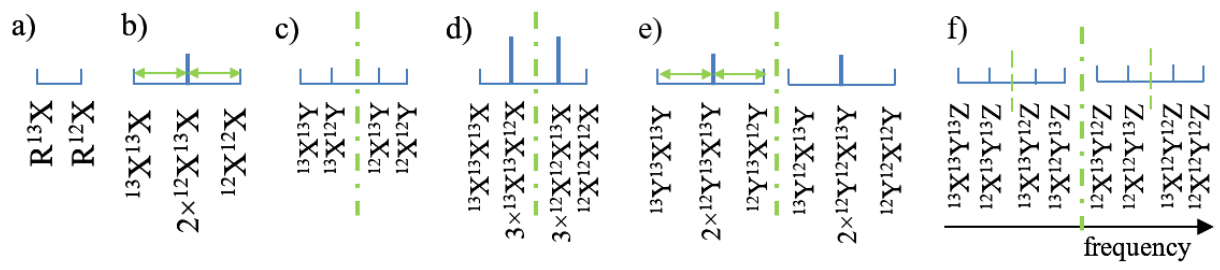

Figure 3.13. Stick spectra at $[^{13}C\%] = [^{12}C\%]$ for the cases of (a) mono-C, (b) di-C XX, (c) di-C XY, (d) tri-C X_3, (e) tri-C XY_2, and (f) tri-C XYZ defects.

3.4 Harmonic oscillators in quantum mechanics

IR absorption. Configuratino coordinate (CC) diagram

The theory of absorption and emission of light is also based on the harmonic oscillator model in quantum mechanics consideration.[93,96] In the initial electronic state, the defect (molecule) vibrates and the parabolic harmonic potential $U(\xi)$ describes its electronic state. Then the individual allowed vibrational states and corresponding "discrete"[1] energy values U_n are given by:

$$U_n = \hbar\nu_0(\frac{1}{2} + n) \tag{3.14}$$

here n – is the number of the vibration level, ν_0 – is the oscillator frequency value in IR range. These levels are equidistant for the potential parabolic curve, which is in good agreement with observations, especially for small n. At the same time, alternatively, there are more sophisticated models considering more accurate shape of potential curves (see, e.g.[119,120]). The dashed horizontal curves depict the energy levels of the oscillator in Figure 3.14. The transition of the system from its vibration ground state (n=0) to the first excited vibration state (n=1) is possible with absorption of the energy E_{IR}. The state configuration (i.e., the potential curve $U(\xi)$) does not change due to this excitation as the low energy E_{IR} results only in changes of the atomic movement but not in changes of the atomic structure. In other words, the system remains in the same (ground) electronic state A.

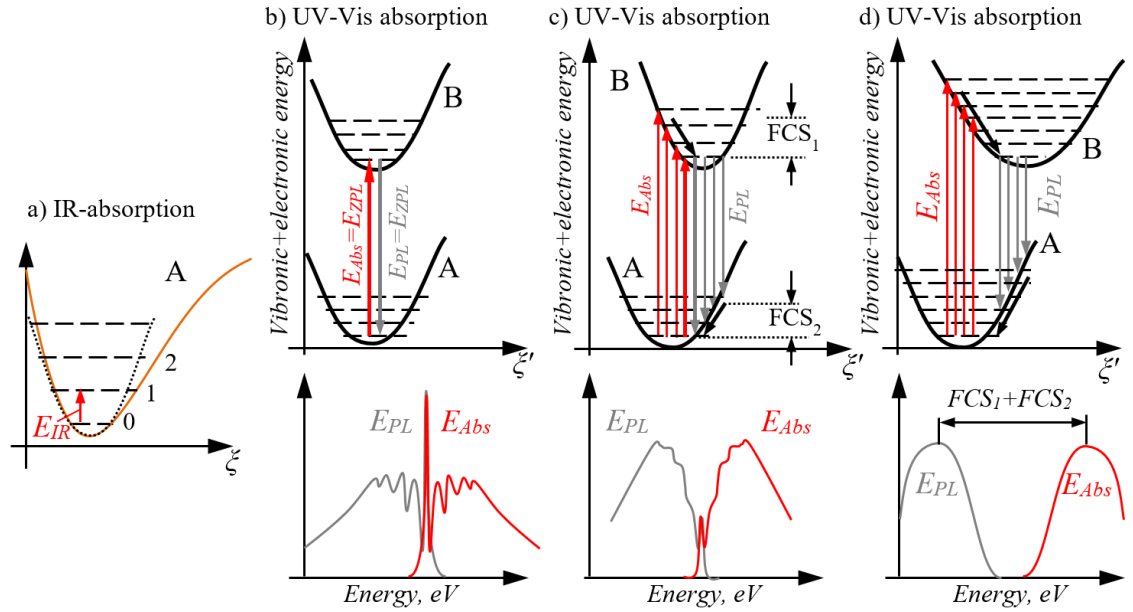

Figure 3.14. Vibrational and electronic transitions for a molecule or a molecule-like defect within the harmonic oscillator model (CC diagrams). The different vibrational states (n=0, 1, 2,…) are indicated by the dashed horizontal lines for the ground (A) and excited (B) electronic states. A and B are depicted for the lattice coupling increasing from (b) to (d). The red arrows up illustrate the probable transitions with the absorption of a phonon (E_{IR} and E_{Abs}). The relaxation of the system on energy FCS is shown by the tilted black arrows in (c, d). The transition from the ground vibrational state of B to the vibration states of A with emission of a photon E_{PL} are shown by the grey arrows. (b) – (d) are adapted from Böer and Pohl.[96]

[1] The thin rotational structure of the states is not needed in the analysis of further experiments.[94,219]

UV-Vis absorption of point defects on CC diagrams

Absorption of significantly higher energy ($E_{Abs}>>E_{IR}$) results in the process of photo-excitation or photoionization accompanied by the transition of the defect from the ground electronic state A to another, excited or ionized, electronic state B. In the configuration coordinate (CC) diagram in Figure 3.14 (b-d), the configuration coordinate ξ' has a similar meaning to the atomic displacement ξ (cf. Figure 3.7). The two electronic states are represented by the two potential energy curves $U(\xi')$. The electronic and vibronic energy of the defect center and its nearest neighbors here is plotted as a function of the distance (ξ') between the defect atom and one representative neighbor.[96] The shape of the energy curve $U(\xi')$ is usually different for the two different electronic states. The shift of parabolas' minima along the CC axis illustrates that the atoms of the excited defect have changed the equilibrium distances due to the excitation.

The CC diagrams for the point defect in Figure 3.14 (b-d) describe the four-step processes including light absorption (E_{Abs}), vibrational relaxation (FCS_1), light emission (E_{PL}), and the second vibrational relaxation (FCS_2). The corresponding absorption-emission spectra are illustrated for each case at the bottom. In accordance with the Frank-Condon principle,[121] the absorption and emission processes are instantaneous relative to the slow processes of vibrational relaxation. Due to the light excitation, the defect transfers to the electronic state B and relaxes into the vibrational state n=0, emitting FCS energy in the form of vibrational quants. The values of FCS here characterize the degree of the electron-phonon coupling for the system defect-lattice.[96] The sum (FCS_1 + FCS_2) can be found experimentally as the difference between the spectral positions of the absorption and emission peak maxima. The individual values of FCS_1 and FCS_2 can be found theoretically with good accuracy, most commonly from the DFT. For GaN and AlN, these values can be typically as high as $FCS_1 \approx FCS_2 \approx 0.3\ldots0.7$ eV;[59,61,62,100,122] the highest value of $FCS_1+FCS_2 \approx 2$ eV is attributed to V_N vacancies in AlN since the heavy surrounding Al atoms vibrate at very low frequency.[122] Higher shift energies can appear for defects that have DX-configuration.[123–127] Figure 3.14 illustrates the cases of weak (b), medium (c), and high (d) coupling and corresponding different FCS energy resulted in a different view of the absorption-emission spectra. The coupling increases with higher ionicity of the lattice binding forces and lower elastic force constant.[96] Also, deep defect levels show a stronger coupling than shallow states.[96]

For weak coupling, the parabola for the excited electronic state (Figure 3.14 (b)) is not shifted significantly from the ground-state parabola. Then the wavefunctions of the same-n vibrational states keep overlapped and provide a high probability of the transition.[96] This causes the most probable transition to be the minimum-to-minimum zero-phonon line with a narrow linewidth (E_{ZPL} energy in Figure 3.14). With increasing intermediate coupling, the relative strength of the zero-phonon line gradually decreases, and the phonon replica broaden, which renders them less distinct (Figure 3.14 (c)). Finally, for strong coupling of the defect all features combine into a broad absorption "line" (Figure 3.14. (d)).[96]

3.5. Properties and structure of point defects calculated by DFT

DFT calculations of defect structure, ZPL, absorption, and emission energy

The above theoretical aspects make it possible to experimentally establish the atomic structure of a vibrating point defect. Modern computational methods make it possible to predict a set of properties for defects with a known structure. Below, the point defects examined by DFT are classified and systemized. DFT considers the multi-particle problem of the interaction of charged bodies. In this approach, the total energy of the system is expressed in terms of which are all functionals of the charge density: ion-electron potential energy, ion-ion potential energy, electron-electron energy, kinetic energy, exchange-correlation energy. The method overlaps many parameters of the defects, not only the energies of absorption and emission, but also the relative intensities and frequencies of vibrations and cross-section for optical and electrical processes and vibrational frequencies. I provide detailed descriptions just for a few of the defects, while the broader information about the others can be found in following references. Defects that are found or suspected within the framework of this work are given special attention in the corresponding paragraphs of the chapter on the identification of the structure of defects.

The defect formation energy is a linear function of the Fermi level, while the charge state of the defect determines the slope (Figure 3.15 (a -c)): a constant function for a neutral charge state, a positive (negative) slope for a positive (negative) charge state. The distance of the inflection points from one of the bandgap edges gives the transition energy (E_{ZPL}).

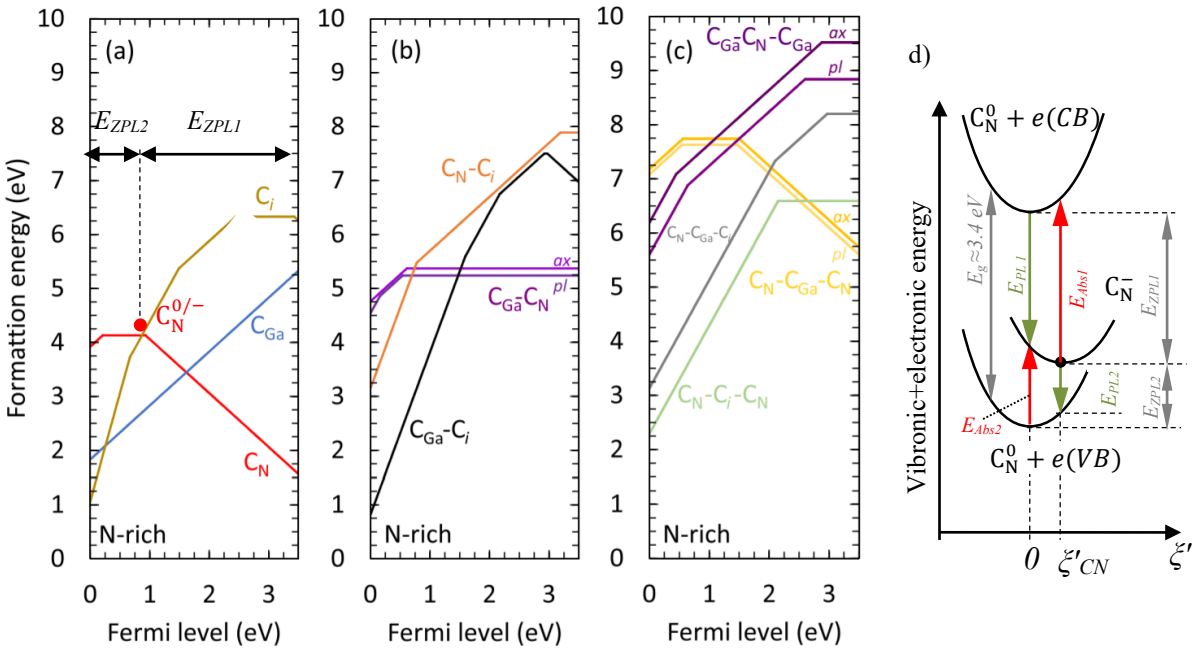

Figure 3.15. Formation energy versus Fermi level for C-related defects and complexes in GaN, under N-rich condition. (a) Species containing one carbon: C_{Ga}, C_N, and C_i., (b) complexes with two carbons: C_{Ga}-C_N (in planar (pl) and axial (ax) configurations), C_N-C_i, and C_{Ga}-C_i. (c) complexes with three carbons are shown: C_N-C_{Ga}-C_N (pl and ax), C_{Ga}-C_N-C_{Ga} (pl and ax), C_N-C_i-C_N, and C_N-C_{Ga}-C_i. In (d), the CC diagram of C_N defect illustrates the ZPL energies: E_{ZPL1} and E_{ZPL2} for the transition level $C_N^{0/-}$ and the corresponding processes of absorption $C_N^- + E_{Abs1} \rightarrow C_N^0 + e(CB)$, $C_N^0 + e(VB) + E_{Abs2} \rightarrow C_N^-$ and recombination $C_N^- \rightarrow C_N^0 + e(VB) + E_{PL2}$, $C_N^0 + e(CB) \rightarrow C_N^- + E_{PL1}$. (a) – (c) are reproduced from the work of Lyons, et al.[34]

The three groups of authors recently investigated forms of carbon defects in GaN and came to similar conclusions.[34,59,60,62] In this research I prefer the classification of defects into mono-carbon (mono-C), di-carbon (di-C), and tri-carbon (tri-C) by the number of carbon atoms in the structure (1, 2, and 3, respectively). Results of DFT calculation with the same separation into mono-C, di-C, and tri-C defects are presented by Lyons et al. (Formation energy vs. Fermi energy diagrams are shown in Figure 3.15 (a, b, c)).[34] By means of these diagrams, one can learn the most probable forms of carbon defects in the system in the thermodynamic equilibrium. It should be noted, the formation of defects is determined by the doping process or the incorporation of carbon into the growing GaN surface rather than the thermodynamic equilibrium condition in the bulk material. It will be demonstrated in this work, DFT discovers vibrational properties of defects with extremely precise accuracy (Mono-C and Tri-C defects in Chapter 5). Furthermore, the optical signatures of defects well coincide in theory and experiment. Since the models proposed in the literature for tri-C defects have extremely high formation energy (see, e.g., Figure 3.15 (c)) do not satisfy the structural features established in Chapter 5, I do not describe the possible properties of such defects here. At the same time, in the course of Chapters 5 and 6, the results of yet unpublished calculations of the tri-C defect model, which satisfies all experimental observations, will be discussed. The more surprising it seems that Tri-C defects exist at high concentration despite high formation energy ~7 eV, leaving behind many defects with lower forming energy.

By this example, the formation energy may not be relevant for the evaluation of real defect concentration. On the other hand, the DFT describes very well the properties of the defects while the atomic structure is reliably known. Below the most actual data for GaN and AlN are introduced.

Mono-C defects in GaN: C_N, C_{Ga}, C_i, C-H

The various mono-C defects in GaN are discussed in literature.[34,59–63,100,127–130] C_N can act as a shallow acceptor with ~0.3 eV activation energy. Recent first principles calculations indicate that the C_N is a deep acceptor with the −/0 transition level at 0.9 eV, [59–62,100,129] that is in a good agreement with the photoluminescence bands 2.17 (YL) and 2.85 eV (BL_C) respectively observed in GaN:C,Si.[131] C_{Ga} can have a transition energy level close to the conduction band minimum. Earlier calculations show that the transition levels of this defect lies in the band gap, forming a donor state with activation energy ~0.2 eV, [127,128,132] when, as in later works, the defects has the charge state "+" and the transition level is expected above CB minimum.[62,100]

C_{Ga} and C_N defects most commonly have charge states +1 and -1, respectively. Also, they can incorporate in roughly equal numbers, that may lead to self-compensation and the Fermi level pinning at the middle of the bandgap.[132] Though the self-compensation was recently demonstrated, the mechanisms are still unclear; C_{Ga} is proposed as one of pronounced compensating defect.[40] Another candidate to the compensation is positively charged V_N defect (see below).[62] A pair of vibrational modes associated to C_N in the range 760 – 780 cm^{-1} was discussed during the last decade,[133–135] though theoretical evaluations of the vibrational frequencies of these defects are contradictive and could be associated with both C_N and C_{Ga} defects.[136,137] Objecting to evidence of Wu et al.,[133] in fact, the absolute majority of vibrational modes should appear in pairs of similar frequencies with different polarization due to the dif-

ference in *a* and *c* lattice parameters. Furthermore, the calculated ratio of the two peaks, proposed as the evidence,[133] in fact is not a constant; I observe the ratio depending on the laser wavelength (1.3:1 at 2.81 eV (Figure 5.6.) vs. 2.3:1 calculated by Wu et. al.) With this respect, the evidence based on the similarity of one theoretical and one experimental value needs strengthening. Only recently have been presented the DFT calculations of the C_{Ga} and C_N defect vibrating frequencies for different charge states,[34,133] though, only a few frequencies from the expected sets are calculated.[136,137] In Sect. 5.1, I turn back to this issue and complete the picture by new experimental data and calculations, including the isotope shift analysis.

Another possible form of mono-C defect in GaN is an interstitial configuration (C_i), predicted to show amphoteric behavior. It acts as a deep acceptor in n-type GaN and as a deep donor in p-type GaN.[62,128] C_i includes several possible positions of the carbon atom between the Ga and N atoms. Unlike substitutional defects (C_{Ga}, C_N), C_i is incorporated into the structure, but none of the host atoms are removed. Wright et al.[128] first and then Matsubara and Bellotti (Figure 3.16)[62] described and calculated five configurations of C_i defects different in the position of C between the host atoms. Vibrational modes of C_i defects are highly depending on the charge state.[34] In charge states "0" or "+" it should have one vibrational mode at 674 or 745 cm^{-1}, while in other charge states ("4+", "2+", or "-") the vibrations are expected above 850 or below 440 cm^{-1}. For any charge state, there is a vibration frequency above 1300 cm^{-1} that could differentiate C_i from C_{Ga} or C_N (all frequencies of C_{Ga} and C_N are below 850 cm^{-1}).[34]

The passivation by hydrogen of an acceptor, Mg, in GaN has already led to the Nobel Prize.[4] In the case of carbon, C-H complexes are also sometimes more energetically favorable than the previously discussed mono-C defects.[59] In particular, in p-type material C_{Ga}-H_i has lower and C_N-H_i has comparable formation energy of than C_N or C_{Ga},[59] i.e., the hydrogen-carbon complexes can appear in GaN. For comparison, another defect, H_i has the lowest formation energy and can be a deep donor center, providing +/- transition level ~0.5 eV below the conduction band.[59] Typically, C-H vibrations can be detected at high frequencies of around 3000 cm^{-1}.[94] The groups of peaks earlier associated with C-H vibrations[138] also exist in our samples. These peaks exactly coincide with the molecular C-H groups, and in our samples could appear as spectrometer artefacts (the signals have no isotopic shift, no polarization dependence and mostly not reproducible). By this reason, I exclude these signals from the further analysis.

FCS_1, FCS_2, E_{Abs}, and E_{PL} for electronic transitions from C_N^- to C_N^0 are indicated in Figure 3.17 (a): the absorption C_N^- + 2.95 eV → $C_N^0 + e(CB)$ (i.e., ionization of C_N^- defect due to the absorption of photon at E_{Abs} = 2.95 eV results in the C_N^0 defect and the free electron in the

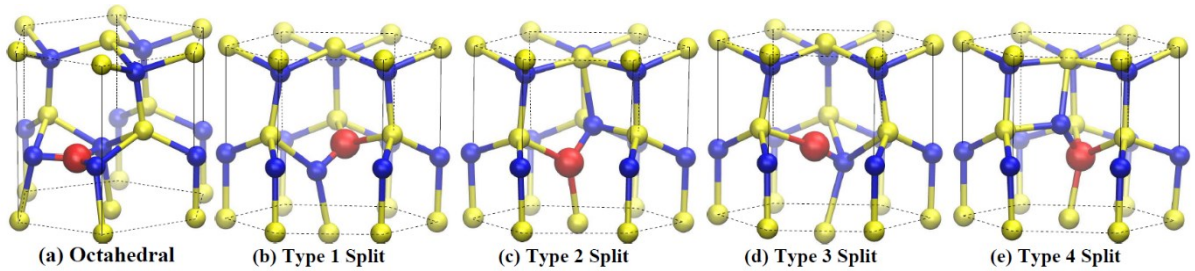

Figure 3.16. Ball and stick representations of the positions of C_i in GaN C atom is denoted by red sphere, while Ga and N are denoted by yellow and blue spheres, respectively. Relaxed configurations of (a) octahedral interstitial position with "4+" charge state, (b) "type 1" split interstitial position with "+" charge state, (c) "type 2" split interstitial position with "−" charge state, (d) "type 3" split interstitial position with "2+" charge state, (e) "type 4" split interstitial positions with "2−" charge state. Reproduced from the work of Matsubara and Bellotti.[62]

conduction band (CB)), and the emission C_N^0+e(CB) → $C_N^- + 2.14\ eV$ (i.e., capturing of the CB electron by C_N^0 results in the emission at E_{PL} = 2.14 eV and the change of the defect charge state to "-").[100] The same processes are depicted in Figure 3.15 (d) for the transitions with E_{ZPL1}. The same processed but different values of energy are depicted for the transition level $C_N^{0/+}$ in Figure 3.17 (b).[100] In experiments (in contrast to the Figure 3.14), the shape of the absorption band differs from the emission band due to the continuum of the zone final states (CB-states in the case of C_N). [139] Model functions for approximating absorption and emission bands found a good agreement with experiments.[140] The cross-section of the UV-Vis defect-to-CB absorption is determined as:[139]

$$\sigma(\hbar\omega) \propto \int_0^\infty \frac{e^{-(E+E_{abs}-\hbar\omega)/\Gamma^2}\sqrt{E}}{\hbar\omega(E+E_{abs})^2}dE \tag{3.15}$$

where $\hbar\omega$ is the energy of light, E_{abs} is the spectral position of the band and Γ – is vibrational broadening parameter.[139] The well-known dispersion of the conduction (or valence) band energy states in κ-space results in the step-like shape of the absorption signal Figure 3.17 (c). In contrast to Figure 3.14, the absorption and emission spectra are not mirrored since almost all emission transitions happen after the relaxation of electrons to the state at κ ≈ 0 (CB minimum or VB maximum).

Di-C defects in GaN: C_i-C_{Ga}, C_i-C_N, C_N-C_{Ga},

Coulomb interaction can result in chemical compensation of defects C_{Ga}^+ and C_N^- by each other and formation of carbon pairs with energy preference. The energy prevalence from the formation of close C_{cation}-C_N pairs is predicted for both GaN and AlN.[63] In AlN, such the simplest defects has a quite high formation energy, while other configurations of di-C defects were not tested by DFT calculations.[122] However, C_{Ga}-C_N in GaN shows the formation energy lower and can be one of possible configurations of di-carbon defects in GaN. Accordingly to the calculations of Deak et al.,[60] Matsubara and Bellotti,[62] Lyons et al.,[34,100] and much earlier works of Wright et al.,[128] C_i-C_N and C_i-C_{Ga} defects at different configurations should be considered as probable. According to Deak et al., a passivated nearest-neighbor C_N-C_{Ga} complex is the

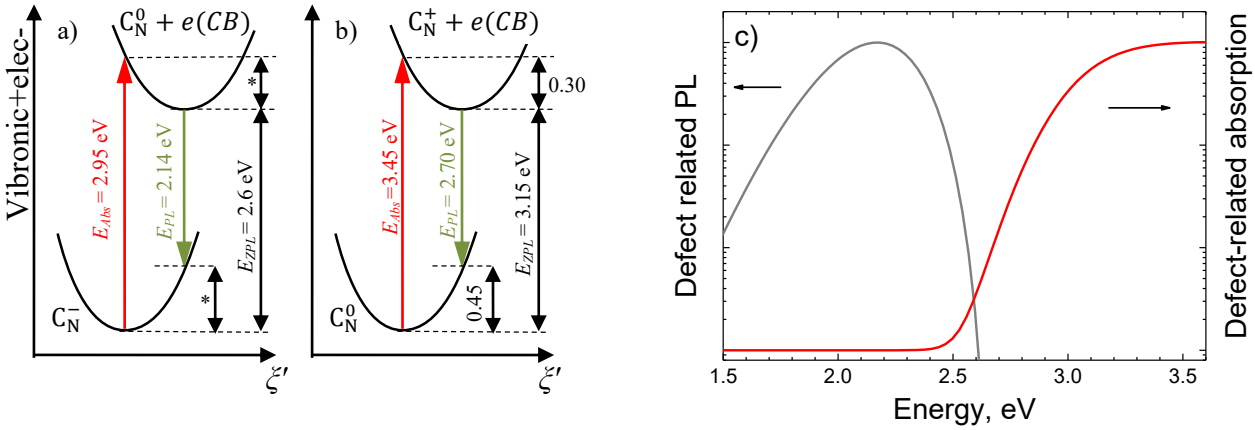

Figure 3.17. (a, b). The configuration-coordinate diagrams for the C_N defect shown for the two initial charge states, "1-" and "0" (adapted from Lyons et al.)[100]. For these charge states, calculations predict the photoionization of C_N with the peak of optical absorption at E_{Abs}= 2.95 eV, 3.45 eV. The recombination of the conduction band electron with C_N is predicted to occur with a peak of emission at E_{PL}=2.14 eV, 3.15 eV (FCS_1 = 0.35 eV and FCS_2 = 0.46 eV are marked by asterisk). (c) Model emission and absorption (Eq. (3.15)) spectra of defect-to-band transitions C_N^0+e(CB) → $C_N^- + E_{PL}$ and $C_N^- + E_{Abs} \rightarrow C_N^0 + e(CB)$.[131]

second lowest energy carbon defect in n-type material after C_N defects.[60] Matsubara and Bellotti, found also quite low formation energy for C_i-C_N and C_i-C_{Ga} in p-type GaN.[62] Lyons et al. found very low formation energy for C_i-C_{Ga} defect in p-type GaN grown in N-rich condition. Summarizing, the presence of carbon pairs in GaN is probable. Because of the variety of C_i defects, three C_i-C_N and three C_i-C_{Ga} stable complexes are possible.[62] Only C_i-C_N pair has the vibrational frequency above 1700 cm^{-1} (as it will be demonstrated for Di-C defects in GaN).

Intrinsic defects with low formation energy in GaN

The intrinsic defects are also variable in GaN and can appear at quite high concentration. The simplest of them are vacancies of Ga and N atoms (V_{Ga}, V_N). V_N can be a pronounced defect in GaN with 3+/+, +/0, 0/- levels in the bandgap due to very low formation energy (e.g., in p-type material). This defect by understandable reasons cannot be recognized by the SIMS methods, but can influence on optical and electrical properties of material. V_N formation energy highly depends on the Fermi level position and can compensate negatively charged C_N defects pinning the Fermi level in the middle of the bandgap.[62] Complexes of vacancies with carbon are also possible at reasonable formation energies.[141] V_{Ga}-C_N at charge states "2+" or "4+" is expected to exist in p-type material while V_N-C_{Ga} may appear in the n-type material with charge state "4-".

Pairs of intrinsic defects are also found probable. Twenty one combination of simple intrinsic defects were considered by Le et al.[142] One of them is the pair of vacancies V_N-V_N with very low formation energy in p-type GaN. This defect has two transition levels, 0/+ and +/2+ at ~0.8 and ~1.2 eV below CB minimum, correspondingly. V_{Ga}-Ga_N is another probable defect in p-type material. The values of formation energies are similar to simple V_N defect.[142]

Figure 3.18 summarizes the transition levels of several defects that can appear at concentrations sufficient for optical characterization methods. As can be seen, many defects can have similar absorption and emission energies that complicate their determination by absorption or emission. Therefore, the characterization of PL or absorption signal requires the coincidence of many parameters in addition to the spectral position, such as Franck-Condon shift, temperature dependences, the lifetime, linewidth, polarization, etc. As an example, the diagram shows

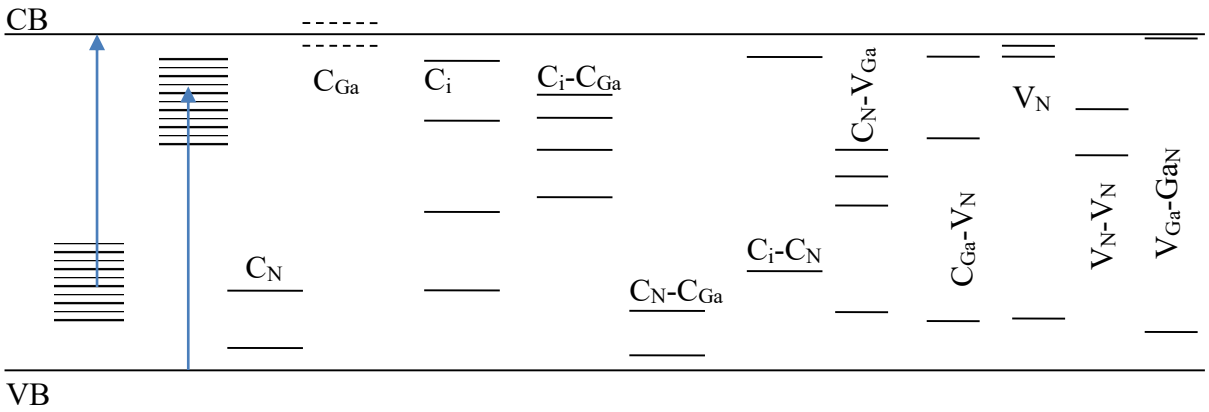

Figure 3.18. The thermodynamic transition energy levels of different defects in accordance with DFT calculations. [34,60,62,100,141,142] *The levels in the dashed ranges are in principle able to originate absorption bands starting at ~2.6 eV.*

the approximate position of the transition level for the absorption with energy 2.8 eV, taking into account typical parameters for defect-related absorption. In contrast, the methods of vibrational spectroscopy used in this work are more specified for the determination of the defect structure.

Large variety of point defects in AlN

At the low density of extended defects, point defects define optical and electrical properties of AlN. The level of impurities in our samples is controlled by the change in the growth parameters (see the description of the samples); therefore, the change of carbon concentration in AlN crystals is sometimes comparable to the change concentrations of oxygen and silicon. In this way, a detailed analysis would require describing a huge variety of defects that could be present in the samples. However, in this work, I identified only di-C and tri-C defects that are poorly discussed in the literature,[17,100,122,143] while the most discussed mono-C defects (C_N, C_{Al}, C_i) up to now were not found in the vibrational spectra. Perhaps, the only report on various carbon complexes (inc. Di-C and Tri-C) has been published recently (see Figure 3.19).[122] On the other hand, the UV absorption band at 4.7 eV (in the focus of Chapter 7) is associated with carbon doping and it seems reasonable to discuss the defects with suitable transition levels in the bandgap.[143] It includes intrinsic defects, such as aluminum and nitrogen vacancies (V_{Al},[144–150] V_N[17,151]), and extrinsic defects from unintentional background doping by silicon, oxygen, and carbon. These three impurities provide not only isolated substitutional defects (i.e., oxygen and carbon substituting nitrogen, and carbon and silicon substituting aluminum: O_N, C_N, C_{Al}, Si_{Al}),[79,88,89,152–154] but are also assumed to form complexes, such as V_{Al}-nSi_{Al},[155] V_{Al}-nO_N (n=1…4 is a number of Si or O atoms),[46,149–151,155–159] and C_N-Si_{Al}.[160]

Absorption band at 4.7 eV

Theory predicts several charge states of the defect carbon substituting both places of nitrogen (C_N) and aluminum (C_{Al}).[100,122,143] C_N can be determined as a deep acceptor while C_{Al} can behave like a deep donor.[127,161] C_{Al} as well as C_N can be in positive, neutral, and negative charge states, with both (+/0) and (0/−) levels occurring within the AlN band gap. [100,122,143] It was reported that a transition level (0/−) of C_N defect located 4.1-4.2 eV below the CB minimum can be associated with an emission peak at 3.5 eV and an absorption signal peaking at 4.7 eV.[17,82,143] An additional peak of emission at 2.8 eV at the excitation 4.2 - 5.0 eV can be associated to donor-acceptor pair recombination involved the same level of C_N as it coincides with

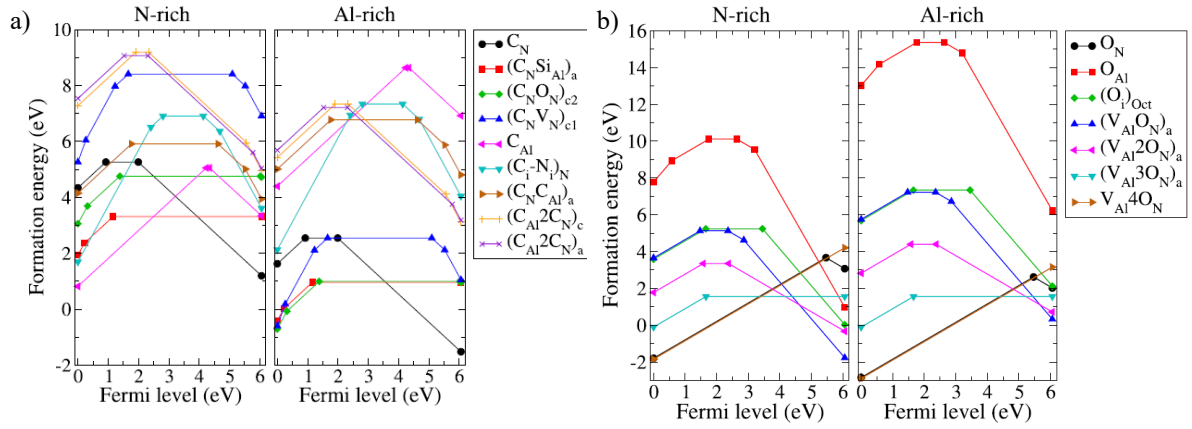

Figure 3.19. Dependence of the formation energies on the Fermi level for different defects and defect complexes in AlN in N-rich and Al-rich conditions. (a)—carbon-containing defects, (b)—oxygen-containing defects. Reprinted from Aleksandrov et. al.[122]

calculations though the experimental evidence is not presented yet.[17,143,151] On the other hand, Jin et al. considered the band at 4.7 eV as a multipeak signal and assume V_N defect to be absorbing at 4.65 eV.[87] Taking account the huge Franck-Condon shift reported for V_N by Aleksandrov et. al. (~2 eV),[122] the emission 2.8 eV[17] seems possible here. C_{Al} defect has two (+/0) and (0/−) transitions close to each other approximately 4.2-4.4 eV above the VB maximum, and can appear at high concentration p-type AlN grown in N-rich conditions.[100,122] The position of the energy levels hint to the energy of absorption and emission similar to one reported for C_N. Furthermore, carbon-vacancy (C_N-V_N) and carbon-oxygen (C_N-O_N) complexes that have relatively low formation energy in Al-rich grow condition,[122] have transition levels near to the $C_N^{0/1-}$.[156] As a result, the transition level +/0 of these two complexes can provide the optical absorption of energy 4.5 – 5.2 eV in the range of the mentioned 4.7 eV absorption band as well as the tri-carbon defects $C_{Al}2C_N$ (see Figure 3.19).[122]

The specific shape of the 4.7 eV absorption band is still open question. The model function for the defect-to-band transition (Eq. (*3.15*)) would not fit the signal. Following earlier researches, I approximate it by the Gaussian function. This implies that, for some reason, the optical transition seems close to the internal and the band-state continuum does not impact the absorption.

Compensation of the main dopant by intrinsic defects and complex formation

For the discussion of optical properties and the change of the defect charge state, it makes sense to discuss the evaluation of the Fermi level position based on the most expected defects in AlN crystals. The thermal equilibrium UV-Vis absorption involves the charge states of defects determined by the Fermi level but other charge states can be activated after optical excitation or in different samples with different equilibrium points. Sample areas AlN-B1 – AlN-B3 (see description of samples) differ in their concentrations of impurities, and as sequence, point defects that determine the Fermi level position. The donor-to-acceptor ratio R is calculated using chemical analysis assuming all oxygen, silicon, and carbon atoms form effective donors (O_N, Si_{Al}) and acceptors (C_N).[100,155,156] However, other defects also important for the determination of the charge balance. For N-rich growth conditions of AlN with the significant influence of acceptors as in areas B1 (R=0.7) and, possibly, B2 (R=2.0), also C_{Al} might manifest as a donor-like compensating defect; the formation energy of C_{Al} is among the lowest for carbon defects discussed in literature.[63,100,122,143] Furthermore, C_{Al} is suggested as a donor defect found in AlN by means of optical and electron-resonance methods.[162,163] Due to the donor like behavior, nitrogen vacancies can act as compensation centers preventing effective p-type doping, and Al vacancies can compensate the material of n-type.[17,87,151,156,164–167] Also, carbon pairs and tri-carbon defects exist in the bulk AlN as was found experimentally.[20,21] Similarly, relatively high oxygen concentration in areas B2 as well as B3 (R=3.7) can lead to significant formation of V_{Al} and (V_{Al}-nO_N) compensating centers, as their formation energies can be comparable to O_N in N-rich growth of AlN with domination of donors.[122,155,156,168] Nevertheless, a direct correlation between the positions of the Fermi level in different regions with the ratio R can be assumed. Then, sample area AlN-B2 is perfectly compensated and has the Fermi level most close to the middle of the bandgap, while in areas AlN-B1 and AlN-B3 their equilibrium Fermi-levels are shifted respectively down and up from the position of AlN-B2, i.e., the empty defect states in the bottom half and the occupied states in the upper half of the bandgap appear.

4. Experimental methods

4.1. Measurements of optical absorption or transmission

Corrected absorption coefficient, transittance, reflectivity, and scattering

An absorption/transmission experiment (IR or UV-Vis) consists of comparing the intensity at given wavelength λ of light passing through a sample $I(\lambda)$ and in an identical system without a sample $I_0(\lambda)$. Moreover, the light intensity decreases not only due to the absorption of the sample but due to Rayleigh scattering and reflection (R) affecting measurements of weak absorption and shifting the baseline. The UV-Vis spectrometer (PerkinElmer LAMBDA 1050) uses photomultipliers located directly after the samples. The light emitted by the sample (PL) due to (weak) excitation by the spectrometer light source can impact the signal and affect the measurement result especially at intense sample absorption. Therefore, some caution should be in interpreting the strongest absorption signals (e.g., the 4.7 eV band in AlN) though, in most cases the PL component is much weaker the passing light beam and does not influence. The transmittance measured in the experiment is equal to $T_{meas} \equiv I(\lambda)/I_0(\lambda) = T - R + PL$ where T is the target transmittance.

Rayleigh scattering on the surface and in the volume of the sample depends on the wavelength λ as function $a\lambda^{-4}$ with fitting parameter a. Therefore, for the large wavelengths in IR range it looks like an additional horizontal shift of the transmittance (absorption) values. It only worsens the signal-to-noise ratio, but does not lead to distortion of the spectra and relaxes sample surface preparation requirements. In UV-Vis spectra, the scattering distorts the shape of the spectra and can be corrected by a simple function $a\lambda^{-4}$.

The fundamental property of the interface between air (n_1) and sample (n_2) is the reflection depended on the wavelength. The reflectivity of the normal reflection is included in the Fresnel formulas ("fractional transmittance") for correction of the UV-Vis spectra.[169] It provides a slight vertical shift of spectra in the visible range increasing in the UV range. With these assumptions, I use T_{meas} to find the "true" T that is presented in units of absorbance $A = 10^{-T}$ or as corrected absorption coefficient α in cm^{-1} determined classically as $T = \exp(-\alpha l)$, where l is the sample thickness:

$$\alpha[cm^{-1}] = -(l[cm])^{-1} * \ln\frac{(1-R)^4 + 4*(T_{meas}*R)^2 - (1-R)^2}{(2*T_{meas}*R^2)}, \qquad R = \left|\frac{n_1 - n_2}{n_1 + n_2}\right|$$

Secondary parameters CIT and DOP

For the photochromism investigation in UV-Vis range two parameters derived from the transmission spectra are introduced. First, the wavelength-dependent relative change in transmission (CIT) caused by UV irradiation or annealing is determined using the formula:

$$CIT = (T_a - T_b)/(T_a + T_b),$$

where T_a and T_b are the transmission after and before the influence, respectively. Likewise, the second parameter, the wavelength-dependent degree of polarization

$$DOP = (T_\parallel - T_\perp)/(T_\parallel + T_\perp)$$

is used to compare the transmission for two corresponding linear polarizations ($T_\parallel$ and $T_\perp$ for E∥c and E⊥c, respectively).

UV-Vis spectrometer Lambda 1050

All optical UV-Vis absorption spectra were recorded at room temperature (RT) using a double beam, double monochromator spectrophotometer (PerkinElmer LAMBDA 1050). Measurements with polarized light were facilitated by two Glan-Thompson polarizers inserted in the sample and reference beam paths; the polarizers are efficient for wavelengths longer than 225 nm (5.5 eV). The equipment allows to measure the difference between the intensity of the reference and the sample beams in the five orders of magnitude. for the polarizations E∥c and E⊥c, respectively, were calculated taking into account the Fresnel correction. The areas B1 – B3 shown in Figure 2.1. GaN (c-plane "GaN" sample series) and AlN (A and B) crystals. GaN c-cut wafers size (5…10)×(4…6)×(0.5…1) mm^3. bordered by a rectangular aperture (0.5×3 mm^2) and held precisely during all manipulations, including all UV-Vis absorption measurements for the photochromism experiments.

Experimental details of photochromism measuements in AlN

The UV irradiation for the photochromism experiments is performed using either the diffused light of a Hg-lamp (with the band-pass interference filter selecting the Hg-line at 254 nm / 4.88 eV) or the line at 266 nm (4.66 eV) of a Nd:YAG continuous wave laser (FQCW266, CryLaS GmbH). The Hg-lamp nominal electric power of 6 W (Heraeus TUV6WE) provides less optical power density than the laser beam which has a nominal optical power of 55 mW, focused in the aperture areas. In contrast, the UV-Vis spectrometer light source does not change the sample state even after multiple or long measurements. The visible light irradiation is performed with LEDs emitting around 2.72 eV (455 nm, nominal optical power 3W) or 3.22 eV (385 nm, 1.5 W) and with defocused lasers emitting at 2.41 eV, 2.54 eV, 2.81 eV, or 3.81 eV (514, 488, 442, 325 nm, respectively; nominal optical power 50–100 mW).

The annealing is performed in several steps with a sequential increase in time and/or temperature, as illustrated by the time-temperature dependence (insert in Fig. 3 (b)). The sample which is glued on one side to the optical aperture (aluminum plate 40x50x4 mm^3) is brought in contact on the other side with a massive heating plate (covered with Al foil) with an internal temperature controller. No additional UV irradiation is performed between the steps. All optical measurements are carried out after cooling down to RT.

4.2. Infrared absorption (FTIR)

Spectrometer Bruker Vertex 80v

Fourier-transform infrared (FTIR) absorption measurements were performed in the mid-infrared spectral range on a Bruker Vertex 80v spectrometer equipped with a globar source, a potassium bromide beam splitter, and a liquid nitrogen cooled mercury cadmium telluride detector. For measurements below RT, a liquid-helium-flow cryostat (Oxford OptistatCF) with zinc selenide windows was used. The spectra were recorded with a resolution of 0.5 cm^{-1} at RT and 0.25 cm^{-1} at 10 K. For polarization dependent measurements, a holographic wire grid polarizer on a KRS-5 substrate was used. I am also very grateful to Dr. G. Gätner for additional measurement of the GaN090 sample in the range of Restrahlen band absorption (Figure 5.1).[1]

FTIR under additional UV-Vis excitation (photo-FTIR)

Additional FTIR measurements were carried out under below-bandgap illumination (photo-FTIR). Cadmium telluride detector is insensitive to visible light, that prevents direct influence of the pumping light on the signal during the photo-FTIR experiment. The exciting light of wavelengths 385 nm (3.2 eV) or 455 nm (2.72 eV) was guided by an optical fiber from a power light-emitting-diode source (Omicron LedHUB) into the sample chamber of the FTIR spectrometer using a vacuum-tight feedthrough. The fiber output was positioned in such a way that it was outside of the FTIR sample beam and that the LED light was incident under ~ 60-70° to the sample surface. Nominal LED powers below 3000mW were used in a continuous mode. Note, that the detector of the spectrometer is not sensitive in the ranges of the additional excitation. Though some difference in spectra were observed when the polarization of the incident light is changed from E⊥c to E∥c, this minor difference was ambiguous (possibly due to a change in the position of the fiber relative to the sample, or different reflectance for the not normal incident beam). With this respect, I do not discuss the polarization of the excitation in the visible range during the FTIR experiment.

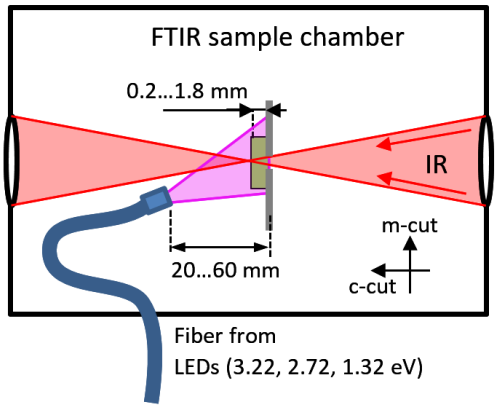

Figure 4.1. The position of the sample and optical fiber in the spectrometer chamber is shown schematically. The direction of IR irradiation propagation is shown by red arrows. c-axis directions in the cases of c-cut and m-cut wafers are indicated.

[1] Institute of Experimental Physics, TU Bergakademie Freiberg, Freiberg, Germany

4.3 Raman scattering and PL spectroscopy

Raman scattering experiments

The Raman backscattering experiments include excitation of the sample with the laser light and observation of the light frequency shift (given in units of cm^{-1} relative to the initial laser frequency) due to the inelastic scattering of the light in the matter. The measurements were carried out at RT at excitation wavelengths of 325, 442, 488, and 514 nm (3.81, 2.81, 2.54 eV and 2.41 eV) using Raman microscope spectrometer Horiba LabRAM HR800. Half-wave plates suited for the ultraviolet and visible spectral range were used to change the direction of the electric field vector E of the incident, linearly polarized light. The outcome backscattered light went through the film analyzer. The orientation of the beam and the direction of polarization is usually given in Porto notation. I also express my deep appreciation to Prof. A. Hoffmann and Dr. H. Sheel[1] for the available Dilor XY (568 nm / 2.18 eV, Figure 6.11) spectrometer.

Photoluminescence experiments

Raman spectrometer (Horiba LabRAM HR800) records the light including the Raman lines and PL signals (that are usually located above 1000 cm^{-1}). It is simple then to consider separately the broad PL signals and the sharp Raman peaks. The RT spectra with PL signals are shown without additional correction for the spectral response. The power of the exciting laser was attenuated by neutral density filters. Additional measurements (with correction of the spectral response)[19] were carried out with excitation of 2.81 eV at equipment of TU Bergakademie Freiberg.[2]

[1] Technische Universität Berlin, Institut für Festkörperphysik, Berlin, Germany

[2] Institute of Applied Physics, TU Bergakademie Freiberg, Freiberg, Germany

5. Determination of the defect types in GaN and AlN

In this part of the work, the variety of vibrational modes in GaN and AlN is discussed. All discussed signatures of defects have spectral positions dependent neither on [C] nor on other parameters of samples. Contrary to popular belief, not only mono-C defects such as C_N take place in GaN and AlN at reasonable concentrations. Observations based on of the isotope-mass effect provide trustable identification of the di-C and tri-C defects in GaN and AlN. The number of atoms in the defect structure is virtually unambiguous consequence of isotope-related vibrational mode splitting in most cases. In AlN, any signatures of mono-C defects are not found, but in GaN, four intensive peaks from a mono-C defect allow us to identify its structure.

FTIR and Raman methods allow investigation of the vibrational properties of the defects and facilitate a deeper understanding of their molecular structure. The analysis usually begins form the checking of the appearance and the magnitude of the isotope-mass effect for the modes induced by carbon doping. Then type of the normal vibrational mode is recognized from comparison with the typical ranges of vibrations in counterpart materials (e.g., carbon-containing groups in molecules, crystals, carbon clusters, etc.). Next step, then measurements of ^{13}C-related signals and the polarized measurements provide information about the type of molecular symmetry, internal structure, and orientation of the crystal c-axis.

In GaN, in total 20 C-related vibrational modes were found, and the structure of five different defects was approved by the vibration frequency shift due to the $^{12}C \rightarrow ^{13}C$ isotope replacement. In AlN much lower number of modes was found with the C isotope effect, thus, only five modes of two defects are identified directly to have carbon origination. This is largely due to high background impurity concentrations of oxygen in AlN samples and narrow range of carbon concentrations comparing to GaN sample series. The C doping of AlN is performed by changing the growth parameters, hence, silicon and oxygen concentrations changed in a few times at the same time as C changed. All this limits the accurate identification of new vibrational modes as carbon-related if the clear isotopic effect is not detected. In GaN, the external source of carbon doping provided the three-order change of chemical carbon concentration at virtually constant low levels of silicon and oxygen and hydrogen below 6×10^{17} cm^{-3}. Isotope enrichment is also better controlled for GaN.

The overview of carbon related modes, so far without evidence and details, is shown in Figure 5.1 for both materials in wide spectral range. Figure 5.1 (a) includes the Raman spectra of three different GaN samples. The reference sample GaN000 shows the typical modes characteristic of a perfect GaN crystal and multi-phonon scattering in the wide range below 1500 cm^{-1}. Other two samples, GaN019 and GaN300 doped with C, also include these signals. In addition, GaN:C spectra contain unique peaks: vibrational modes of carbon defects and the intrinsic modes induced by the defect-related disordering. The vibrations directly related to carbon are labeled following the number of C-atoms in the defect structure, mono-C (MC), di-C (DC), and tri-C defects (TC). Note that there are also modes CH (one carbon + hydrogen), and TC3, TC4 in the range 2650-2850 cm^{-1} not included in Figure 5.1.

Figure 5.1 (b) shows the IR absorption spectrum of sample GaN090, which despite an intensive Restrahlen band and multi-phonon absorption,[170] provides detectable carbon-related peak at 777 cm^{-1}. Restrahlen band interferes with observations for most other GaN samples. The modes marked by asterisk are not visible for the particular measurement but detectable as shown

later. The indicated spectral regions of mono-C, di-C, and tri-C are discussed in more detail in the respective subchapters below.

Note that apart from the lines related directly to the carbon atoms' vibrations, an indirect influence of the carbon doping to vibrational properties can clearly be seen, at least for GaN. Peaks labeled by X and LO are not necessarily originated from carbon defects, even though they increase together with carbon concentration. For example, carbon doping result in the appearance of longitudinal optical phonons (1LO), their overtones (2LO, 3LO) and unknown peaks (e.g., 2327 cm^{-1} in Figure 5.1 (a)) without isotopic effect.

Three different spots of AlN-D crystal with different absorption coefficient at 4.7 eV are measured. The sample in the spot near to the SIMS measurement area, is shown by the red solid line (medium abs. at 4.7 eV). The C-related vibrations in AlN are limited by the four peaks marked in Figure 5.1 as Di-C and Tri-C. Their structure is approved by the isotope mass effect analysis. In GaN the vibrations further identified by isotope effect are marked by blue circles.

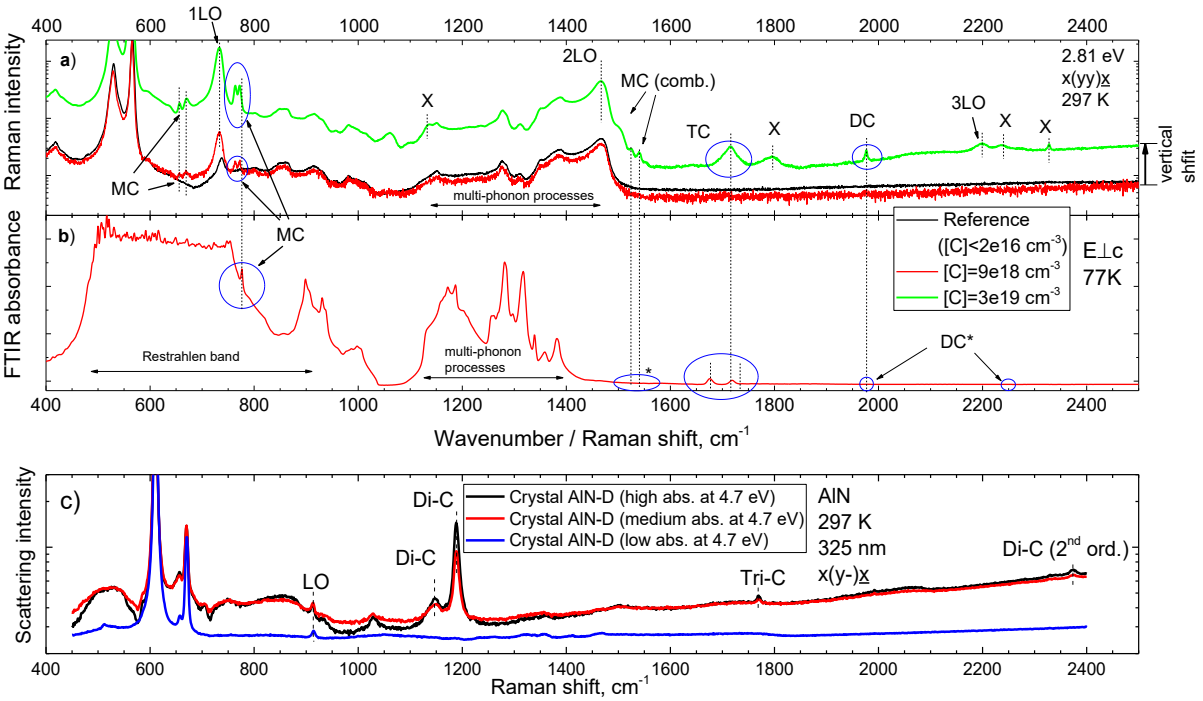

Figure 5.1. The overview of carbon defect vibrational modes in GaN:C and AlN:C in the scattering and absorption spectra. (a) The Raman spectra are shown for the reference GaN sample GaN000 with [C]<2.4×10^{16} cm^{-3} and two C-doped samples GaN090 and GaN300 with [C] 9×10^{18} cm^{-3} and 3×10^{19} cm^{-3} for 2.81 eV excitation at x(yy)x geometry. (b) The absorption spectrum for E⊥c at 77 K is shown for crystal GaN090. The integrated absorption peak area of MC and TC modes is counted to be 86 and 235 cm^{-2}, respectively (discussed in Chapter 6). (c) AlN inhomogeneous crystal AlN-D is measured in three points. The area with medium absorption coefficient $\alpha_{UV}\approx$ 1400 cm^{-1} at 4.7 eV (cf. Figure 7.1) corresponds to SIMS measurement area while the two other points are given here for comparison. The most of the vibrational modes discussed in this chapter are labelled.

5.1. Modes of mono-C defects in GaN

Appearance of MC1 – MC4 modes and their second harmonics

Carbon doping influences on the Raman spectra of GaN crystals. In Figure 5.2, the five intrinsic vibrational modes in undoped sample GaN000 and doped GaN350 sample with the maximum [C] are shown for five different polarizations (see labels above the upper x-axis). The C doping influence on the intrinsic modes of GaN crystal and produces additional unique bands associated with vibrations of C atoms. From Figure 5.1 (a) and Figure 5.2, one distinguishes several differences between the reference sample and GaN:C (Figure 5.1 (a), Figure 5.2) in the spectral range 650 - 800 cm^{-1}: the appearance (i) of the strong peak LO for x(yy)x and x(zz)x polarizations, (ii) the two peaks (MC1, MC2), and (iii) the two peaks (MC3, MC4) on the left of LO. The effect on LO modes and accompanied changes in scattering spectra are not related to the isotope analysis and discussed in the next chapter. For the discussion of mono-C modes, Figure 5.3 shows close the region of interest at two selected Raman polarizations (a) and the region of doubled frequencies (b) for identification of the second harmonics of MC signals. Similarly, the IR absorption spectra (c) for one available polarization E⊥c and the range of its second harmonics is shown in Figure 5.3 (d, e).

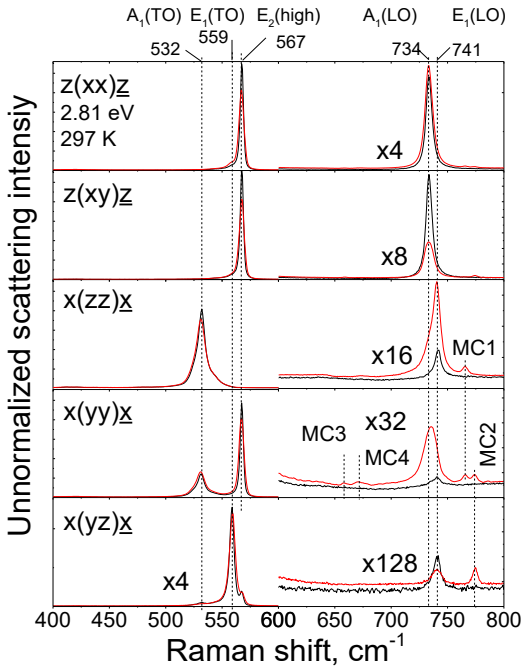

Figure 5.2. Raman spectra at 2.81 eV excitation at RT illustrate GaN intrinsic modes in the reference GaN000, and in heavily doped sample GaN350. Data before normalization. The spectral positions of the modes A_1(TO), E_1, E_2(high) remain virtually unchanged (±0.25 cm^{-1} in different samples due to the measurement error). The modes of longitudinal optical phonons A_1(LO) E_1(LO) change significantly in intensity upon carbon doping. Modes increasing proportionally to carbon concentration are labeled MC1-MC4.

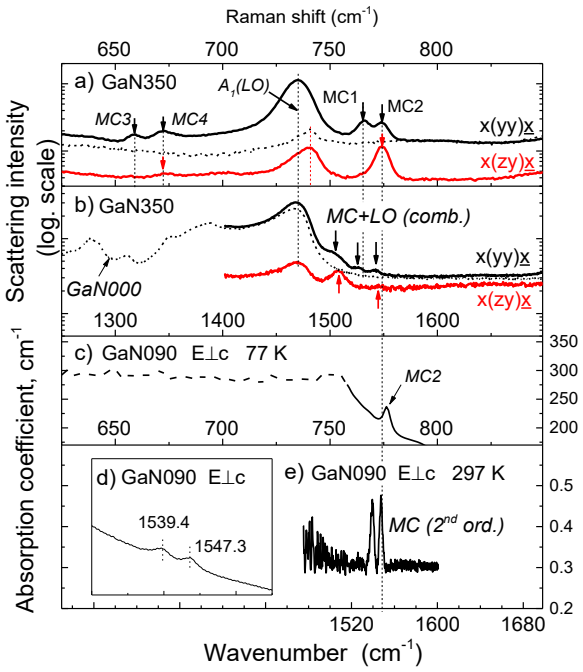

Figure 5.3. (a, b) Raman scattering spectra of sample GaN350 at excitation 2.81 eV for two polarizations x(yy)x and x(zy)x. The spectral curves of reference sample GaN000 are depicted by the dotted line for x(yy)x polarization IR absorption spectra (c, d, e) of sample GaN090 at 77K for E⊥c polarization at RT. The original spectra before the background correction are given on the insert (d). The dashed spectral curve in (c) illustrates the distorted signal due to intense absorption in the Restrahlen band range.

The two peaks MC1 and MC2 at 766 and 774 cm^{-1}, respectively, are shown closer in spectra of GaN350 in Figure 5.3 (a). In earlier works, they were experimentally investigated by several groups by attenuated total reflection (ATR) FTIR and Raman scattering.[133–135] In Figure 5.3 (c) these vibration modes are observed directly in the absorption spectra: the MC2 band is prominent in Figure 5.3 (c), whereas MC1 has no strong identification at E⊥c polarization (MC1, as follows from the Raman polarized measurements, should be detectable at E∥c polarization but the sample geometry complicates such measurement).

Replicas of MC1 and MC2 modes appear in the second-order range of scattering and absorption (Figure 5.3 (b, d)). I suggest that the broad and intense scattering peaks in the range 1500 - 1525 cm^{-1} can be the combination vibration due to the coupling of MC1 and MC2 modes with LO intrinsic modes A_1 and E_1, while the two less intense narrower peaks at 1526 and 1541 cm^{-1} are the second harmonics of MC1 and MC2 (all peaks marked by arrows). The frequencies of the second-order vibrations are expected lower the simple algebraic doubling due to the anharmonic effect.[171] As in the first order FTIR, MC2 without MC1 is visible for E⊥c polarization(Figure 5.3 (d, e)); the splitting of the second-order signal can be explained by the Fermi resonance in the case of originally degenerated vibration MC2.

Origination of MC1-MC4 from mono-C defect

The origination of MC1 and MC2 modes from mono-C defects and the second-order nature of the absorption signals has an experimental evidence based on the isotope mass effect. The key for this interpretation is the application of the harmonic spring oscillator model. Different isotopomers[1] of a carbon defect retain the stiffness of molecular bonds since the chemical properties of isotopes are very similar. Nevertheless, the frequency shift occurs due to the difference of atomic masses, and this makes it possible to analyze the difference between isotopomers. The samples with different C isotope abundance are compared in Figure 5.4 by their scattering (a, b) and IR absorption spectra (c-e). Only ^{12}C-pure and ^{13}C-pure isotopomers can be presented in the crystals with natural 99% ^{12}C abundance (GaN019, GaN090) and 99% ^{13}C (C13) abundance of carbon isotopes, respectively. The mix-isotopomers exclusively manifest in spectra of sample C1213. Isotope abundance 1:1 makes all isotopomers statistically equivalent, thus, the latest sample includes also ^{12}C-pure and ^{13}C-pure isotopomers at equal [C].

The original peaks MC1 and MC2 related to ^{12}C-pure isotopomers are absent in sample C13 ($[^{12}C] < 2\times10^{16}$ cm^{-3}), however, peaks with similar polarization properties appear in the lower frequency range (at 745 and 753 cm^{-1}) - they are associated with ^{13}C-pure isotopomers ($[^{13}C] \sim 2.5\times10^{18}$ cm^{-3}). Moreover, both pairs of peaks, the original MC1-MC2 and their representations in sample C13, are found in sample C1213 ($[^{12}C] \sim [^{13}C] \sim 2.5\times10^{18}$ cm^{-3}). The ^{13}C-related representation of MC1 peak is located close to the intensive LO-phonon intrinsic mode at 735 cm^{-1}, making it difficult but not impossible to observe. MC2 mode and its ^{13}C representation are observed separately from MC1 at x(yz)$\underline{x}$ geometry in Figure 5.4 (b). It is also essential that there are no additional peaks associated with mix isotopomers for sample C1213. Thus, the double splitting of MC1 and MC2 modes determines that each mode corresponds to a defect with one C atom.

[1] i.e., defects different only in the isotope composition. One can distinguish three groups of isotopomers: "^{12}C-pure" and "^{13}C-pure" containing only 12C or 13C atoms, respectively, and "mix" isotopomers containing both isotopes

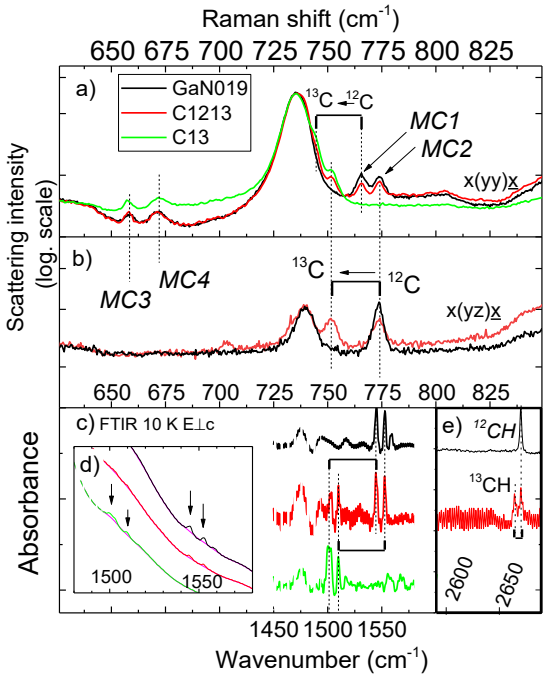

Figure 5.4. Isotope effect of MC1-MC4 modes in the scattering spectra (a, b) at excitation 2.81 eV at two polarizations x(yy)x and x(zy)x for samples GaN019 (black lines), C1213 (red), C13 (green) with the abundance of ^{13}C 1% (natural), 50%, and 99%, respectively. In FTIR spectra (c, d), the second harmonics of MC for the samples GaN090, C1213, and C13 are shown at 10 K. The original spectra and the subtracted background are shown in (d). In the insert (e) spectra of samples GaN005 and C1213 demonstrate the CH mode.

CH mode at 2670 cm^{-1}

A similar double splitting is shown for the vibrational frequency of a peak at 2670.3 cm^{-1} in IR absorption spectra of samples GaN005 and C1213 captured at 10 K for E⊥c polarization with labelled CH in Figure 5.4 (e). Both peaks in sample C1213 have the same amplitude (reasoned by [^{12}C] = [^{13}C]), and in the absence of additional similar peaks at frequencies below, only a single carbon atom is indicated in the defect structure. In this case, the extremely small frequency shift (~6.1 cm^{-1}) indicates extremely light neighbor of C atom.

Carbon-Hydrogen origination of CH mode

The peak is sharp (FWHM ~ 2 cm^{-1}) and located far from any intrinsic vibrational modes, thus, the approximation of the diatomic XY harmonic oscillator is relevant here. The frequency of vibration is:

$$\nu_{XY} = \sqrt{\frac{k(m_X + m_Y)}{m_X m_Y}}, \tag{5.1}$$

where k is the stiffness of the molecular bond, m_X and m_Y are masses of X and Y atoms. The isotopic shift then can be expressed by the frequency ratio:

$$\left(\frac{\nu_{XY}}{\nu_{XY}^*}\right)^2 = \frac{m_X^* m_Y (m_X + m_Y)}{m_X m_Y (m_X^* + m_Y)}, \tag{5.2}$$

that at $m_X = m_C = 12\ a.m.u., m_Y = m_H = 1\ a.m.u., m_X^* = m_C^* = 13\ a.m.u.$ gives ν_{CH}^* equal to 2662.7 cm^{-1} close to experimental value (2664.2 cm^{-1}). The difference seems to be

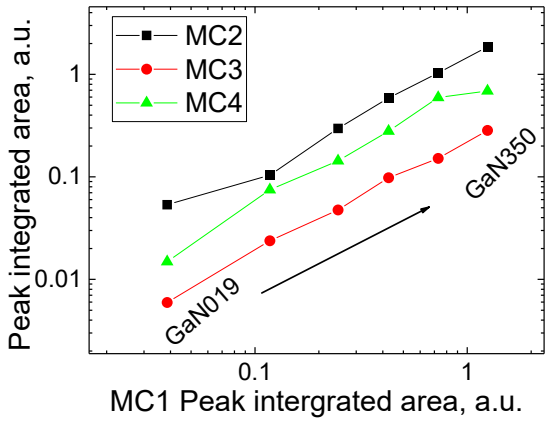

Figure 5.5. Integrated peak area of modes MC2 – MC4 is shown as a function of MC1 integrated area for different chemical concentration of carbon [C] in "GaN" sample series.

acceptable given the measurement error and mostly the deviation of the oscillator from the harmonic model. In GaAs and GaP, ^{12}C-H (^{13}C-H) vibrational modes observed at 2660.2 (2652.6) cm^{-1} and 2635.1 (2628.4) cm^{-1} provide a mismatch with the harmonic model 0.3 cm^{-1} and 1.25 cm^{-1} respectively.[172,173] In this way, the observations of CH isotopic shift and the absolute frequencies are in good agreement with the stretching of C-H bonds. In sample C13 ^{13}C-H peak was not detected, possibly due to lower hydrogen concentration. Hydrogen was not artificially introduced and only its tailing at [H] in the range 1 – 6×10^{17} cm^{-3} were measured for "GaN" sample series. The most solid evidence could be obtained via the deuterium experiment, which is out of the scope of this work.

MC1 – MC4 modes: C_N, C_{Ga}, or C_I?

To clarify the neighbors of carbon in MC1-MC4 vibrational modes is more nontrivial task. Due to the range of allowed frequencies of the host crystal (below the LO mode) the host atom kinetics influences the isotope shift of these carbon-related modes.

No isotopic shift is observed for modes MC3 and MC4 (Figure 5.4) though these peaks are linearly proportional to MC1 and MC2. Figure 5.5 includes data of 6 samples from "GaN" series with maximum [C]. As will be shown in the chapter 5, there are signals MC1 – MC4 bright enough for accurate measurements in these samples. The integrated area of individual modes MC2 – MC4 is shown as a function of MC1. The accurate linear dependence here is the first argument to attribute modes MC1 – MC4 to the same defect. As will be shown below, the quad of peaks is expected from DFT calculations, moreover, the calculated isotopic shift of MC3 and MC4 is below 1 cm^{-1} due to the resonance coupling with the host atoms vibrations (band modes).

In Figure 5.4 (c, d), the absorption low-temperature (LT) spectra of sample GaN019 are presented. At 10 K, two modes appear at 1539 and 1552 cm^{-1} in the second-order range of the absorption spectra. The representations of these modes responsible for the ^{13}C-pure isotopomers are observed in both samples C13 and C1213 at 1501 and 1510 cm^{-1}. Due to the multi-phonon absorption in the region below 1500 cm^{-1},[170] the noise significantly disturbs the measurements (dashed part of the spectra), but ^{13}C representations are clearly distinguishable. To illustrate this, the original spectral curves and the polynomial background used for these spectra are shown in Figure 5.4 (d). The values of the frequency ratio *f (Eq.* (3.12)) for the pure isotopomers is the same for the first-order MC1 and MC2 and the peak in second-order range:

$$f = \frac{1501}{1544} = \frac{1510}{1553} = \frac{753}{774} = \frac{745}{766} = 1.0285 \pm 0.0005 \quad (5.3)$$

The exact match of f for these cases allows identifying these peaks as the first- and the second-order vibrations of the same mode. This also excludes the origination of this peak from C_i defect which should vibrate at 1539 cm^{-1} according to DFT calculations.[34] Based on DFT calculations, the isotopic effect for this C_i mode is expected in two times lower (~21 cm^{-1}).[117]

In MC1-MC4 vibration modes the moving of the defect carbon atom is inevitably accompanied by the normal vibrations of many neighboring host atoms since all four frequencies are not far from the phonon band range. In accordance with Eq. (3.12), the host atoms can significantly reduce the isotopic shift. Mathematically, it can be expressed as the relation of the vibrational amplitudes and masses of carbon atoms versus the host atoms:

$$m_C \xi_C^2 = \eta \sum_{i=Ga,N} m_i \xi_i^2 \quad (5.4)$$

where $\eta \gg 0$ is the delocalization degree of the vibrational mode. If MC1 and MC2 modes are absolutely localized, the triatomic X-C-X molecule approximation is applicable within the isotopic defect in linear diatomic chain approximation.[116] Here X indicates two nearest neighbors of the carbon atom in the chain. For an antisymmetric stretching frequency v_3 of a linear X_2Y molecule there is a well-known relation of the masses m_X, m_Y, and the stiffness k of X-Y bond:[94]

$$v_3 = \sqrt{\frac{k(2m_X + m_Y)}{m_X m_Y}} \quad (5.5)$$

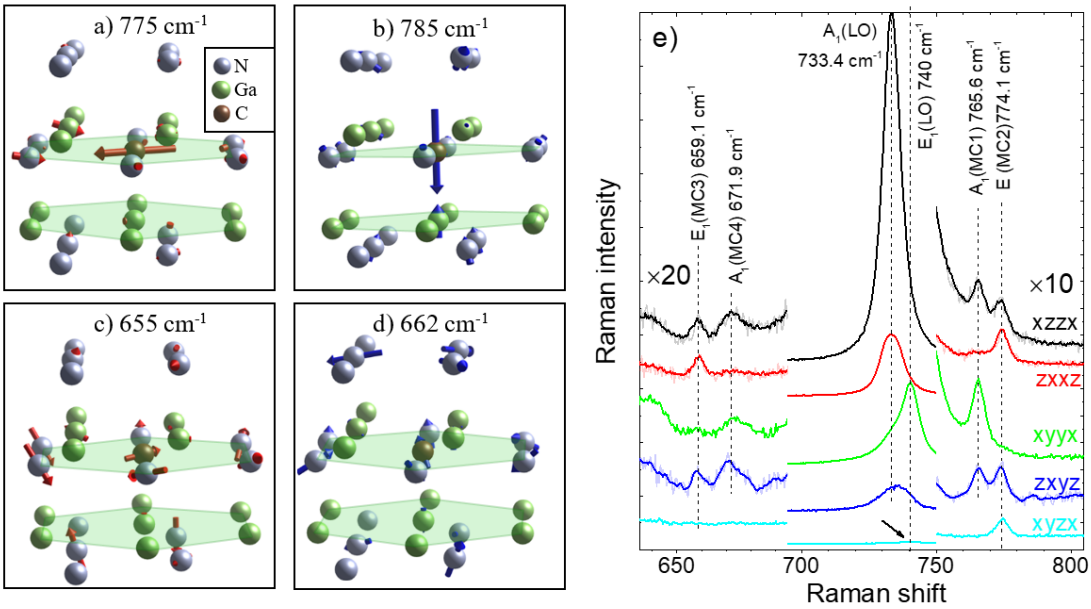

Figure 5.6. (a – d) Displacements of atoms are shown by arrows for the four vibrational modes of C_N defect at at frequencies 775, 785, 655, and 662 cm^{-1}, according to DFT.[117] The modes are associated with Raman peaks MC1, MC2, MC3, MC4, respectively. The relative displacement of C atoms prevails over vibrations of proper atoms only for modes MC1 and MC2; for MC3 and MC4, carbon atoms give insignificant impact to the oscillator energy. The modes MC2 – MC4 are doubly degenerated. The c-planes are colored. (e) The fragment of spectra in Figure 5.2 for sample GaN350 at 2.81 eV excitation

Table VI. Experiment vs theory comparison of frequencies for MC1 – MC4 modes. The Keating and Kane (K&K) calculations performed by Kaczmarczyk et al. for C_N and C_{Ga} defects.[136,137] *The DFT calculations are carried out by Lyons et al.*[34,117]

	Experiment			*f* (*Eq.* (5.5))		K&K		DFT			
	^{12}C	^{13}C	*f*	$^{13}C_{Ga}$	$^{13}C_N$	$^{12}C_{Ga}$	$^{12}C_N$	$^{12}C_{Ga}$	*f*	$^{12}C_N$	*f*
MC1	766	745	1.028	1.028	1.037	765*	765*	843	1.027	**775**	1.032
MC2	774	753	1.028	1.028	1.037	775*	775*	836	1.026	**785**	1.032
MC3	659	659	1.0	-	-	**660****	610**	831	~1	**655**	1.00
MC4	672	672	1.0	-	-	**670****	615**			**662**	1.00

*K&K provides the set of related frequencies as a function of the scale factor s. Using the marked modes for evaluation of s (s=-0.1 and s=0.25 for C_{Ga} and C_N, respectively), the two other frequencies (**) can be compared with the experiment. (see Fig. 4.7 from [136])

C_N and C_{Ga} defects are represented by the "molecules" of Ga_2C and N_2C, respectively. Though the values of *k* are unknown, one can easily calculate the isotopic shift since *k* is identical for different isotopomers anyway. If Y atom is ^{12}C (^{13}C) and X atoms are ^{69}Ga (similar for ^{71}Ga) or ^{14}N, the $^{12}C \rightarrow ^{13}C$ isotopic shifts can be evaluated at $m_X = 69$ a.m.u. or $m_X = 14$ a.m.u., respectively. Then, the pair of original frequencies shift from 766 and 774 cm^{-1} to lower range (the values of ν_3 are given in Table VI via the frequency ratio $f = \nu_{12C} / \nu_{13C}$ for both cases). The evaluation for Ga-C-Ga (i.e., C_N) provides the spectral positions of ^{13}C isotopomer frequency at 738 cm^{-1} far from the observed values, while N-C-N (C_{Ga}) perfectly fits the experiment. However, calculated in this way frequencies show the *maximum* possible shift that could appear just theoretically at absolute localization of the vibration. At reasonable degree of delocalization, the frequency ratio *f* can be lowered for Ga-C-Ga from 1.037 to the experimental one (1.028). With this respect, N-C-N vibration seems less suitable since the maximum localization is improbable for this spectral range. To get the true delocalization degree of the vibration, one of the ways is to perform DFT calculations.

Carbon substituting nitrogen in "-" charge state is a perfect candidate as the calculated vibration frequencies are located at 763, 757, and 751 cm^{-1}, as was reported.[34] The proposed set of the frequencies, however, not perfectly describes the four experimentally found signals MC1 – MC4 despite close frequency range. It should be noted that C_i and C_{Ga} defects can vibrate at frequencies 674, 745 cm^{-1}, and 726 cm^{-1}, respectively,[34] hence, additional indication is needed for the identification of the defect type. In the published report,[34] the vibrations associated to the second-nearest-neighbor (nitrogen) shell of the carbon atoms were not considered. Performed by Lyons modeling of a larger piece of material result in two more vibrational frequencies shown in Figure 5.6 (c, d).[117] In Table VI, the frequencies found from calculations are mismatched with the experimental data less than 2%. The modeling of $^{13}C_N$ defect resulted in the value of frequency ratio f = 1.032 between the maximum (1.037) and experimental (1.028). For C_{Ga} defect with frequencies far from the range of GaN phonon vibrations, the isotopic ratio is very close to the result of the triatomic approximation ($\eta \rightarrow 0$ in Eq. (*5.4*)).

Modes MC1 – MC4 have full agreement with the modes found in DFT (Figure 5.6). The polarized measurements of the scattering show E-type vibrations of modes MC2 and MC3 corresponding to the displacements of C atoms in the basal c-plane Figure 5.6 (b, c), while the other two modes correspond to A_1 irreducible representation and the predominantly axial vibrations of the C atom. Since MC3 and MC4 are the band modes, the surrounding host atoms have the amplitudes larger than for the C atom resulting to the zero isotopic shift. The shift calculated

for the vibrations in Figure 5.6 (c, d) is below 1 cm^{-1} (f = 1.00). The mode MC2 is expected to be doubly degenerated that could originate the splitting in the second order (Figure 5.4). Summarizing, the Raman measurements proves the C_N origination of the MC1 - MC4 modes, which identify a defect by appearing together. Interesting that similar modes at 659 cm^{-1} were earlier detected in GaN:Mg, Mn or GaMnN while vibrations at ~670 cm^{-1} are associated to formation of vacancies after Ar^+, Mg^+, P^+, C^+, or Ca^+ ionic implantation.[174–176] These modes should not be confused.

5.2. Di-carbon defects in GaN

Appearance of modes DC1, DC2 in FTIR and Raman spectra

In GaN:C at medium and high carbon concentrations, vibrational modes at two similar frequencies, DC1 and DC2, are found at 1978 and 2251 cm^{-1} in IR absorption spectra at RT (Figure 5.7). The absorption peaks DC1 and DC2 are shown for two polarizations E⊥c and E∥c. Furthermore, DC1 appears at 1980 cm^{-1} in Raman scattering at excitation 2.81 eV; the x(yy)x geometry is representative to demonstrate it (Figure 5.7 (a)). The mode can also be detected for several other geometries (e.g., z(xx)z, x(zz)x, …) but the FTIR observations are sufficient for identification of the vibration nature.

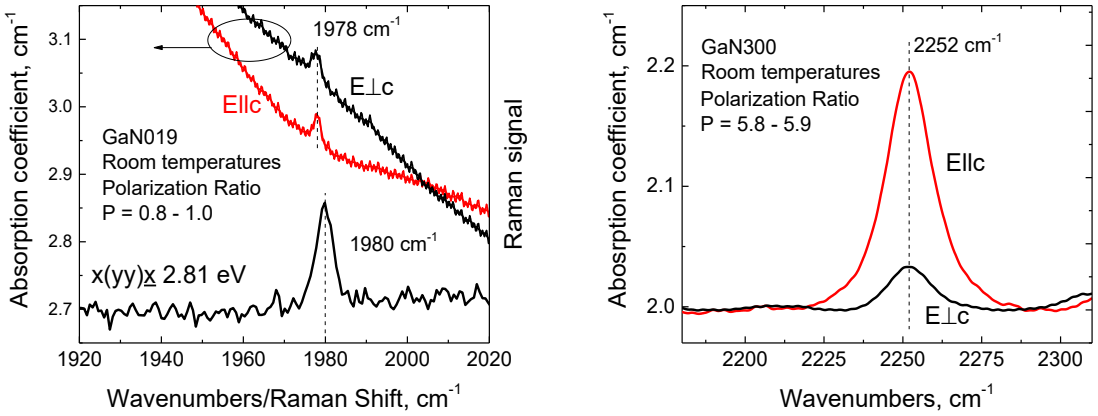

Figure 5.7. IR spectra of samples KG842 (a) and KG870 (b) GaN019 and GaN350 for two polarizations E⊥c and E ∥c. Mode DC1 at 1978 cm-1 has low intensity similar at both polarizations. DC1 mode is also detected by means of scattering. Stronger peak at 2252 cm^{-1} prevails at E∥c polarization and was not found in Raman spectra.

Isotope effects for DC1, DC2.

As in the case of mono-C defect, the splitting of DC modes in sample C1213 identifies the number of carbon atoms in the defect structure. The absorption spectra at 10 K for E⊥c polarization are shown in Figure 5.8 for three samples: ^{12}C doped GaN058 and two ^{13}C-doped samples C13 and C1213. A slight difference in the spectral positions of ^{12}C-related peaks DC1 and DC2 between the spectra in Figure 5.7 and Figure 5.8 are reasoned by the different temperatures of measurement. Both modes exhibit classical isotopic splitting into four peaks each, which is characteristic of the two carbon atoms on inequivalent structural positions (XY-defect).

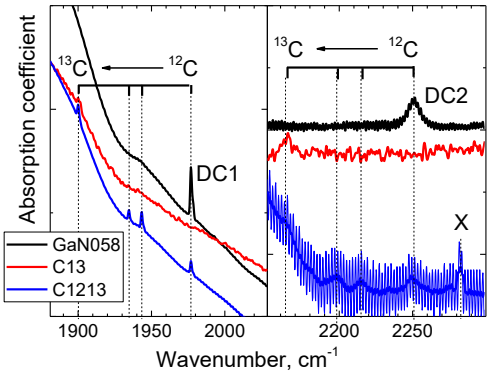

Figure 5.8. The isotope splitting of modes DC1 and DC2 in samples GaN058, 13C and 1213C at LT GaN058 shows the modes DC1 and DC2 at 1976.9 cm^{-1} and 2250 cm^{-1}, respectively, related to the ^{12}C-pure isotopomers, when spectra of sample C13 contain similar peaks at 1900.2 and 2164.2 cm^{-1}, respectively, related to ^{13}C-pure isotopomers. In C1213 all these modes are found in addition to the modes of the mix isotopomers. The peak labeled X shows no isotope effect.

In spectra of both ^{13}C-enriched samples, ^{13}C-pure isotopomers provide vibrations at 1900.2 and 2164.2 cm^{-1}. The frequency ratio for end peaks in splitting corresponds precisely to the theoretical maximum ratio (Eq. (3.13)) given by the isotope masses:

$$f = \frac{1976.9}{1900.2} \approx \frac{2250.0}{2164.2} \approx 1.040 \pm 0.0005, \qquad f \approx \frac{13}{12} \tag{5.6}$$

Hence, the oscillator energy is stored exclusively in carbon atoms, other atoms do not participate in the normal mode vibration.

Unlike MC1 and MC2 modes, the spectrum of sample C1213 shows additional modes related to the mix isotopomers, that could not be found in samples C12 or C13 (the frequencies are listed in Table VII). The resulting symmetrical quadruplet signals very well obey the invariant principle of the isotope replacement.[1] The intensities of peaks are equal within the quadruplets in complete agreement with the expected stick-spectra shown above the spectral curves (cf. Figure 3.13). These observations evidence to di-C origination of DC1 and DC2, moreover, in both cases, two C atoms occupy inequivalent XY positions when the mix-isotopomers provide the two different vibrational frequencies. Next, the type of vibration and the orientation of the vibrating dipole moment can be determined. The range of 2000–2300 cm^{-1} corresponds to stretching vibrations of C=N, C≡N, C=C, and C≡C pairs with double or triple chemical bonds.[94] Tri-atomic defect structures with an additional N atom, such as chain-like CNC or CCN groups, both linear and non-linear can have the antisymmetric stretching frequency in the same range. However, tri-atomic formations can be excluded from discussion, based on the isotopic splitting. Antisymmetric stretching mode involves all three atoms in motion, hence, f = 1.04 becomes impossible. Similar defects (linear N-C-N and C-C-N) were found in GaAs (antisymmetric stretching at about 1970 and 2070 cm^{-1}, respectively).[177,178] C-C-N showed a similar splitting into 4 peaks due to ^{12}C→^{13}C replacement indicating two C atoms, however, it

[1] the peaks are organized in nearly symmetrical quadruplets, as the frequency ratio is equal for pairs of the invariant isotope replacements

Table VII. DC1, DC2 frequencies for different isotopomers, the frequency ratio f, the polarization ratio P, the tilt angle γ, and the appearance of the vibration in Raman are indicated.

Mode	^{12}C-^{12}C	^{12}C-^{13}C	^{13}C-^{12}C	^{13}C-^{13}C	*f*	*P*	γ, °	Raman
DC1	1976.9	1943.9	1934.7	1900.2	1.0404	0.91	53-57	+
DC2	2250.0	2216.8	2197.5	2164.2	1.0397	5.88	31-33	-

provided frequency ratio f=1.017 << 1.040 as the third (nitrogen) atom stores significant part of the vibration energy. Therefore, tri-atomic structures are excluded, and one choice between stretching modes of C=C and C≡C.

Carbon pair defect vibrations are described in literature.[34,62] According to the DFT calculations, C_i-C_N in GaN vibrates at similar frequency (2049 cm^{-1} or 2057 cm^{-1}) being at the charge state "+".[34,62] An interesting structure C_N-C_i + C_N with similar vibration properties is expected to have low formation energy (in the original paper it is labeled C_N-C_i-C_N, see also Figure 3.15 above).[34] This complex defect has three carbon atoms in the structure, but there is no direct bond between C_N-C_i and the nearly located C_N (Figure 5.9). The predicted vibration frequency (2052 cm^{-1} for charge state "0") is the same as for the independent C_N-C_i pair, i.e., the character of vibration is similar to one for the carbon pair and the isotopic replacement of the separated C_N part must not result in the additional splitting.

Orientation of the defects in crystal. C_N-C_i?

In Figure 5.7, DC1 and DC2 were shown for the two linear polarizations, E⊥c and E∥c. From these spectra, the tilt angle γ of the vibrating pairs can be evaluated. The orientation of the vibrating dipole moment coincides with the direction of the carbon-carbon bonds the for the considered case. The angle φ between the direction of the electric field of light $\vec{E}$ and the c-axis is equal to 0˚ and 90˚ at E∥c and E⊥c, respectively. Then, taking into account the crystallographically equivalent representations due to the wurtzite symmetry,[179] in the dipole approximation of the absorption the polarization ratio *P* (from Eq. (3.3)):

$$P = \frac{A(90,\gamma)}{A(0,\gamma)} = \frac{2}{sin^2\gamma} - 2, \qquad \gamma = arcsin\left(\frac{2}{2+P}\right)^{1/2} \tag{5.7}$$

In Figure 5.9 the tilt angle γ is plotted as a function of *P (Eq. (5.7))*. The intensity of peaks obtained from Figure 5.7 allows to evaluate the tilt angle for DC1 and DC2 as ~55° and

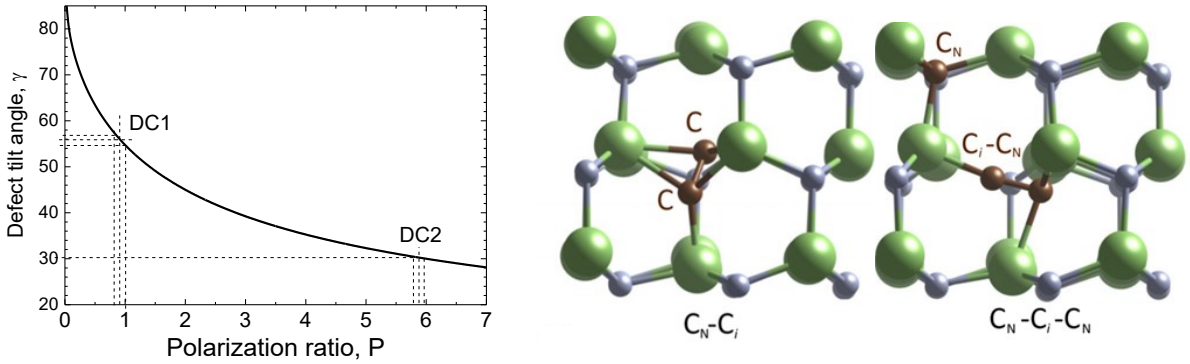

Figure 5.9. Tilt angle of the vibrating dipole moment as a function of the polarization ratio P for a defect in a wurtzite crystal. The calculated models of C_N-C_i and C_N-C_i-C_N (in this work called C_N-C_i+C_N) defects reprinted from work of Lyons et al.[34]

~30°, respectively. According to DFT calculations,[34,62] the two defects C_N-C_i pair in the charge state "+" and C_N-C_i +C_N ("2+") complex of three C atoms (shown in Figure 5.9) vibrate with the frequency 2052 – 2057 cm^{-1}. The tilt angle of these defects are 55.8° and 75.6°, respectively.[117] Thus, the tilt angle and the frequency of DC1 mode are very close to values of C_i-C_N pairs. Another defect vibrating with DC2 mode can be associated with another pair that has very hard C≡C bond, harder than any calculated defect.

5.3. Di-carbon and Tri-carbon defects in AlN

Di-C1, Di-DC2 and Tri-C1 Raman modes in AlN

This Section considers three signals (Di-C1, Di-C2, and Tri-C1) from three different defects in AlN. In Figure 5.10, Raman spectra of sample AlN-D ([C]=5.8×10^{18} cm^{-3}) are shown for the incident 3.81 eV (325 nm) laser light polarized either parallel E∥c (e.g., x(zz)x + x(zy)x) or perpendicular to the crystal's c-axis E⊥c (e.g., x(yz)x + x(yy)x). One recognizes intrinsic modes, which represent the vibrations of the AlN host atoms. According to earlier studies,[111,112,114,180] the modes at 610, 671, and 912 cm^{-1} are attributed to transverse (A_1(TO), E_1(TO)) and longitudinal (E_1(LO)) optical phonons. The mode E_2(high) at 659 cm^{-1} is related to nitrogen sub-lattice vibrations.[106,181] The lines Di-C1 and Di-C2 are located at 1189 cm^{-1} and 1148 cm^{-1}. I suggest Di-C1 and Di-C2 modes are reasoned by two different defects as their relative intensity changes in different samples (peak area ratios are given Figure 5.10 (b)). This can be seen from comparison of two spots on sample AlN-D (first area in the SIMS crater and the additional (add.) in the point of maximum signal Di-C1 on sample periphery). Di-C1 can reach ~20% of A_1(TO) intrinsic vibration being then extremely bright defect mode. The second harmonic scattering can be observed at 2376 cm^{-1}.

Another defect-related peak (labeled Tri-C1) is observed at 1772 cm^{-1} in good agreement with the peak position of the tri-carbon defect (at 1769 cm^{-1}) found by FTIR method and described in detail.[20] Here, I do not provide the structural analysis of tri-C defect in AlN, as it is the axial molecule-like C=C=C defect very similar to one originating TC2 in GaN (see Section 5.5).

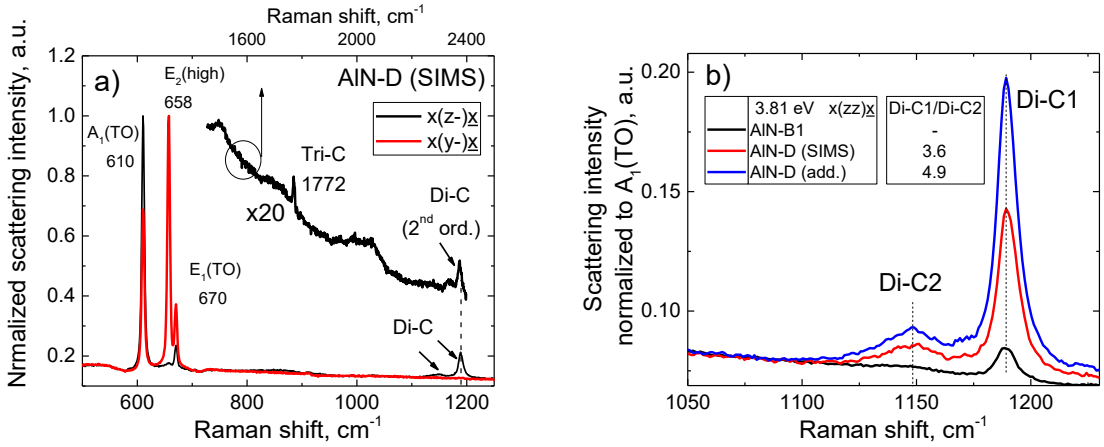

Figure 5.10. Raman spectra (a) of m-plane grown sample AlN-D with [C]= 5.8e18 cm^{-3} for two geometries x(z-)x and x(y-)x, when the scattered light detected without the analyzer. The intrinsic modes are labelled. The polarization dependence demonstrates absence of the defect-related signals for x(y-)x. Di-C1 and Di-C2 peaks at 1147 and 1189 cm^{-1} are shown closer (b) for x(zz)x polarization in two distant areas of sample AlN-D and in area AlN-B1. The used laser wavelength 3.81 eV (325 nm).

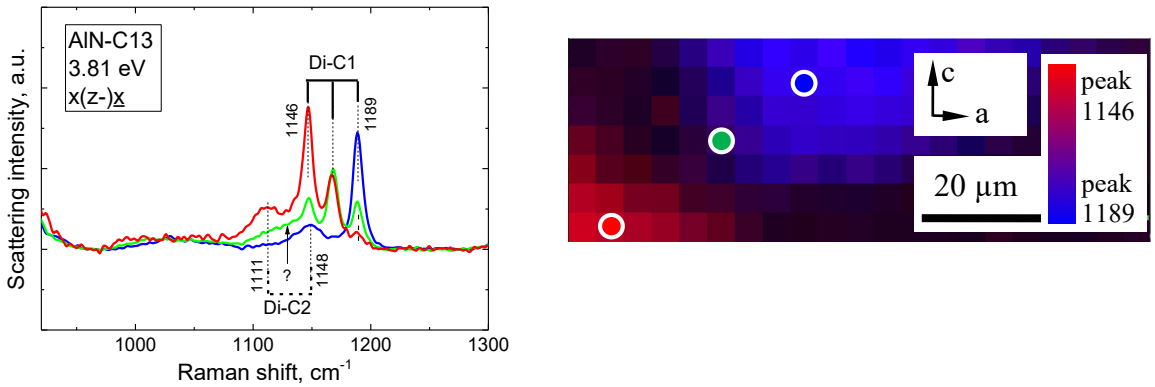

Figure 5.11. Raman spectra recorded at three spots within an area on sample C13 shown on the right. The crystallographic orientation and the scale bar are shown on the inserts of the map. The color and brightness illustrate the intensity of peaks at 1146 and 1189 cm^{-1}.

Isotope effects of DC1 and DC2

In sample AlN-C13 inhomogeneously doped with ^{12}C and ^{13}C, new peaks appear near to the original vibrations Di-C1 and Di-C2 in the Raman spectra. As demonstrated in Figure 5.11, three nearby measurement spots provide lines at 1146 cm^{-1} and 1168 cm^{-1} additional to Di-C1 with the same narrow line shape (FWHM ≈ 9.8 cm^{-1}) and different relative intensity. Furthermore, a broad peak with similar shape as Di-C2 peak (FWHM ≈ 16 cm^{-1}) is found at 1111 cm^{-1}. It is particularly striking that the peak heights of the three lines at 1146 cm^{-1}, 1168 cm^{-1}, and 1189 cm^{-1} vary significantly between the three measuring points, whereas the peak positions remain unchanged. These three lines are equidistant with a displacement of ~22 cm^{-1} as should be for the isotope replacement. For the Di-C2 vibrational mode, the number of peaks in the splitting is not so obvious. While the original Di-C2 peak at 1146 cm^{-1} and its counterpart at 1111 cm^{-1} can be clearly seen, only a shoulder-like unresolvable structures appear between them (labeled by a question mark in Figure 5.11).

The observed features, such as line shapes and the symmetrical triplet splitting, are sufficient to claim the carbon isotopes related origination of the peaks in the range 1100 – 1200 cm^{-1}. The three lines at 1146 cm^{-1}, 1168 cm^{-1}, and 1189 cm^{-1} (Di-C1) all seem to originate from different isotopomers of the same carbon defect, while the two lines at 1111 cm^{-1} and 1148 cm^{-1} (Di-C2) belong to ^{13}C-pure and ^{12}C-pure isotopomers of another carbon defect. It is easy to verify that a larger number of peaks in a given isotope splitting do not fit up to 1141 cm^{-1} (the maximum shift for ^{12}C→^{13}C replacement), e.g., the defect can include only two carbon atoms. An additional argument here is that the peak relative intensities in the triplet obey to the law of the statistical distribution for the two carbon isotopes on two equivalent sites (Figure 3.12 (b)). Therefore, the end peaks are associated with the ^{12}C-pure and ^{13}C-pure isotopomers and find the frequency ratio:

$$f(\mathrm{DiC1}) = \frac{1146}{1189} = 1.038, \qquad f(\mathrm{DiC2}) = \frac{1111}{1148} = 1.033 \tag{5.8}$$

The number of peaks in the isotope splitting, again is the key to the defect structure, though in this case, the conclusion is not obvious due to the specifics of the vibrational mode. The triplet Di-C1 is most likely originated by the defect with two carbon atoms in equivalent positions. Peak areas of 1189 cm^{-1} (^{12}C, blue) and 1146 cm^{-1} (^{13}C, red) are depicted on the double-color map in Figure 5.11. Dark pixels correspond to the low intensity of both signals,

while violet – marks equality of both peaks (for such spectral curves, 1168 cm^{-1} peak of mix isotopomers dominates). It was discussed in the theoretical part, that the two isotopes are distributed on the two sites in the defect structure *randomly* according to the binomial distribution. The integral areas of the peaks in the triplet follow then the specific dependences on the isotope abundance (Figure 3.12 (b)), if divided to the full triplet area. This was observed for the most of spectra consisted the map in Figure 5.11 (b) including the three spectral curves in Figure 5.11 (a). From this, one can deduce the relative ^{12}C and ^{12}C abundances in the sample volumes probed by the Raman measurement by finding [^{13}C%] values that reproduce the intensity ratios in the triplets. I obtain [^{13}C%] values of 5%, 45%, and 85% for the spectral curves in Figure 5.11 (a) at which the calculated probabilities and the experimental normalized intensities correspond very well to each other. The color gradient in Figure 5.11 (b) then also illustrates the isotope distribution. The quite high variations of the ^{13}C content on the micrometer scale are not properly described by the SIMS measurements that indicates the ^{13}C isotope content to be in the range of 14 – 35% on a lateral length scale of 200 μm.

Another principal variant of di-C defect can be considered as candidates to Di-C1 and Di-C2 vibrations. In addition to the C_X-C_X stretching, C_Y-X-C_Y symmetrical stretching mode provides the same isotopic splitting. C-C bond stretching can be normally found at 600 - 1300 cm^{-1} for different molecules.[94] On the other hand, the range of around 1200 cm^{-1} can be associated with the symmetrical stretching of C-N-C or C-O-C, and even C-C-C groups. It is important that the frequency in the second case does not depend on the mass of the immobile central atom but depends only on the force constant *k* which is close for the three tri-atomic groups. Using Eq. (5.5) for antisymmetric stretching mode at the known frequency ν_3=2059.5 cm^{-1} for the linear ^{14}N-^{12}C-^{14}N in GaAs, one can find the force constant *k*.[178] Then, as *k* should be similar in different crystals, for "inversed" linear ^{12}C-^{14}N-^{12}C molecule with the C-N bonds, one can get now the symmetric stretching frequency $\nu_1 = \sqrt{k/m_C} = 1258$ cm^{-1}, that has reasonable agreement with the measure of Di-C1 1189 cm^{-1}.

Orientation of the defects in crystal

The isotope analysis cannot clarify further the defect structure. In any case, as the signals Di-C1 and Di-C2 appear only for E∥c and absent for E⊥c (Figure 5.10), the polarization data indicate the defect is aligned parallel to c-axis. The tension-compression of chemical bond stretching vibration provides the change of the polarizability along the c-axis, while changes in the basal plane are compensated or absent. A non-zero basal component proportional to $\sin^2\beta$ can be present in the case the tri-atomic molecule is slightly bent. Although it begs to attribute Di-C1 or Di-C2 signals to symmetric stretching (ν_1) of the Tri-C defect originating also Tri-C1 signal (antisymmetric stretching ν_3), this suggestion is incorrect. The absence of scattering at E⊥c polarization is impossible for ν_1 as Tri-C is tilt relative to c-axis. In addition, it is difficult to find two strictly symmetrical positions along the c-axis of the AlN crystal for both C-X-C and C-C defects. With this respect, the di-C defects in AlN need additional structure calculations.

5.4. Tri-carbon defects in GaN

Spectral positions of TC modes

Tri-C defects, found in both GaN and AlN, have the most sophisticated molecular structure and correspondingly the most intricate isotopic splitting, comparing to previous cases. In GaN the four main modes TC1-TC4 are unambiguously attributed by us to tri-C defects, based on the isotopic effects.

Vibrational modes are shown at 297 K and 10 K for E⊥c and E∥c polarizations in Figure 5.12 for sample GaN140 with the natural abundance of the isotope ^{12}C ~99%. The most intense peaks, TC1 and TC2, are found at frequencies 1678 and 1717 cm^{-1}, while the weaker modes TC3 and TC4 are located at 2803 and 2833 cm^{-1}. Mode TC5 appears as a shoulder or a peak at 1734 cm^{-1} overlapped with the intensive peak TC2 only at high concentrations of carbon.

An additional piece of sample GaN140 was cut in m-plane making available the measurements for both polarizations, E⊥c and E∥c. Vibrational modes TC1 and TC2 have similar height at E⊥c, as well as the pair of peaks TC3 and TC4. However, measurements at E∥c exhibit pronounced differences of the peaks in each of the two pairs of peaks: modes TC1 and TC3 disappear while in contrast, modes TC2 and TC4 reach maxima of intensity.

Peak TC1 shifts significantly (to 1673.9 cm^{-1}) when cooled to 10K, and becomes symmetrical and much narrower in contrast to TC2 and TC4 modes which maintains its shape and position at different temperatures (Figure 5.12). Significant narrowing and a slight shift (0.8 cm^{-1}) can be also mentioned for mode TC3. The strong difference of polarization properties and the LT narrowing allow to recognize and differentiate the peaks TC1 and TC2 in the further isotope splitting analysis. The temperature broadening and the shift of the TC1 mode indicates the coupling of the basal tri-C defect with phonons. Theory differentiates cases of coupling with all phonons in crystal and with a single preferential phonon frequency.[182] In Figure 5.12 (c) the thermal shift of the vibration frequency is shown by black symbols and the line broadening by red symbols. Similar linewidth broadening and shift to lower energy with increasing temperature have been observed in numerous systems.[182,183] The best fitting appears for the model of anharmonic coupling with a single-phonon frequency (dashed lines).

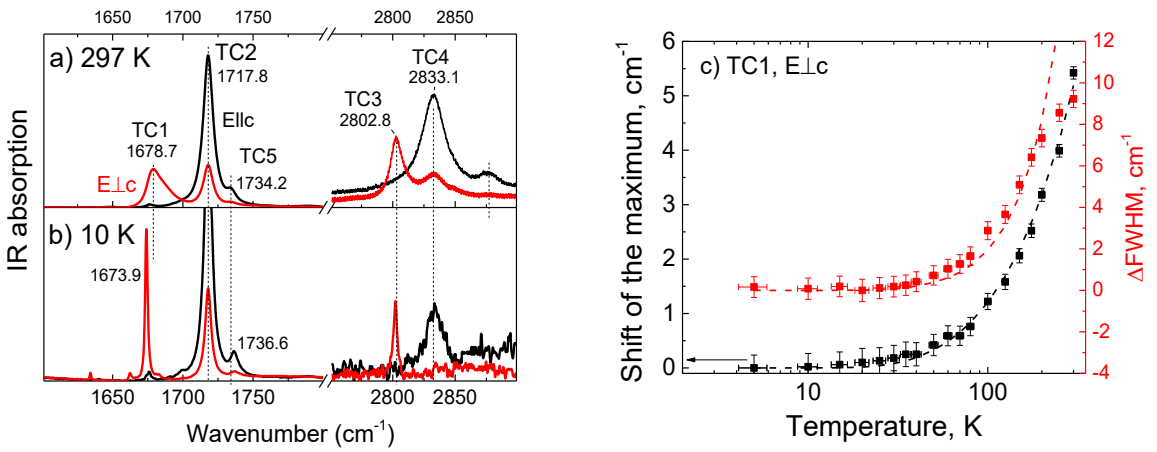

Figure 5.12. IR absorption spectra containing the vibrational modes TC1, TC2, TC3, TC4 and TC5 measured through the m-facet of sample GaN140 (a) at RT and (b) at T = 10 K for two polarization E∥c and E⊥c. (c) Temperature dependence of TC1 mode spectral position and broadening (ΔFWHM) and the approximation by Eq. 57, 58 from [182] for the model of the coupling with a single frequency phonon.

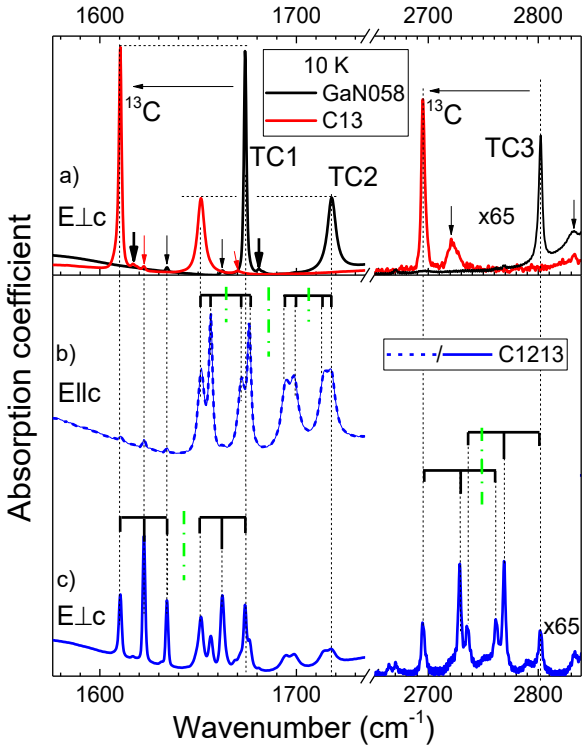

Figure 5.13. Isotope effect for tri-C vibrational modes in GaN. LT FTIR spectra (normalized to the respective peak maximum), illustrating the isotope effect (a) in the samples GaN058 and C13 while the mix isotopomers are represented in spectra of sample C1213 for E⊥c (b) and E∥c (c) polarization, respectively. The splitting to a pair of symmetrical triplets (c) or quadruplets (b) can be observed for the original modes TC1, TC2, and TC3.

Isotope effect of TC modes

Figure 5.13 shows IR absorption spectra of samples GaN058, C13, and C1213 recorded at LT (10 K). The vibrational modes of the ^{12}C-pure and ^{13}C-pure isotopomers in spectra of samples GaN058 and C13, respectively, are displayed in Figure 5.13 (a). The peaks in the spectra of sample C13 at 1610.5, 1651.3, 2695, and 2722 cm^{-1} have the same shape and polarization as the original TC1 - TC4 modes, respectively. With this respect and because of the same frequency ratio equal to the maximum one:

$$f = \frac{1673.9}{1610.5} \approx \frac{1717.8}{1651.3} \approx \frac{2803}{2695} \approx \frac{2833}{2722} = 1.040 \pm 0.001, \qquad (5.9)$$

The peaks in Figure 5.13 (a) can be associated with the ^{12}C-pure and ^{13}C-pure isotopomers. The ^{13}C-related representation of the TC5 mode is found at 1670.4 cm^{-1} (marked by a wide black arrow between the modes of two TC1 isotopomers) and also provides the same ratio. As in the case of DC1, DC2, the isotopic shift corresponds exactly to the square root from the mass ratio (Eq. (3.13)): 1.041, and hence, the vibration mode involves the carbon atoms only.

Several additional peaks are detected for sample C1213 with the mixed isotope composition. In the spectra for E∥c shown in Figure 5.13 (b), the eight peaks TC2-1 to TC2-8 represent vibrational mode TC2 for all possible isotopomers (Table VIII). Peaks TC2-1 – TC2-4 and TC2-5 – TC2-8 are grouped into two marked quadruplets of 1:1:1:1 intensity (integrated peak area).

Table VIII. Individual vibrational frequencies of different isotopomers in sample C1213 for the basal tri-C defect with molecule symmetry C_S. Calculated values from Eq. (5.10)

Peak label	ν_i, cm^{-1}				Isotopomer
	GaN058 T = 10 (297) K	C13 T = 10 (297) K	C1213 T = 10 K	Eq. (5.10) 2β = 154°	
TC2-1 (TC2)	1717.8 (1718)	-	1717.8	1718.5	^{12}C-^{12}C-^{12}C
TC2-2	-	-	1714.4	1716.9†	^{12}C-^{12}C-^{13}C
TC2-3	1699.2	-	1699.0	1699.9†	^{13}C-^{12}C-^{12}C
TC2-4	-	-	1694.6	1695.3	^{13}C-^{12}C-^{13}C
TC2-5	1675.8 (1676)	-	1675.8	1674.3	^{12}C-^{13}C-^{12}C
TC2-6	-	-	1672.4	1670.4†	^{12}C-^{13}C-^{13}C
TC2-7	-	-	1656.5	1654.9†	^{13}C-^{13}C-^{12}C
TC2-8	-	1651.5 (1652)	1651.7	1651.0	^{13}C-^{13}C-^{13}C

†estimated from the principal equidistance of these modes from the position of the degenerated mode of a symmetrical defect 1708.4 and 1662.6 cm^{-1} (green dash-dot lines in Figure 5.13 (b))

Although peaks TC2-5 and TC2-7 seem higher than the others, the total area of quadruplet TC2-1 – TC2-4 is equal to that of quadruplet TC2-5 – TC2-8. Note that the sharp peaks dominated for E⊥c are effectively suppressed for E∥c polarization.

The splitting of mode TC2 into eight lines of equal intensity clearly identifies the 8 isotopomers with individual vibration frequencies. It is a direct evidence, that n = 3 carbon atoms occupy crystallographically inequivalent sites in the defect structure (i.e., form XYZ-molecule). As expected for the stick spectra of XYZ (shown in Figure 5.13 (b) and Figure 3.13 (f)) structure, the defect signature is presented by the two quadruplets with the symmetric positions of peaks.

In the spectra captured at E⊥c (Figure 5.13 (c)), peaks TC1-1 – TC1-6 and TC3-1 – TC3-6 represent the vibrations of different isotopomers. The sixfold line splitting of modes TC1 and TC3 can also be explained by a defect containing three carbon atoms, but in these defects the carbon atoms occupy two equivalent sites (Y) and a third unique site (X) in between (XY_2 with C_{2v} symmetry, Figure 3.9 (c)). The isotope distributions also give rise to eight isotopomers but two of them are identical in two cases, so that two of the individual frequencies (with sub-numbers 2 and 5) are doubly degenerate. The observed splitting pattern of two triplets each with 1:2:1 intensity ratio is fully consistent with Tri-C defect (the model stick-spectra are shown in Figure 5.13 (c)). The same sixfold splitting is observed for TC3 mode. The overlapping of the two triplets for TC3 (stick spectra are shown) does not contradict to the invariance principle of the isotope replacement and just emphasizes the spectral symmetry of the stick spectra.

Orientation of the defects in crystal. Axial and basal configurations

The polarization dependence of the absorption peaks Figure 5.14 (a) gives information on the orientation with respect to the crystal coordinate system for the two configurations of tri-C defect responsible for the vibrations TC1 and TC. The absorption spectral curves of sample GaN140 at $\varphi = 0°$ (E∥c) and $\varphi = 90°$ (E⊥c) were demonstrated in Figure 5.12. The full-range dependence of the absorption peaks on φ reveals that TC1 attain a maximum at E⊥c and becomes zero for E∥c, while TC2 has a non-zero minimum at E⊥c and reaches a maximum for E∥c. One can determine the orientation of the oscillating electric dipole moment $\Delta\vec{\mu}$ belonging to the actual normal mode via Eq. (3.3): $A(\varphi,\gamma) = A_0(sin^2\gamma + (2 - 3sin^2\gamma)\cdot cos^2\varphi)$ where

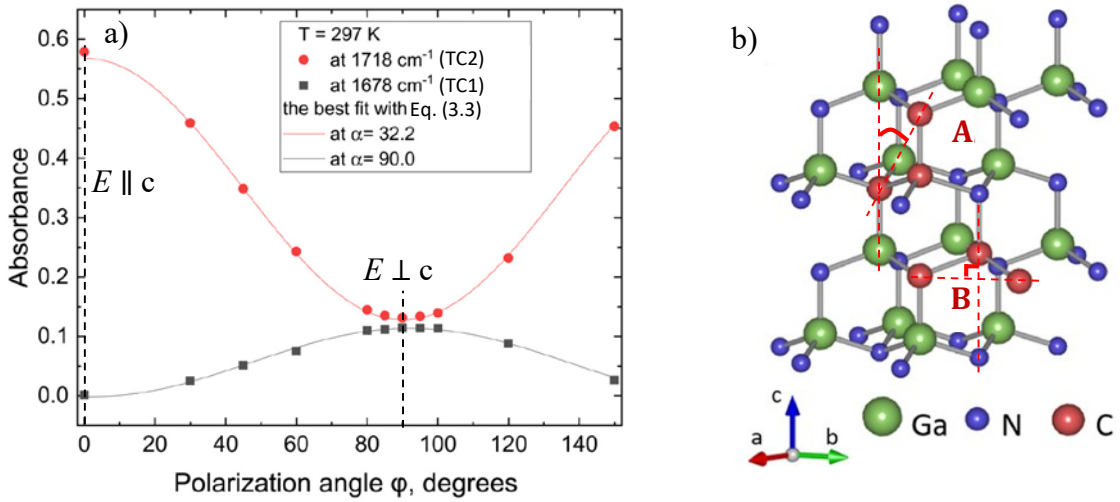

Figure 5.14.(a) Complete polarization dependence of peak integrated area of modes TC1 and TC2 in sample GaN140 obtained at 297 K and the best approximation with Eq. (3.3). The spectral curves at φ = 0° (E∥c) and 90° (E⊥c) were shown in Figure 5.12. (b) Tri-C defect of axial (A) or basal (B) configurations, substituting three host atoms in the GaN lattice. The tilt angles are marked.

the vibrational absorption A is considered as a function of the tilt angle γ between $\Delta\vec{\mu}$ and the GaN crystal's c-axis.

Using Eq. (3.3) for the calculation of the polarization dependence shown in Figure 5.14, the tilt angle γ can be determined by the best fitting of the calculated curve to the experimental data. The polarization dependence of the peak TC1 is best described by $\gamma = 90°$ meaning that the direction of the oscillating electric dipole moment is parallel to the c-plane. This in particular includes the directions [01.0], [10.0], and [11.0], which are parallel to the connection lines of each two nearest N (or Ga) atoms in the basal plane of the N (or Ga) sublattice (Figure 5.14 (b)). For the peak TC2, γ is found to be 33° ± 1°, a value that is close to the angle 35.38° (calculated using the VESTA program[102] and lattice parameters relevant for GaN[184]) between the c-axis and the directions of the lines connecting two nearest N (or Ga) atoms located in two sublattice c-planes shifted by $c/2$ (corresponding to the directions [42.-3], [42.3], [24.-3], [24.3], [2-2.3], and [-22.3]).

The oscillating dipole moment of the antisymmetric stretching mode is oriented along the line between the two end atoms of the triatomic molecule-like defects in the symmetrical XY_2 case (C_{2v} molecule symmetry). This alignment is not perfect in the asymmetrical XYZ case (C_s molecule symmetry) where the two directions may be tilted to each other within the molecule's symmetry plane (cf. Figure 3.11). However, this tilt is expected to be small in the present case of a molecule-like defect consisting of three atoms of the same chemical element.

Summarizing, the observations of polarized absorption, it is most reasonable to assume that the two end atoms of the tri-C defects substitute two nearest N (or Ga) atoms within the same c-plane in the case of the defect configuration associated with TC1, while in the case of the defect configuration associated with TC2, the end C atoms substitute two nearest N (or Ga) atoms located in two c-planes which are shifted by $c/2$. The former defect configuration is called the basal (or planar) tri-C defect, the latter one the axial tri-C defect. Both defect configurations are depicted in Figure 5.14 (b) suggesting the substitution of three host atoms by three carbon atoms. The axial and basal Tri-C defects A and B in Figure 5.14 (b) are for simplified illustrative

purposes, while Chapter 6 (Figure 6.10) discusses stable and metastable defect basal configurations, charge states, and shows the positions of atoms according to the DFT calculation.

Detail structure of tri-C defects. Order of carbon-carbon bonds

It is worth dwelling in more detail on the example of three-carbon clusters showed very illustrative similarity to Tri-C defects in GaN. Carbon clusters with different numbers of atoms were well studied at the end of the last century.[185–187]. Unlike molecules containing a C-C-C chain in the structure, clusters are the simplest and closest analogs of tri-C defects in GaN or AlN. In the case of tri-C clusters, three frequencies (ν_2, ν_1, ν_3) are expected in the ranges at ~200, ~1100 and ~2000 cm^{-1}.[171,185–187] These frequencies are determined by the particular stiffness k of the chemical bond between the C atoms, their mass and the angle between the bonds β. Antisymmetric vibrations were found experimentally at 2040 and 1722 cm^{-1} for tri-C clusters with different configurations.[171,188] In particular, it was shown that in the Ar or Kr matrix, tri-carbon clusters have frequency ν_3 (antisymmetric stretching) of about 2040 cm^{-1} and another vibrational mode at 3250 cm^{-1}.[171] Frequency ν_2 (bending mode) is evaluated as 82 cm^{-1}.[171,187] One can see a direct correspondence of cluster modes ν_3 with TC1, TC2, TC5 modes in GaN, while the mode at 3250 cm^{-1} seems like TC3 and TC4.

The range around 3000 cm^{-1} is usually associated with hydrogen vibrations (e.g., C-H). However, from the isotopic splitting it is clear that TC3 and TC4 are not able to be associated with hydrogen and involve three C atoms. It should be demonstrated that TC3 and TC4 modes at ~2800 cm^{-1} cannot correspond to any normal mode of tri-C vibrations, even with an extremely high stiffness of the bonds. For comparison, force constants of C-C, C=C, and C≡C bonds are $\sim 5\times10^5$, $\sim 10\times10^5$, and $\sim 15\times10^5$ dyn/cm in molecules C_2H_6, C_2H_4, C_2H_2 and it results in carbon-carbon stretching vibration frequencies at 995, 1827, 2181 cm^{-1}, respectively. The antisymmetric stretching frequency 1700 – 2000 cm^{-1} corresponds to the force constants k of the C=C bonds (see [171]) and even hypothetical increase of k in 1.5 time could not result in frequencies ~2800 cm^{-1}. In agreement with the interpretation of the cluster modes,[171] modes TC3 and TC4 are ascribed to the combination vibrations of ($\nu_1 + \nu_3$). With this respect, the complex found experimentally and associated with vibrations TC1 – TC4 is labeled below as C=C=C emphasizing the obligatory presence of hard short bonds between carbon atoms.

The resulting frequency ν_1 is expected to be less than the simple difference of ($\nu_1 + \nu_3$) and ν_3 frequencies by approximately 7 cm^{-1} due to the anharmonicity effect.[171] The DFT calculations of C=C=C basal configuration of tri-C defect in "-" charge state provided by Lyons show excellent matching with the experimental data in absolute frequency of vibrations ν_1 and ν_3, and the isotopic effects (see Table IX).[117] The discrepancy between experimental positions of TC1 and ν_3 calculations is only 0.2% deserves an exclamation mark at the end of this sentence! The calculated ν_1 is on ~0.964 times lower than the experimental frequency obtained from TC3 and TC4. Nevertheless, as it is shown below, there are some differences in the molecular angle between C=C=C evaluated below.

Molecular angle of axial and basal C=C=C defects

The antisymmetric stretching modes of tri-C isotopomers provide information on the angle 2β between C=C bonds. Herzberg[94] derived a formula relating the corresponding isotopomer frequencies of symmetrical XY_2 molecules depending on atomic masses and β:

$$\left(\frac{\nu_3^{(i)}}{\nu_3^{(j)}}\right)^2 = \frac{m_X^{(j)} m_Y^{(j)} (m_X^{(i)} + 2m_Y^{(i)} sin^2\beta)}{m_X^{(i)} m_Y^{(i)} (m_X^{(j)} + 2m_Y^{(j)} sin^2\beta)} \quad (5.10)$$

Table IX. Individual vibrational frequencies of different isotopomers in sample C1213 for the basal tri-C defect with molecule symmetry C_{2v}. The experimental results are compared with DFT[117] and Eq. (5.10).

Peak label	ν_3, cm^{-1}			$\nu_1 + \nu_3$, cm^{-1}	ν_1, cm^{-1}			Isotopomer
	Exp., 10 (297) K	Eq. (5.10) 2β = 134.8	DFT 2β = 161	Exp., T = 10 K	Exp.	DFT	DFT (×0.964)	
TC1-1 (TC1)	1673.9 (1679)	1675.5	1671	2803.5	~1122	1165	1123	^{12}C-^{12}C-^{12}C
TC1-2	1662.3	1663.3	1660	2769.3	~1100	1142	1101	^{13}C-^{12}C-^{12}C ^{12}C-^{12}C-^{13}C
TC1-3	1651.5*	1651.1	1649	2736.7	~1078	1120	1080	^{13}C-^{12}C-^{13}C
TC1-4	1634.1*	1633.9	1627	2760.6	~1120	1164	1122	^{12}C-^{13}C-^{12}C
TC1-5	1622.5†	1621.5	1617	2729.0	~1100	1142	1101	^{13}C-^{13}C-^{12}C ^{12}C-^{13}C-^{13}C
TC1-6	1610.5†	1609.1	1606	2695.0	~1078	1120	1080	^{13}C-^{13}C-^{13}C

* the same faint peak found in GaN140 (Figure 5.12), GaN019 (Figure 5.13)
†found also in C13 (Figure 5.13)

Here, 2β is the angle between two X-Y bonds, the subscripts i and j correspond to the isotopomers before and after the isotope substitution, $\nu_3^{(i),(j)}$ are the individual frequencies of the antisymmetric stretching mode, $m_{X,Y}^{(i),(j)}$ are the atomic masses of the central (X) or the end (Y) carbon atoms (equal to 12 or 13 a.m.u.). Eq. (5.10) can be applied to individual frequencies of the isotopomers forming the TC1 splitting (summarized in Table IX). Taking one of the frequencies as reference, e.g., $\nu_3^{(1)}$, the frequencies for such isotope replacements, which conserve the C_{2v} molecule symmetry, can be calculated: replacement of the central atom ($\nu_3^{(4)}$of both Y atoms ($\nu_3^{(3)}$), and of all three atoms ($\nu_3^{(6)}$). Thereby, the bonding angle 2β is treated as fitting parameter. The best fit to the experimental line positions (mismatch below 1.6 cm^{-1}) is obtained for 2β = 134±8°. For the two missing modes ($\nu_3^{(2)}, \nu_3^{(5)}$), when the two Y sites are occupied by different isotopes, one expects their frequency positions half the way between the modes for the substitution of both Y atoms:

$$\nu_3^{(2)}, \approx \left(\nu_3^{(1)} + \nu_3^{(3)}\right)/2 \text{ and } \nu_3^{(5)} \approx \left(\nu_3^{(4)} + \nu_3^{(6)}\right)/2. \quad (5.11)$$

This is observed in good agreement with experiment. The DFT calculations of the isotopomers provide the set of frequencies described by the classical equation (Eq. (5.10)).[117] The bond angle between the C=C bonds found from the DFT model 2β = 161˚ is much larger the experimental value 134˚, that is the largest difference of the model and the experiment.

Eq. (5.10) can be used for the calculation of the peak positions and 2β angle of the axial C=C=C defect of lower molecule symmetry C_s (XYZ, Table VIII) with caution. The experimental TC2 modes with subnumbers 1, 4, 5, and 8 are in best agreement with the model for 2β = 154°. The frequencies for the replacement of only one end atom are no longer degenerated; however, the experimental peaks 2, 3 and 6, 7 stay equidistant from the center of corresponding marked quadruplet (green dash-dot lines in Figure 5.13 and still

$$\left(\nu_3^{(2)} + \nu_3^{(3)}\right)/2 \approx \left(\nu_3^{(1)} + \nu_3^{(4)}\right)/2 \text{ and } \left(\nu_3^{(6)} + \nu_3^{(7)}\right)/2 \approx \left(\nu_3^{(5)} + \nu_3^{(8)}\right)/2. \quad (5.12)$$

Since Eq. (5.10) is not strictly valid for the case of the asymmetric axial configuration of the tri-carbon defect, it allows for a mismatch of 2 cm^{-1} between the experimental and calculated line positions to realistically estimate a lower limit of the bond angle at $2\beta > 140°$ (instead of exact $2\beta = 154°$).

Due to the insufficient [C] in sample C1213, the splitting of TC4 and TC5 modes is not observed, and the number of atoms cannot be established (clusters with different numbers of carbon atoms and double bonds can have similar frequencies)[185]. However, similarity of TC4-TC2 (by polarization) and TC4-TC3 (by spectral range) allows for the association of TC4 with the ($\nu_1 + \nu_3$) combination vibration of the axial defect. The mode TC5 is associated with unknown multi-C defect, e.g., C_{Ga}-$C_{N\text{-}off}$-C_{Ga}.

5.5. Summary

C_N defects in GaN (and AlN)

Table X below summarizes 13 vibrational frequencies associated with particular C-containing defects in GaN. Some interesting conclusions follow from the analysis of the vibrations caused by carbon in GaN and AlN. In AlN, no peaks with the corresponding isotopic splitting of mono-C defects have been found in principle, while in GaN a set of vibrational modes (MC1 -MC4) has been found and fully satisfies to the DFT-calculated model of C_N. The modes MC1 (766 cm^{-1}) and MC2 (774 cm^{-1}) are associated with the predominant vibration of the C atom while modes MC3 and MC4 involve the nearest shells of the defect atom (delocalized band mode). The double isotope splitting of modes MC1-MC2 and unchanged frequency of MC3-MC4 in isotope experiments as well as polarization of the vibrational modes corresponds to the DFT model of C_N defect. No signatures of C_{Ga} are observed in GaN material. However, it is possible that the change of doping or growth conditions could result in its appearance.

C-H vibrations in GaN.

C-H vibrations in GaN located in FTIR spectra at 2670 cm^{-1} (CH) are identified based on the isotopic shift (6.1 cm^{-1}) due to $^{12}C \rightarrow {}^{13}C$ replacement, close to one found via the model of the diatomic harmonic oscillator. The absolute values and the magnitude of the isotope shift are found in good agreement with C-H complexes in GaP and GaAs. The additional deuterium experiment is required for unambiguous identification of the hydrogen nature of this vibration.

Di-carbon in GaN

The two modes related to di-C defect are found at 1978 (DC1) and 2251 cm^{-1} (DC2). Based on the four-fold isotopic splitting of both signals, the frequency ratio in the isotope replacement, the typical spectral range of the vibration frequencies (C=C and C≡C, resp.), and comparison with the defects in other crystals, these signals are assigned to localized stretching mode vibrations of carbon pairs with the double and triple chemical bonds, respectively. Polarization dependences indicate the tilt angles of carbon pair for DC1 and DC2 ~55˚ and ~30˚ regarding the c-axis of GaN crystal. C_N-C_i is a good candidate for DC1 vibration since in charge state "+" it should have a vibration frequency ~2050 cm^{-1} and a tilt angle 55.6˚ according to DFT calculations. Correspondences for DC2 are not found.

Tri-carbon defects in GaN

The vibrations at (1678 cm^{-1}, 2803 cm^{-1}) and (1718 cm^{-1}, 2832 cm^{-1}) labeled (TC1, TC3) and (TC2, TC4) are associated with vibrational modes (ν_3, $\nu_1+\nu_3$) of tri-C defect in basal and axial configurations, respectively. The frequency of symmetric stretching ν_1 and asymmetric stretching ν_3 well coincide with the DFT model. The range of the vibration frequencies assumes C=C bonds in both configurations. The basal configuration shows C_{2v} molecular symmetry confirmed by the sixfold isotope splitting due to the two end atoms on equivalent positions. The axial configuration possesses lower molecular symmetry C_s and provides eightfold isotope splitting since all three atoms are on unique positions (eightfold isotope splitting). The isotope analysis also allows the estimation of the angle 2β between C=C bonds, equal to 134 ± 8° for the basal and over 140° for the axial configuration. These values are between the corresponding angle of the perfect lattice ~109° and the molecular angle of the basal defect ~160° calculated by DFT. The preferred site occupation of the tri-carbon defects is C_N=$C_{Ga\text{-}off}$=C_N (basal and axial). The complementary site occupation C_{Ga}=$C_{N\text{-}off}$=C_{Ga} or another multi-carbon defect may be tentatively associated with a minor peak TC5 at 1734 cm^{-1} appearing only for the highest carbon concentrations.

Carbon vibrations in AlN

In AlN, the Raman modes Di-C1, Di-C2 are detected at 1189 and 1148 cm^{-1}, respectively. Only for Di-C1, the triple isotope splitting is observed while for Di-C2 peak the splitting structure was not resolved. The spectral range and the isotope splitting correspond to C-C stretching mode of the carbon pair or symmetrical stretching mode of linear C_Y-X-C_Y defect. Here, X can be an atom of N, O, C, Al (from likely to unlikely). Since X is stationary in the symmetric vibrational mode, its mass has no effect on the frequency (example: DFT of ν_1 for Tri-C in Table IX). With this respect, the type of X atom cannot be established reliably. In fact, even the third C atom can occupy the X site (then, the defect should be classified like Tri-C, but linear, in contrast to the bent one, discussed below). Two equivalent positions of C atoms in the lattice are not recognized and calculations of different defect configurations are required for the further analysis.

Only one peak related to tri-C defect is found by FTIR (see detail description in [20]) and Raman. Its frequency and polarization properties are close to TC2 in GaN. In ^{13}C-erniched sample, the peak is represented by eight different isotopomers (XYZ-like defect with C_s symmetry), with a maximum shift between ^{12}C- pure and ^{13}C-pure isotopomers precisely equal to the isotope mass ratio. From the polarization dependences, the vibrating dipole tilt angle close to 34° can be found. The high frequency of 1788 cm^{-1} rather corresponds to a double carbon bond, and the angle between C=C bonds can only be approximated by 150 and above. The mode is active in Raman and has the same order of intensity as the Di-C1 mode.

Conclusion

Chapter 5 describes the experimental results of the isotopic analysis, which is the key to establishing the structure of carbon defects. Finally, the vibrational modes of the C_N defect in GaN have been unambiguously established and decoded. No vibrational signals were found for C_N modes in AlN, C_{Ga}, or C_{Al} despite high [C]. The structure of tri-C defects is described in great detail, making it an ideal subject for further studies. As will be shown below, this defect

is very pronounced in GaN and determines some optical properties. A correspondence was found between the vibrations of di-C defects and DFT model of C_N-C_i pair.

Table X summarizing all found modes in GaN, can be used as a roadmap to inspect the result of the doping procedure. An example of such a study is Chapter 6 included two groups of samples with different [C] grown in homo- and heteroepitaxy.

Table X. Summary of vibrational modes in GaN. Table includes the vibrational frequency in cm^{-1} (Freq.), detection method (R = Raman, IR = IR absorption), schematically shown bond, and description

	Label	Freq.	Method		Description
Mono-C	MC1	766	R	Ga-C-Ga	Axial vibration of C_N
	MC2	774	IR/R	Ga-C-Ga	Basal vibration of C_N
	MC3	659	R	…Ga-N-Ga-C-Ga-N-G…	Basal vibration of C_N in the band mode involved surrounding host atoms
	MC4	673	R		Axial vibration of C_N in the band mode involved surrounding host atoms
	2xMC	~1550	IR/R	MC2 2nd harmonics	The double frequency vibration of MC2 (Fermi resonance?)
	CH	2670	IR	C-H	C-H stretching mode
Di-C	DC1	1978	IR/R	C=C (C≡C?)	Stretching mode of C=C or C≡C chemically bonded pair of carbon atoms with the tilt angle ~55 respective to c-axis. C_N-C_i? C_N-C_i+C_N?
	DC2	2250	IR	C≡C	Stretching mode of another configuration of chemically bonded pair of carbon atoms with C≡C bond and the tilt angle ~30 respective to c-axis.
Tri-C	TC1	1678	IR	C_X=C_Y=C_X	Antisymmetric stretching mode (v_3) of the basal tri-C defect with symmetry C_{2v} and $\beta \approx 134^\circ$ between the two double C=C bonds.
	TC2	1718	IR/R	C_X=C_Y=C_Z	Antisymmetric stretching mode (v_3) of the axial tri-C defect with symmetry C_s and $\beta > 140^\circ$ between the two double C=C bonds.
	TC3	2803	IR	C_X=C_Y=C_X	Combination vibration of the antisymmetric (v_3) and symmetric (v_1) stretching, $v_1 + v_3$ of Tri-C basal defect
	TC4	2832	IR	C_X=C_Y=C_Z	Similar to TC3 but for the Tri-C axial defect
	TC5	1734	IR	C=C=C ?	Another tri-C defect or multi-C cluster?

6. Light-induced defect-related effects in GaN:C

In the previous Chapter, many vibrational modes were described and associated with particular defects based on the isotope effect. Table X above summarizes the vibrational modes and the structure of the related defects for GaN crystals. This Chapter is focused on that how defects manifest their properties in samples of “GaN” and “GaG” series. In general, it includes the data of PL, Raman scattering (at resonance excitation), IR absorption, and UV-Vis absorption. First of all, the overview of the vibrational modes in GaN is completed by the quantitative comparison and distinguishing the major and minor signals according to their intensity at different [C] in different sample series. In addition to "GaN" series (bulk-like HVPE GaN on sapphire) discussed previously, "GaG" (bulk-like HVPE layer grown on Am-GaN) are shown for comparison. I do not detract from the significance of “minor” signals, since under other conditions of doping and growth, they can manifest themselves stronger. Furthermore, it would be incorrect to compare the number of different defects only in terms of the intensity of vibrational modes due to the different cross-sections of these defects in IR or Raman. In addition, the most sensitive method, PL, could detect as low concentrations of defects as 10^{12} - 10^{13} cm^{-3} that could just minorly appear in vibrational spectra.

In second, several “major” and “minor” defects, simultaneously interact with the excitation by blue (2.72 eV ≈ 0.8×E_g) or UV (3.22 eV ≈ 0.95×E_g) light during the FTIR experiment. This discovers the initially inactive fraction of the defects, while the duration and the dependences of the effect on the excitation power and [C] clarify its mechanism. The model of the band-mediated charge transfer seems a good explanation for the sum of the observations.

In the Raman Resonance Scattering, mono-C (C_N), di-C (C_N-C_i), and tri-C (C=C=C) defects vibrate with multiple amplification of the scattering intensity if excited in the range of defect absorption. It allows not only observe C_N at the lowest concentration of intentional doping ([C] = 3.2×10^{17} cm^{-1}) but induces not typical processes of scattering. In addition, Raman spectra show the anharmonic decay of the intrinsic vibrations at the highest [C].

When defects appeared at different [C] have been recognized, the UV-Vis absorption and PL in GaN are considered. The experimental results are compared with the DFT models of

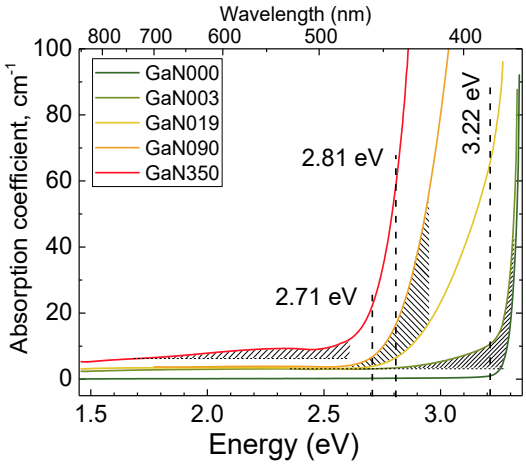

Figure 6.1. UV-Vis absorption of several samples of “GaN” series. Three absorption signals that have different nature are marked: absorption above 2.6 eV at low [C], similar but more intense absorption band at medium [C], and an additional broad band in the range 1.8 – 2.6 eV associated with the highest [C].

tri-C (C=C=C and C-C-C) and C_N defects. The UV-absorption measurements of the relatively thick samples "GaN" and "GaG" series are complemented by the third "GaSap" series (HVPE films with the thickness of ~ 40 μm, not separated from the sapphire template). Figure 6.1 illustrates the specifics of the UV-Vis absorption of GaN:C at different [C]. The values of absorption coefficient α_{UV} shall be important for understanding the photo-FTIR experiments in Section 6.2. In particular, α_{UV} at 2.72 eV does not exceed 20 cm^{-1} while at 3.22 eV it can be above 500 cm^{-1}, as will be shown later. The three shaded areas conventionally show the absorption energy ranges in which the optical excitation is accompanied with different PL bands. The main broad absorption band has its edge at 2.6-2.8 eV. For *all* samples, it can be roughly approximated by the same model function (defect-to-band transition, Eq. (3.15)) taken with parameters expected for C_N defect, and different only in the amplitude. Despite this, better approximations are available in the wide range of fitting parameters, hence, it is impossible to detect directly the difference in the absorption band shape, even though the signal includes several overlapping components. The variability of the UV-Vis absorption processes below and above [C] = 1.9×10^{18} cm^{-3} can be indicated by the PL at resonance excitation in the range 2.2 – 2.8 eV. The found PL signals satisfy the models of two defects, C_N and tri-C defect.

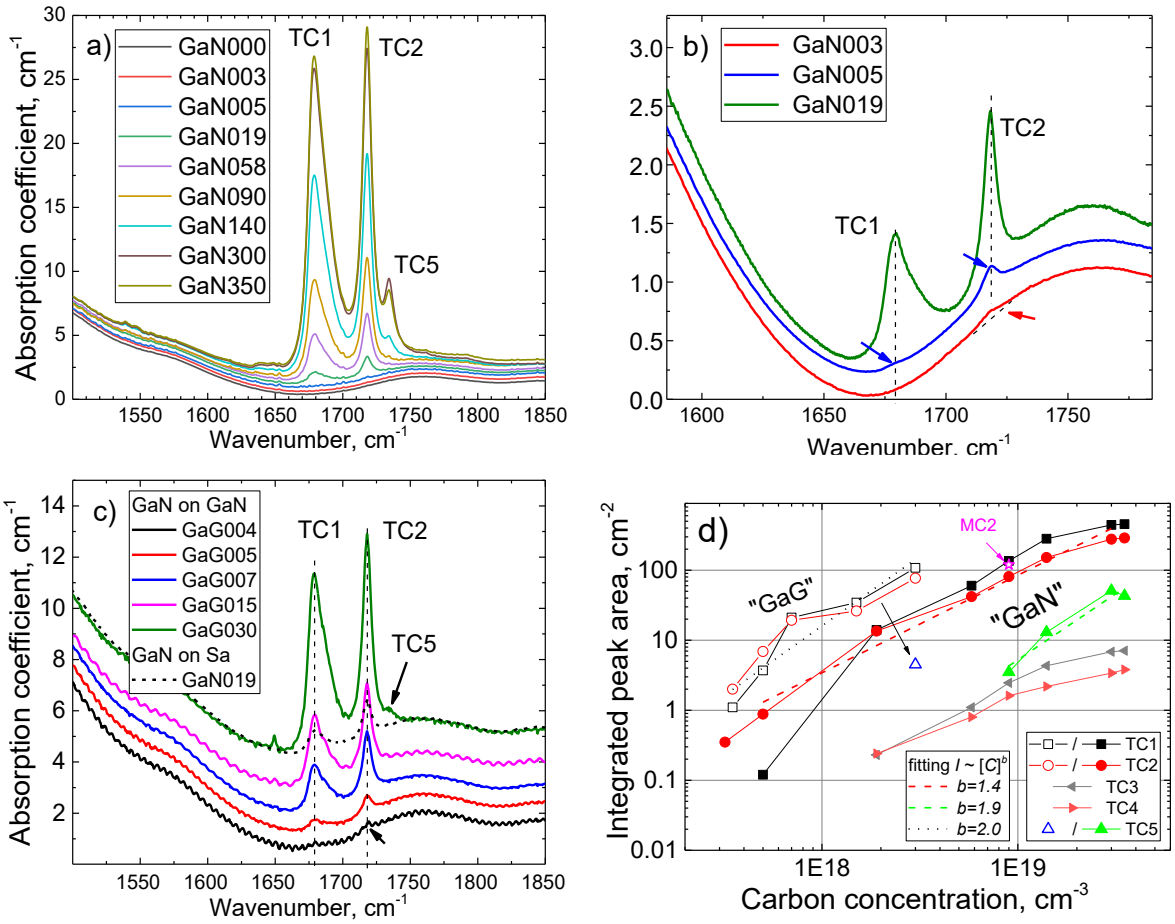

Figure 6.2. IR absorption spectra (vertically shifted) in the range of the dominating C=C=C related modes TC1 and TC2 (a) for all "GaN" samples, (b) for GaN003 – GaN019 and (c) for "GaG" samples comparing to GaN019. Spectra captured at RT for E⊥c polarization (d) Summarized integrated peak area of C=C=C defect vibration modes in "GaN" (filled symbols) and "GaG" (open symbols) sample series. The best fitting by $y = a[C]^b$ is shown with dashed lines. The mono-C mode intensity (MC2) is evaluated for the peak at 777 cm^{-1} only in GaN090 (see spectrum in Figure 5.1.)

6.1. Major and minor defect vibrations in FTIR spectra

Tri-C modes TC1-TC2 dominate in IR absorption

The strongest signals in FTIR absorption spectra are TC1 and TC2 modes of tri-C defects (Figure 6.2). This pair of signals reaches very high intensity as for point defects (area ~1000 cm^{-2}). Upon close inspection (see Figure 6.2 (b)), these modes are detected starting from the lowest levels of intentional doping in this study ([C]=3.2×10^{17} cm^{-3}), only in the reference sample with [C] < 2.4×10^{16} the concentration of C=C=C defects is so low that cannot be detected the corresponding signals. Although a reliable evaluation is possible only with additional assessment of the defect optical absorption cross-section, from the approximate sensitivity of an FTIR spectrometer for this sample thickness (~1 mm) one could expect the detection limit to be in the order of 10^{14} defects per cm^3.

TC1 and TC2 are even stronger in the "GaG" series of HVPE GaN grown on Ammonothermal GaN substrate and doped by methane during the growth. Figure 6.2 (c) compares IR absorption of sample GaN019 with samples GaG004 - GaG035. From the comparison, one can see TC1 and TC2 in a few times more intense despite lower carbon concentration [C] in the latter. In Figure 6.2 (d), the data of integrated area peak for "GaN" and "GaG" series are summarized, including the minor band TC5 and the combination vibrations TC3 and TC4. At any [C], "GaG" samples show higher intensity of C=C=C IR absorption. Since TDD and other structural defects in GaG samples are less pronounced (e.g., TDD is two orders lower), this observation excludes the idea that C=C=C defects could be located in the area of threading dislocations, seed grains, etc.

Comparison of C=C=C and C_N defects in GaN090

It is of practical interest to compare C=C=C and C_N defects, since the latter are classically expected to be dominant in the samples.[40,100,134,189] Unfortunately, the position of the MC1 and MC2 modes does not allow to observe them directly in FTIR absorption for most samples; the only the spectrum of GaN090 demonstrated in the previous chapter (Figure 5.1) gives the following integrated peak intensities: $I_{int}(MC2)$ = 125 cm^{-2}, $I_{int}(TC1)$ = 137 cm^{-2}, $I_{int}(TC2)$ = 95 cm^{-2}. (intensity of MC1 is low at E⊥c polarization). The point $I_{int}(MC2)$ is added in Figure 6.2 (d) for comparison. The intensity of signals from all three defects is comparable, and none of the three defects confidently dominates over the others at [C] = 9×10^{18} cm^{-3} according to the FTIR data. Considering that one tri-C defect requires three C atoms, one can calculate that 50%, 35%, and 15% of C atoms go to form of basal C=C=C, axial C=C=C and C_N defects, respectively, i.e., 85% of C atoms constitute tri-C defects. This, however, is a significant simplification, at least, since the IR cross sections for these three defects is required for reliable comparison.

Note that for "GaN" series, the estimation of C=C=C concentration via the dipole sum rule for TC1 and TC2 modes resulted in number of C atoms corresponding or even exceeding the chemical concentration of C. Using already high values of cross-section,[18] the estimated values exceed the chemical concentration of C starting from [C] = 5.8×10^{18} cm^{-3}. The accuracy of this approach allows only assuming that a significant fraction of C atoms forms C=C=C defects. Since the other modes of IR absorption demonstrate 1-2 orders lower intensity (shown below), C can be supposed to be mainly at C_N and C=C=C defects. Following this, it can be expected that the prevalence of C=C=C in "GaG" samples leads to reduce of the mono-C defect modes (MC1-M4) relative to the "GaN" series; however, in experiments the picture is opposite.

As it will be demonstrated, besides the TC modes the vast majority of signals associated with C (incl. MC1-MC4 vibrational modes) have enhanced intensity in "GaG" samples. It questions the fraction of carbon left out of C_N and C=C=C in "GaN" series. Although no clear answer has been found in this work, after presenting all experimental data, this question is discussed again in the end of this Chapter (Section 5.5).

The minor modes in FTIR spectra at low and mid [C]

The intensities of first-order vibrational modes DC1, DC2, CH and the second-order MC mode are one-two orders weaker than TC1 and TC2, therefore called here "minor". Spectra containing these signals are shown in Figure 6.3. The measurements of the IR absorption were performed only in "GaN" sample series. The data on the integrated intensity are summarized in Figure 6.3 (d) clarifying of what defects are present at low, medium, or high carbon concentrations in addition to C_N and C=C=C, which are always present.

In the reference sample GaN000, N-H vibrations are found,[190] which are not detected in the other samples. Even at [C] = 3.2×10^{17} cm^{-3}, hydrogen bonding with carbon (CH signal) is clearly represented and thereafter the corresponding absorption peak weakens with an increase in [C]. It can be concluded that in the absence of C atoms, hydrogen tends to bond with nitrogen, but when C has been incorporated, the formation of C-H groups is preferred. In addition, very faint DC1 signal is detected at the lowest [C] and the intensity increases up to

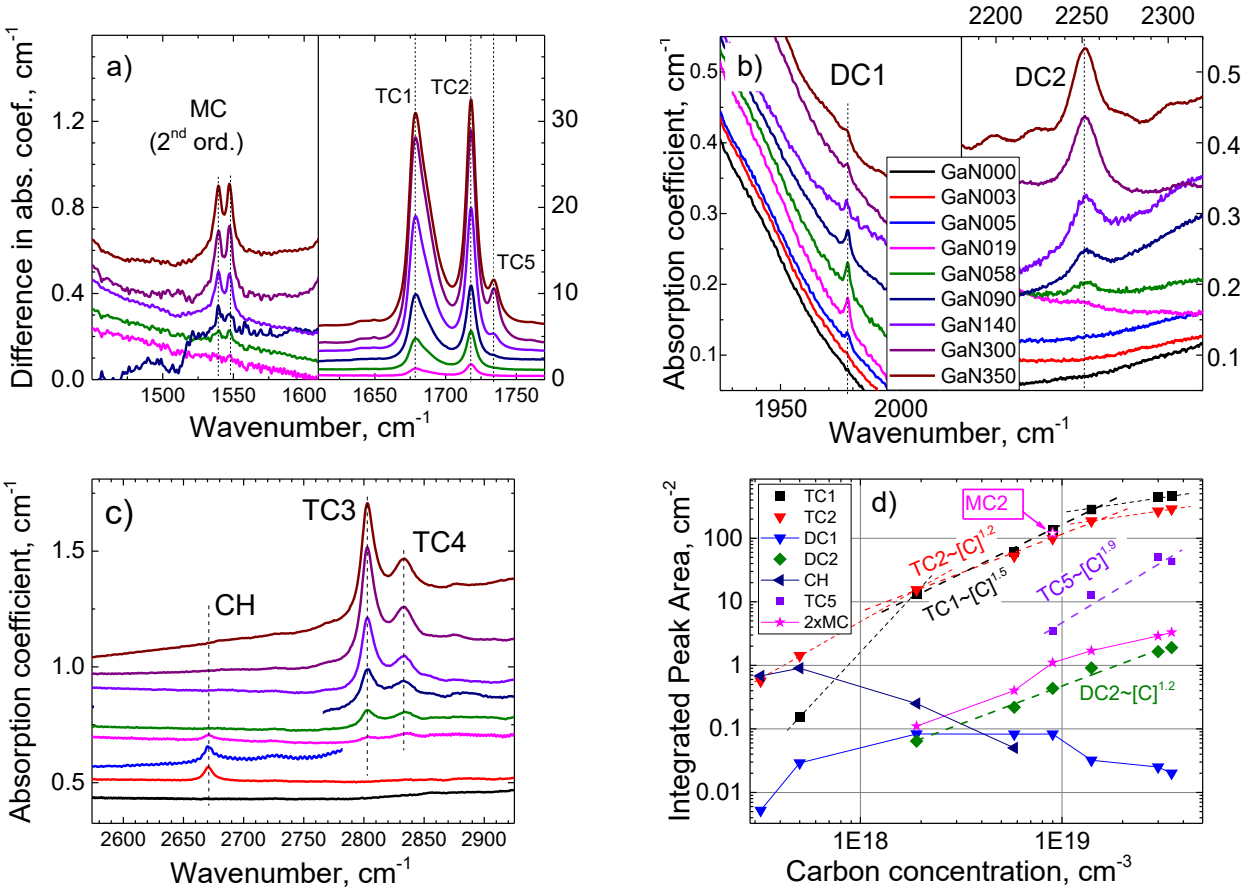

Figure 6.3. (a) IR absorption spectra of samples GaN019 – GaN350 containing the second-order modes of mono-C (MC) and modes TC1, TC2, TC5 after the subtraction of the spectral curve of sample GaN005. (b) DC1, DC2 modes and (c) CH first-order modes and TC3, TC4 combination vibrations in spectra at different [C]at RT for E⊥c polarization, spectra are shifted vertically for visualization. (c) Comparison of integrated peak area of major and minor vibrational modes in sample series "GaN". The best fitting by $y = a[C]^b$ is shown by the dashed lines. The increment of TC1 and TC2 determined by b values depends on [C] (lower at high [C]).

1.9×10^{18} cm^{-3}. This seeming decrease of CH and DC1 intensity will be clarified in the investigation of the light-induced effects in the photo-FTIR research (Section 6.2). It will be demonstrated, that these defects anyway can be detected in FTIR with high [C] under the excitation in the visible or UV range. Starting from 1.9×10^{18} cm^{-3}, another di-C defect of different configuration (DC2) appears in "GaN" samples. Furthermore, it becomes possible to observe the second-order of MC2 vibrations. At medium concentrations, the intensity of C=C=C defect modes TC1, TC2 increases, significantly superlinear with [C] (TC1 ~ $[C]^{1.2}$, TC2 ~ $[C]^{1.5}$), though this increment is expectedly larger at low and sublinear at high concentrations (shown by dashed lines in Figure 6.3 (d)).

The minor modes in FTIR spectra at high [C]

At the highest concentrations, a multi-C defect (probably, a different configuration of C=C=C structure) originating TC5 vibration appears while the major modes TC1 and TC2 slows down to the dependence $[C]^b$ at $0.45 < b < 0.55$. One can assume that at higher concentrations (i.e., 1×10^{20} cm^{-3}), the corresponding TC5 defect may prevail since its intensity depends on the concentration with a power $b \approx 1.9$. Similarly, the DC2 modes of the C≡C pair increase with the carbon concentration with a power of 1.1-1.3 and also reaches the maximum fraction at the highest [C]. Finally, two modes, DC1 and CH visibly disappear at mid-high [C]. The integrated intensities of the peaks discussed above indicate only the particular RT ground states of defects at equilibrium population of electrons. It should also be remembered that during the FTIR experiment, all the light from the source (globar) hits the sample providing weak excitation with an energy below 0.5 eV. Since the defect state changes due to ionization or excitation, e.g., when the intense light shines the samples, the corresponding vibrational mode changes the intensity too. These effects are discussed just below.

6.2. Light-induced changes in FTIR spectra (photo-FTIR).

Simultaneous change of IR modes under 3.22 eV, 2.72 eV and 1.32 eV excitation

FTIR spectra can illustrate how several types of defects change the state under the UV-Vis irradiation. Figure 6.4 shows the IR absorption spectra of sample GaN019, one of the most sensitive to the UV-Vis excitation in FTIR experiments. Samples were excited by light (with an energy of 1.32 eV, 2.72 eV, or 3.22 eV) inside the sample chamber during the measurement of IR absorption at RT (see the chamber geometry in Figure 4.1). The spectrum shown with the dashed line (Figure 6.4 (a)) is recorded immediately after the installation of the sample on the measurement position. As for the last 30 minutes (or longer), the sample was interacting with the daylight, it returns to the equilibrium state in the dark, or strictly speaking, under relatively weak IR irradiation of the globar source. It was checked that the modes do not change when the long-pass filter between the globar source and the sample blocks the light with energy above 2000 cm^{-1}. The observed very slow increase in the TC1 mode intensity was multiple times accelerated by irradiation at 1.32 eV up to the maximal values. Under further irradiation of 1.32 eV or being in the dark, the IR absorption does not differ with one shown by the green spectral curve. In next step, partial suppression of TC1 and TC2 (blue curve) was stimulated by the irradiation at 3.22 eV with LED power of 30 mW. Then, at higher power of excitation (above 150 mW), the virtually complete disappearance of these modes is observed (red curve).

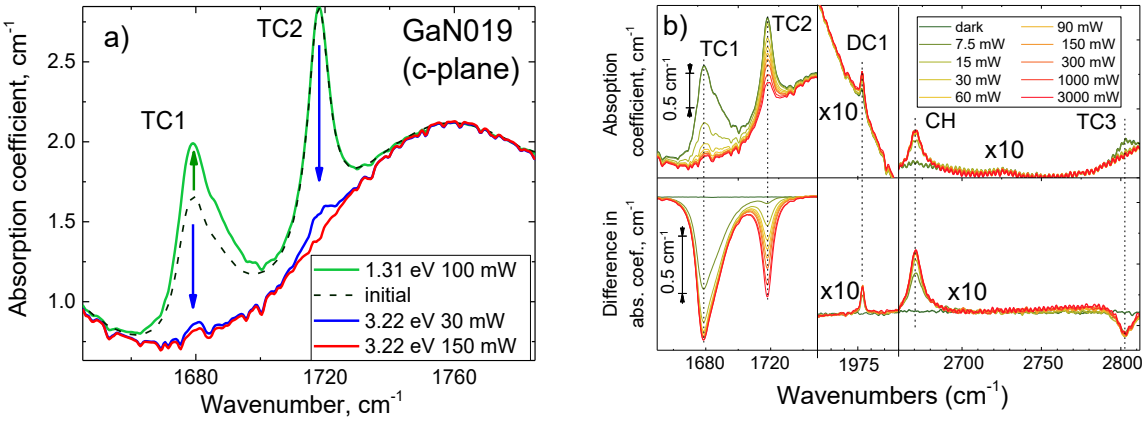

Figure 6.4. (a) IR absorption spectra of the c-cut GaN019 sample. Unstable initial state immediately after being placed in the spectrometer chamber (dashed line), stimulated restoration with the 1.31 eV excitation to a stable state (green line) and suppression of signals stimulated by UV light (3.22 eV) (unchanged while the irradiation is "on"). (b) Spectral curves of the same sample at different 2.72 eV LED excitation power and the same spectra after subtraction of the "dark" spectra.

The effect of pumping at 3.22 eV and 2.72 eV is qualitatively similar but quantitatively different. Sample GaN019 is more sensitive to 3.22 eV than to 2.72 eV excitation, and pumping with energy 3.22 eV, even at low power 30 mW, quickly suppresses both vibrational modes (Figure 6.4 (b)) so that the difference of TC1 and TC2 cannot be detected. At 2.72 eV excitation, only partial decrease of TC2 mode is observed in the whole range of the output LED power up to 3000 mW while TC1 completely disappears at excitation power starting from 300 mW. From this, one can conclude, TC1 mode and the corresponding defects are more sensitive to the light excitation.

In contrast, samples at higher [C] become practically insensitive[1] to the high-energy pumping 3.22 eV, but still show significant changes at low-energy pumping 2.72 eV. Figure 6.5 (a) contains absorption spectra in the dark and under the 2.72 eV excitation of samples GaN350 and GaN140 (the main piece with thickness 732 μm and the additional one, 312 μm). To explain this effect, the penetration of light is discussed below. However, first of all, we note that many other modes change at the same time in addition to TC1 and TC2. The difference of the two absorption curves in Figure 6.5 $\Delta\alpha_{IR} = \alpha_{IR}$ (dark) – α_{IR} (2.72 eV) is represented in the bottom part for all three crystal measured pieces. The curves of samples GaN140 and GaN350 contain the second-order MC signal (C_N), which also decreases upon excitation at 2.72 eV. This indicates the interaction of C_N defects with the light excitation of 2.72 eV energy. The behavior of other signals is similar in all samples and excitation energy. Modes TC3 and TC4, having the same origin with TC1 and TC2, always change proportionally. The change in the DC1 and CH mode intensity at 3.22 eV excitation is opposite to the change of TC1 and TC2. Changes of DC1 and CH modes are shown in Figure 6.4 (b) for 2.72 eV excitation of sample GaN019.

[1] In GaN350, 3.22 eV excitation with power 1500 mW originated only the detectable reproducible decrease of TC1 in ~1%, spectra not shown.

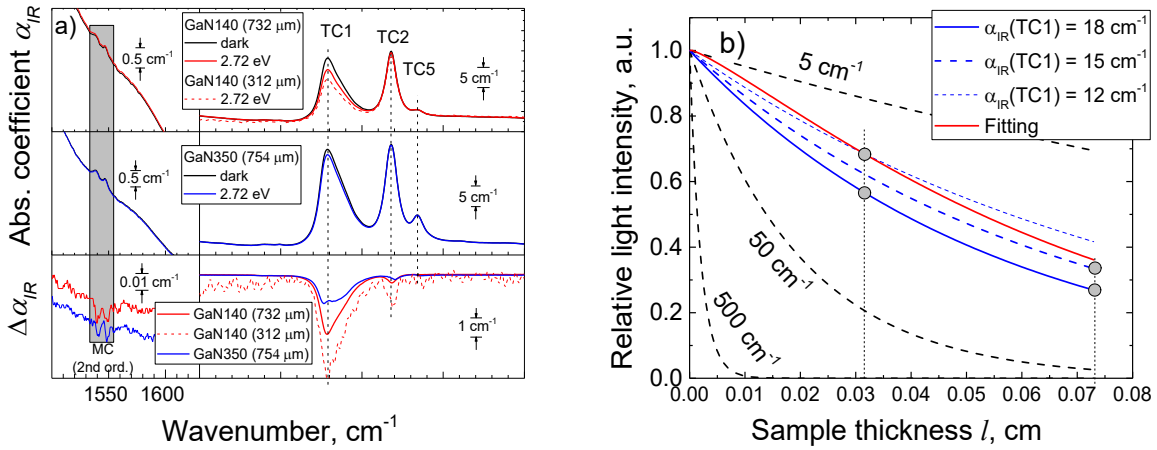

Figure 6.5. (a) IR absorption spectra of samples GaN140 (736 μm or 312 μm) and GaN350 (754 μm) in the dark and under the 2.72 eV excitation. The difference between "dark" spectra and "excited" spectra is plotted in the bottom ($\Delta\alpha_{IR}$). The signatures of C_N defect (MC) and C=C=C defect (TC) decrease under the excitation. (b) Illustration of the light intensity distribution according to of the Burger-Lambert-Beer law (shown for α = 5…500 cm^{-1}). Both piece of GaN140 provide the same α_{IR} = 18 cm^{-1} measured in the dark (two spots on the blue solid curve). In contrast, α_{IR} is equal to 15 or 12 cm^{-1} at the 2.72 eV excitation (spots on the corresponding dashed curves). Fitting of possible intensity distribution under the excitation is shown by the red line (see the text).

Distribution of the intensity of light on the sample depth

Since material absorbs in UV-Vis range (at 2.72 eV $\alpha_{UV} \approx 5…20$ cm^{-1}) the intensity of the excitation light is distributed in the penetration depth l of the crystal accordingly to the Burger-Lambert-Beer law:

$$I_{UV} = I_{UV0}\, exp(-\alpha_{UV} l), \tag{6.1}$$

where I_{UV0} is incoming and I_{UV} is transmitted light intensity. The same dependence describes the distribution of IR radiation during the FTIR measurement of the absorption coefficient α_{IR}:

$$I_{IR} = I_{IR0}\, exp(-\alpha_{IR} l). \tag{6.2}$$

In Figure 6.5 (b), the distribution of the intensity (Eq. (6.1) and (6.2)) is demonstrated for different values of α in the range 5…500 cm^{-1}. FTIR measurements of two GaN140 pieces with different thicknesses without the excitation at 2.72 eV (Figure 6.5 (a)) can confirm that the condition given by Eq. (6.2) is met (the two points lie on the same curve at $\alpha_{IR} \approx 18$ cm^{-1} in Figure 6.5 (b)). However, for the measurements during the UV-Vis excitation, the two thicknesses provide two different values of α_{IR} (the points on α_{IR} = 15 cm^{-1} and α_{IR}= 12 cm^{-1} curves). The effect is explained by the dependence of the absorption coefficient α_{IR} on the intensity of UV-Vis excitation distributed in the depth according to Eq.(6.1). IR absorption then goes out of the homogeneous absorption approximation breaking the condition the Burger-Lambert-Beer law. With this respect, transmittance (or absorbance) is more reasonable values measured by the FTIR spectrometer directly, while the absorption coefficient has conventionally averaged value.

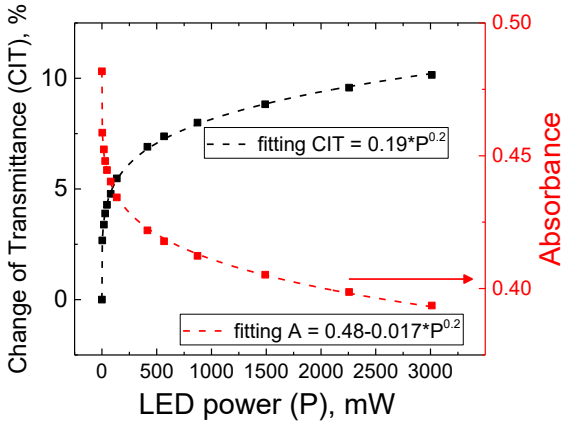

Figure 6.6. The values of absorbance (A) and the change of transmission (CIT) at different power output LED power (P). The fitting with functions is shown by the dashed lines. Experimental values for sample GaN140 are indicated by dots

Furthermore, the effect is complicated by the non-linear dependence of the transmittance on power of excitation. Figure 6.6 indicates the sublinear dependence of the change in transmittance (*CIT*)[1] and the absorbance (*A*) on LED power (*P*). Approximation of the empiric result is given by the function P^w with the exponent equal to 0.2 for GaN140 with thickness of 732 μm. The fitting functions $CIT \sim P^{0.20}$ and $A \sim P^{0.20}$ are shown by the dashed lines.

Suggesting then the dependence:

$$\alpha_{IR}(l) = \alpha_{IR0}\left(1 - \left(\frac{I_{UV}}{I_{max}}\right)^{w}\right), \tag{6.3}$$

one can fit the IR radiation intensity distribution based on experimental values for GaN140 sample: the exponent w = 0.2 of power dependence, absorption of light at 2.72 eV α_{UV} = 12 cm^{-1}, and the magnitude of TC1 mode α_{IR0} = 18 cm^{-1} in the dark, and I_{UV0} / I_{max} = 1, (fitting parameter) as it shown in Figure 6.5 (b). The two experimental points are now located closer to this curve. Establishing the true IR intensity distribution requires numerous additional photo-FTIR measurements at different irradiation power, different [C], and different thicknesses. It should have a more complex form, at least, because Eq. (6.1) also does not describe the intensity distribution since in most cases the UV-Vis absorption saturation effect occurs at high excitation power.

Power dependences in GaN019, GaN140, and GaN350

Different crystals and different vibrational modes of the same crystal keep the same type of the empiric dependence P^w on the excitation power but in general show different value of *w*. From Figure 6.7, one can estimate *w* in the range 0.2…0.5 for TC1 (a) and TC2 (b) in the three presented samples. Despite the impressive nominal power of the light sources (3.0 W at 2.72 eV and 1.5 W at 3.22 eV), neither saturation of the effect nor complete suppression were reached for most of the samples and vibrational modes. At 2.72 eV excitation, only TC1 in GaN019

[1] CIT ≡ $(I_1 - I_2)/(I_1 + I_2)$ more trustily compares the two intensities I_1 and I_2, see the experimental methods (Section 4.1)

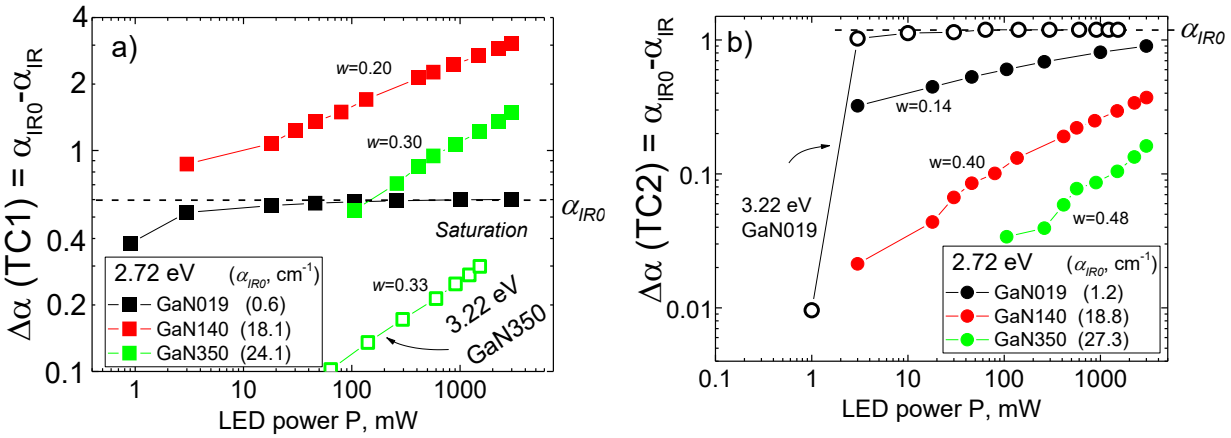

Figure 6.7. The decrease of TC1 (a) and TC2 absorption coefficient α_{IR} at excitation with energy 2.72 eV (filled dots) or 3.22 eV (open dots) counted from the values measured in the dark (initial α_{IR} given in brackets). The effect of excitation at 3.22 eV energy on both TC1 and TC2 is weaker for GaN350 (a) and stronger for GaN019 (b).

shows the complete disappearance ($\Delta\alpha=\alpha_{IR0}$), while the other signals obey accurate power dependences represented as straight lines in the log-log scale.

The first of the important factors affecting the magnitude of the effect is the absorption coefficient α_{UV} in the excitation range. High α_{UV} (e.g., ~500 cm^{-1} at 3.22 eV in GaN350) diminishes the penetration depth.[1] The shallow penetration depth prevents large change of α_{IR} since only the shallow upper layer ~50 – 100 μm can be *effectively* excited by the light. With this respect, excitation at 2.72 eV induces stronger changes in sample GaN350 (cf. in Figure 6.7 (a)). In this case, $\alpha_{UV} \approx 20$ cm^{-1} at 2.72 eV provides more gradual distribution of the excitation light. On the other hand, low α_{UV} minimize the interaction of defects with the light. In GaN019, only 30 mW power of excitation at 3.22 eV ($\alpha_{UV} \approx 20$ cm^{-1}) provides >95% suppression of modes TC1 and TC2 ((a)), while 2.72 eV excitation ($\alpha_{UV} \approx 5$ cm^{-1}) does not provide complete disappearance of modes even at 3000 mW (Figure 6.7 (b)). In other words, high intensity is needed to compensate the low cross-section of the defect absorption (expressed by fitting parameter I_{max}.

Another important factor is the rate of the initial state restoration correlated with [C]. In particular, at high [C] (GaN140, GaN350), the initial state is restored in less than 15 seconds (time between nearest measurements). For samples with low [C] the decay is measurable.

Time dependences of the light-induced effects

The changing of IR absorption peak integrated area A_{IR} prolongs for a few minutes after the change in lighting conditions. Measurements of the samples showed an exponential time dependence of the intensity change:

$$A_{IR} = y_0 + A_{IR0} \exp((t - x_0)/t_0), \qquad (6.4)$$

[1] The values of α_{UV} at high [C] in the range 400 – 500 cm^{-1} can be found in Figure 6.15 (c), while the distribution of the light density on the depth is shown for $\alpha_{UV} = 500$ cm^{-1} in Figure 6.5 (b).

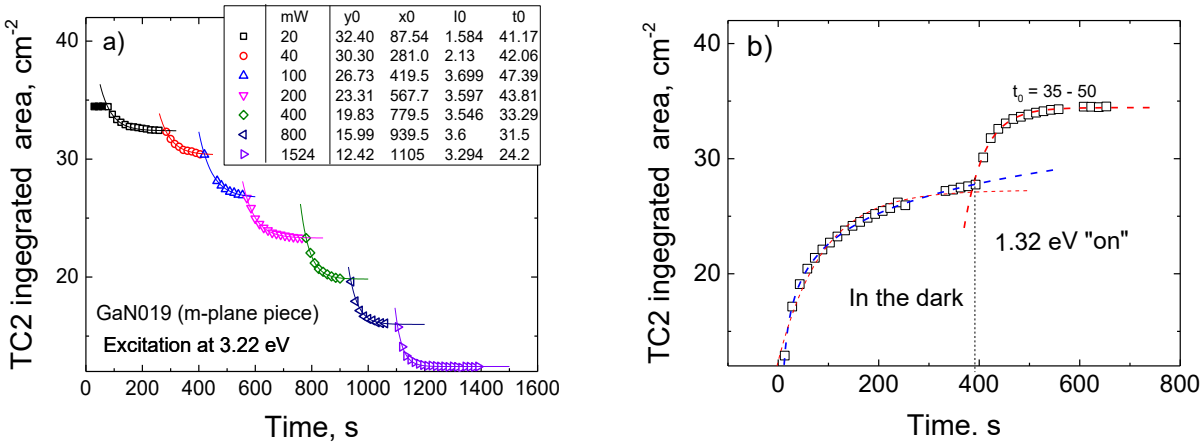

Figure 6.8. (a) Change of the peak integrated area in time under the excitation at 3.22 eV at different power (mW) approximated with Eq.(6.4) In this set of experiments, an additional m-cut sample GaN019 with thickness 1.8 mm was measured. The light source is located farther from the sample providing lower effective illumination (comparing to Figure 6.5). (b) the restoration of TC2 mode in the dark and under 1.32 eV irradiation approximated by the exponential functions (red lines). The better fitting of the restoration in the dark is provided by logarithmic function (blue curve).

where x_0 is the moment of the LED power switching, y_0 is the asymptote, I_0 is the amplitude and $1/t_0$ is an equivalent of rate (the values are shown in Figure 6.8). The time dependences of IR absorption of GaN019[1] is shown during a gradual increase in the irradiation power at 3.22 eV from 20 to 1524 mW. The accumulation time of one measurement point was 15 seconds. At low and high power of excitation, the change process has a visibly different rate. The time parameter t_0 at 1524 mW is found ~1.7 times lower than at lower power. In Figure 6.8 (b), the further process of the initial state restoration is shown, first in the dark, and then under the action of restoring radiation at 1.32 eV. The restoration in the dark is poorly approximated by an exponential function (the best approximation is shown in the figure by red), while the logarithmic function perfectly describes the growth of the yet not asymptotic signal.

Excitation of inactive defects

The influence of the light excitation on the defect density at different [C] is shown in Figure 6.9. The filled symbols show the mode intensities without irradiation, while the open symbols demonstrate the intensity under the joint irradiation by 2.72 eV and 3.22 eV light. The amplification of DC1 vibrational modes by several times occurs in all spectra contained this signal.

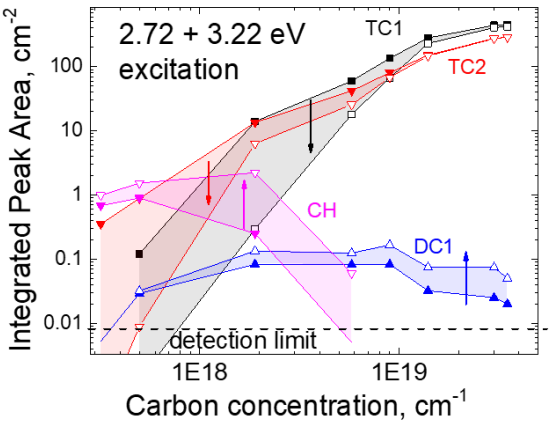

Figure 6.9. Maximum change of peak integrated area in FTIR experiment due to the joint 2.72 eV + 3.22 eV optical excitation (LED outcome optical power 3.0 W + 1.5 W). The filled symbols correspond to the area in the dark, while the open symbols are the values under the excitation. The dashed line shows the detection limit for the specific FTIR measurements.

[1] In these optimized measurements, I examine an additional m-cut GaN019 wafer in ~ 5 times thicker than the c-cut GaN019 discussed in other experiments. In addition, the excitation source was placed further away from the sample, lowering the light density

The mode of C-H vibrations is also amplified many times and it manifest in GaN058 sample only under excitation at all. The modes of C=C=C defects are significantly reduced or even become less than the detection limit at low [C], while with increasing concentration the effect diminished. In fact, the intensity of TC1 is suppressed by more than 90%, at GaN058 or lower [C] and in GaN090, while at higher [C], the decrease is less than 50% (In GaN350 it is only a few percent). It should be considered that the saturation of the effect was not achieved thus not all defects are activated and observed in FTIR.

On the origin of the photo-FTIR changes

A change in the vibrational mode intensity is possible when the number of oscillators changes. The oscillator here is the chemical bond between the atoms of the defect, while the condition for the mode IR activity is the presence of the oscillating dipole $\Delta\vec{\mu}$ (Figure 3.11). Thus, the reason for the vibration disappearance can be a break in a chemical bond or a change in charge distribution reducing the oscillating dipole. In other words, the defect can transform into an induced state which could be a metastable configuration or/and another charge state. Any significant heating of the sample by the light can be excluded, since TC1 mode, extremely sensitive to temperature, does not change either the spectral position or the width.

Hypothesis 1. C=C=C defect dissociates under the influence of light (decrease in TC1, TC2 in experiment). On its place, the light-induced structure including the vibrating C=C group now originates vibrations DC1 (the increase of DC1 vibrations). A few questionable points leave no chance for this hypothesis. First of all, the DC1 modes existed in some samples before the light excitation (neglecting the daylight influence). Second, it seems doubtful (but possible) that the decrease in the intensity of TC modes is several orders of magnitude smaller than the increase of DC1 mode. Third, the metastable state alone cannot explain the different recovery rates correlated with [C]. Finally, this hypothesis does not explain the accompanying disappearance of MC modes and the appearance/gaining of CH vibrational modes. With this respect, it seems more reasonable to look for the reason not in particular defects but in the material itself.

Hypothesis 2. Light induces a depletion layer on the surface of the crystal. In this layer, the defects change the charge state as there is the charge transfer between the excited and unexcited regions of the crystal. This hypothesis, however, requires much larger absorption coefficients and larger inhomogeneity of the excitation intensity on the depth. Such phenomenon would not be observed in samples with α_{UV} in the range between 5 and 50 cm^{-1} (e.g., in GaN019 which, in contrast, the most sensitive to the excitation). Thus, in most cases, the effect is observed even with quasi-homogeneous light intensity distribution. On the other hand, charge transfer remains possible between charged defects at the microscopic level or between the areas with the fluctuated impurity regions (the next *Hypothesis*).

Hypothesis 3. The charge transition between different point defects in the volume of the material results in simultaneous change of their charge states from equilibrium to non-equilibrium ones. Under resonant excitation in the absorption range of defects, the first step is the defect photoionization and this induces charge carriers of predominantly one type (as opposed to above-bandgap excitation). The ionized defect can return to its initial state capturing a charge carrier. The time scale of this process highly depends on the ionized charge state. For example, after the excitation $C_N^- + E_{Abs} \rightarrow C_N^0 + e^-(CB)$, the return of the neutral state C_N^0 to C_N^- state occurs with a characteristic time of several microseconds at LT, according to the model based

on the observations of non-exponential PL decay.[131] On the other hand, the capture of a free electron by a positive ion of another point defect (for example, V_N^+, V_N^{2+}, Tri-C^+ , $(C_N\text{-}C_i)^+$, $(C_N\text{-}C_i\text{+}C_N)^+$) is at least one order faster. With this respect, it is probable, that the excited carriers redistribute between defects providing their transition to the nonequilibrium charge states. The induced nonequilibrium states themselves are stabilized since only one type of carrier is predominantly generated by the light. At low [C], the large distance between the defects results in slow relaxation in the dark, while at high [C] above 1×10^{19} cm^{-3} the defects are located closer and simplify the reverse process. Photo-EPR experiments confirm charge transfer between defects in C-doped GaN with time scales similar to the light effects in FTIR and optical excitation conditions (~ 1 eV and ~ 2.7 eV). In addition, similar processes can be the cause of Bulk Photovoltaic Effect [27] and photochromism, which were observed in our samples. The expectation of the new charge states reasons the question, where are the vibrations of defects in the induced charge states?

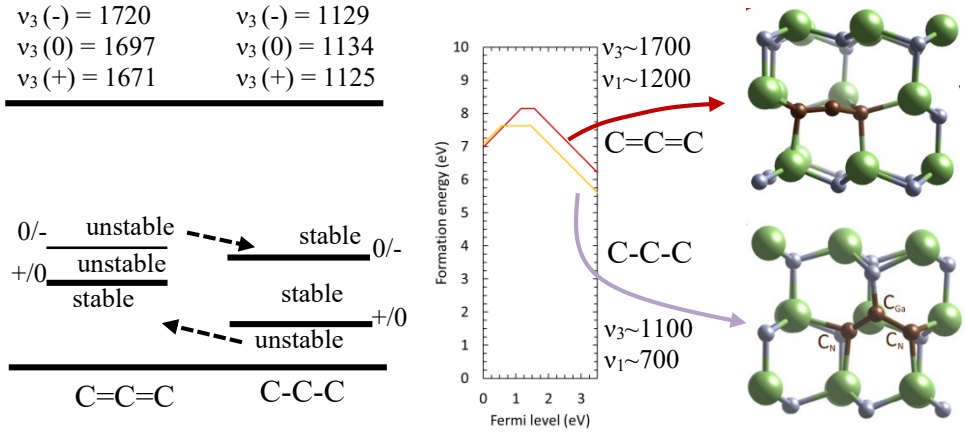

Figure 6.10. Calculation of the formation energy, vibration frequencies in different charge states, and the position of carbon atoms in the lattice of GaN for two configurations of Tri-C defects: C=C=C and C-C-C, performed by Lyons[34,117]

Charge states and meta-stable states of Tri-C defect

Usually, a change of the defects' charge state results in a little change in vibration frequency, although this is not a straight rule. In the theoretical reports, examples of typical small and extraordinary large frequency shifts can be found with a change in the charge state of some defects.[34,59,62] For example, C_N-C_i pair vibrates at ~1240 ("3+") or at ~2050 cm^{-1} ("+" charge state),[34,62] but C_{Ga}-C_i has frequencies 1455 ("3+"), 1462 ("2+"), 1459 cm^{-1} ("+"), and only 1059 cm^{-1} ("0") significantly differs.[62] The large frequency shift can be attributed to a significant change of the defect configuration resulting in a large change of the stiffness k attributed to the change of the carbon-carbon bond order. In fact, such a change in the charge state is associated with a rearrangement of the defect and is in many ways similar to a metastable state, since it requires very deep relaxation.[127]

Such restructuring is expected not only for C_N-C_i suspected of vibration mode DC1. Two configurations of tri-C defects, C=C=C and C-C-C also correspond to similar transformation. Despite solid argumentation of the double C=C bonds in tri-C defects (Section 5.4), an alternative configuration C-C-C predicted by DFT to have lower formation energy in charge

states "0" and "-" (but not "+").[34,117] The two configurations C=C=C and C-C-C differ by the chemical bond of the central C atom with the nearest N atom as it is shown in Figure 6.10. The formation of the C-N bond would result in elongation and softening of the carbon-carbon bonds and the increase of frequencies ν_3 from ~1700 cm^{-1} to ~1200 cm^{-1}, according with the calculations (vibrational frequencies and the models are shown in Figure 6.10) The formation energy of both configurations is so close that does not allow to determine the preferable form authentically. In addition, the C=C=C defects in FTIR spectrometer were observed under Globar radiation. The peak energy of this irradiation is about 0.4 eV that, in fact, could be enough for a transfer from C-C-C to C=C=C in charge states "0" or "–". Summing up, the induced charge states are not necessary should be observed in similar range.

6.3. Resonance Raman spectra of major and minor defects

Normalization of Raman spectra

The enhancement of the Raman cross-section near an electronic transition is known as *resonant Raman scattering*.[93] Similar effects on Di-C1 and Tri-C1 Raman modes were observed by us in AlN[21] and by other authors in different materials.[90,191–193] The modes of C_N defect can be effectively observed in Raman (even without long detection integration) when excited in the defect-related absorption range, e.g., at 2.81 eV. Figure 6.11 (a) shows the unprocessed Raman scattering spectra of the four samples from the "GaN" series at x(yy)$\underline{x}$ polarization. The scattering intensity depends on the light-excited volume of the crystal and cannot be compared directly especially for the excitation in the range of the strong defect absorption. Since defects have a significant effect on intrinsic vibrations, it becomes difficult to normalize the spectra of two different crystals for numerical comparison as all possible references, the integrated area of the strongest intrinsic modes or the whole spectrum integrated area, are under the influence of the defect concentration. The bright luminescence signals discussed in the next Section are normally located in the range well above 2000 cm^{-1} but tails of the high-energy PL bands can be excluded by a smooth polynomial background function.

Anharmonic processes due to carbon doping influenced the intrinsic vibrations

At high concentrations of defects, the balance between the intensity of intrinsic modes is disturbed due to anharmonic processes. In the classical interpretation, the perfect crystal is a

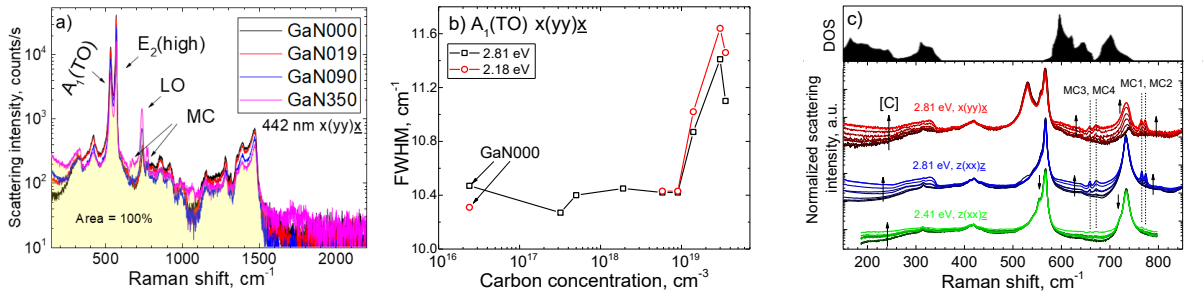

Figure 6.11. (a) Unprocessed Raman scattering spectra of four different samples before normalization at 2.81 eV excitation in x(yy)x geometry. The area for further normalization is colored (100%). (b) Full width on half maximum of A_1(TO) peak at 2.81 and 2.18 eV excitation in x(yy)x geometry at different carbon concentration [C]. (c) The normalized spectra of "GaN" sample series for two excitation energies 2.4 eV, 2.8 eV and z(xx)$\underline{z}$ or x(yy)$\underline{x}$ geometry. The trend of carbon concentration [C] is shown by the arrows. The density of phonon states (DOS) is reproduced from work of Bungaro, et al.[105]

system of coupled oscillators vibrating without damping in the approximation of the harmonic forces of the first-order interatomic interactions.[97] In such an approach when the interactions are harmonic, the energy of each normal vibration mode is always conserved and the vibration mode frequency is presented in a spectrum by the Dirac delta function (neglecting the hardware broadening and the crystal inhomogeneity).[97] The damping of the oscillator due to the anharmonic forces leads to line broadening in the spectra[97,182] over the basic values of the width. In terms of phonons, the FWHM of a phononic line is inversely proportional to the lifetime of the corresponding phonon before decay into several individual phonons.[194] This is especially actual for polar modes (such as TO phonon mode) in presence of charged point defect (centers of phonon decay). The presence of point defects at not "0" charge state distorts the periodic potential of the perfect lattice. As a result, in samples with high concentration of impurity atoms GaN090 – GaN350 abrupt broadening of the A_1(TO) mode at x(yy)$\underline{x}$ occurs both with resonant excitation (2.81 eV) and with excitation out of resonance (2.18 eV in Figure 6.11). With this respect, the anharmonic processes have a significant effect on the system at [C] = 9×10^{18} cm^{-3} and above.

Resonant amplification of the defect-related and phonon-band scattering

The broadening of the bands is not associated with resonant excitation of the crystal being a straightforward illustration of the lattice imperfections. There is another unrelated significant process at the excitation of the crystal in the absorption range of point defects. Figure 6.11 (c) compares the excitation in the defect-absorption range (2.81 eV) for two polarization z(xx)$\underline{z}$ and x(yy)$\underline{x}$ and the excitation at 2.41 eV. The spectral curves are normalized to the integrated area in the range from 150 to 1535 cm^{-1} and shifted vertically (the three independent offsets). The brightest feature observed for both polarizations at 2.81 eV excitation is the increase of the flat signals in the spectral regions 150 - 330 cm^{-1} and 510 - 740 cm^{-1}. Though these signals are visibly increase with [C], the vibrations are not originated in C-atoms. These ranges correspond to the ranges of high phonon Density of States (DOS) summarized on the whole Brillouin zone (cf. Figure 3.2),[105] and hence should be associated with the vibrations of the host atoms.

The creation of a phonon in the act of Raman scattering cannot lead to the appearance of an uncompensated momentum in the system (momentum conservation law), therefore only processes in Γ point (with $\vec{\kappa}_1 \approx 0$) of the Brillouin zone are allowed in the first-order processes. The phonons at $\kappa \neq 0$ are forbidden but can contribute to the spectrum if an additional phonon, e.g. defect-related mode, participates (then, still $\vec{\kappa}_1 + \vec{\kappa}_2 \approx 0$).[90,93] The two-phonon or even multi-phonon acts of scattering become more probable at the resonance excitation when the intermediate (virtual) states coincide with the real electronic states of the system.[193] The energy 2.41 eV is out of the absorption range for most samples hence, the band-scattering is not observed; at [C] = 9×10^{18} cm^{-3} and above due to the weak absorption band in the range 1.9 – 2.5 eV (see Figure 6.1 in Sect. 6.1), the phonon band-scattering becomes to appear, but the effect is not as outstanding as at 2.81 eV. The most attractive application of the Resonance Raman is based on that peaks of point defects appear at least one order brighter comparing to the non-resonance excitation (e.g., MC1 - MC4 in Figure 6.11 (c)). An important note is that the intensities of all peaks, mono-C, di-C, and tri-C, are amplified relative to the intrinsic vibrations A_1(TO) or E_2(high).

Coupling of the intrinsic and defect vibrations

Figure 6.12 (a) shows the balancing of the intensity between different vibrational modes in x(yy)x geometry at normalization to the integrated area in the range 150 – 1535 cm^{-1}. In samples with different [C], I compare the intensity of the two allowed first-order modes A_1(TO) and E_2(high), the acoustical and optical phonon bands, LO peak, and MC1+MC2 integrated area (shown in the modified scale ×20).[1] In the reference sample (GaN000), the two intense modes A_1(TO) and E_2(high) include ~67 % of the full integrated area, while the remaining intensity is distributed between the other counted bands (~4%) and uncounted signals, such as the overtone modes or the second-order scattering[2]. At the highest [C], A_1(TO) and E_2(high) intensity decreases to ~48% and all amplified modes increase the intensity up to ~25% (includes MC1+MC2 reached 0.7%).

The proportionality of the vibrational mode intensities becomes clear if one of the modes is used as x-axes. LO mode is chosen as x-axes in Figure 6.12 (b) (that corresponds to trend of [C] too). The intensity of optical, acoustical phonons, and the mono-C defect vibrations increase in straight linear proportion with the LO mode. The decrease of the two modes, E_2(high) and A_1(TO), seems also linear to LO. Furthermore, samples of "GaG" series (shown by open symbols) obey the same linear dependences. These observations indicate the strong vibrational coupling between C_N defect and the crystal lattice as expected due to the band modes MC3 and MC4 located in the optical phonon band.

Vibrational modes of C_N defect

Similar to TC modes, Raman signals are observed starting from 3.2×10^{17} cm^{-3} (two peaks MC1 and MC2 are visible relative to the reference sample (dashed line) in Figure 6.13 (a)). For longer wavelength (out of the resonance condition) the drop of the method sensitivity

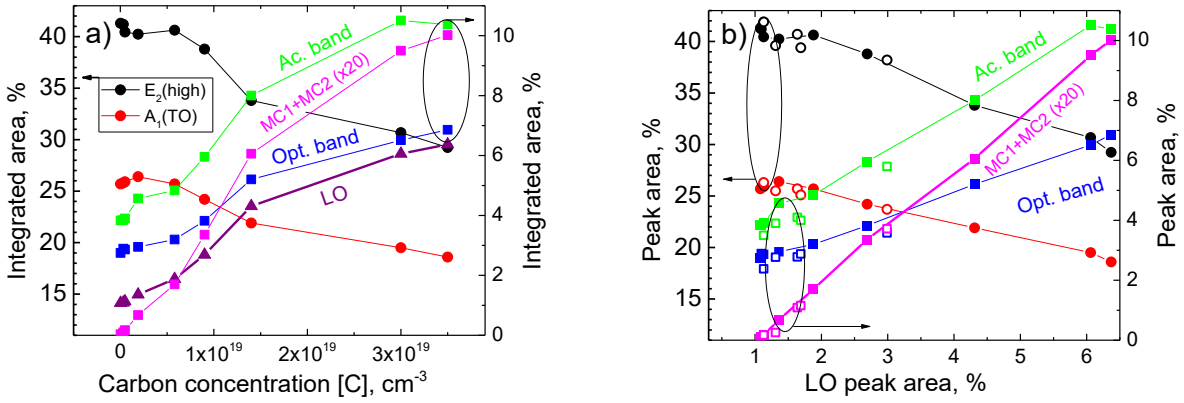

Figure 6.12. (a) The peak area normalized to the integral intensity in the range 150 – 1535 cm^{-1} (100%) for 2.81 eV excitation in x(yy)x geometry. (b) the same data as a function of LO peak area. Filled and open symbols correspond to "GaN" and "GaG" sample series, respectively. The areas "Ac. band" and "Opt. band" are integrated in the ranges 150 – 325 and 585 – 710 cm^{-1}, respectively. The sum intensity (MC1+MC2) of mono-C defect is reproduced in modified scale.

[1] Corresponding integration ranges are A_1(TO): 508 – 549 cm^{-1}, E_2(high): 549 – 590 cm^{-1}, ac. band: 150 – 325 cm^{-1}, opt. band: 585 – 710 cm^{-1}, and LO: 710 – 757 cm^{-1}.

[2] An example of the overtone mode is the peak 410 cm^{-1} in Figure 6.11 (b), while the mentioned second order signals are pronounced above 780 cm^{-1} (Figure 6.11 (a))

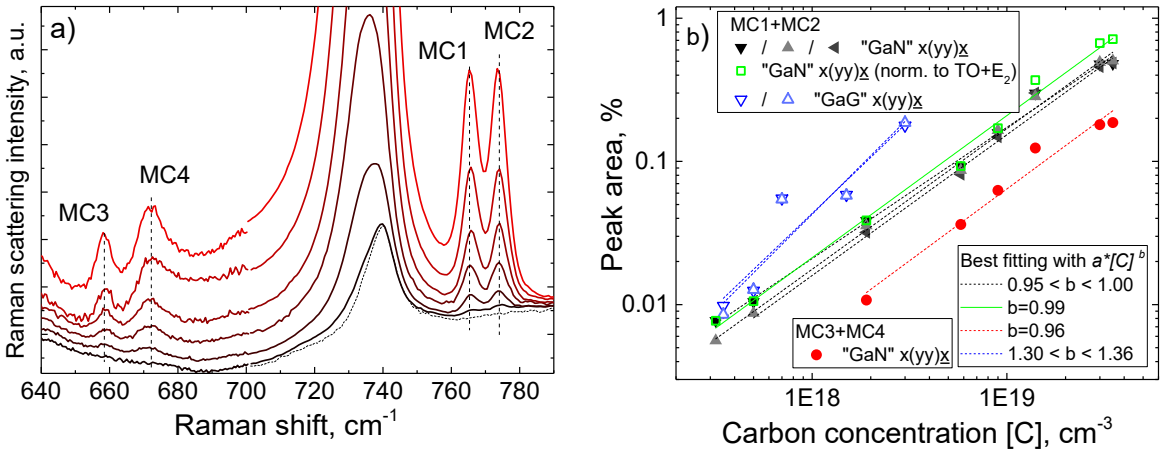

Figure 6.13. (a) Raman spectra of MC1 – MC4 modes at different concentration of carbon [C] at excitation 2.8 eV and x(yy)x polarization and (b) summarized peak area for three independent spectra sets for x(yy)x and z(xx)z polarizations. All data sets indicate sublinear (b<1) dependence of peak area on concentration of carbon for sample series "GaN".

makes it complicated to detect C_N at low [C]. The integrated intensity MC1+MC2 and MC3+MC4 is summarized in Figure 6.13 (b) and approximated by the function $y = a[C]^b$. Different black/grey symbols show the integrated peak area of MC1+MC2 measured at twice x(yy)x polarization and once at z(xx)z at similar conditions. In "GaG" samples (open triangles), signals MC1 – MC2 are in 2 – 7 times brighter presented (measured twice). At this normalization, the approximation shows b in the range 0.91 – 1.00 for the «GaN» series. Thus, one can conclude that in the "GaN" series the fraction of mono-C defects decreases with increasing [C] or holds nearly unchanged. Applying normalization to E_2(high) mode instead of the whole integrated area can contribute to underestimation of b. On the other hand, an overestimation of b can be associated with the influence of light on the charge state of defects at low and medium [C]. Thus, b is not a reliable identifier of the defect fraction in this experiment. In contrast, the parameter $b > 1.3$ for Tri-C defects in "GaN" samples in Figure 6.2 and Figure 6.3 obtained from the FTIR experiment reliably indicates the increase of Tri-C fraction.

The minor modes in Raman spectra

Several weaker signals, DC1, TC2 as well as the second-order MC are found in Raman spectra (Figure 6.14). The spectral curves are presented for samples of "GaN" series. Since not all signals in this range have the identification in ^{13}C-isotope doping, the spectrum of sample C13 is shown. The vibrational nature of peaks TC2 and DC1 is assigned by the isotope mass effect, as was discussed in Chapter 5. The mode marked by "?" has unclear origination, since despite the direct proportionality to neighboring TC2 it shows unclear isotope effect.

The integrated area of TC2, and DC1 are presented in Figure 6.14 (b) by filled symbols for "GaN" series and by open symbols for "GaG" series. The intensity of MC1 mode (first order) is also represented. As was announced, the comparison shows that all defect signals appear brighter in the "GaG" series. It is seen that the slope of TC2 and the trend direction of DC1 differ from one obtained by FTIR experiments (Figure 6.9 and Figure 6.3 (d)). The increase of TC2 now appears at the power $b \approx 1.9$ (for samples with medium [C]), while in FTIR without the UV-Vis excitation it was equal to 1.5 or even lower. The overestimation of b in Raman has the same origin as the photoinduced change in FTIR (Figure 6.9), high b is a result of the TC2 mode disappearance under the light excitation at low concentrations. The data of photo-FTIR

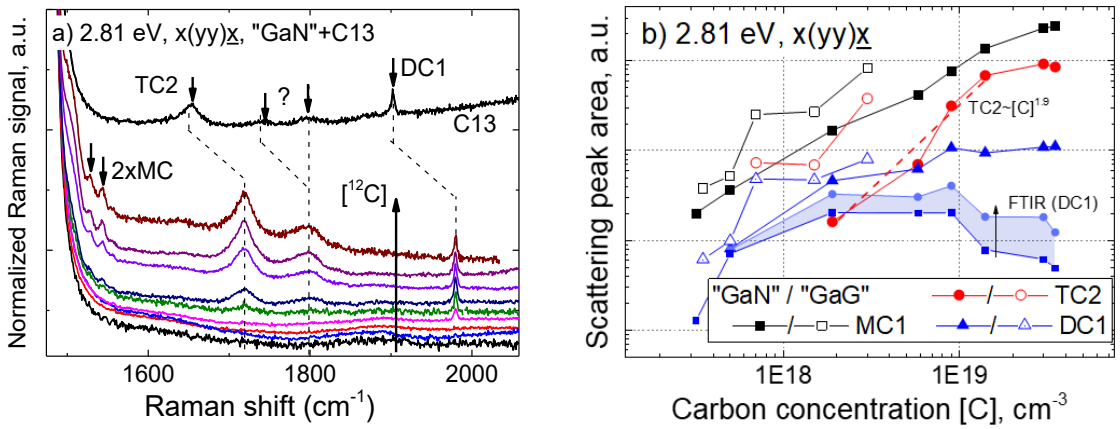

Figure 6.14. (a) Raman spectra of all samples of "GaN" series and the ^{13}C-doped C13 sample. The known carbon-related signals TC2 and DC1 are marked. The second-order of Mono-C modes is labeled by 2×MC. The theoretical maximum isotopic shift is marked by the dashed lines. (b) the integrated area of peaks MC1, TC2 and TC1 in "GaN" and "GaG" sample series (normalized to area 150 – 1500 cm^{-1}). The results of FTIR and photo-FTIR intensity is reproduced for comparison (normalized to GaN005).

for DC1 are reproduced in Figure 6.14 (b). These spectra normalized to the sample GaN005 emphasize the numerical and qualitative difference in the measurements by the Raman and FTIR. The excitation in the photo-FTIR experiment can only partially bring the values of FTIR modes closer to the results of Raman measurement.

To summarize, in this section resonance Raman scattering provided the observation of C_N defects starting from [C]=3.2×10^{17} cm^{-3}, but the comparison of samples should be performed with caution. Only active fraction of the defects (for example, the case of DC1) are detected in the crystal. Therefore, the dependences obtained in Raman differ significantly from those obtained by FTIR.

6.4. UV-Vis absorption and PL

UV-Vis absorption

The main optical characteristics of materials are the absorption and emission discussed in this Section. Raman spectrometer was used to record photoluminescence signals upon excitation of 3.81, 2.81, 2.41, and 2.18 eV. These spectra were not corrected to the system response, therefore, one can expect some shift in the spectral positions of the well-known PL bands.[140]

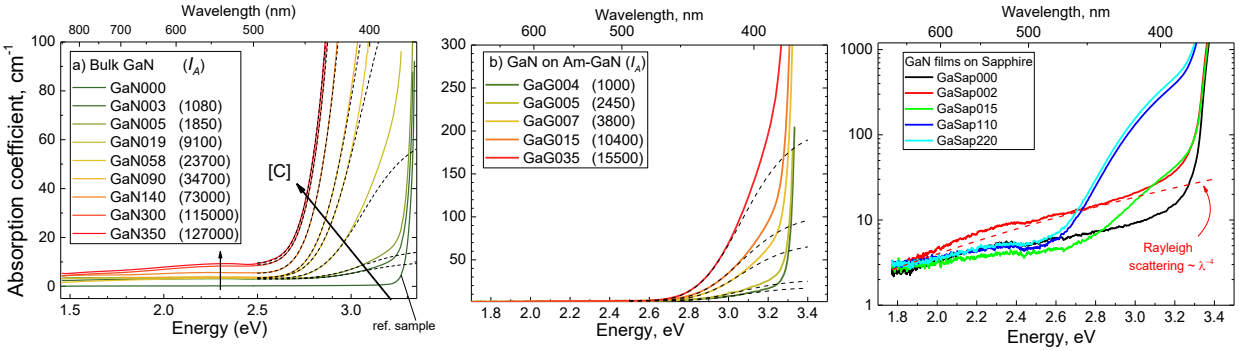

Figure 6.15. UV-Vis absorption spectra at RT for "GaN"(a), "GaG"(b), and "GaSap"(c) sample series. The Rayleigh scattering impact is shown for sample GaSap002. The approximation of the defect-to-band absorption (Eq. (3.15)) is fitted at E_A= 3.0 eV, Γ = 0.22 eV and different amplitudes (I_A) for numerical comparison of the absorption intensity.

The setup described in our earlier work was used for more accurate experiments at the excitation energy of 2.81 eV at RT corrected to the system spectral response.[19] In this article, additional LT measurements of "GaN" sample series can be found.[19] The PL bands are summarized in Table XI.

Figure 6.15 shows UV-Vis absorption spectra of GaN samples of the three series at RT. The bandgap absorption in GaN crystals starts at 3.4 eV.[2,195] The abrupt increase in absorption in the spectral range above 3.4 eV can be found for the reference sample GaN000 (Figure 6.15 (a)) and some thin lightly-doped samples in Figure 6.15 (b, c). All C-doped samples show the defect-related absorption in the range above 2.6 eV. An additional absorption step-like signal starting at 1.8 – 2.0 eV appears at [C] in above 9×10^{18} cm^{-3} in "GaN" series. Figure 6.15 (a) shows "thick" samples (400 - 1200 μm) for which absorption coefficient values below 120 cm^{-1} are investigated. In "thin" (30-50 μm) films "GaSap" on sapphire substrates (light passes through a transparent ~500 um sapphire) and in bulk-like "GaG" samples with thickness of 300 – 500 μm, higher absorption coefficients can be measured (Figure 6.15 (b, c)). "GaSap" films have unpolished as-grown surfaces providing additional significant contribution of the Rayleigh scattering (shown by the dotted line for GaSap002). These thin films were used only here to demonstrate the shape of the UV-Vis bands at high [C] for absorption coefficients well above 100 cm^{-1}.

The shape of the absorption band of the defect-to-band transition is determined by the initial and final electronic states of the system and can be described by Eq. (3.15):[139]

$$\sigma(\hbar\omega) = I_A \int_0^\infty \frac{e^{-(E+E_A-\hbar\omega)/\Gamma^2}\sqrt{E}}{\hbar\omega(E+E_A)^2} dE.$$

Table XI. Parameters of PL peaks in "GaN" samples at LT or RT at different excitation energy (Abs.)

	Defect	PL peak	LT	RT	Abs.	FWHM	[C]
BLc	C_N(+/0)	2.95 eV	-	+	3.8	-	All
BL2	C_N-H_i	3.03 eV	+	-	3.8	-	Low, Mid
YL1	C_N(0/-)	2.16 eV	?	+	2.8, 3.8	0.38 – 0.39	All
YLc	C_N? DC? TC? V_N?	2.11 eV	+	+	2.4, 2.8	0.39 – 0.40	Mid, High
RLc	TC (+/0)	1.60 eV	+	-	2.4 – 3.0	0.29	Mid, High
TCE1	TC (0/-)	1.65 eV	?	+	2.2, 2.4, 2.8	0.30 – 0.32	High
TCE2	TC (0/-)	1.40 eV	?	+	2.2, 2.4, 2.8	0.13 – 0.14	High
GL2	V_N (+/2+)?	2.34 eV	+	?	2.8, 3.8	0.25	Low (Mid)

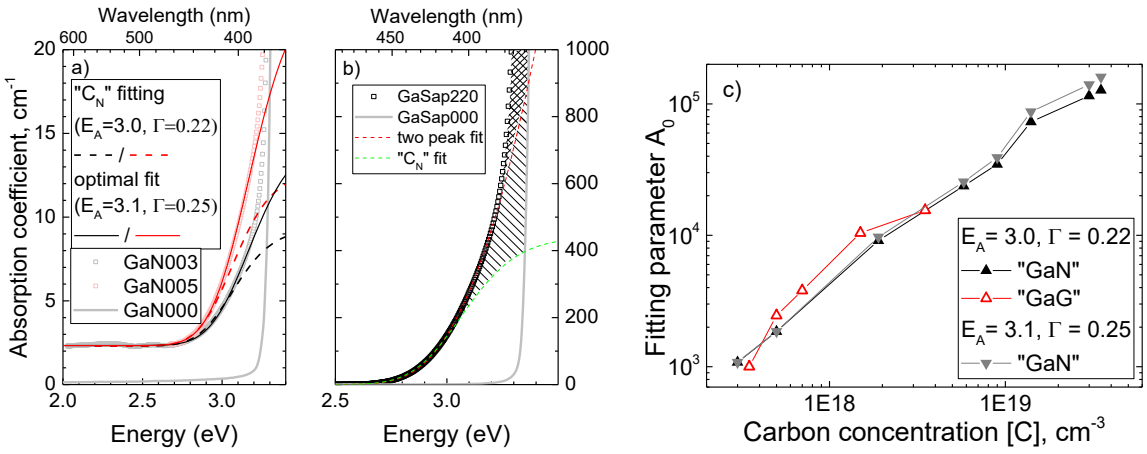

Figure 6.16. (a, b) Fitting of the absorption spectra by model function (Eq. (3.15)) with different parameters. C_N model function is not the best fitting of the absorption spectrum. Summarized magnitude of the absorption signal A_0 at different [C] in samples of "GaN" and "GaG" series.

In the equation, $\hbar\omega$ is the energy of light, E_A determines the spectral position of the band and Γ – is the vibrational broadening parameter.[139] The absorption signals appearing in the samples are too broad for individual analysis but the quantitative evaluation of the absorption intensity (I_A) related to the superposition of all similar absorption bands can be performed. In Figure 6.15 (a, b) the fitting with parameters E_A = 3.0 eV and Γ = 0.22 eV is used for approximation of all spectra following the parameters of the PLE band of carbon related PL signal YL1 (C_N).[140] Since YL1 is observable in our samples, it makes sense to expect this absorption peak to contribute on the absorption spectrum. However, the proposed parameters are not the best and fit the experimental data only up to 3 eV.

As an alternative, the model functions at E_A = 3.1 eV and Γ = 0.25 eV are shown in Figure 6.16 (a) for GaN003 and GaN005. The alternative fitting curve coincides with the experimental points up to 3.2 eV. The same can be obtained using the sum of two different band for the fitting in Figure 6.16 (b) though, such interpretation is too speculative. In fact, change of parameters of the single-function approximation just minorly influence on the relative of the signal intensity in different samples (Figure 6.16 (c)). Approximating the dependence of the absorption magnitude as $I_A \sim [C]^b$ one can find b in the range 1.00 – 1.06 for both cases of the fitting parameters. Since the broad bands cannot be distinguished in the spectra, the UV-Vis absorption has to be complimented by the analysis of PL spectra. It emphasizes the difference between the absorption processes at low and high concentrations of carbon doping.

YL1, BL_C, and BL2 emission bands at above-bandgap excitation

In all C-doped samples, the above-bandgap excitation (3.81 eV) of all "GaN" and "GaG" samples results in appearance of two broad bands in photoluminescence spectra (Figure 6.17). At different power of excitation (given in % of the maximum power), these bands have virtually unchanged spectral positions (the two dashed vertical lines) in all samples GaN003 - GaN350 and GaG003 - GaG035. The small "technical" shift visible at the highest excitation power (when both bands are bright) is associated with the overlapping of the two signals and reproduced in all samples. The scale of spectra GaN003 and GaN300 is hold compatible. The total brightness of the emitted light (including carbon-unrelated near-band-edge (NBE) emission)[19] lose approximately one order of magnitude at an increase of [C] at the same excitation

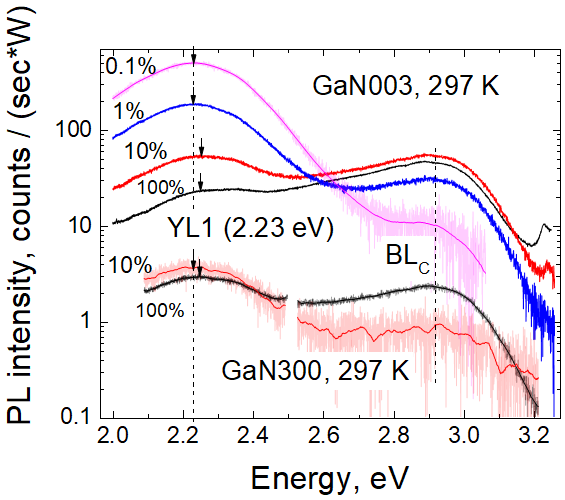

Figure 6.17. Photoluminescence spectra of samples GaN003 and GaN300 at 3.81 eV excitation normalized to the excitation power (in %, shown for each curve) at RT. The PL intensity is in ~2 orders lower in sample GaN300 at the same excitation power. The positions of YL1 (2.23) and BLC (2.96) is the same for the two samples. The small shift at the high power in both samples is reasoned by the overlapping of the two bands. Spectra are not corrected to the system response.

parameters. This effect is most likely associated with the appearance of non-radiative recombination centers at high carbon concentrations.[19] For the two samples presented in Figure 6.17, the PL intensity is in several orders higher at [C] = 3×10^{17} cm^{-3} than at 3×10^{19} cm^{-3} at equivalent conditions of the excitation. In the latest reviews of PL band in GaN, there are two well-described related signals YL1 (2.2 eV) and BL$_C$ (2.95 eV) typical for carbon doped GaN that perfectly suit according to their ZPL position and excitation conditions.[131,140] In the provided spectra, the peak maxima are slightly shifted (2.23 eV and 2.96 eV) since the data were not corrected to the spectral response of the Raman spectrometer.

Consideration should be given to the difference between the two signals, BL$_C$ and BL2 (has maximum at 3.03 eV at the 3.81 eV excitation, LT spectra in Figure 6.18 (a)); latter was also found in some samples of "GaN" series at LT.[19,38] The main difference between BL$_C$ and BL2 is that BL2 prevails at LT and disappears under prolonged irradiation of 3.81 eV,[38,131,189,196] which leads to the appearance of the band peaked at 2.2-2.3 eV.[38] An increase in the excitation power leads, on the contrary, to the appearance of BL$_C$ emission and the disappearance of the YL1 band. With this respect, the pair of peaks in Figure 6.17 is fully consistent with the described behavior YL1 and BL$_C$. The two bands are associated with the primary and secondary ionization of C_N defects.[131] Thus, after the excitation of an electron-hole pair, the recombination path through C_N defects is preferred over other radiation paths of recombination. A much more complex and interesting picture is revealed upon resonant selective excitation of point defects accompanied to the generation of electrons and holes in unequal numbers.

GL2, YL1, and YL$_C$ luminescence bands at below-bandgap excitation

The light at 2.8 eV can be effectively absorbed and re-emitted by samples GaN003 and GaN005 despite the low absorption coefficient (Figure 6.18 (a)). The absorption spectra and the accompanying PL are depicted by the same color. At RT, the emission signal at 2.16 eV (corrected to spectral response) and the absorption band both homogeneously intensify when [C] increases. The PL band at 2.16 eV seems to be the YL1 band due to similar FWHM and the spectral position.[19,38,131,189] Normally, YL1 can be effectively excited by energy above 2.7 eV

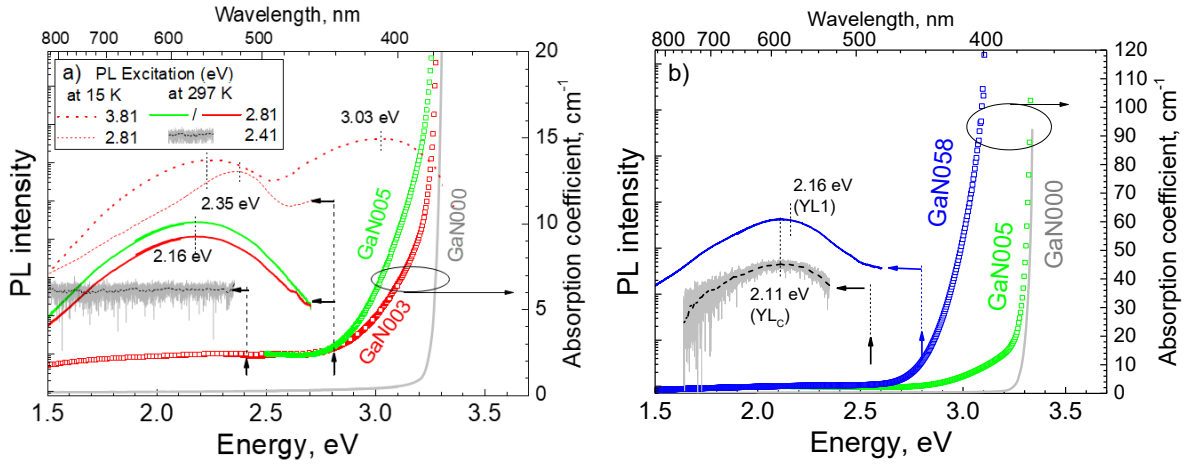

Figure 6.18. The absorption data for samples GaN003 (red), GaN005 (green), and GaN058 (blue) are shown by the square open symbols. By the solid lines of the same color), the RT photoluminescence spectra at excitation 2.81 eV are shown corrected to the system response. The dashed black curve corresponds to uncorrected RT PL spectra of GaN003 (a) and GaN058 (b) at 2.41 eV excitation. The two red dashed curves correspond to corrected PL spectra of GaN003 at 15 K reproduced from our work.[19] The absorption of GaN000 is shown by gray curves.

at low and room temperatures in samples with low [C].[19,140] However, in "GaN" sample series, YL1 is practically could not be observed at LT at all for excitation 2.81 eV since another peak at 2.35 eV (see reproduced LT spectra[19] in Figure 6.18 (a)) dominates in the spectra at low [C] and RL_C PL band at 1.6 eV dominates at high [C].[19] A similar peak at 2.34 eV with the same width (FWHM = 0.25 eV) was earlier recognized as GL2 from V_N defects.[197] It is left questionable why the transition $V_N^{+/2+}$ associated with GL2 at evaluated ZPL ~2.85 eV can be effectively excited in our samples at energy 2.81 eV. Perhaps, due to the prevalence of electrons at 2.81 eV excitation, the positively charged vacancies become more effective centers of emission than neutrally charged C_N. Nevertheless, at RT, the 2.34 eV peak gives way to bright yellow luminescence YL1. On this step, PL identifies at least two different absorption processes at energy 2.81 eV for samples with low [C].

The changes in emission properties are observed at further increase of [C]. The specifics of yellow luminescence band in samples with medium or high [C] is shown by the representative spectra of sample GaN058 in Figure 6.18 (b). In contrast to samples GaN003 and GaN005, the yellow emission band shifts to 2.11 eV in spectra of GaN058 and can no longer be associated with YL1. The shift 0.05 eV between the two yellow bands is better seen in Figure 6.19 (a); the samples there can be divided on two groups. The spectra of samples GaN003, GaN005 and GaN019 containing the YL1 signal seem identical after normalization. Spectra of the three other samples with [C] = 9×10^{18} cm^{-3} and higher show the same redshift of the peak of 0.05 eV. This band is called YL_C in further discussion. The most important factor separating the two bands is that the YL_C band is observed even at 2.41 eV excitation, in contrast to YL1 (cf. Figure 6.18 (a) and (b)). It was shown for GaN that due to internal electric fields, PL bands can shift up to 0.8 eV.[198] A red shift 0.1 eV was also shown for yellow luminescence band.[198] In the described cases, however, the magnitude of the shift depends on the excitation power and other parameters, while Figure 6.19 (a) shows exactly the same peak position for three different samples, which, moreover, does not depend on the irradiation power. Sum up, the appearance of YL_C indicate one more process which should contribute also in absorption spectrum.

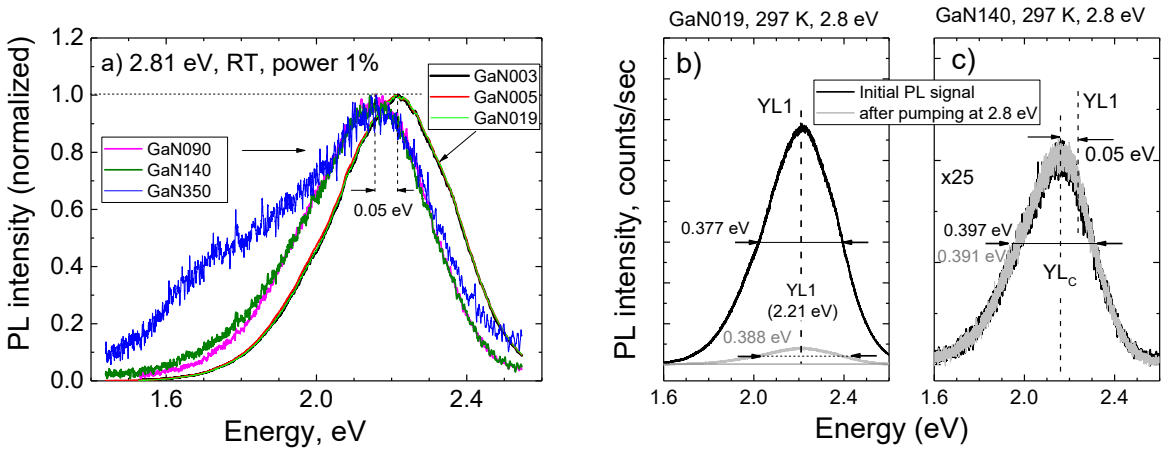

Figure 6.19. PL spectra recorded at 2.81 eV excitation in Raman spectrometer (not corrected) for different samples of "GaN" series at 1% of the excitation power. The saturation of the YL1 band contrasting to the behavior of the band at high [C] is shown. For the first measurement, the laser power was attenuated to 1% by the neutral filter, then the filter was removed for 2 minutes (pumping), returned, and after 30 seconds the second measurement was carried out.

Another important difference YL1 and YL_C can be demonstrated in a simple experiment (Figure 6.19 (b, c)). YL1 band can be suppressed by 2.81 eV pumping in contrast to YL_C band at higher [C]. The PL spectra of representative samples GaN019 and GaN140 were taken at excitation with the neutral density filter (1%). Since these data were not corrected for the spectral response of the system, YL1 is peaked at 2.21 eV.[34,140] The red-shifted peak in GaN140 is located 0.05 eV on the left from the YL1 position. After the first measurement at weak excitation, when the laser was attenuated by the neutral density filter, the samples were irradiated for two minutes without the filter, the filter was returned, and in 30 seconds the measurement with the filter was repeated. The difference between the two curves is significant at low carbon concentrations; the signal decreases by a factor of 7 - 12, while the two measurements of YL_C give identical result. It is possible that the excited carriers here were recaptured by the traps during the pumping. It looks suspicious that the YL_C and YL1 bands have almost the same FWHM; more accurate investigation of the origin of these bands is required.

Red luminescence and YL_C bands at the highest [C]

The YL_C band remains unchanged in GaN350 sample while the two new red luminescence bands appear at 1.65 eV and 1.40 eV. The relative intensity of all three peaks does not change at different excitation power. The two red bands are well approximated by Gaussian curves and can be excited at lower excitation energy 2.41 or 2.18 eV selectively from YL_C. Thus, these two peaks can be associated with the absorption band 2.0-2.5 eV, which is a distinctive feature of samples with the high carbon concentration $[C] > 9\times10^{18}$ cm^3. In our report,[19] we described another red band RL_C at 1.6 eV dominated in these samples at LT. The effective range of RL_C excitation is located between 2.4 and 3.0 eV. This is the fourth absorption process in the range of 2.8 eV.

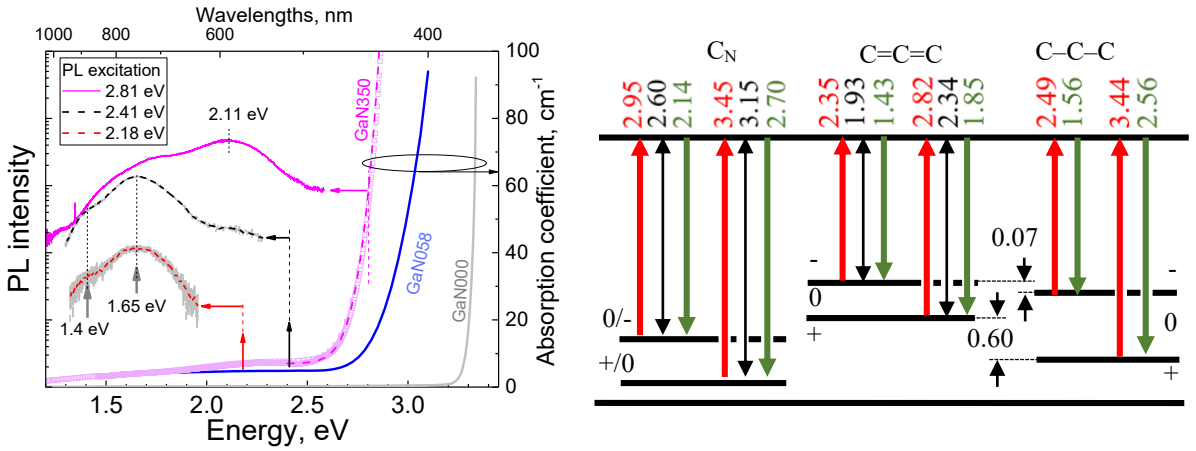

Figure 6.20. The UV-Vis absorption spectra of samples GaN000, GaN058, and GaN350 and the photoluminescence spectra of GaN350 at three different excitation energies. The corrected spectrum at 2.81 eV excitation shows the peak at 2.11 eV (YL1 - 0.05 eV) and the additional shoulder at lower energies. At lower excitation energy 2.41 eV or 2.18 eV (both uncorrected) the two emission lines at 1.4 eV and 1.65 eV are selectively excited. On the diagram, there are absorption (arrows up), emission (arrows down), and ZPL (two-side arrows) energies listed for different charge states of C_N defect[100] (MC1 – MC4), C=C=C defect (TC1 – TC4),[117] and C-C-C defect.[34]

Absorption and emission of tri-C defects

Several emission and absorption bands can be well explained by the tri-C defect model. The configuration C=C=C detected in FTIR has two transition levels in the bandgap, (0/+) and (-/0) distanced from the CB minimum to 2.3 and 1.9 eV, correspondingly (Figure 6.20). The additional C-C-C configuration has the (-/0) level at similar position, but (0/+) level is located 0.6 eV deeper.

The described visible range absorption from 2.0 to 2.5 eV and emission bands of 1.4 and 1.65 eV are found at concentrations above 9×10^{18} cm^{-3}, correlating with the minor TC5 mode. The band of emission at 1.4 eV and absorption at 2.35 eV expected for C=C=C ("-") are in good agreement with the experimental observations. TC5 and TC2 have similar polarizations and could be related to the different charge states of the same defect; however, according to the calculated frequencies (Figure 6.10), the frequency must shift in the opposite direction. With this respect, it is difficult to highlight differences in structure of defects associated with TC2 and TC5. C=C=C ("-") (associated with TC5 or not) is only minorly presented at the highest [C], while C=C=C in its main "0" charge states can originate TC1-TC4 vibrations. This charge state of C=C=C should be related with the absorption band at 2.8 eV that is always presented (but coincides with the absorption of C_N defect)

Excitation of 2.4–3.0, causing emission at 1.6 eV (RL_C) at LT.[19] The +/0 transition level of C=C=C can match this observation taking account additional non-radiative transition to the mediated shallow state of the defect.[19] It can be assumed that at RT the emission of this defect passes through another configuration of the metastable Tri-C with an energy of 2.1 eV (YL_C). The energy of YL_C. lies between 1.85 and 2.56 eV calculated for C=C=C and C-C-C defects, respectively. The difference between the two forms is reasoned by the breaking of one C-N bond with energy benefit of 0.6 eV. Finally, both RL_C and YL_C are found only in samples with high density of tri-C defects ([C] = 5.8×10^{18} cm^{-3} and above).

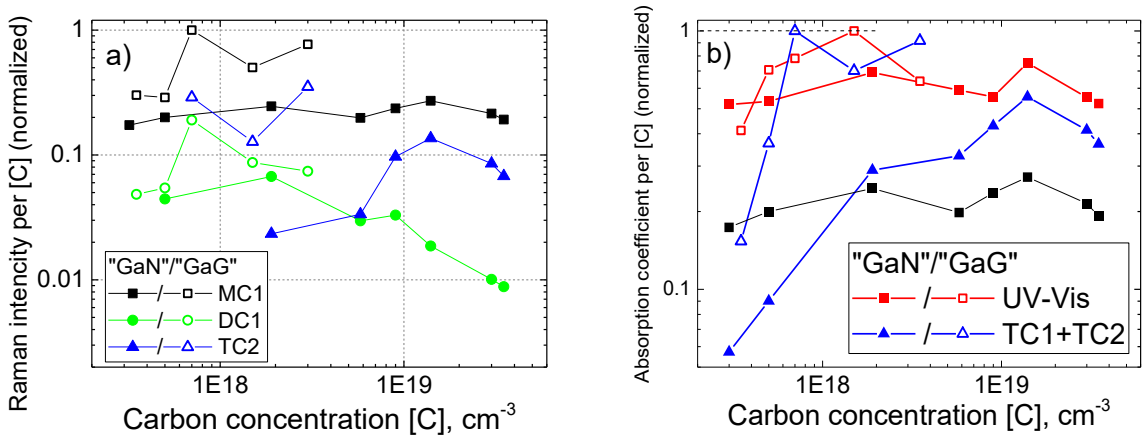

Figure 6.21. (a) Intensity of different vibrational Raman modes normalized to MC1 in GaG007 and recalculated per unit of chemical carbon concentration [C]. (b) Intensity of TC1+TC2 vibrational modes and A_0 amplitude parameter of the model function normalized to values in samples GaG007 and GaG015, correspondingly (recalculated per [C]). MC1 for "GaN" samples is shown for comparison in both windows.

6.5. Summary

The intensities of all detected defect vibrational modes are compared in samples of the "GaN" and "GaG" series with different C concentrations. All C-doped GaN samples contain C_N and tri-C (C=C=C) defects. Most of them contain also C_N-C_i ("+") identified by DC1. Hydrogen prefers bonding with C atoms than with N atoms since C-H bonds are presented in a part of samples at low [C].

All vibrational signatures and the amplitude of UV-Vis absorption recalculated per [C] are several times brighter in "GaG" samples versus "GaN" series (Figure 6.21). This has no unambiguous interpretation and requires further research. It can be assumed that C in GaN samples can be stored in an inactive form. For example, C can saturate various structural defects, such as voids[199] or dislocations, which are expected to be more pronounced in "GaN" samples due to structural imperfections reasoned by heteroepitaxy on sapphire templates. On the other hand, better lattice perfection of "GaG" crystals itself seems another possible reason for more pronounced vibrational properties of the defects relative to the GaN lattice. Regardless of the reason, at the same [C], the optical and vibration processes are more pronounced in samples grown on Am-GaN templates, hence, in this context, such doping is more effective. UV-Vis absorption above 2.6 eV correlates with both C_N and tri-C defects (Figure 6.21 (b)) since all three are proportional to [C]. The significant decrease in most of the signals at concentrations above [C] = 1×10^{19} cm^{-3} can be caused by the appearance of TC5 and DC2 defects (taking own part of C) and related decrease of fraction of C_N and Tri-C defects absorbing in UV range. On the other hand, it can be associated with anharmonic processes detected in Raman scattering in the same range of [C].

It is shown directly that C_N, tri-C C_N-C_i and C-H are sensitive to light excitation or able to capture free carriers from the bands. Simultaneous change of the vibrational modes MC, DC, TC, and CH due to the excitation at 2.72 or 3.22 eV during FTIR experiment (photo-FTIR) indicates the change of configuration and the charge state of these defects. Since the effect has different relaxation times depending on [C], the creation and disappearance of light-induced defect forms cannot be the only reason. The band-mediated charge transfer is proposed to play

a key role in this process. Power- and time-dependences of this effect were measured however, formal theoretical approach is required for complete description of physics in photo-FTIR processes.

In the samples grown on sapphire, the intensity of C_N vibrations (MC1-MC4) increases linearly or weaker with increasing [C]. C_N is probably responsible for the PL bands at 2.16 (YL1) and 2.95 (BL_C) found at room temperature in all samples under excitation above the bandgap. It indicates that C_N provides the predominant path of recombination within other *radiative* recombination processes at equal concentrations of photoinduced electrons and holes. C_N defect also makes a significant contribution to strong defect-related absorption above 2.6 eV, however, at least two other different processes contribute to the absorption at energy 2.8 eV at different [C]. Hence, C_N is not the only defect that forms this broad step-like UV-Vis absorption band.

The analysis of PL bands at 2.8 eV excitation indicates RL_C (1.6 eV), GL2 (2.35 eV), and a new band YL_C (2.11 eV) in addition to 2.16 eV (YL1) emission. YL_C can be excited at 2.41 eV in contrast to YL1 but has a similar FWHM. YL_C is tentatively associated with tri-C defects since appears in samples at [C] = 5.8×10^{18} cm^{-3} or higher when the bright signatures of tri-C defects exist. Accordingly, YL_C and RL_C bands are in good agreement with the tri-C defect in the "0" charge state, which implies that tri-C also can contribute to the absorption band above 2.6 eV at RT. Its vibrational frequencies (TC1-TC4) also correspond to the DFT model of C=C=C (“0”). Since the YL1 and YL_C bands are very similar in shape and clearly anticorrelate, one should think about possible uncounted factors that could lead to an abrupt shift of the YL1 emission band in the part of samples. YL_C has the redshift 0.05 eV relative YL1 band (the same in all samples), and YL1 is much brighter.

The distinguishing features of the absorption and emission are observed in samples at [C] > 10^{19} cm^{-3}. The two emission bands 1.4 eV, 1.65 eV, and the absorption band 1.9 - 2.5 eV agree with the values for “-” charge state of tri-C defect. Another defect appearing at high [C] is C≡C carbon pairs (DC2) but this defect has no theoretical description and its absorption and emission energies are unknown. The intensity of this defect was not changing during photo-FTIR experiments so possibly it does not interact with the light.

Finally, the Resonance Raman technique allowed observations of the modes MC1 – MC4 of C_N starting from low [C] when excited in the range of defect absorption. C_N defects are in strong coupling with the lattice vibrations. At resonance excitation in the range of the UV-Vis absorption, the resonance effect results in the gain not only defect-related modes but also of the intrinsic phonon bands from the whole Brillouin zone. The accurate proportionality of MC1-MC4 with these induced phonon scattering is remarkable.

7. Photochromism in AlN

In previous Chapter, a model of the band-mediated charge transfer in GaN was proposed based on photo-FTIR observations. In this Chapter, the model is considered from a different perspective in AlN. The chapter shows how UV-Vis spectra change under the influence of UV radiation, visible-range radiation, and also at elevated temperatures. The charge transfer model is a good explanation for the observed effects. It should be noted that the behavior of AlN and GaN materials is very similar. In particular, in GaN, as well as in AlN, the light with energy $0.8\times E_g$ induces the change in the visible coloration.[1] On the other hand, it is found that the light with energy $0.8\times E_g$ suppresses the vibrational modes of tri-C defects not only in GaN, but also in AlN. Unfortunately, it was not possible to achieve sufficient lighting density of AlN samples at 4.7 – 4.9 eV *during* the FTIR experiment, as was done for GaN (Sect. 6.2). For this reason, only a few measurements of FTIR in AlN *after* UV irradiation were carried out.

UV-Vis absorption AlN

The large bandgap of AlN crystals (~6.2 eV)[200,201] implies that pure crystals are transparent down to wavelengths of close to 200 nm and have negligible intrinsic conductivity even at high temperatures.[83] One of the problems associated with UV applications of AlN is the strong absorption band at 4.7 eV caused by defects in AlN. This band appears in C-doped samples and has the shape unusual for the defect-to-band optical processes. Despite this, it is often associated to C_N (-/0) transition level.[17,160] V_N is proposed as a partial origin of this multicomponent band in latest works, furthermore, many of other defects have similar positions of energy in the bandgap as was mentioned in Sect. 3.5. UV absorption spectra of AlN crystals with different chemical concentrations of C ([O], [Si] also differ) are discussed below. Since the proportionality of 4.7 eV absorption band and [C] is not observed, one can use the impurity ratio R = ([O]+[Si])/[C] better correlated with the behavior of the 4.7 eV absorption band.

The UV-Vis absorption spectra recoded at RT are shown in Figure 7.1. Here are three groups of samples (three bulk grown crystals AlN-A, AlN-B, and AlN-D). In set of A samples

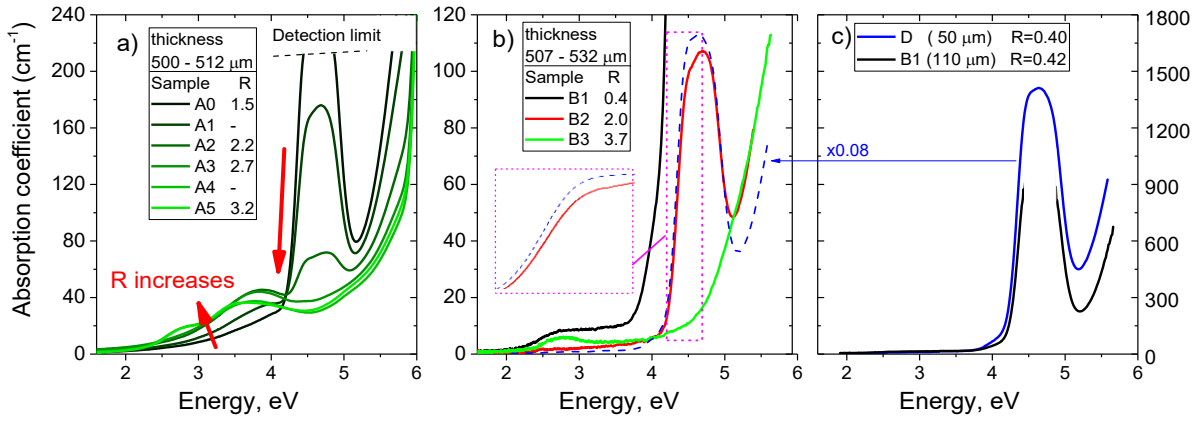

Figure 7.1. Absorption spectra of AlN at RT for E⊥c. (a) spectra of six c- cut wafers from AlN-A crystal, (b) three independent sample areas on the m-cut wafer of crystal AlN-B, and (c) a point on m-cut wafer of sample AlN-D corresponded to the position of the SIMS probe (shown in comparison with AlN-B1). The dashed spectral curve reproduces the spectrum of AlN-D in the modified scale in (b).

[1] The energy $0.8\times E_g$ is approximately 4.9 eV for AlN while for GaN it is ~2.7 eV.

(crystal AlN-A cut to six c-plane wafers) R changes only in the narrow range 1.5 – 3.2, nevertheless, overlapping the range of R when the absorption band at 4.7 eV becomes to manifest. Two extreme cases are shown in Figure 7.1 (b) by the spectra of sample areas AlN-B1 (R = 0.4 <<2) and AlN-B3 (R = 3.7 >>2). They are taken on single m-plane wafer of crystal AlN-B (see Figure 7.2) The third spectral curve is the intermediate case with R = 2 (AlN-B2). Finally, sample AlN-D (thin m-cut of crystal AlN-D) is measured in the area included the SIMS crater. The spectra of AlN-B1 and AlN-D both have R ≈ 0.4 and demonstrate the high absorption α_{UV} >>1000 cm^{-1} at 4.7 eV (Figure 7.1(c)). The m-plane wafers can provide observations of two linear polarizations E⊥c and E∥c discussed below, while for the c-cut wafers of A-crystal, any geometry corresponds to E⊥c. Accordingly, the m-cut samples in Figure 7.1 (b, c) were measured with the additional polarizers to keep E⊥c polarization that also corresponds to measurements of c-plane wafers AlN-A and to the most researches of the absorption.[17,74,202,203]

The 4.7 eV absorption band manifests in A0 – A2[1] and B1 - B2 sample areas with R < 2 with the magnitudes from a few tens to two 1400 cm^{-1}. The absorption bands span close energy range in different samples, however, comparison of the absorption band at 4.7 eV in samples AlN-D and AlN-B2 in Figure 7.1 (b) identify different peak shape of the absorption band at high and low α_{UV}. When R increases, instead of the band at 4.7 eV, several unresolved absorption bands appear in the range below 4.0 eV. Remarkable, that in area AlN-B2 no absorption bands are found (α<5 cm^{-1}) below 4.0 eV so area AlN-B2 appears colorless to the eye. In other samples with R < 2 the absorption provides pale brown visible coloration.

In general, the absorption band at 4.7 eV, usually referred to as "carbon-related", [17,20,21,160] is not proportional to [C], although absorption coefficient values clearly correlate with [C]. This can be seen from comparing A0, A1 and A2, B1,[2] and B2. It is also interesting to compare samples AlN-B2 and AlN-B3: despite the equal concentration of C, only AlN-B2 contains the corresponding band. In this respect, one can have three suggestions that possibly can complement each other. First, not only carbon defects, but different types of defects are responsible for the 4.7 eV absorption band (for example, compensation of C_N by V_N is proposed). Second, carbon doping induces not one but several types of carbon defects in comparable concentrations, but only a few are responsible for the 4.7 eV absorption band. Third, only some of the defects absorbing at 4.7 eV are active at the moment of measurement (e.g., defects change the charge state). For some cases, as will be shown below, at least the third assumption is true. Also, that apparently several different defects originate this absorption band will be demonstrated.

Possible origins of photochromism. Similarity of AlN and GaN

It was found that several absorption bands in AlN and GaN change the intensity under the UV irradiation while the new states of the crystals remain then stable (metastable) at RT. Photos (Figure 7.2) demonstrate the color of samples and the change of coloration due to the prior excitation at 0.8×E_g (4.88 eV) energy. The initially transparent AlN-B2 area and the slightly brownish B3 area become brightly colored brown after irradiation with 0.8×E_g. The

[1] here and below "AlN-" prefix in the sample area name can be omitted for clarity.

[2] Although the absorption maximum for AlN-B1 is not seen, one can estimate it as ~1100 cm^{-1}

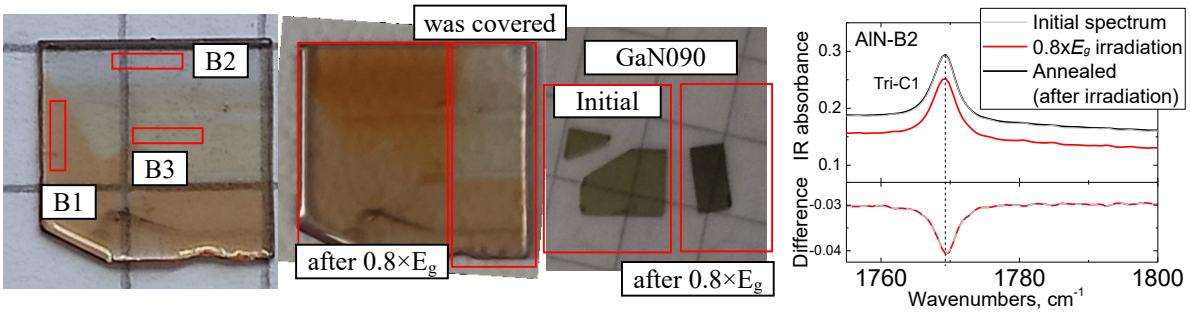

Figure 7.2. The m-cut of crystal AlN-B and the three areas of the optical measurements are shown. The uncovered part of the sample was shined by UV irradiation with energy 4.88 eV ≈ 0.8×E_g that resulted in the change of visible coloration (can hold for many hours). Darkening of sample GaN090 occurs due to the excitation with energy 2.7 eV ≈ 0.8×E_g (disappeared in 2 hours). The unprocessed IR absorbance spectra illustrate the influence of the light on the state of tri-C defect in AlN-B2. In contrast to photo-FTIR of GaN, the light excitation with the 4.88 eV source was performed between the two measurements. The difference of the initial and the irradiated absorption spectra is shown in the bottom. The annealing at 600 K during 2 h returns the absorption spectrum with signal of tri-C defect to the initial intensity.

difference between the pale brownish, dark brown areas and induced brown coloration, as well as the invisible UV-range changes will be discussed in detail below. It is noteworthy that GaN exhibits a similar but less stable darkening effect of the sample after irradiation 0.8×E_g (2.81 eV). The image shows that the irradiated part of the sample GaN090 is darker than the unexcited piece. This additional coloration practically disappeared in 2 hours at RT (possibly, one can stabilize the excited state at lower temperatures). Undoubtedly, the induced optical absorption in GaN requires a more detailed study, which, nevertheless, remains outside the scope of this work. It is the stability of the induced coloration in AlN that makes it possible to call this effect Photochromism that can be measured reliably and reproducibly at RT.

The origin of the effect can be different in organic materials and in crystals. Classically, in the organics, photochromism is related to some metastable states of molecules. Similarly, metastable color centers ("F centers") in alkali halides are the classical example of photochromism in crystals.[204] Furthermore, photochromic effects are found in a large variety of other crystals such as CaF_2, GaN, $SrTiO_3$, and synthetic diamonds.[205–211] The key feature of photochromism is the stability of the induced properties even after the radiation ended, which can be caused by two different reasons: (i) physical change of the defects due to irradiation, i.e. the light-induced dissociation of defect complexes or strong local lattice relaxation (including light-induced re-bonding) as proposed earlier for GaN[205,206] or fluorides,[207,208] and/or (ii) change of the defect population, e.g., *the band-mediated charge transfer* between defects as proposed for synthetic diamonds[209] or $SrTiO_3$[210,211].

The first study of photochromism in AlN (as ceramic) dates back to 1992,[212] in which the authors suggested that the creation of UV-induced meta-stable states for V_{Al}-O_N would give rise to a change in absorption and emission. However, this Chapter shows that photochromism in AlN originates from *the band-mediated charge transfer* which results in a changed (meta-) stable population of ordinary point defects. With this respect, in the case of AlN, photochromism allows determining the Fermi level and the active defect levels in the bandgap. The observed effects are significant and should be accounted for in the development of optical devices.

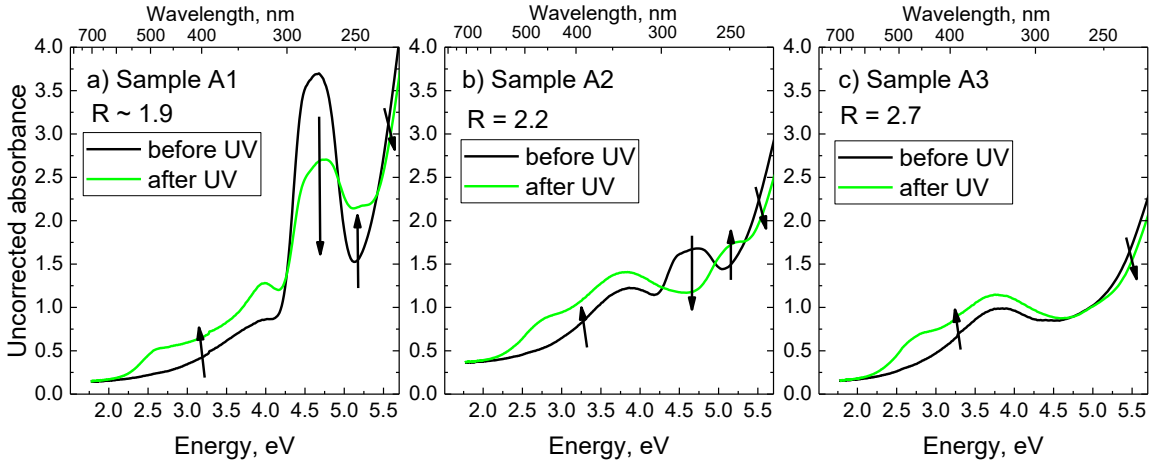

Figure 7.3. Photochromism of samples AlN-A1, AlN-A2, and AlN-A3. The two spectra are taken before and after intense radiation at 4.66 eV for each sample.

7.1. Photochromism in AlN-A and AlN-B samples

UV-Vis spectra of photochromic samples

Pronounced photochromism appears in sample areas A1-A3 (Figure 7.3), and in AlN-B2 (Figure 7.4). In these areas the absorption coefficient changes from the initial values (black spectral curves) to the meta-stable (stabilized) values induced by the excitation (green curves). The lifetime of the induced changes depends on the sample. In A1, A2, and B2 areas, the absorption coefficients change only a few percent per day and the visible difference of coloration can be found even in a few weeks after the UV irradiation at 4.66 eV (or 4.88 eV). In areas A3, A4, A5, and B3 the effect also appears, but it is not stabilized and vanishes at RT in the next several hours. Areas A0 and B1 show just little changes of the absorption spectra detectable no longer 1 hour. Thus, the most pronounced and stable effect is found in AlN with the intermediate donor-to-acceptor ratio R close to 2.

Optically induced absorption and optical restoration of the initial state

As the sample was highly excited with the energy of 4.7 eV, the accompanying decrease of absorption coefficient in this spectral range can be called absorption saturation. For example, in Figure 7.4 the absorption coefficient α decreases approximately two times, from 115 to 60 cm^{-1}. At the same time, the induced absorption bands appear below 4.2 eV in sample area AlN-B2. It may seem that there is a direct connection between the appearance of bands in the visible spectrum and the disappearance of the UV band at 4.7 eV, however, this connection is mediated. Similar bands in the visible range can be observed in areas A1-A3 in Figure 7.3 but in sample area AlN-A3 the intensity of the visible absorption grows despite the complete absence of the band at 4.7 eV. Thus, the observed effect is more likely to be related to general material properties or processes than to one specific type of point defects.

Figure 7.4 shows several stabilized absorption spectra taken in area AlN-B2 after different given dose of UV irradiation. The spectral curve taken prior to the irradiation (RT equilibrium population of defects) corresponds to the maximum α_{UV} at 4.7 eV (black curve). After

long irradiation under intense UV laser light, α_{UV} reaches its minimum (green curve).[1] The intermediate curves illustrate a similar but weaker influence of the UV-line of Hg-lamp with lower power density. The dose of the UV irradiation was step-by-step accumulated from 5 to 80 minutes. With the accumulation of the UV irradiation dose, the change in transmittance (or absorption) was monotonically enhanced in the whole observed spectral range and gradually approached saturation.[2]

When the irradiation is off, the induced values of the absorption coefficient change only a few percent per day, though, the states are meta-stable at RT. However, faster and complete restoration of the initial absorption spectrum can be accomplished in two ways: with annealing and with intense irradiation in the range of 2 – 4 eV. Figure 7.4 (b) shows the absorption spectra of sample during the optical restoration. LED source with the nominal power 50 mW and wavelength 340 nm (3.64 eV) was used. The different curves correspond to different duration of the restoring irradiation with the LED. From first seconds, the AlN crystal begins to restore the initial absorption spectrum as is shown with the dark area. The restoration seems to proceed with conditionally proportional changes in different spectral ranges. In the absence of the restoring irradiation between the steps, the absorption spectra did not change and crystal was irradiated again for the further restoration. By this way, after 180 sec of the accumulated irradiation dose, the spectra are restored to the state undistinguishable with the initial one. Several tested souses of intense irradiation in the range from 2–4 eV provided similar monotonic and proportional restoration (the tested energies are shown in Figure 7.4 (b) under the spectral curves).

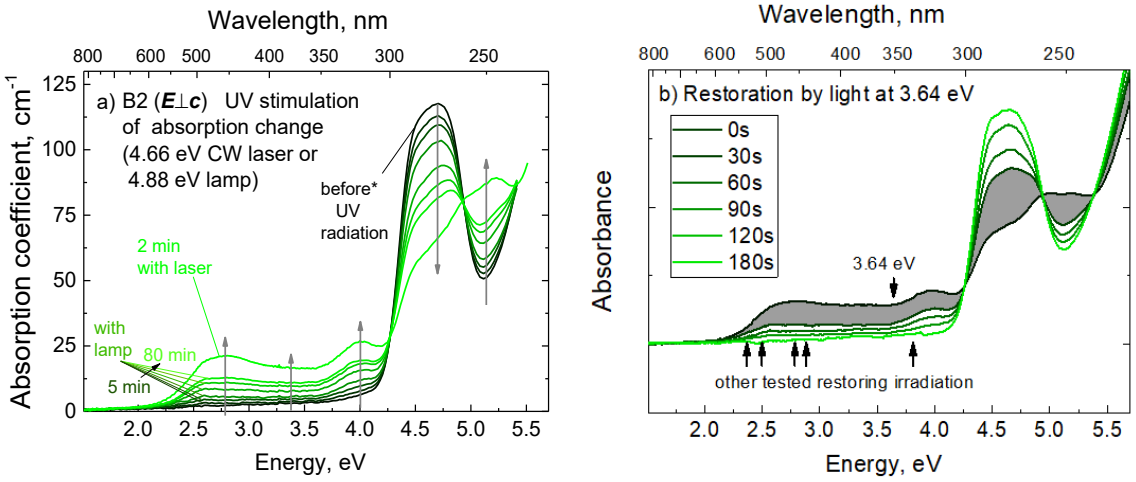

Figure 7.4. (a) Stimulation of the absorption change (photochromism) in area AlN-B2 by UV irradiation (2 min of the CW laser at 4.66 eV or 5-80 min of 4.88 eV Hg-lamp). (b) Complete restoration of the initial spectrum by the excitation in the range below 4 eV. The spectra shown for 3.64 eV (50 mW) radiation (different wavelengths tested)

[1] The continuous-wave (CW) laser excited the sample during 2 minutes at 266 nm (4.66 eV).

[2] The dose of irradiation with the Hg-lamp UV-line at 254 nm (4.88 eV) is proportional to the duration of the illumination. The duration of all previous steps is counted as there was no restoration of the initial state between the steps; the duration of each next step of irradiation also increased (5, 5, 10, 20, 20, 20 minutes)

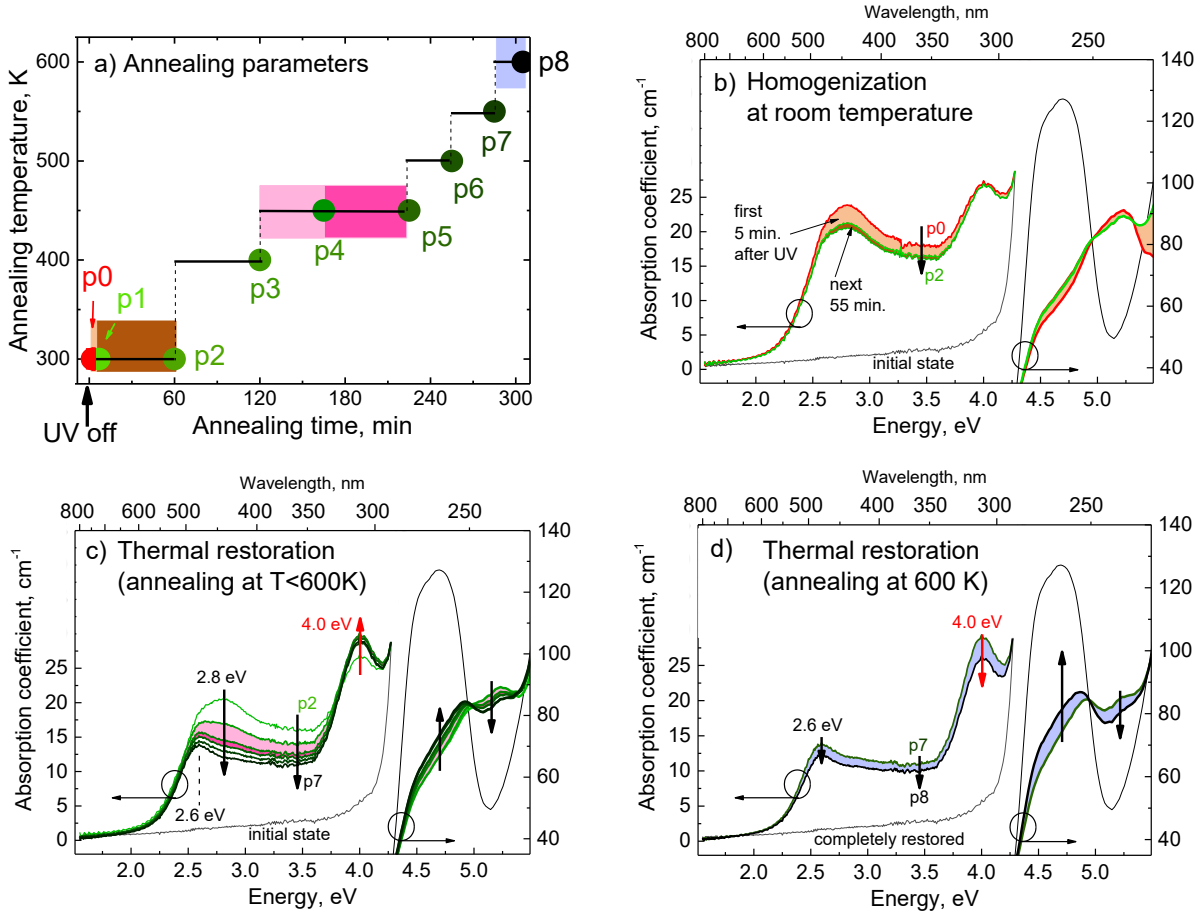

Figure 7.5. Restoration of the initial state by thermal annealing. (a)The time and temperatures of the annealing steps are shown in the insert. (b - d) Spectra p0 – p8 measured after completion of the respective successive annealing step. The filled color areas demonstrate the change of absorption between steps. All spectra are measured for E⊥c polarization after the cooling of samples to RT.

Thermal restoration of the initial state

More complicated changes of the absorption spectra were found during the annealing at different temperatures. Duration and temperatures of annealing steps are shown in Figure 7.5 (a). Measurements after each step from p0 to p8 are shown as absorption spectra of individual color in Figure 7.5 (b-d). The spectral curve with the highest α_{UV} at 2.8 eV (red curve p0 in Figure 7.5 (b)) corresponds to the measurement immediately after the UV irradiation, and the light-brown adjacent area (p0 – p1) indicates how the absorption changes in the dark during the first 5 minutes after the UV irradiation. This first-minutes change, likely due to homogenization and equilibration, is not discussed in this work. After this rapid effect, further measurements at RT do not reveal significant changes; the corresponding minimal difference in the absorption spectra taken 5 minutes (p1) and 60 minutes (p2) after the UV irradiation at RT is shown by the narrow dark-brown area.

The changes upon further annealing strongly vary for different spectral ranges and different temperatures. The band at 2.8 eV disappears first at 450 K annealing (the two pink areas in Figure 7.5 (a, c) between p3 and p5), the peak of absorption shifts to 2.6 eV. These observations allow us to differentiate the bands 2.6 eV and 2.8 eV. Behavior of the induced absorption band at 4.0 eV draws attention. The restoration of this induced absorption band begins only at

600 K annealing (the blue area between p7 and p8) but at lower temperature, even in 120 minutes after the UV excitation, it still increases (see, e.g., p2 and p3 in Figure 7.5 (c)). Obviously, the growth of this band cannot be associated with the direct influence of UV light on the related defect. Only at higher temperatures, all photochromic changes, including the band at 4.0 eV, are clearly restored to the initial state.

Identification of defects by polarized UV-Vis absorption

Additional polarization measurements are performed for reliably identification of the defects involved in the photochromism. In fact, the polarization degree is a constant for some particular initial and final electronic states. In the case when the individual absorption bands are observed independently, the polarization spectra contain information about the electronic states, and hence, molecular symmetry of an involved defect can be clarified. In the present work, the overlapping of absorption bands of different optical transitions with different polarization properties is observed. With this respect, I reason only comparison of the polarization properties from different areas of the AlN crystal in order to emphasize the similarities and differences in the defect composition.

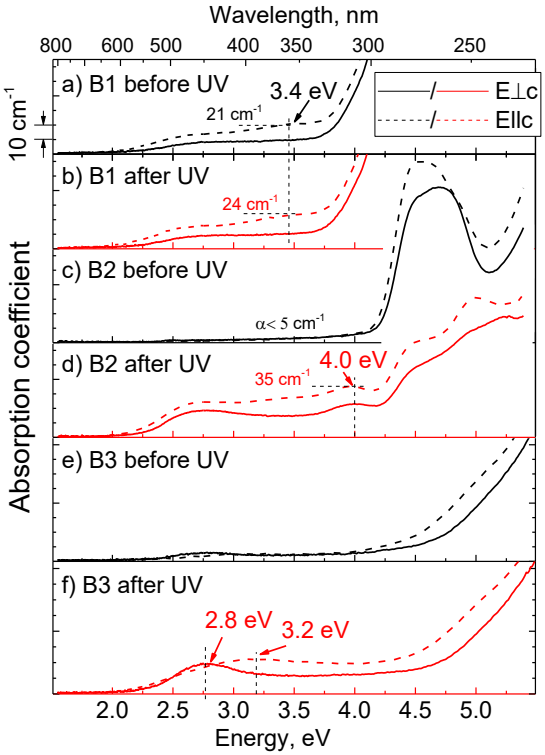

Figure 7.6. The absorption spectra before (black lines in a, c, e) and after (red lines in b, d, f) the UV irradiation for areas B1- B3 for two polarizations of light: E⊥c (solid lines) and E∥c (dashed lines). The scale mark "10 cm^{-1}" is relevant for all absorption spectra.

In , the absorption spectra at E⊥c and E∥c are shown in Figure 7.6 for areas B1 – B3 before (a, c, e) and after (b, d, f) UV irradiation. The bands peaking at 2.8, 3.2, 3.4, and 4.0 eV are marked for different areas and listed in Table XII with the other bands. Further analysis of the polarized absorption is illustrated in Figure 7.7 to provide a clear numerical comparison of the experimental data. Figure 7.7 (a) shows original absorption spectra decomposed to three Gaussian peaks with similar polynomial background line for both polarizations. The peak parameters are provided in the insert. The degree of polarization (DOP, Figure 7.7 (b - d)) and the change in transmittance (CIT, Figure 7.7 (e, f)) are calculated from original spectra in .

The absorption spectra above 4.3 eV for area AlN-B1 with the strong 4.7 eV band could not be measured even after the thinning down of the sample; thus, the DOP curves are also not available. That is why it is replaced by the DOP data from AlN-D with similar impurity ratio and UV absorption properties. The UV-induced changes in area AlN-B1 are negligible and unstable (disappear within ~30 - 60 minutes after the irradiation ended). Apparently, the sample cannot be significantly changed by UV irradiation. One explanation might be that due to the low penetration depth (below 10 μm) for 4.7eV radiation at high $\alpha_{UV} \approx 1000$ cm^{-1}, the defects

in the bulk volume remain largely unaffected: actually, gradual absorption changes appeared in a similar sample after X-ray irradiation that were meta-stable (did not change after 2 weeks under ambient conditions).[20] The change of the sample coloration in AlN-B2 could be visible even in one week after UV-irradiation. Though, the changes in area B3 disappear in several hours after UV, they are strong and comparable with the magnitude of effects in area AlN-B2.

Comparison of DOP curves for sample areas AlN-B1 and AlN-B2 is provided in Figure 7.7 (c). DOP of AlN-B2 is shown before UV irradiation, 5 min after (p1), and after the last step of the restoring annealing at 600 K (p8 in Figure 7.5). In the spectral range above 4 eV, both samples demonstrate similar positions and magnitudes of the minimum (at 4.3-4.4 eV) and the maximum (at 4.9 eV) of the DOP curves despite clearly different impurity (defect) concentrations in the samples. In accordance with the two highest peaks from the Gaussian approximation in Figure 7.7 (a), one distinguishes the low-energy and the high-energy halves of the complex "carbon-related" absorption band centered at around 4.5 eV and 4.8 eV, respectively. These components are attributed to different defects and discussed separately. Although at least three peaks are required for adequate fitting of both polarized spectra (E⊥c and E∥c), I avoid further separation of the peaks as the proposed model is conditional. The 4.5 eV peak prevails for E∥c polarization when the 4.8 eV peak is depolarized or demonstrates a weak E⊥c polarization (DOP can be distort by overlapping with E∥c-polarized bands).

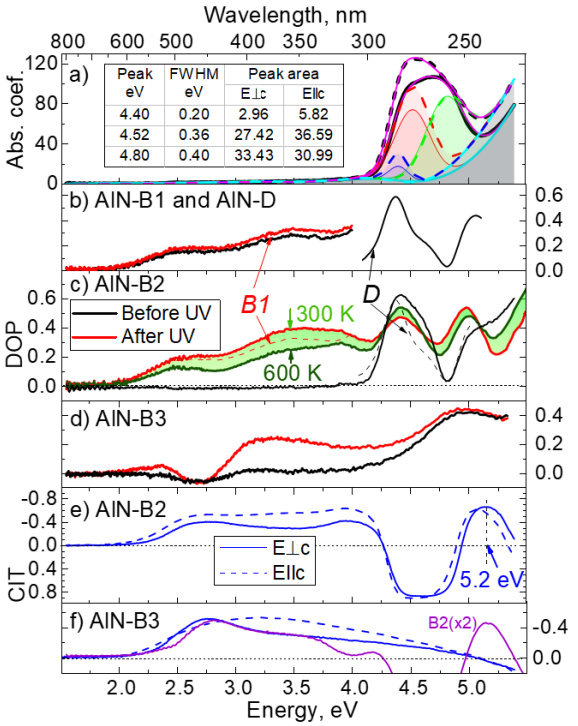

Figure 7.7. (a) The multi-component Gaussian fitting of the absorption band at 4.7 eV indicates the three peaks for E∥c and E⊥c polarizations (parameters are listed in the insert). (c – d) The degree of polarization (DOP) for areas B1, D, B2 and B3 before and after UV irradiation. (c) spectra include the data of samples B1 and D for comparison. Additionally, the change of DOP after the last annealing step (p8) of AlN-B2 area is shown by the green area and the spectral curve. (e, f) The change in transmission (CIT) due to UV irradiation for areas B2 and B3 is shown for polarizations E⊥c (solid lines) and E∥c (dashed lines). CIT of area B2 based on spectral curves p1 and p5 (E⊥c) is show in (f) doubled in magnitude.

The most important observations are done in the spectral range below 4 eV. The DOP curves for areas B1 and B2 coincide in this range. The partial thermally induced restoration does not change the characteristic two-step shape of the DOP curves significantly (marked green area). Thus, the absorption spectra provide reasonable evidence that the absorption at 2.0 – 3.8 eV in areas B1 and B2 is of the same origin. With this respect, one can make a simple conclusion that the main defects associated with the absorption below 4.0 eV are the same in B1 before and in B2 after the UV irradiation and appear at a comparable proportion. In area B2, the DOP decreases due to the annealing and the induced absorption also decreases, however, the curves preserve their characteristic form, and the spectrum remains very close to the DOP of the sample area B1. Then, the further annealing or the restoring irradiation changes the defects in area B2, but not in B1. Thus, the structure of the involved defects is resistive to these influences and cannot be damaged by UV or elevated temperature. Likewise, it is not born of UV exposure as

exists in B1 even before the UV irradiation. The same conclusion is supported by the observations of the growing band at 4.0 eV in 2 hours after UV excitation Figure 7.5 (c)

Finally, Figure 7.7 (f) visualizes CIT for area AlN-B3 for two polarizations. The comparison of CIT at E⊥c with one in sample area AlN-B2 after annealing at 450 K (spectra p1 and p5 in Figure 7.5) indicates appearance of the same induced band 2.8 eV in both samples. The small differences between the two curves at ~2.5 eV are reasoned by the influence of yet unchanged induced band at 2.6 eV in sample AlN-B2.

Summing up, the behavior of the absorption bands and unambiguous appearance of the same absorption signals due to the doping conditions but not only due to UV-excitation excludes the origination of the changes due to the metastable defects. I find the explanation of the observed phenomena in the *band-mediated charge transfer* discussed below. With this model the defects in the bulk material can manifest with different properties since the transition of the charge carriers between defects induces several remote defects to be in the stabilized charge state different with the initial one.

Table XII. Absorption peak positions and spectral ranges as observed in areas AlN-B1, AlN-B2, AlN-B3, probable optical transition type (see Figure 7.8), existence of the band and variation of its intensity before and after UV irradiation, respectively, DOP, and effective annealing temperature T for complete restoration.

Peak, eV	Type	Area	Before UV or after restoration	After UV	Spectral range, eV	DOP	T, K
2.6	$E_{Vis}(D1)$	B1	Yes*	Unchanged*	2.1–3.0	~ 0.1	
		B2	No	Appeared	2.1–3.0	~ 0.1	500-600
		B3	No	Not present	-	-	-
2.8	$E_{Vis}(D2)$	B1	No*	Unchanged*	2.2–3.2	-	300
		B2	No	Appeared	2.2–3.2	~ 0*	400-450
		B3	Weak	Amplified	2.2–3.2	~ -0.10	400-450
3.4	$E_{Vis}(D1)$	B1	Yes*	Unchanged*	3.0–3.6	~ 0.35	-
		B2	No	Appeared	3.0–3.6	~ 0.35	450-600
		B3	-	-	-	-	-
3.2	$E_{Vis}(D2)$	B3	Yes	Amplified	2.0–4.5	~ 0.30	-
4.0		B2	No	Amplified	3.8–4.2	< 0.30	600
4.5**	$E_{UV}(D1)$	B1	> 1200 cm^{-1}	Too intense	4.1–4.8**	-	-
		B2	~ 120 cm^{-1}	Attenuated	4.1–4.8**	> 0.50	500-600
		B3	No	Not present	-	-	-
4.8**	$E_{UV}(D1)$	B1	>1200 cm^{-1}	Too intense	4.5–5.1**	-	
		B2	~ 100 cm^{-1}	Attenuated	4.5–5.1**	~ 0.0	500-600
		B3	No	Not present	-	-	-
5.1	$E_{ind}(D1)$	B2	-	Amplified	5.0–5.4	< 0.2	450-600

**The UV-induced absorption change is negligible and restores at room temperature.*
***from the Gaussian Fitting in Figure 7.7 (a)*

7.2. The band-mediated charge transfer model

Charge exchange diagrams

The model of band-mediated charge transfer between defects D1 and D2 is shown in Figure 7.8. In the specific example shown in Figure 7.8 (a), an electron which initially belongs to defect D1 is being excited by $E_{UV}(D1)$ and then transferred via the conduction band to another remote unoccupied defect (D2).[1] Analogously, the transfer of a hole is possible via the valence band (excitation $E_{UV}(D2)$) and leads to the identical result. The possibility of the transfer implies the absence of immediate recombination of the UV-excited carriers to their initial states (on D1 or D2). On the contrary, the carriers, driven by Coulomb interactions or due to Brownian motion, reach the remote defect that can capture the electron (or hole) effectively.

The change of the D1 and D2 population influences the optical properties. In thermodynamic equilibrium, the Fermi level (E_F) determines the initial charge states for defects D1 and D2 as i and j, respectively. In the most general case, the range of the charge states of D1 and D2 spans from (i-1) to (i+2) and from (j-2) to (j+1), respectively, thus, four absorption bands are possible in the equilibrium before the UV irradiation, these transitions are shown by arrows labeled E_{UV} and E_o in Figure 7.8 (a, b). The number of defects, D1 and D2, in the initial charge states and the related UV absorption both decrease due to the UV irradiation ($E_{UV} \approx 4.7$eV). In contrast, the UV irradiation leads to an increase of population for the nonequilibrium charge states i+1 and j-1 and the related absorption in the visible range ($E_{Vis} \approx 2 - 4$ eV) and UV range ($E_{ind} > E_{UV}$). Thus, another four absorption transitions labeled E_{Vis} and E_{ind} can be active for the non-equilibrium population.

The diagrams in Figure 7.8 (c, d) illustrate the restoration process of the AlN crystal with 2–4 eV irradiation or due to annealing at elevated temperatures. Transitions labeled E_{Vis}

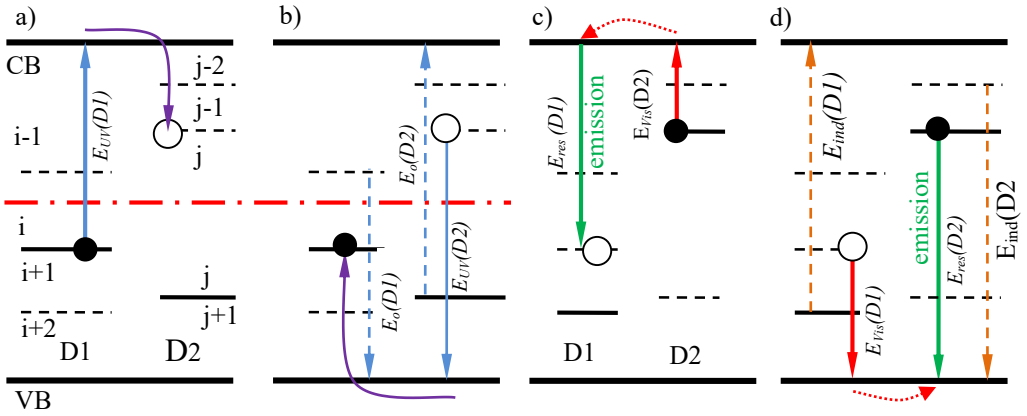

Figure 7.8. Energy diagrams for the CB-mediated (a) and VB-mediated (b) charge transfer caused by the UV irradiation (with E_{UV} energy). In general, four different absorption processes could appear for D1 and D2 (blue arrows E_{UV} and E_o) in their initial charge states i and j. The equilibrium defect population is shown schematically by E_F (the states below E_F are occupied by electrons, and above E_F are occupied by holes). Diagrams (c) and (d) show four other absorption processes available at non-equilibrium population after the UV irradiation (arrows E_{Vis} and E_{ind}), when defects D1 and D2 are in the charge states i+1 and j-1. Here, D1 and D2 can be excited thermally or optically (arrows E_{Vis}) to initiate the thermal or optical restoration via CB-mediated (c) and VB-mediated (d) reverse charge transfer. Emission E_{res} with energies higher than the absorbed energy E_{Vis} is possible during the restoration.

[1] I.e., D2 is initially occupied by a hole

initiate the reversed carrier transfer and return the system to its initial state. Optical activation of these transitions in the experiment is possible by excitation in the range of 2 – 4 eV. If the related defect levels are not very deep, the defect can be also ionized thermally. The processes of restoration can promote emission/luminescence (arrows $E_{Res}(D1)$ and $E_{Res}(D2)$) at energies even higher than the optical excitation energy. Perhaps, such emission was observed by Okada et al. after X-Ray/UV irradiation of AlN ceramic samples[213–215] or by Spiridonov et al. after UV irradiation of high-oxygen AlN.[216]

Summing up, the behavior of the absorption bands and unambiguous appearance of the same absorption signals due to the doping conditions but not only due to UV-excitation excludes the origination of the changes from the metastable defects. I find the explanation of the observed phenomena in the band mediated charge transfer discussed below. With this model the defects in the bulk material can manifest with different properties since the transition of the charge carriers between defects induces several defects to be in the stabilized charge state different with the initial one.

7.3. Absorption bands in AlN

Table and diagram of absorption processes in AlN-B2

Below, there is a brief description of absorption bands appearing after the UV irradiation in area B2 and proposed suggestions to the origin of the absorption. The defect levels and the optical transitions are visualized in Figure 7.9. The blue arrows (4.5 and 4.8 eV) illustrate the processes of the original absorption in the sample area before the UV irradiation, and the orange arrows (2.6, 2.8, 3.4, and 4.0 eV) correspond to the UV induced absorption bands. The charge transfer via CB and VB is shown schematically accompanying the absorption changes at different temperatures.

2.8 eV absorption band

The 2.8 eV induced absorption band reverts back to the initial state at lower temperatures (400 K) compared to the other bands in area B2 (p3 in Figure 7.5 (c)). The related optical transition is assumed to take place from electron-occupied defect states in the upper half of the bandgap, as the high [O] (R=3.7) as expected, results in a high position of the Fermi level due to prevalence of donor-like O_N defects (see e.g. [168]). The band has been earlier reported to be polarization-dependent in oxygen-dominated samples and its intensity correlates with high oxygen concentrations.[74,85,158,217] From the absorption peak energy and the temperature of the thermally-induced restoration, the position below CB is estimated to be 1.0 – 2.5 eV and 1.0 – 1.2 eV, respectively. Thus, both thermal and optical activation of the state can be associated with the same defect level, only if this value is roughly close to 1 eV. The O_N defect in the DX-configuration corresponds well and can explain the large values of FCS energy equal to 1.8 eV. However, the “same defect” assumption requires further experimental evidence.

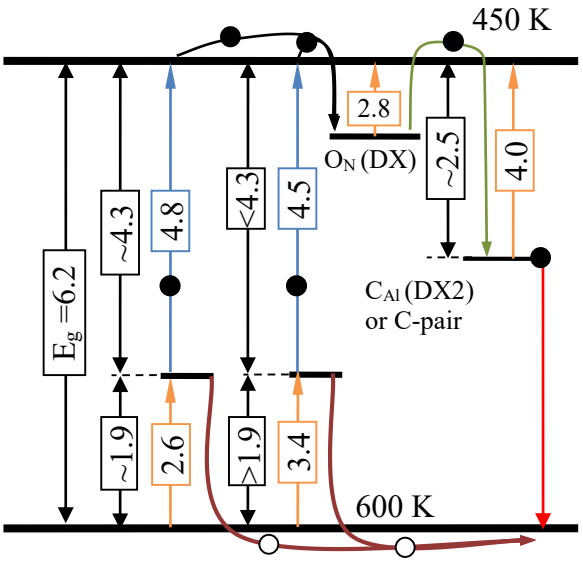

Figure 7.9. The diagram of observed absorption peaks in area AlN-B2. The double-headed arrows illustrate the position of defect states (ΔE). Single-headed arrows show the absorption energies from the initial states (blue) or after UV irradiation (orange). The transfer of electrons and holes is shown by the lateral arrow paths within CB and VB.

4.0 eV induced absorption band

The absorption band at 4.0 eV, only evident in area B2, is the most thermally stable induced band in the 2–4 eV range. Even at temperatures of 600 K (see p8 in Figure 7.5), the direct thermal activation from the defect level seems unlikely. The related defect behaves as a very deep trap capturing charge carriers released from other traps, e.g., electrons at medium temperatures (300 - 450 K), when the absorption still increases, or holes at higher temperatures, when the induced absorption decreases and finally disappears. The DOP of the band is positive (stronger for E||c) but it is also influenced by the overlapping band at 3.4 eV (E||c), as shown in Figure 7.6 A defect with suitable properties would be C_{Al} (i.e., in DX2 ground state configuration, ZPL 2.7 eV)[127] or the carbon pair defect (absorption between 3.8 – 5.1 eV is expected)[21]. Different charge states of C_{Al} are expected in the range 2 – 2.7 eV below CB,[100,127,143] which would fit well to the 4.0 eV induced band and also to the 4.5 eV band generally observed in carbon-dominating samples ($E_{Vis}(D2)$ and $E_{UV}(D2)$ transitions in Figure 7.8, respectively), or both, since the relaxation to the DX2 state gives a large additional energy shift.[127]

2.6 eV absorption band

The band at 2.6 eV becomes prominent in area B2 of the AlN crystal after partial annealing and is clearly seen in area B1, while it does not arise at all in area B3. Its restoration starts above 550 K (p5), thus a direct thermal activation is probable, considering that the E^{ZPL} is in the range from 1.4 to 1.9 eV above the valence band, as one expects in acceptor-doped area B1 (R=0.7). It could be also well correlated with the concentration of carbon. The $C_N^{1-/0}$ transition level fits, as its energy above VB is reported to be around 1.8–1.9 eV.[17,100,143] This level is also discussed in relation to the original absorption at 4.8 eV.

3.4 eV absorption band

The 3.4 eV band shows up in B2 area as an induced band and also is prominent in B1 area (Fig. 4). Assuming that this band should be very broad, it is also associated it with high

DOP values (~0.35) in both sample areas. One distinguishes it from the 3.2 eV band in B3 area, since although the latter also shows a pronounced positive DOP (~0.3) they have different shapes. The 3.4 eV absorption band could be associated with the transitions from VB to different charge states of V_{Al}-nO_N complexes, as calculated and observed in other studies,[156,168,218] or with excitations of electrons at V_N defects which should demonstrate a large value of FCS energy.[122] Abundance and configuration of V_{Al}-nO_N defects might depend on the oxygen concentration, but there is not enough evidence to propose a particular configuration.

5.2 eV induced absorption band

Finally, since the 5.2 eV band appears only in samples with the pronounced 4.7 eV absorption band, it could be the secondary ionization of a defect with an original absorption of 4.5 eV or 4.8 eV (Figure 7.9), i.e., an E_{ind}-type transition (Figure 7.8).

The photochromic original absorption bands around 4.7 eV in area B2

The peak at 4.5 eV dominates for E∥c polarization while the peak at 4.8 eV, oppositely, pronounced for E⊥c. The energy of the complementary transitions E_{Vis} and E_{UV} for the 4.8 eV peak can be estimated as E_{Vis}≈ 2.6 eV (using $E_{Vis} + E_{UV} \equiv E_g$ and $E_{UV}^{FCS} \approx E_{Vis}^{FCS} \approx 0.6$ eV). This indicates that both 2.6 eV and 4.8 eV bands can be attributed to the same transition level as mentioned previously, $C_N^{1-/0}$. Likewise, the original 4.4-4.5 eV band and the induced 3.4 eV band have high DOP in the range of 0.35–0.5. Here, $E_{UV}^{FCS} \approx E_{Vis}^{FCS} \approx$ 0.8-0.9 eV seems high but it is still a reasonable value for AlN (as discussed above). As the absorption 3.4 eV appears in B1 (R=0.7, acceptors dominate), this transition likely takes place in the lower part of the bandgap (transition type $E_{Vis}(D1)$ in Figure 7.8 and Figure 7.9).

To understand the nature of photochromism, we measured the absorption polarization in the UV-Vis range and performed two series of experiments on the thermal and optical restoration of the AlN initial state. It was found that optical excitation in the spectral range of the induced absorption bands (2 - 4 eV) promotes rapid restoration of the initial state. A gradual heating up to 600 K also leads to accelerated step-by-step restoration of the samples. Based on polarized UV-Vis absorption measurements, we clearly determine that the photoinduced absorption bands are associated with defects also typical for unirradiated AlN with high carbon concentration. Thus, we exclude the unique forms of defects created directly by radiation. Moreover, two groups of 2.6 eV (in C-doped samples) and 2.8 eV (O-doped) absorption bands are established and distinguished by the polarization properties. These two groups of defects have different recovery temperatures and consequently differ significantly in the activation energy. Understanding the structure of these defects requires further investigation.

7.4. Summary

Photochromism induced by the radiation with energy ~0.8×E_g is the first similar feature of semi-insulating AlN and GaN samples, although further study of photochromism in GaN is required.

The investigation of photochromism in AlN provided important information about the defect levels and allows a comparison of the Fermi level positions in different sample areas. In particular, pairs of complementary absorption bands 2.6 eV - 4.8 eV and 3.4 eV - 4.5 eV are found. The 2.6 and 3.4 eV with prevailing E‖c polarization can serve as an identifier of the Fermi level near the VB. The contrast, the 2.8 eV band has a different polarization and indicates that the Fermi level is closer to CB. Further investigation of the activation and deactivation of absorption bands might be possible using controlled co-doping, e.g., with beryllium.

From a practical point of view, photochromism can lead to significant "UV bleaching" (decrease of the UV absorption coefficient under UV irradiation) in AlN. This is relevant for visible range and UV emitting devices on AlN substrates. Furthermore, the spectrometer-measured absorption coefficient values will differ from practical values depending on the irradiation power. In the investigated AlN crystal, the absorption coefficient α_{UV} at 4.7 eV decreases from ~110 to ~55 cm^{-1} in area B2, while in area B1 such changes were not observed due to α_{UV} > 1000 cm^{-1}. The decrease in 4-5 eV UV absorption is accompanied by the appearance of an induced absorption in the range of 2–4 eV. The induced changes are meta-stable at room temperatures but are completely reversible at temperatures above 600 K or by adequate irradiation in the range of 2 – 4 eV. Hence, the optical transmission of AlN in the visible and UV ranges depend on each other and one can be controlled by the other.

It is most likely that both di-C and tri-C defects contribute to UV absorption of AlN. Unfortunately, theoretical reports do not provide satisfactory models of these defects that first of all should vibrate the same frequency. However, the absorption in UV range is expected for tri-C of di-C defects based on observations of the Raman scattering enhancement for di-C at 3.81 eV and for tri-C at 5.08 eV energy of the laser in Raman experiment.[21] Furthermore, it was demonstrated (Figure 7.2) that tri-C defects change the state due to the 4.88 eV ≈ 0.8×E_g radiation. This is, in fact, the second similar feature of AlN and GaN crystals (see Sect.6.2). The band mediated charge transfer between defects seems to be a reasonable explanation of the similar behavior of the two materials.

Photochromism is significant particularly when the compensation, i.e., the balance between the specific defects, is nearly ideal such as in area AlN-B2. Such conditions might provide high UV transparency in the AlN single crystals even without extreme purity. The role of point defects in AlN could be further clarified by additional inspection of the emission stimulated by the restoration of the initial state after the UV irradiation, which was however beyond the scope of this work.

8. Conclusion and outlook

This research aimed to obtain direct experimental evidences of the formation of different C-containing defects in GaN:C and AlN:C, identify their types, and describe their optical properties at different chemical C concentration [C]. In GaN crystals, even at the lowest level of intentional doping in this study [C]=3.2×10^{17} cm^{-3}, C-related vibrational modes were detected. Hence, even at [C] one order lower than in typical industrial semi-insulating layers, the resonant Raman scattering and IR absorption techniques proved to be reliable methods for the detection of defects. Since C doping compensating other dopants is attractive for applications in electronics, the shown techniques help to recognize defects in grown crystals and link them with particular optical and electrical properties of material. Analysis of the isotope-mass effect in ^{13}C enriched samples reliably identified the origination of numerous vibrational signatures from 9 defects with different structure (7 in GaN, 2 in AlN).

In GaN, four intense vibrations of C_N defect (MC1 – MC4) were found in all GaN:C samples. The low detection threshold was achieved due to the resonance excitation of the Raman scattering in the range of the defect absorption (below the bandgap). The vibrational modes were fully consistent with the DFT model in spectral positions, isotopic shifts, and polarization. Confirmed that other very pronounced defects in GaN were tri-C complexes despite the high formation energy. Intense vibrational modes of tri-C were observed in all GaN:C samples, but predominated at [C] > 5×10^{18} cm^{-3}. Most likely, tri-C defects provided the compensation of C_N defects and the photoluminescence (PL) band YL_C (different with known YL1) in this range of [C]. At lower [C], the compensation could be reasoned by V_N (identified by GL2 PL band). In addition, weak peaks of C_N-C_i pairs, C-H vibrations and C≡C pairs were identified. Though C_N-C_i and C-H interact with light, their role in optical and electrical processes was not clarified. At used growth and doping conditions, no C_{Ga} defects exist in samples or their vibrations could not be detected. Significant drop of the material quality was recognized by abrupt broadening of the Raman lines at [C] > 10^{19} cm^{-3}.

Tri-C manifests in basal and axial configurations of triatomic C=C=C bent molecule-like structures with possible metastable forms. This structure fully corresponds to the DFT model with emission bands at ~1.4, ~1.9 eV and absorption at ~2.3, ~2.8 eV, similar to ones observed at high [C]. However, the pronounced Tri-C defects evidence that the defect density cannot be reliably evaluated from the values of the formation energy obtained, e.g., in DFT calculations considering the defect formation processes in the bulk crystal for the system in thermodynamic equilibrium.

Light excitation with energy ~$0.8\times E_g$ during the FTIR measurement led to a simultaneous change in the state of several defects in GaN. Vibrations of C_N and C=C=C defects weaken or completely disappear. At the same time, the amplification of signals from C_N-C_i pairs and C-H defects simplifies their observation. The occurring processes are in good agreement with the band-mediated charge transfer model. Similar effect of the tri-C mode disappearance was observed in AlN.

The band-mediated charge transfer model explains photochromism as well. The phenomenon of photochromism was observed in a part of AlN and GaN crystals. In GaN, this effect has appeared as a few-hour visible darkening of the sample. The photochromism was stronger and more stable in AlN crystals with a characteristic C-related absorption band at 4.7 eV of below 200 cm^{-1} (R=([O]+[Si])/[C] ≈ 2). When irradiated with intense UV light, the samples lost

as much as half of the absorption intensity at 4.7 eV, while clearly visible brown coloration of the samples appears. When the absorption band at 4.7 eV initially has a magnitude greater than 1000 cm^{-1} (high [C], R≪2) or in the absence of the absorption band ([O]>>[C]) the photochromism is not stable though the change of absorption spectra can be detected. The balance between C, O, and intrinsic defects is suggested as the key factor of the intense stable photochromism.

The effect of photochromism is new to GaN and AlN and requires further study. In AlN, the effect makes it possible to control the transparency of the crystal in the range of 4-5 eV by irradiation in the range of 2-4 eV (and vice versa). Thus, it can find application in optical memory and logic devices. In addition, the variability of the UV absorption should be taken into account when designing optical devices.

In AlN crystals, intensive vibrational modes of di-C and axial tri-C defects but not mono-C defects (C_N, C_{Al}) were found. Further theoretical and experimental work is required to understand the structure of defects in AlN and study their properties. It is not clear why vibrational modes of C_N and C_{Al} defects are not observed in AlN. Probably, as in the case of CN or tri-C in GaN, these defects are coupled with the lattice that could in larger measure broaden the peaks of mono-C defects in AlN. No calculations of either di-C or tri-C defects in this material have been provided so far, although experimental observations of the resonant Raman effect hint at the absorption of these defects in the UV range. Moreover, the shape of the intense absorption band at 4.7 eV important for UV application does not satisfy the classical model of the defect-band transition, which has no explanation at the moment

It was found that, at the same chemical concentration [C], all vibration modes and UV-Vis absorption are a few times more pronounced in the homoepitaxial GaN samples grown on Am-GaN and doped with methane precursor than in GaN grown on sapphire and doped with pentane. Further study of this topic can answer how co-doping with donor impurities (acceptor impurities) affect the relative concentrations of the defects; how to control the proportions of C-containing defects by changing the growth parameters; is band-mediated charge transfer a necessary and sufficient explanation of such phenomena defects as photochromism and the bulk photoelectric effect associated with C doping.

Hopefully, this study answered how carbon forms complexes and provided the understanding of carbon-containing defects to such an extent that instead of the offensive word “defect” one could use a more meaningful “structural feature”.

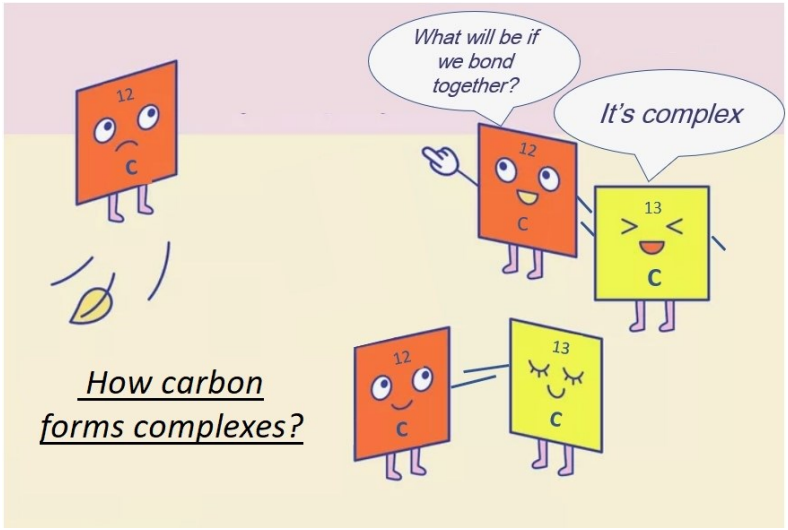

A. Reference list

[1] B. Gil, *III-Nitride Semiconductors and Their Modern Devices* (Oxford University Press, 2013).

[2] S.C. Jain, M. Willander, J. Narayan, and R. Van Overstraeten, "III-nitrides: Growth, characterization, and properties", J. Appl. Phys. **87**, 965 (2000).

[3] *III-Nitride Ultraviolet Emitters*, 1st ed. (Springer International Publishing, Cham, 2016).

[4] S. Nakamura, "Background story of the invention of efficient blue InGaN light emitting diodes (Nobel Lecture)", Ann. Phys. **527**, 335 (2015).

[5] S. Kimura, H. Yoshida, K. Uesugi, T. Ito, A. Okada, and S. Nunoue, "Performance enhancement of blue light-emitting diodes with InGaN/GaN multi-quantum wells grown on Si substrates by inserting thin AlGaN interlayers", J. Appl. Phys. **120**, 113104 (2016).

[6] J. Piprek, "Energy Efficiency Analysis of GaN-Based Blue Light Emitters", ECS J. Solid State Sci. Technol. **9**, 015008 (2019).

[7] H.-Y. Ryu, "Analysis on the Luminous Efficiency of Phosphor-Conversion White Light-Emitting Diode", J. Opt. Soc. Korea **17**, 22 (2013).

[8] M. Kneissl, T.Y. Seong, J. Han, and H. Amano, "The emergence and prospects of deep-ultraviolet light-emitting diode technologies", Nat. Photonics **13**, 233 (2019).

[9] Y. Taniyasu, M. Kasu, and T. Makimoto, "An aluminium nitride light-emitting diode with a wavelength of 210 nanometres", Nat. 2006 4417091 **441**, 325 (2006).

[10] M. Kneissl, Z. Yang, M. Teepe, C. Knollenberg, O. Schmidt, P. Kiesel, N.M. Johnson, S. Schujman, and L.J. Schowalter, "Ultraviolet semiconductor laser diodes on bulk AlN", J. Appl. Phys. **101**, 123103 (2007).

[11] Y. Aoki, M. Kuwabara, Y. Yamashita, Y. Takagi, A. Sugiyama, and H. Yoshida, "A 350-nm-band GaN/AlGaN multiple-quantum-well laser diode on bulk GaN", Appl. Phys. Lett. **107**, 151103 (2015).

[12] Z. Zhang, M. Kushimoto, T. Sakai, N. Sugiyama, L.J. Schowalter, C. Sasaoka, and H. Amano, "A 271.8 nm deep-ultraviolet laser diode for room temperature operation", Appl. Phys. Express **12**, 124003 (2019).

[13] H. Hirayama, S. Fujikawa, N. Noguchi, J. Norimatsu, T. Takano, K. Tsubaki, and N. Kamata, "222–282 nm AlGaN and InAlGaN-based deep-UV LEDs fabricated on high-quality AlN on sapphire", Phys. Status Solidi **206**, 1176 (2009).

[14] M.A. Khan, T. Matsumoto, N. Maeda, N. Kamata, and H. Hirayama, "Improved external quantum efficiency of 293 nm AlGaN UVB LED grown on an AlN template", Jpn. J. Appl. Phys. **58**, SAAF01 (2018).

[15] R. Kirste, Q. Guo, J.H. Dycus, A. Franke, S. Mita, B. Sarkar, P. Reddy, J.M. LeBeau, R. Collazo, and Z. Sitar, "6 kW/cm2 UVC laser threshold in optically pumped lasers achieved by controlling point defect formation", Appl. Phys. Express **11**, 082101 (2018).

[16] N. Tillner, C. Frankerl, F. Nippert, M.J. Davies, C. Brandl, R. Lösing, M. Mandl, H.-J. Lugauer, R. Zeisel, A. Hoffmann, A. Waag, and M.P. Hoffmann, "Point Defect-Induced UV-C Absorption in Aluminum Nitride Epitaxial Layers Grown on Sapphire Substrates by Metal-Organic Chemical Vapor Deposition", Phys. Status Solidi **257**, 2000278 (2020).

[17] D. Alden, J.S. Harris, Z. Bryan, J.N. Baker, P. Reddy, S. Mita, G. Callsen, A. Hoffmann, D.L. Irving, R. Collazo, and Z. Sitar, "Point-Defect Nature of the Ultraviolet Absorption Band in AlN", Phys. Rev. Appl. **9**, 54036 (2018).

[18] K. Irmscher, I. Gamov, E. Nowak, G. Gärtner, F. Zimmermann, F.C. Beyer, E. Richter, M. Weyers, and G. Tränkle, "Tri-carbon defects in carbon doped GaN", Appl. Phys. Lett. **113**, 262101 (2018).

[19] F. Zimmermann, J. Beyer, F.C. Beyer, G. Gärtner, I. Gamov, K. Irmscher, E. Richter, M. Weyers, and J. Heitmann, "A carbon-doping related luminescence band in GaN revealed by below bandgap excitation", J. Appl. Phys. **130**, 055703 (2021).

[20] K. Irmscher, C. Hartmann, C. Guguschev, M. Pietsch, J. Wollweber, and M. Bickermann, "Identification of a tri-carbon defect and its relation to the ultraviolet absorption in aluminum nitride", J. Appl. Phys. **114**, 123505 (2013).

[21] I. Gamov, C. Hartmann, J. Wollweber, A. Dittmar, T. Straubinger, M. Bickermann, I. Kogut, H. Fritze, and K. Irmscher, "Carbon pair defects in aluminum nitride", J. Appl. Phys. **126**, 215102 (2019).

[22] M. Kneissl, T. Kolbe, C. Chua, V. Kueller, N. Lobo, J. Stellmach, A. Knauer, H. Rodriguez, S. Einfeldt, Z. Yang, N.M. Johnson, and M. Weyers, "Advances in group III-nitride-based deep UV light-emitting diode technology", Semicond. Sci. Technol. **26**, 014036 (2011).

[23] S. Nakamura, T. Mukai, and M. Senoh, "Candela-class high-brightness InGaN/AlGaN double-heterostructure blue-light-emitting diodes", Appl. Phys. Lett. **64**, 1687 (1998).

[24] U.K. Mishra, P. Parikh, and Y.F. Wu, "AlGaN/GaN HEMTs - An overview of device operation and applications", Proc. IEEE **90**, 1022 (2002).

[25] K. Kojima, F. Horikiri, Y. Narita, T. Yoshida, H. Fujikura, and S.F. Chichibu, "Roles of carbon impurities and intrinsic nonradiative recombination centers on the carrier recombination processes of GaN crystals", Appl. Phys. Express **13**, 012004 (2020).

[26] Y. Linkai, Q. Haoran, H. Jialin, Z. Mei, Z. Degang, J. Desheng, Y. Jing, L. Wei, and L. Feng, "Influence of dislocation density and carbon impurities in i-GaN layer on the performance of Schottky barrier ultraviolet photodetectors", Mater. Res. Express **5**, 046207 (2018).

[27] I. Levine, I. Gamov, M. Rusu, K. Irmscher, C. Merschjann, E. Richter, M. Weyers, and T. Dittrich, "Bulk photovoltaic effect in carbon-doped gallium nitride revealed by anomalous surface photovoltage spectroscopy", Phys. Rev. B **101**, 245205 (2020).

[28] I. Gamov, C. Hartmann, T. Straubinger, and M. Bickermann, "Photochromism and influence of point defect charge states on optical absorption in aluminum nitride (AlN)", J. Appl. Phys. **129**, 113103 (2021).

[29] V.M. Fridkin, "Bulk photovoltaic effect in noncentrosymmetric crystals", Crystallogr. Reports 2001 464 **46**, 654 (2001).

[30] N. Yafune, S. Hashimoto, K. Akita, Y. Yamamoto, H. Tokuda, and M. Kuzuhara, "AlN/AlGaN HEMTs on AlN substrate for stable high-temperature operation", Electron. Lett. **50**, 211 (2014).

[31] A. Hickman, R. Chaudhuri, S.J. Bader, K. Nomoto, K. Lee, H.G. Xing, and D. Jena, "High Breakdown Voltage in RF AlN/GaN/AlN Quantum Well HEMTs", IEEE Electron Device Lett. **40**, 1293 (2019).

[32] M. Khaouani, A. Hamdoune, H. Bencherif, Z. Kourdi, and L. Dehimi, "An ultra-sensitive AlGaN/AlN/GaN/AlGaN photodetector: Proposal and investigation", Optik (Stuttg). **217**, 164797 (2020).

[33] P. Fay, J. Debdeep, and P. Maki, *High-Frequency GaN Electronic Devices* (Springer International Publishing, 2020).

[34] J.L. Lyons, E.R. Glaser, M.E. Zvanut, S. Paudel, M. Iwinska, T. Sochacki, and M. Bockowski, "Carbon complexes in highly C-doped GaN", Phys. Rev. B **104**, 075201 (2021).

[35] T. Narita, H. Yoshida, K. Tomita, K. Kataoka, H. Sakurai, M. Horita, M. Bockowski, N. Ikarashi, J. Suda, T. Kachi, and Y. Tokuda, "Progress on and challenges of p-type formation for GaN power devices", J. Appl. Phys. **128**, 090901 (2020).

[36] T. Narita, K. Tomita, Y. Tokuda, T. Kogiso, M. Horita, and T. Kachi, "The origin of carbon-related carrier compensation in p-type GaN layers grown by MOVPE", J. Appl. Phys. **124**, 215701 (2018).

[37] M. Iwinska, R. Piotrzkowski, E. Litwin-Staszewska, T. Sochacki, M. Amilusik, M. Fijalkowski, B. Lucznik, and M. Bockowski, "Highly resistive C-doped hydride vapor phase epitaxy-GaN grown on ammonothermally crystallized GaN seeds", Appl. Phys. Express **10**, 011003 (2017).

[38] E. Richter, F.C. Beyer, F. Zimmermann, G. Gärtner, K. Irmscher, I. Gamov, J. Heitmann, M. Weyers, and G. Tränkle, "Growth and Properties of Intentionally Carbon-Doped GaN Layers", Cryst. Res. Technol. 1900129 (2019).

[39] M. Bockowski, M. Iwinska, M. Amilusik, B. Lucznik, M. Fijalkowski, E. Litwin-Staszewska, R. Piotrzkowski, and T. Sochacki, "Doping in bulk HVPE-GaN grown on native seeds – highly conductive and semi-insulating crystals", J. Cryst. Growth **499**, 1 (2018).

[40] R. Piotrzkowski, M. Zajac, E. Litwin-Staszewska, and M. Bockowski, "Self-compensation of carbon in HVPE-GaN:C", Appl. Phys. Lett. **117**, 012106 (2020).

[41] C. Li and J. Wang, "The effect of atomistic substitution on thermal transport in large phonon bandgap GaN", Jpn. J. Appl. Phys. **60**, 071003 (2021).

[42] P. Bagheri, P. Reddy, J.H. Kim, R. Rounds, T. Sochacki, R. Kirste, M. Bockowski, R. Collazo, and Z. Sitar, "Impact of impurity-based phonon resonant scattering on thermal conductivity of single crystalline GaN", Appl. Phys. Lett. **117**, 082101 (2020).

[43] R.L. Xu, M.M. Rojo, S.M. Islam, A. Sood, B. Vareskic, A. Katre, N. Mingo, K.E. Goodson, H.G. Xing, D. Jena, and E. Pop, "Thermal conductivity of crystalline AlN and the influence of atomic-scale defects", J. Appl. Phys. **126**, 185105 (2019).

[44] A. Fariza, A. Lesnik, S. Neugebauer, M. Wieneke, J. Hennig, J. Bläsing, H. Witte, A. Dadgar, and A. Strittmatter, "Leakage currents and Fermi-level shifts in GaN layers upon iron and carbon-doping", J. Appl. Phys. **122**, 025704 (2017).

[45] K. Kishimoto, M. Funato, and Y. Kawakami, "Control of p-type conductivity at AlN surfaces by carbon doping", Appl. Phys. Express **13**, 015512 (2020).

[46] I. Kogut, C. Hartmann, I. Gamov, Y. Suhak, M. Schulz, S. Schröder, J. Wollweber, A. Dittmar, K. Irmscher, T. Straubinger, M. Bickermann, and H. Fritze, "Electromechanical losses in carbon- and oxygen-containing

bulk AlN single crystals", Solid State Ionics **343**, 115072 (2019).

[47] T. Kim, J. Kim, R. Dalmau, R. Schlesser, E. Preble, and X. Jiang, "High-temperature electromechanical characterization of AlN single crystals", IEEE Trans. Ultrason. Ferroelectr. Freq. Control **62**, 1880 (2015).

[48] C. Xiong, W. Pernice, C. Schuck, and H.X. Tang, "Integrated Photonic Circuits in Gallium Nitride and Aluminum Nitride", Int. J. High Speed Electron. Syst. **23**, (2014).

[49] W. Fu, Z. Shen, Y. Xu, C.-L. Zou, R. Cheng, X. Han, and H.X. Tang, "Phononic integrated circuitry and spin–orbit interaction of phonons", Nat. Commun. 2019 101 **10**, 1 (2019).

[50] X. Sun, P. Wang, T. Wang, L. Chen, Z. Chen, K. Gao, T. Aoki, M. Li, J. Zhang, T. Schulz, M. Albrecht, W. Ge, Y. Arakawa, B. Shen, M. Holmes, and X. Wang, "Single-photon emission from isolated monolayer islands of InGaN", Light Sci. Appl. 2020 91 **9**, 1 (2020).

[51] M. Arita, F. Le Roux, M.J. Holmes, S. Kako, and Y. Arakawa, "Ultraclean Single Photon Emission from a GaN Quantum Dot", Nano Lett. **17**, 2902 (2017).

[52] S. Kako, M. Holmes, S. Sergent, M. Bürger, D.J. As, and Y. Arakawa, "Single-photon emission from cubic GaN quantum dots", Appl. Phys. Lett. **104**, 011101 (2014).

[53] S. Xia, T. Aoki, K. Gao, M. Arita, Y. Arakawa, and M.J. Holmes, "Enhanced Single-Photon Emission from GaN Quantum Dots in Bullseye Structures", ACS Photonics **8**, 1656 (2021).

[54] G. Callsen, S. Tamariz, and N. Grandjean, "Room temperature single photon emission from planar GaN/AlN quantum dot samples grown by MBE", 1 (2019).

[55] Y. Xue, H. Wang, N. Xie, Q. Yang, F. Xu, B. Shen, J. Shi, D. Jiang, X. Dou, T. Yu, and B. Sun, "Single-Photon Emission from Point Defects in Aluminum Nitride Films", J. Phys. Chem. Lett. **11**, 2689 (2020).

[56] N. Mendelson, D. Chugh, J.R. Reimers, T.S. Cheng, A. Gottscholl, H. Long, C.J. Mellor, A. Zettl, V. Dyakonov, P.H. Beton, S. V. Novikov, C. Jagadish, H.H. Tan, M.J. Ford, M. Toth, C. Bradac, and I. Aharonovich, "Identifying carbon as the source of visible single-photon emission from hexagonal boron nitride", Nat. Mater. 2020 203 **20**, 321 (2020).

[57] C. Jara, T. Rauch, S. Botti, M.A.L. Marques, A. Norambuena, R. Coto, J.E. Castellanos-Águila, J.R. Maze, and F. Munoz, "First-Principles Identification of Single Photon Emitters Based on Carbon Clusters in Hexagonal Boron Nitride", J. Phys. Chem. A **125**, 1325 (2021).

[58] A.B.D. Shaik and P. Palla, "Optical quantum technologies with hexagonal boron nitride single photon sources", Sci. Reports 2021 111 **11**, 1 (2021).

[59] M. Matsubara and E. Bellotti, "A first-principles study of carbon-related energy levels in GaN. II. Complexes formed by carbon and hydrogen, silicon or oxygen", J. Appl. Phys. **121**, 195702 (2017).

[60] P. Deák, M. Lorke, B. Aradi, and T. Frauenheim, "Carbon in GaN: Calculations with an optimized hybrid functional", Phys. Rev. B **99**, (2019).

[61] J.L. Lyons, A. Janotti, and C.G. Van De Walle, "Carbon impurities and the yellow luminescence in GaN", Appl. Phys. Lett. **97**, 152108 (2010).

[62] M. Matsubara and E. Bellotti, "A first-principles study of carbon-related energy levels in GaN. I. Complexes formed by substitutional/interstitial carbons and gallium/nitrogen vacancies", J. Appl. Phys. **121**, 195701 (2017).

[63] P. Bogusławski, E.L. Briggs, and J. Bernholc, "Amphoteric properties of substitutional carbon impurity in GaN and AIN", Appl. Phys. Lett. **69**, 233 (1996).

[64] H. Fujikura, T. Konno, T. Yoshida, and F. Horikiri, "Hydride-vapor-phase epitaxial growth of highly pure GaN layers with smooth as-grown surfaces on freestanding GaN substrates", Jpn. J. Appl. Phys. **56**, 085503 (2017).

[65] M. Bockowski, M. Iwinska, M. Amilusik, M. Fijalkowski, B. Lucznik, and T. Sochacki, "Challenges and future perspectives in HVPE-GaN growth on ammonothermal GaN seeds", Semicond. Sci. Technol. **31**, 093002 (2016).

[66] V. Avrutin, D.J. Silversmith, Y. Mori, F. Kawamura, Y. Kitaoka, and H. Morkoç, "Growth of bulk GaN and AlN: Progress and challenges", Proc. IEEE **98**, 1302 (2010).

[67] D. Ehrentraut, E. Meissner, and M. Bockowski, *Technology of Gallium Nitride Crystal Growth*, 1st ed. (Springer Berlin Heidelberg, Berlin, Heidelberg, 2010).

[68] M. Zajac, R. Kucharski, K. Grabianska, A. Gwardys-Bak, A. Puchalski, D. Wasik, E. Litwin-Staszewska, R. Piotrzkowski, J. Z Domagala, and M. Bockowski, "Basic ammonothermal growth of Gallium Nitride – State of the art, challenges, perspectives", Prog. Cryst. Growth Charact. Mater. **64**, 63 (2018).

[69] K. Grabianska, R. Kucharski, A. Puchalski, T. Sochacki, and M. Bockowski, "Recent progress in basic ammonothermal GaN crystal growth", J. Cryst. Growth **547**, 125804 (2020).

[70] R. Kucharski, M. Zajac, A. Puchalski, T. Sochacki, M. Bockowski, J.L. Weyher, M. Iwinska, J. Serafinczuk, R. Kudrawiec, and Z. Siemia¸tkowski, "Ammonothermal growth of GaN crystals on HVPE-GaN seeds prepared with the use of ammonothermal substrates", J. Cryst. Growth **427**, 1 (2015).

[71] T. Hashimoto and S. Nakamura, "*A Pathway Toward Bulk Growth of GaN by the Ammonothermal Method*" in *Springer Ser. Mater. Sci.* (Springer Verlag, 2010), pp. 161–182.

[72] T. Hashimoto, E.R. Letts, D. Key, and B. Jordan, "Two inch GaN substrates fabricated by the near equilibrium ammonothermal (neat) method", Jpn. J. Appl. Phys. **58**, SC1005 (2019).

[73] R. Chierchia, T. Böttcher, H. Heinke, S. Einfeldt, S. Figge, and D. Hommel, "Microstructure of heteroepitaxial GaN revealed by x-ray diffraction", J. Appl. Phys. **93**, 8918 (2003).

[74] C. Hartmann, L. Matiwe, J. Wollweber, I. Gamov, K. Irmscher, M. Bickermann, and T. Straubinger, "Favourable growth conditions for the preparation of bulk AlN single crystals by PVT", CrystEngComm **22**, 1762 (2020).

[75] R.T. Bondokov, J. Chen, K. Yamaoka, S. Wang, S.P. Rao, T. Suzuki, and L.J. Schowalter, "*LARGE, UV-TRANSPARENT ALUMINUM NITRIDE SINGLE CRYSTALS*", (23 May 2019).

[76] I. Bryan, Z. Bryan, S. Mita, A. Rice, L. Hussey, C. Shelton, J. Tweedie, J.P. Maria, R. Collazo, and Z. Sitar, "The role of surface kinetics on composition and quality of AlGaN", J. Cryst. Growth **451**, 65 (2016).

[77] C. Hartmann, J. Wollweber, S. Sintonen, A. Dittmar, L. Kirste, S. Kollowa, K. Irmscher, and M. Bickermann, "Preparation of deep UV transparent AlN substrates with high structural perfection for optoelectronic devices", CrystEngComm **18**, 3488 (2016).

[78] C. Hartmann, J. Wollweber, A. Dittmar, K. Irmscher, A. Kwasniewski, F. Langhans, T. Neugut, and M. Bickermann, "Preparation of bulk AlN seeds by spontaneous nucleation of freestanding crystals", Jpn. J. Appl. Phys. **52**, 1 (2013).

[79] C. Hartmann, A. Dittmar, J. Wollweber, and M. Bickermann, "Bulk AlN growth by physical vapour transport", Semicond. Sci. Technol. **29**, 084002 (2014).

[80] W.-H. Chen, Z.-Y. Qin, X.-Y. Tian, X.-H. Zhong, Z.-H. Sun, B.-K. Li, R.-S. Zheng, Y. Guo, and H.-L. Wu, "The Physical Vapor Transport Method for Bulk AlN Crystal Growth", Molecules **24**, (2019).

[81] K. Goto, N. Takekawa, T. Nagashima, R. Yamamoto, G. Pozina, R. Dalmau, R. Schlesser, R. Collazo, B. Monemar, Z. Sitar, M. Boćkowski, and Y. Kumagai, "Study of Dislocations in Homoepitaxially and Heteroepitaxially Grown AlN Layers", Phys. Status Solidi **217**, 2000465 (2020).

[82] T. Nagashima, Y. Kubota, T. Kinoshita, Y. Kumagai, J. Xie, R. Collazo, H. Murakami, H. Okamoto, A. Koukitu, and Z. Sitar, "Structural and Optical Properties of Carbon-Doped AlN Substrates Grown by Hydride Vapor Phase Epitaxy Using AlN Substrates Prepared by Physical Vapor Transport", Appl. Phys. Express **5**, 125501 (2012).

[83] Y. Kumagai, Y. Kubota, T. Nagashima, T. Kinoshita, R. Dalmau, R. Schlesser, B. Moody, J. Xie, H. Murakami, A. Koukitu, and Z. Sitar, "Preparation of a Freestanding AlN Substrate from a Thick AlN Layer Grown by Hydride Vapor Phase Epitaxy on a Bulk AlN Substrate Prepared by Physical Vapor Transport", Appl. Phys. Express **5**, 055504 (2012).

[84] R. Boichot, D. Chen, F. Mercier, F. Baillet, G. Giusti, T. Coughlan, M. Chubarov, M. Pons, R. Boichot, D. Chen, F. Mercier, F. Baillet, G. Giusti, T. Coughlan, M. Chubarov, and M. Pons, "Epitaxial Growth of AlN on (0001) Sapphire: Assessment of HVPE Process by a Design of Experiments Approach", Coatings **7**, 136 (2017).

[85] M. Bickermann, B.M. Epelbaum, and A. Winnacker, "Characterization of bulk AlN with low oxygen content", J. Cryst. Growth **269**, 432 (2004).

[86] M. Bickermann, B.M. Epelbaum, and A. Winnacker, "PVT growth of bulk AlN crystals with low oxygen contamination", Phys. Status Solidi **0**, 1993 (2003).

[87] L. Jin, K. Zhao, S. Xu, Z. Qin, H. Cheng, L. Zhang, H. Qi, J. Li, R. Zheng, and H. Wu, "Optical property in colorless AlN bulk crystals: investigation of native defect-induced UV absorption", Scr. Mater. **190**, 91 (2021).

[88] Z.G. Herro, D. Zhuang, R. Schlesser, and Z. Sitar, "Growth of AlN single crystalline boules", J. Cryst. Growth **312**, 2519 (2010).

[89] B.M. Epelbaum, M. Bickermann, S. Nagata, P. Heimann, O. Filip, and A. Winnacker, "Similarities and differences in sublimation growth of SiC and AlN", J. Cryst. Growth **305**, 317 (2007).

[90] R. Loudon, "Theory of the resonance Raman effect in crystals", J. Phys. **26**, 677 (1965).

[91] J.L. Birman, *Theory of Crystal Space Groups. Infra-Red and Raman Lattice Processes of Insulating Crystals* (Springer Berlin Heidelberg, 1974).

[92] M. Cardona, R.K. Chang, G. Güntherodt, M.B. Long, and H. Vogt, *Light Scattering in Solids II* (Springer

Berlin Heidelberg, Berlin, Heidelberg, 1982).

[93] P.Y. Yu and M. Cardona, *Fundamentals of Semiconductors. Physics and Materials Properties*, 4th ed. (Springer, London New York, 2010).

[94] G. Herzberg, *Molecular Spectra and Molecular Structure, II. Infrared and Raman Spectra of Polyatomic Molecules*, 1954th ed. (Sixth Printing, New York, 1949).

[95] P.R. Bunker, *Molecular Symmetry and Spectroscopy* (Elsevier, Ottawa, Canada, 1979).

[96] K.W. Böer and U.W. Pohl, "*Optical Properties of Defects*" in *Semicond. Phys.* (Springer International Publishing, 2018), pp. 629–676.

[97] D.B. Baldassare and R.C. Powell, *Crystal Symmetry, Lattice Vibrations, and Optical Spectroscopy of Solids. A Group Theoretical Approach* (World Scientific Publishing Co. Pte. Ltd., Singapore, 2014).

[98] C.A. Arguello, D.L. Rousseau, and S.P.S. Porto, "First-order raman effect in wurtzite-type crystals", Phys. Rev. **181**, 1351 (1969).

[99] M. Thomas, "Semiconductors — basic data, 2nd ed. Edited by O. Madelung, Springer, Berlin 1996, viii, 317 pp., hardcover, DM 88.00, ISBN 3-540-60883-4", Chem. Vap. Depos. **3**, 288 (1997).

[100] J.L. Lyons, A. Janotti, and C.G. Van de Walle, "Effects of carbon on the electrical and optical properties of InN, GaN, and AlN", Phys. Rev. B **89**, 035204 (2014).

[101] E.A. Robinson and M.W. Lister, "A LINEAR RELATIONSHIP BETWEEN BOND ORDERS AND STRETCHING FORCE CONSTANTS", Can. J. Chem. **41**, 2988 (1963).

[102] K. Momma and F. Izumi, "VESTA 3 for three-dimensional visualization of crystal, volumetric and morphology data", J. Appl. Crystallogr. **44**, 1272 (2011).

[103] E.W. Montroll and R.B. Potts, "Effect of defects on lattice vibrations", Phys. Rev. **100**, 525 (1955).

[104] P. Mazur, E.W. Montroll, and R.B. Potts, "Effect of defects on lattice vibrations, II: Localized vibration modes in a linear diatomic chain on JSTOR", J. Washingt. Acad. Sci. **46**, 2 (1956).

[105] C. Bungaro, K. Rapcewicz, and J. Bernholc, "Ab initio phonon dispersions of wurtzite AlN, GaN, and InN", Phys. Rev. B - Condens. Matter Mater. Phys. **61**, 6720 (2000).

[106] J. Zhang, T. Ruf, M. Cardona, O. Ambacher, and M. Stutzmann, "Raman spectra of isotopic GaN", Phys. Rev. B - Condens. Matter Mater. Phys. **56**, 14399 (1997).

[107] K.R. Bagnall, C.E. Dreyer, D. Vanderbilt, and E.N. Wang, "Electric field dependence of optical phonon frequencies in wurtzite GaN observed in GaN high electron mobility transistors", J. Appl. Phys. **120**, 155104 (2016).

[108] B.M. Janzen, P. Mazzolini, R. Gillen, A. Falkenstein, M. Martin, H. Tornatzky, J. Maultzsch, O. Bierwagen, and M.R. Wagner, "Isotopic study of Raman active phonon modes in β-Ga2O3", J. Mater. Chem. C **9**, 2311 (2021).

[109] W. Zheng, R. Zheng, F. Huang, H. Wu, and F. Li, "Raman tensor of AlN bulk single crystal", Photonics Res. **3**, 38 (2015).

[110] W. Zheng, R. Zheng, F. Huang, H. Wu, and F. Li, "Raman tensor of AlN bulk single crystal: erratum", Photonics Res. **8**, 412 (2020).

[111] U. Haboeck, H. Siegle, A. Hoffmann, and C. Thomsen, "Lattice dynamics in GaN and AlN probed with first- and second-order Raman spectroscopy", Phys. Status Solidi **0**, 1710 (2003).

[112] V.Y. Davydov, Y.E. Kitaev, I.N. Goncharuk, A.M. Tsaregorodtsev, A.. Smirnov, A.O. Lebedev, V.M. Botnaryk, Y.V. Zhilyaev, M.B. Smirnov, A.P. Mirgorodsky, and O.K. Semchinova, "Phonon spectrum of wurtzite GaN and AlN", J. Cryst. Growth **189**–**190**, 656 (1998).

[113] G. Pezzotti, H. Sueoka, A.A. Porporati, M. Manghnani, and W. Zhu, "Raman tensor elements for wurtzitic GaN and their application to assess crystallographic orientation at film/substrate interfaces", J. Appl. Phys. **110**, 013527 (2011).

[114] M. Kuball, "Raman spectroscopy of GaN, AlGaN and AlN for process and growth monitoring/control", Surf. Interface Anal. **31**, 987 (2001).

[115] S. Subedi and J.J. Nakarmi, "Vibrational frequency analysis of CH3Cl molecule; ab initio study", Himal. Phys. **5**, 142 (2015).

[116] S.A. Kiselev, S.R. Bickham, and A.J. Sievers, "Anharmonic gap mode in a one-dimensional diatomic lattice with nearest-neighbor Born-Mayer-Coulomb potentials and its interaction with a mass-defect impurity", Phys. Rev. B **50**, 9135 (1994).

[117] *Dr. John L. Lyons, US Naval Research Laboratory, Washington DC 20375* (private communication, 2021).

[118] P.C. Cross and J.H. Van Vleck, "Molecular vibrations of three particle systems with special applications to the ethyl halides and ethyl alcohol", J. Chem. Phys. **1**, 350 (1933).

[119] F.R. Halpern, "Quantum mechanics of the anharmonic oscillator", J. Math. Phys. **14**, 219 (1973).

[120] K.S. Viswanathan, "The theory of the anharmonic oscillator", Proc. Indian Acad. Sci. - Sect. A **46**, 203 (1957).

[121] E.U. Condon and P.M. Morse, *Quantum Mechanics*, 1st ed. (McGraw-Hill Book Co., New York, 1929).

[122] I.A. Aleksandrov and K.S. Zhuravlev, "Luminescence line shapes of band to deep centre and donor–acceptor transitions in AlN", J. Phys. Condens. Matter **32**, 435501 (2020).

[123] M. Lamprecht, C. Grund, S. Bauer, R. Collazo, Z. Sitar, and K. Thonke, "Slow decay of a defect-related emission band at 2.05 eV in AlN: Signatures of oxygen-related DX states", Phys. Status Solidi **254**, 1600338 (2017).

[124] K. Thonke, M. Lamprecht, R. Collazo, and Z. Sitar, "Optical signatures of silicon and oxygen related DX centers in AlN", Phys. Status Solidi **214**, 1600749 (2017).

[125] M. Lamprecht, C. Grund, B. Neuschl, K. Thonke, Z. Bryan, R. Collazo, and Z. Sitar, "Very slow decay of a defect related emission band at 2.4 eV in AlN: Signatures of the Si related shallow DX state", J. Appl. Phys. **119**, 155701 (2016).

[126] M. Lamprecht and K. Thonke, "Determination of donor and DX center capture characteristics by pulsed photoluminescence", J. Appl. Phys. **123**, 095704 (2018).

[127] P. Bogusławski and J. Bernholc, "Doping properties of C, Si, and Ge impurities in GaN and AlN", Phys. Rev. B **56**, 9496 (1997).

[128] A.F. Wright, "Substitutional and interstitial carbon in wurtzite GaN", J. Appl. Phys. **92**, 2575 (2002).

[129] E.E. Reuter, R. Zhang, T.F. Kuech, and S.G. Bishop, "Photoluminescence Excitation Spectroscopy of Carbon-Doped Gallium Nitride", MRS Proc. **537**, G3.67 (1998).

[130] J.A. Chisholm and P.D. Bristowe, "Computational study of the effect of Al and In on the formation energies and acceptor levels of Mg and C dopants in GaN", J. Phys. Condens. Matter **13**, 8875 (2001).

[131] M.A. Reshchikov, M. Vorobiov, D.O. Demchenko, Ü. Özgür, H. Morkoç, A. Lesnik, M.P. Hoffmann, F. Hörich, A. Dadgar, and A. Strittmatter, "Two charge states of the CN acceptor in GaN: Evidence from photoluminescence", Phys. Rev. B **98**, 125207 (2018).

[132] C.H. Seager, A.F. Wright, J. Yu, and W. Götz, "Role of carbon in GaN", J. Appl. Phys. **92**, 6553 (2002).

[133] S. Wu, X. Yang, H. Zhang, L. Shi, Q. Zhang, Q. Shang, Z. Qi, Y. Xu, J. Zhang, N. Tang, X. Wang, W. Ge, K. Xu, and B. Shen, "Unambiguous Identification of Carbon Location on the N Site in Semi-insulating GaN", Phys. Rev. Lett. **121**, 145505 (2018).

[134] S. Ito, H. Kobayashi, K. Araki, K. Suzuki, N. Sawaki, K. Yamashita, Y. Honda, and H. Amano, "Resonant Raman and FTIR spectra of carbon doped GaN", J. Cryst. Growth **414**, 56 (2015).

[135] M.F. Cerqueira, L.G. Vieira, A. Alves, R. Correia, M. Huber, A. Andreev, A. Bonanni, and M.I. Vasilevskiy, "Raman and IR-ATR spectroscopy studies of heteroepitaxial structures with a GaN:C top layer", J. Phys. D. Appl. Phys. **50**, (2017).

[136] G. Kaczmarczyk, Schwingungsverhalten Lokaler Defekte in Breitband-Halbleitern, der Technischen Universität Berlin, 2006.

[137] G. Kaczmarczyk, A. Kaschner, A. Hoffmann, and C. Thomsen, "Impurity-induced modes of Mg, As, Si, and C in hexagonal and cubic GaN", Phys. Rev. B - Condens. Matter Mater. Phys. **61**, 5353 (2000).

[138] M.O. Manasreh, J.M. Baranowski, K. Pakula, H.X. Jiang, and J. Lin, "Localized vibrational modes of carbon-hydrogen complexes in GaN", Appl. Phys. Lett. **75**, 659 (1999).

[139] A. Alkauskas, M.D. McCluskey, and C.G. Van de Walle, "Tutorial: Defects in semiconductors—Combining experiment and theory", J. Appl. Phys. **119**, 181101 (2016).

[140] M.A. Reshchikov, "Measurement and analysis of photoluminescence in GaN", J. Appl. Phys. **129**, 121101 (2021).

[141] Y. Xu, Z. Li, X. Yang, L. Shi, P. Zhang, X. Cao, J. Nie, S. Wu, J. Zhang, Y. Feng, Y. Zhang, X. Wang, W. Ge, K. Xu, and B. Shen, "Migration of carbon from Ga sites to N sites in GaN: a combined PAS and hybrid DFT study", Jpn. J. Appl. Phys. **58**, 090901 (2019).

[142] H. Li, M. Huang, and S. Chen, "First-principles exploration of defect-pairs in GaN", J. Semicond. **41**, 032104 (2020).

[143] R. Collazo, J. Xie, B.E. Gaddy, Z. Bryan, R. Kirste, M. Hoffmann, R. Dalmau, B. Moody, Y. Kumagai, T. Nagashima, Y. Kubota, T. Kinoshita, A. Koukitu, D.L. Irving, and Z. Sitar, "On the origin of the 265 nm absorption band in AlN bulk crystals", Appl. Phys. Lett. **100**, 191914 (2012).

[144] Y. Taniyasu, M. Kasu, and N. Kobayashi, "Intentional control of n-type conduction for Si-doped AlN and AlXGa1−XN (0.42⩽x⩽1)", Appl. Phys. Lett. **81**, 1255 (2002).

[145] M.L. Nakarmi, K.H. Kim, K. Zhu, J.Y. Lin, and H.X. Jiang, "Transport properties of highly conductive n-type Al-rich Al xGa 1-xN (x≥0.7)", Appl. Phys. Lett. **85**, 3769 (2004).

[146] Y. Taniyasu, M. Kasu, and T. Makimoto, "Electrical conduction properties of n-type Si-doped AIN with high electron mobility (>100 cm2 V-1 s-1)", Appl. Phys. Lett. **85**, 4672 (2004).

[147] I. Gorczyca, N.E. Christensen, and A. Svane, "Influence of hydrostatic pressure on cation vacancies in GaN, AlN, and GaAs", Phys. Rev. B - Condens. Matter Mater. Phys. **66**, 075210 (2002).

[148] T. Schulz, M. Albrecht, K. Irmscher, C. Hartmann, J. Wollweber, and R. Fornari, "Ultraviolet luminescence in AlN", Phys. Status Solidi Basic Res. **248**, 1513 (2011).

[149] N. Nepal, M.L. Nakarmi, J.Y. Lin, and H.X. Jiang, "Photoluminescence studies of impurity transitions in AlGaN alloys", Appl. Phys. Lett. **89**, 092107 (2006).

[150] K.B. Nam, M.L. Nakarmi, J.Y. Lin, and H.X. Jiang, "Deep impurity transitions involving cation vacancies and complexes in AlGaN alloys", Appl. Phys. Lett. **86**, 222108 (2005).

[151] B.E. Gaddy, Z. Bryan, I. Bryan, R. Kirste, J. Xie, R. Dalmau, B. Moody, Y. Kumagai, T. Nagashima, Y. Kubota, T. Kinoshita, A. Koukitu, Z. Sitar, R. Collazo, and D.L. Irving, "Vacancy compensation and related donor-acceptor pair recombination in bulk AlN", Appl. Phys. Lett. **103**, 161901 (2013).

[152] G.A. Slack and T.F. McNelly, "Growth of high purity AlN crystals", J. Cryst. Growth **34**, 263 (1976).

[153] M. Bickermann, B.M. Epelbaum, O. Filip, P. Heimann, S. Nagata, and A. Winnacker, "Structural properties of aluminum nitride bulk single crystals grown by PVT", Phys. Status Solidi **5**, 1502 (2008).

[154] C. Hartmann, J. Wollweber, S. Sintonen, A. Dittmar, L. Kirste, S. Kollowa, K. Irmscher, and M. Bickermann, "Preparation of deep UV transparent AlN substrates with high structural perfection for optoelectronic devices", CrystEngComm **18**, 3488 (2016).

[155] J.S. Harris, J.N. Baker, B.E. Gaddy, I. Bryan, Z. Bryan, K.J. Mirrielees, P. Reddy, R. Collazo, Z. Sitar, and D.L. Irving, "On compensation in Si-doped AlN", Appl. Phys. Lett. **112**, 152101 (2018).

[156] Q. Yan, A. Janotti, M. Scheffler, and C.G. Van de Walle, "Origins of optical absorption and emission lines in AlN", Appl. Phys. Lett. **105**, 111104 (2014).

[157] J. Pastrňák, S. Pačesová, and L. Roskovcová, "Luminescent properties of the oxygen impurity centres in AlN", Czechoslov. J. Phys. **24**, 1149 (1974).

[158] G.A. Slack, L.J. Schowalter, D. Morelli, and J.A. Freitas, "Some effects of oxygen impurities on AlN and GaN", J. Cryst. Growth **246**, 287 (2002).

[159] A. Uedono, S. Ishibashi, S. Keller, C. Moe, P. Cantu, T.M. Katona, D.S. Kamber, Y. Wu, E. Letts, S.A. Newman, S. Nakamura, J.S. Speck, U.K. Mishra, S.P. Denbaars, T. Onuma, and S.F. Chichibu, "Vacancy-oxygen complexes and their optical properties in AlN epitaxial films studied by positron annihilation", J. Appl. Phys. **105**, 054501 (2009).

[160] B.E. Gaddy, Z. Bryan, I. Bryan, J. Xie, R. Dalmau, B. Moody, Y. Kumagai, T. Nagashima, Y. Kubota, T. Kinoshita, A. Koukitu, R. Kirste, Z. Sitar, R. Collazo, and D.L. Irving, "The role of the carbon-silicon complex in eliminating deep ultraviolet absorption in AlN", Appl. Phys. Lett. **104**, 202106 (2014).

[161] A. Fara, F. Bernardini, and V. Fiorentini, "Theoretical evidence for the semi-insulating character of AlN", J. Appl. Phys. **85**, 2001 (1999).

[162] V.A. Soltamov, I.V. Ilyin, A.A. Soltamova, D.O. Tolmachev, E.N. Mokhov, and P.G. Baranov, "Identification of the deep-level defects in AlN single crystals: EPR and TL studies", Diam. Relat. Mater. **20**, 1085 (2011).

[163] V.A. Soltamov, I. V. Ilyin, A.A. Soltamova, D.O. Tolmachev, N.G. Romanov, A.S. Gurin, V.A. Khramtsov, E.N. Mokhov, Y.N. Makarov, G. V. Mamin, S.B. Orlinskii, and P.G. Baranov, "Shallow Donors and Deep-Level Color Centers in Bulk AlN Crystals: EPR, ENDOR, ODMR and Optical Studies", Appl. Magn. Reson. **44**, 1139 (2013).

[164] A. Hung, S.P. Russo, D.G. McCulloch, and S. Prawer, "An ab initio study of structural properties and single vacancy defects in Wurtzite AlN", J. Chem. Phys. **120**, 4890 (2004).

[165] Y. Hong-Gang, C. Guang-De, Z. You-Zhang, and and L. Hui-Min, "First principle study of nitrogen vacancy in aluminium nitride", Chinese Phys. **16**, 3803 (2007).

[166] D.F. Hevia, C. Stampfl, F. Viñes, and F. Illas, "Microscopic origin of n -type behavior in Si-doped AlN", Phys. Rev. B **88**, 085202 (2013).

[167] Y. Zhang, W. Liu, and H. Niu, "Native defect properties and p -type doping efficiency in group-IIA doped *wurtzite* AlN", Phys. Rev. B **77**, 035201 (2008).

[168] Q. Zhou, Z. Zhang, H. Li, S. Golovynskyi, X. Tang, H. Wu, J. Wang, and B. Li, "Below bandgap photoluminescence of an AlN crystal: Co-existence of two different charging states of a defect center", APL Mater. **8**, 081107 (2020).

[169] D.C. Look and J.H. Leach, "On the accurate determination of absorption coefficient from reflectanceand transmittance measurements: Application to Fe-doped GaN", J. Vac. Sci. Technol. B, Nanotechnol. Microelectron. Mater. Process. Meas. Phenom. **34**, 04J105 (2016).

[170] J. Yang, G.J. Brown, M. Dutta, and M.A. Stroscio, "Photon absorption in the Restrahlen band of thin films of GaN and AlN: Two phonon effects", J. Appl. Phys. **98**, 043517 (2005).

[171] J. Szczepanski and M. Vala, "The ν1+ν3 combination mode of C3 in Ar and Kr matrices: Evidence for a bent structure", J. Chem. Phys. **99**, 7371 (1993).

[172] B.R. Davidson, R.C. Newman, T.J. Bullough, and T.B. Joyce, "Dynamics of the H-CA, complex in GaAs", Phys. Rev. B **48**, 17106 (1993).

[173] B. Clerjaud, D. Côte, W. Hahn, and W. Ulrici, "Carbon-hydrogen complex in GaP", Appl. Phys. Lett. **58**, 1860 (1998).

[174] W. Limmer, W. Ritter, R. Sauer, B. Mensching, C. Liu, and B. Rauschenbach, "Raman scattering in ion-implanted GaN", Appl. Phys. Lett. **72**, 2589 (1998).

[175] W.E. Fenwick, A. Asghar, S. Gupta, H. Kang, M. Strassburg, N. Dietz, S. Graham, M.H. Kane, and I.T. Ferguson, "Manganese-induced long-range lattice disorder and vacancy formation in metal-organic chemical vapor deposition grown and ion-implanted Ga1−xMnxN", J. Vac. Sci. Technol. A Vacuum, Surfaces, Film. **24**, 1640 (2006).

[176] A. Nikolenko, V. Strelchuk, B. Tsykaniuk, D. Kysylychyn, G. Capuzzo, and A. Bonanni, "Resonance raman spectroscopy of Mn-Mgk cation complexes in GaN", Crystals **9**, 235 (2019).

[177] H.C. Alt, H.E. Wagner, A. Glacki, C. Frank-Rotsch, and V. Häublein, "Isotopic study of mid-infrared vibrational modes in GaAs related to carbon and nitrogen impurities", Phys. Status Solidi **252**, 1827 (2015).

[178] C. Künneth, S. Kölbl, H.E. Wagner, V. Häublein, A. Kersch, and H.C. Alt, "Symmetry and structure of carbon-nitrogen complexes in gallium arsenide from infrared spectroscopy and first-principles calculations", J. Appl. Phys. **123**, 161553 (2018).

[179] I. Gamov, E. Richter, M. Weyers, G. Gärtner, and K. Irmscher, "Carbon doping of GaN: Proof of the formation of electrically active tri-carbon defects", J. Appl. Phys. **127**, 205701 (2020).

[180] L.E. McNeil, M. Grimsditch, and R.H. French, "Vibrational Spectroscopy of Aluminum Nitride", J. Am. Ceram. Soc. **76**, 1132 (1993).

[181] K. Ishioka, K. Kato, N. Ohashi, H. Haneda, M. Kitajima, and H. Petek, "Effect of n- and p-type Doping on Coherent Phonons in GaN", J. Phys. Condens. Matter **25**, 205404 (2013).

[182] M.D. McCluskey, "Local vibrational modes of impurities in semiconductors", J. Appl. Phys. **87**, 3593 (2000).

[183] M.D. McCluskey and E.E. Haller, "Hydrogen in III-V and II-VI Semiconductors", Semicond. Semimetals **61**, 373 (1999).

[184] V. Darakchieva, B. Monemar, A. Usui, M. Saenger, and M. Schubert, "Lattice parameters of bulk GaN fabricated by halide vapor phase epitaxy", J. Cryst. Growth **310**, 959 (2008).

[185] J. M.L. Martin, J. El-Yazal, and J.P. François, "Structure and vibrational spectra of carbon clusters Cn (n = 2-10, 12, 14, 16, 18) using density functional theory including exact exchange contributions", Chem. Phys. Lett. **242**, 570 (1995).

[186] W. Weltner and R.J. Van Zee, "Carbon Molecules, Ions, and Clusters", Chem. Rev. **89**, 1713 (1989).

[187] A. Van Orden and R.J. Saykally, "Small carbon clusters: Spectroscopy, structure, and energetics", Chem. Rev. **98**, 2313 (1998).

[188] J. Szczepanski, C. Wehlburg, and M. Vala, "C3-carbon cluster anion: Structure and asymmetric stretching mode frequency", J. Phys. Chem. A **101**, 7039 (1997).

[189] D.O. Demchenko, I.C. Diallo, and M.A. Reshchikov, "Hydrogen-carbon complexes and the blue luminescence band in GaN", J. Appl. Phys. **119**, 035702 (2016).

[190] S. Suihkonen, S. Pimputkar, J.S. Speck, and S. Nakamura, "Infrared absorption of hydrogen-related defects in ammonothermal GaN", Appl. Phys. Lett. **108**, 202105 (2016).

[191] A.K. Arora and A.K. Ramdas, "Resonance Raman scattering from defects in CdSe", Phys. Rev. B **35**, 4345 (1987).

[192] A. Merlen, J.G. Buijnsters, and C. Pardanaud, "A Guide to and Review of the Use of Multiwavelength Raman Spectroscopy for Characterizing Defective Aromatic Carbon Solids: from Graphene to Amorphous Carbons", Coatings 2017, Vol. 7, Page 153 **7**, 153 (2017).

[193] R.N. Gontijo, G.C. Resende, C. Fantini, and B.R. Carvalho, "Double resonance Raman scattering process in 2D materials", J. Mater. Res. 2019 3412 **34**, 1976 (2019).

[194] D.Y. Song, S.A. Nikishin, M. Holtz, V. Soukhoveev, A. Usikov, and V. Dmitriev, "Decay of zone-center

phonons in GaN with A1, E1, and E2 symmetries", J. Appl. Phys. **101**, 053535 (2007).

[195] H. Morkoç, *Nitride Semiconductors and Devices* (Springer Berlin Heidelberg, Berlin, Heidelberg, 1999).

[196] M.A. Reshchikov, O. Andrieiev, M. Vorobiov, B. McEwen, S. Shahedipour-Sandvik, D. Ye, and D.O. Demchenko, "Stability of the CNHi Complex and the Blue Luminescence Band in GaN", Phys. Status Solidi 2100392 (2021).

[197] M.A. Reshchikov, D.O. Demchenko, J.D. McNamara, S. Fernández-Garrido, and R. Calarco, "Green luminescence in Mg-doped GaN", Undefined **90**, (2014).

[198] M.A. Reshchikov, "Giant shifts of photoluminescence bands in GaN", J. Appl. Phys. **127**, 055701 (2020).

[199] Z. Liliental-Weber, T. Tomaszewicz, D. Zakharov, and M.A. O'Keefe, "Defects in p-doped bulk GaN crystals grown with Ga polarity", J. Cryst. Growth **281**, 125 (2005).

[200] J. Li, K.B. Nam, M.L. Nakarmi, J.Y. Lin, H.X. Jiang, P. Carrier, and S.H. Wei, "Band structure and fundamental optical transitions in wurtzite AlN", Appl. Phys. Lett. **83**, 5163 (2003).

[201] H. Yamashita, K. Fukui, S. Misawa, and S. Yoshida, "Optical properties of AlN epitaxial thin films in the vacuum ultraviolet region", J. Appl. Phys. **50**, 896 (1979).

[202] V.A. Soltamov, M.K. Rabchinskii, B. V. Yavkin, O.P. Kazarova, S.S. Nagalyuk, V.Y. Davydov, A.N. Smirnov, V.F. Lebedev, E.N. Mokhov, S.B. Orlinskii, and P.G. Baranov, "Properties of AlN single crystals doped with Beryllium via high temperature diffusion", Appl. Phys. Lett. **113**, 082104 (2018).

[203] R. Collazo, J. Xie, B.E. Gaddy, Z. Bryan, R. Kirste, M. Hoffmann, R. Dalmau, B. Moody, Y. Kumagai, T. Nagashima, Y. Kubota, T. Kinoshita, A. Koukitu, D.L. Irving, and Z. Sitar, "On the origin of the 265 nm absorption band in AlN bulk crystals", Appl. Phys. Lett. **100**, 191914 (2012).

[204] J.J. Markham, *F-Centers in Alkali Halides* (Academic Press, New York, 1966).

[205] Y.C. Chang, A.E. Oberhofer, J.F. Muth, R.M. Kolbas, and R.F. Davis, "Optical metastability of subband gap (2.2 eV) yellow luminescence in GaN", Appl. Phys. Lett. **79**, 281 (2001).

[206] Y.C. Chang, A.L. Cai, M.A.L. Johnson, J.F. Muth, R.M. Kolbas, Z.J. Reitmeier, S. Einfeldt, and R.F. Davis, "Electron-beam-induced optical memory effects in GaN", Appl. Phys. Lett. **80**, 2675 (2002).

[207] A. V. Egranov, T.Y. Sizova, R.Y. Shendrik, and N.A. Smirnova, "Effect of cationic impurities on the formation of radiation defects in alkaline earth fluorides", Bull. Russ. Acad. Sci. Phys. **79**, 280 (2015).

[208] A. V. Egranov, R.Y. Shendrik, T.Y. Sizova, and V.A. Kozlovskiy, "Are the Photochromic Centers in Alkaline-Earth Fluorides Analogous to DX Centers in Semiconductors?", Bull. Russ. Acad. Sci. Phys. **83**, 314 (2019).

[209] R.U.A. Khan, P.M. Martineau, B.L. Cann, M.E. Newton, and D.J. Twitchen, "Charge transfer effects, thermoand photochromism in single crystal CVD synthetic diamond", J. Phys. Condens. Matter **21**, 364214 (2009).

[210] P. Koidl, K.W. Blazey, W. Berlinger, and K.A. Müller, "Photochromism in Ni-doped SrTiO3", Phys. Rev. B **14**, 2703 (1976).

[211] B.W. Faughnan, "Photochromism in transition-metal-doped SrTiO3", Phys. Rev. B **4**, 3623 (1971).

[212] J.H. Harris and R.A. Youngman, "An Investigation of Light Induced Defects in Aluminum Nitride Ceramics", MRS Proc. **242**, 451 (1992).

[213] G. Okada, T. Kato, D. Nakauchi, K. Fukuda, and T. Yanagida, "Photochromism and thermally and optically stimulated luminescences of AlN ceramic plate for UV sensing", Sensors Mater. **28**, 897 (2016).

[214] G. Okada, K. Fukuda, S. Kasap, and T. Yanagida, "Aluminum Nitride Ceramic as an Optically Stimulable Luminescence Dosimeter Plate", Photonics **3**, 23 (2016).

[215] T. Yanagida, "Inorganic scintillating materials and scintillation detectors", Proc. Japan Acad. Ser. B Phys. Biol. Sci. **94**, 75 (2018).

[216] D.M. Spiridonov, D. V. Chaikin, N.A. Martemyanov, A.S. Vokhmintsev, and I.A. Weinstein, "Specific Features of Spectrally Resolved Thermoluminescence in UV-Irradiated Aluminum Nitride Microcrystals", Opt. Spectrosc. **128**, 1430 (2020).

[217] M. Bickermann, A. Münch, B.M. Epelbaum, O. Filip, P. Heimann, S. Nagata, and A. Winnacker, "Polarization-dependent below band-gap optical absorption of aluminum nitride bulk crystals", J. Appl. Phys. **103**, 073522 (2008).

[218] A. Sedhain, J.Y. Lin, and H.X. Jiang, "Nature of optical transitions involving cation vacancies and complexes in AlN and AlGaN", Appl. Phys. Lett. **100**, 221107 (2012).

[219] R.C. Newman, "Infra-red Absorption due to Localized Modes of Vibration of Impurity Complexes in Ionic and Semiconductor Crystals", Adv. Phys. **18**, 545 (1969).

B. Peer-reviewed Articles

I. Gamov, C. Hartmann, T. Straubinger, and M. Bickermann *"Photochromism and influence of point defect charge states on optical absorption in aluminum nitride (AlN)",* Journal of Applied Physics **129**, 113103 (2021);[28]
https://doi.org/10.1063/5.0044519

I. Gamov, E. Richter, M. Weyers, G. Gärtner, and K. Irmscher,*"Carbon doping of GaN: Proof of the formation of electrically active tri-carbon defects"* (marked as editors-pick), Journal of Applied Physics 127, 205701 (2020);[179]
https://doi.org/10.1063/5.0010844

I. Levine*, I. Gamov*, M. Rusu, K. Irmscher, C. Merschjann, E. Richter, M. Weyers, and Th. Dittrich, *"Bulk photovoltaic effect in carbon-doped gallium nitride revealed by anomalous surface photovoltage spectroscopy",* Phys. Rev. B 101, 245205 (2020);[27]
https://doi.org/10.1103/PhysRevB.101.245205
*equal contribution authors

I. Gamov, C. Hartmann, J. Wollweber, A. Dittmar, T. Straubinger, M. Bickermann, I. Kogut, H. Fritze, K. Irmscher, *"Carbon pair defects in aluminum nitride"* (marked as editors-pick), Journal of Applied Physics, 126, 21 (2019);[21]
https://doi.org/10.1063/1.5123049

K. Irmscher, I. Gamov, E. Nowak, G. Gärtner, F. Zimmermann, F. C. Beyer, E. Richter, M. Weyers, and G. Tränkle. *"Tri-carbon defects in carbon doped GaN",* Appl. Phys. Lett. 113, 262101 (2018);[18]
https://doi.org/10.1063/1.5064432

I. Kogut, C. Hartmann, I. Gamov, Y. Suhak, M. Schulz, S. Schröder, J. Wollweber, A. Dittmar, K. Irmscher, T. Straubinger, M. Bickermann, H. Fritze, *"Electromechanical losses in carbon- and oxygen- containing bulk AlN single crystals"*, Solid State Ionics, 343 (2019)[46]
https://doi.org/10.1016/j.ssi.2019.115072

E. Richter, F.C. Beyer, F. Zimmermann, G. Gärtner, K. Irmscher, I. Gamov, J. Heitmann, M. Weyers, G. Tränkle, *"Growth and Properties of Intentionally Carbon-Doped GaN Layers",* Crystal Research and Technology (2019);[38]
https://doi.org/10.1002/crat.201900129

F. Zimmermann, J. Beyer, F. C. Beyer, G. Gärtner, I. Gamov, K. Irmscher, E. Richter, M. Weyers, and J. Heitmann, *"A carbon-doping related luminescence band in GaN revealed by below bandgap excitation"* Journal of Applied Physics **130**, 055703 (2021);[19]
https://doi.org/10.1063/5.0053940

C. Conference contributions

31st International Conference on Defects in Semiconductors (ICDS-31, 2021)

pre-recorded video and poster presentation

I. Gamov, E. Richter, M. Weyers, G. Gärtner, H. Scheel, N. Jankowski, M. R. Wagner, A. Hoffmann, K. Irmscher, *"Vibrational modes of mono-, di- and tri-carbon defects in GaN:C"*

Deutsche Gesellschaft für Kristallwachstum und Kristallzüchtung e. V. (DGKK-Arbeitskreises "Massive Halbleiter", 2019)

oral presentation

I. Gamov, K. Irmscher, E. Richter, M. Weyers, *"Identification of Tri-Carbon Defects in Gallium Nitride"*

International Conference on Defects-Recognition, Imaging and Physics in Semiconductors (DRIP-18, 2019)

oral presentation

I. Gamov, K. Irmscher, E. Richter and M. Weyers, *"Characterization of carbon defects in GaN"*

International Symposium on Growth of III-Nitrides (ISGN-7, 2018)

oral presentation

I. Gamov, E. Nowak, G. Gärtner, F. Zimmermann, F.C. Beyer, E. Richter, M. Weyers, K. Irmscher, *"Carbon-doped GaN: Identification of tri-carbon defects formed at substantial fraction"*

oral presentation

I. Gamov, C. Hartmann, A. Dittmar, J. Wollweber, M. Bickermann, I. Kogut, H. Fritze, K. Irmscher, *"Di-carbon defects in AlN bulk crystals grown by physical vapor transport"*

D. Acknowledgments

I thank everyone who supported me in my research. First of all, I am very grateful to *Prof. Dr. Matthias Bickermann* for the opportunity and trust to work at his project; his recommendations and advice have always motivated and steered me in the right direction. *Dr. Klaus Irmscher* critically influenced on my cognition of the spectroscopy methods. I am glad that this optimistic and keen person supported me at the beginning of working at Leibniz-Institut für Kristallzüchtung (IKZ) and helped explain the first results. Also, I appreciate the impact of *Dr. John Lyons* on this work; he appeared at the right moment just at the ending of my work; he breathed new life into the project and supported the research with recent calculations. The discussion with him allowed us to combine the computational methods and experiments wonderfully.

Then, I am grateful to the whole committee, *Prof. Dr. Michael Lehmann, Prof. Dr. Michael Reshchikov, Prof. Dr. Michael Kneissl*, and *Prof. Dr. Matthias Bickermann* for reviewing this thesis.

There are also people without whom this research would be fundamentally impossible. They are: *Dr. Eberhard Richter* and *Prof. Dr. Markus Weyers*, who had grown the incredible series of GaN samples, including ^{13}C-enriched; *Dr. Carsten Hartmann* and *Dr. Thomas Straubinger*, who had grown such beautiful gradient AlN crystals.

Dr. Thomas Dittrich and *Dr. Igal Levine* piqued my interest in photovoltaic methods, and only together with them was it possible to understand what occurs in the investigated crystals.

I am also very grateful to *Prof. Dr. Michal Bockowski*, *Dr. Tomasz Sochacki* for GaN-on-GaN samples and interesting ideas, *Prof. Dr. Axel Hoffmann* for scientific adventurism, *Prof. Dr. Michael Reshchikov* for a fresh perspective on the results, *Prof. Dr. Markus Wagner, Dr. Harald Scheel, Dr. Manfred Rammsteiner* for the organization of additional Raman equipment, *Dr. Günter Gärtner, Dr. Franziska Beyer, Dr. Jan Beyer* for help with PL and FTIR measurements, and *Dr. Martin Albreicht* and *Prof. Dr. Thomas Schröder* for rare but valuable hints. I also appreciate the all-around support and warm atmosphere generated by *Dr. Iurii Kogut, Albert Kwasniewski, Dr. Tobias Shultz, Leonardo Cancellara, Palvan Seyidov, Dr. Uta Juda*, and *Ewelina Nowak*.

Last but not least, I express my deepest gratitude to my family, friends, and *M*, who were my reliance.